Engineering Materials

Annelise Kopp Alves *Editor*

Nanomaterials for Eco-friendly Applications

Springer

Engineering Materials

This series provides topical information on innovative, structural and functional materials and composites with applications in optical, electrical, mechanical, civil, aeronautical, medical, bio- and nano-engineering. The individual volumes are complete, comprehensive monographs covering the structure, properties, manufacturing process and applications of these materials. This multidisciplinary series is devoted to professionals, students and all those interested in the latest developments in the Materials Science field.

More information about this series at http://www.springer.com/series/4288

Annelise Kopp Alves
Editor

Nanomaterials for Eco-friendly Applications

Springer

Editor
Annelise Kopp Alves
UFRGS
Porto Alegre, Brazil

ISSN 1612-1317 ISSN 1868-1212 (electronic)
Engineering Materials
ISBN 978-3-030-26809-1 ISBN 978-3-030-26810-7 (eBook)
https://doi.org/10.1007/978-3-030-26810-7

This Springer imprint is published by the registered company Springer Nature Switzerland AG
The registered company address is: Gewerbestrasse 11, 6330 Cham, Switzerland

Contents

CNT Sponges for Environmental Applications

Claudir Gabriel Kaufmann Jr. and Juliano Schorne-Pinto

Abstract The synthesis of 3D architectures composed of carbon nanotubes (CNT) is one of the most exciting and challenging research domains in nanotechnology. These systems have great potential for supercapacitors, catalytic electrodes, artificial muscles and in environmental applications. In this chapter, we present an overview of the CNT sponges, which are characterized by high hydrophobicity, high oil absorption capacity, high-performance in mechanical test and high porosity making it an attractive candidate for environmental applications.

Keywords CNTs · CNT sponge · Environmental applications

Abbreviations

CNTs	Carbon nanotubes
CVD	Chemical Vapor Deposition
DWCNT	Double Wall Carbon Nanotubes
MWCNT	Multiple Wall Carbon Nanotubes
SEM	Scanning Electron Microscopy
SWCNT	Single Wall Carbon Nanotubes
S3DCNT	Three-dimensional Structures of Carbon Nanotubes
TEM	Transmission Electron Microscopy

C. G. Kaufmann Jr. (✉)
Universidade Federal do Rio Grande do Sul, Porto Alegre, Brazil
e-mail: gabriel.kaufmann@ufrgs.br; gabrielklpgodines@gmail.com

J. Schorne-Pinto
Université de Toulouse, Toulouse, France

A. Kopp Alves (ed.), *Nanomaterials for Eco-friendly Applications*,
Engineering Materials, https://doi.org/10.1007/978-3-030-26810-7_1

1 Introduction

Since the first synthesis of CNT by Iijima [23], the scientific community has been searching for methods that provide control and quality in the production of these nanostructures. The control of the morphology and structural arrangement of the CNT is a critical point to the mechanical, magnetic, optical and electrical properties once they are directly related to CNT's structure and atomic arrangement [1]. The available literature shows the existence of a strong correlation between multi-walled carbon nanotubes (MWCNTs) mechanical properties and its structural arrangement. Besides, the mechanical resistance of MWCNTs will often be directly dependent on the degree of structural disorder of these CNT [1, 2].

The principal methods for the production of CNT, according to the literature, are chemical vapor deposition (CVD) [3, 4]; combustion [5]; laser ablation [6] and electric arc [7]. The CVD method produces CNT from the deposition of precursor gases of carbon atoms, and the combustion method by the combustion of percussive carbon gases. In the laser ablation and electric arc method, the production of CNT occurs by the sublimation of carbon atoms from a solid source, often mineral graphite. The CVD technique allows the controlled and orderly production of a wide range of carbon nanostructures and the most diverse elements. The main advantage of CVD in comparison to the other methods mentioned above is that the CVD allows detailed control of all the parameters used in the CNT synthesis, such as gas flow, type of catalyst, temperature, the physical state of the precursors, among others.

Several works are based on the production of CNT by CVD, as well as the production of two-dimensional CNT (2D) structures, such as carbon nano-fibers [8]. Recent works have reported the CVD synthesis of three-dimensional (3D) structures of CNT [9–14]. The main innovation shown in these works was the capacity to produce in just one process 3D macrostructures entire formed by CNT. Most of the syntheses of CNT sponges by CVD have used so far ferrocene (as a catalyst) by aerosol or sublimation [10, 11, 15]. Recently, it was presented the production of these sponges using a nanostructured catalyst powder, the magnesium ferrite ($MgFe_2O_3$) [14].

The production of 3D carbon structures with controlled density and architecture is one of the most desirable steps for building next-generation carbon-based functional materials [11]. These structures have potential application in areas such as supercapacitors [16], catalytic electrodes [17], artificial muscles [18], gas absorbers [19] and environmental applications [15]. CNT sponges have emerged as a viable and revolutionary tool for treating effluents (potable water) and for controlling maritime disasters due to the high degree of oil absorption (industrial liquids and household waste). Other important properties are hydrophobic character and reusability.

CNT and CNT sponges will be covered in this book chapter. The focus of the discussion will be on the routes of synthesis of CNT sponges, their properties and environmental applications.

2 Carbon and Carbon Nanotubes

2.1 Carbon

Carbon is a versatile element, capable of forming a vast amount of compounds. Many bonds can be made with other elements, such as oxygen, hydrogen, nitrogen, among others, as well as with other carbon atoms forming molecules constituted only by carbon. These compounds formed by carbons with structures are called allotropic, i.e., structures with different geometric arrangements. This characteristic differs from other chemical elements. In function of temperature and pressure conditions, compounds formed by carbon can present entirely different structures and properties, as in the case of graphite, diamond and new structures are known as fullerenes, graphene and carbon nanotubes [20].

The carbon-structures presented above have different characteristics, properties, and morphologies. The explanation to these differences is how the carbon atoms are linked to one another, as well its distribution in the structure of these materials. In the case of diamond, the carbon atoms exhibit sp3 hybridization in their atomic orbitals, due to this orientation the diamond presents a very rigid, stable and insulating configuration. The graphite has an sp2 configuration of molecular hybridization, forming a hexagonal structure in layers of carbon; for this reason, the graphite is an excellent electric conductor and presents little stiffness [21].

Until the year 1985, just three allotropes of carbon were known: amorphous carbon, graphite, and diamond. However, the work of Kroto presented a new one, the fullerenes [22] that opens the mind of the research community to new possible allotropes of carbon. The molecules of fullerenes are nanometric structures that show sp2 hybridization, which can present numerous structural configurations, and its name is based in the number of atoms the carbon that was constituting them, such as the fullerenes C60 (constituted by sixty atoms of carbon), C70 (constituted by seventy atoms of carbon), and so on. In the case of the C60 molecule, it consists of 20 pentagonal faces and 12 hexagonal faces, where carbon atoms occupy the 60 vertices; analogously one can compare the structure of this molecule in the form of a soccer ball. Fullerenes present new and unique physicochemical and structural properties, raising the interest of many scientific areas, due to their high potential for application in numerous areas (such as electronics, biological, chemical, physical, and other materials). Beyond the fullerenes, another carbon allotrope was observed in 1991, this one called carbon nanotubes [22, 23].

2.2 Carbon Nanotubes

Carbon nanotubes were elucidated by Iijima in 1991 [23] when the author initially sought the production of fullerenes. In this study, the author used the method of synthesis described by Kroto in 1985 [22], i.e., the method of the electric arc dis-

charge. After the synthesis, Iijima observed the formation of carbon nanostructures in the form of tubes, which he called carbon nanotubes. Depending on the procedure adopted in the synthesis, it is possible to obtain a single wall (SWCNT), double wall (DWCNT) or multiple walls (MWCNT) CNT.

The SWCNT may be understood as a structure formed from a single coiled graphite layer, the ends of which may be closed by halves of fullerenes or may be opened. The carbon atoms in the SWCNT form a hexagonal network, consisting of single and double bonds with sp2 hybridization. These CNTs have diameters less than 100 nm and several micrometers in length, and because they have physical properties of crystalline solids, they can be considered as crystals rather than molecular species [24].

MWCNTs, on the other hand, are formed by several SWCNT in concentric shapes similar to a coaxial cable. The MWCNTs present in their tubes average diameters between 1 and 1000 nm and, like the SWCNT, several micrometers in length [24].

When the CNT is synthesized, there are many possibilities in the direction in which the CNT axis will be generated. In this way, the CNT is defined concerning their physicochemical properties concerning the direction of their vectors and the chiral angle. The chiral vector is defined by the following Eq. 1:

$$\mathrm{Ch} = n\mathrm{a}_1 + m\mathrm{a}_2 \tag{1}$$

where a_1, and a_2 are unit vectors of graphene itself, n, and m are integers (obtained from x and y in each layer). This vector connects two crystallographically equivalent sites on the 2D layer of graphene.

The chiral angle is the angle to the orientation of the C–C bonds in the CNT, each (n, m) defines a different way of rolling the graphite layer. According to the limits of (n, m), we can classify the CNT as armchair when $n = m \neq 0$; zigzag when $n \neq 0$ and $m = 0$ and chirals when $n \neq 0$ and $m \neq 0$. This chirality (Fig. 1) directly influences the physical and chemical properties of CNT: armchair are metallic CNT, and zigzag and chiral are semiconductors [2].

3 Chemical Vapor Deposition (CVD)

The first report of CNT production by this technique occurred in 1959 by Walker et al. [25]. Later in 1993, Yacamám et al. improved the CVD technique for the production of CNT [26]. Figure 2 shows a detailed schematic drawing of the components constituting a classic CVD reactor.

The CVD method produces CNT by the deposition of gaseous and volatile carbon sources such as methane, ethylene, and acetylene [4]. This process requires the use of catalysts for the growth of nanotubes. Generally, the catalysts used are transition metals like Fe, Co, and Ni, in the form of nanoparticles [24]. A dispersing oxide such as MgO is often used near the metal. During the synthesis, the gaseous source (carbon precursor) is decomposed and nucleated in situ by the metal particles of

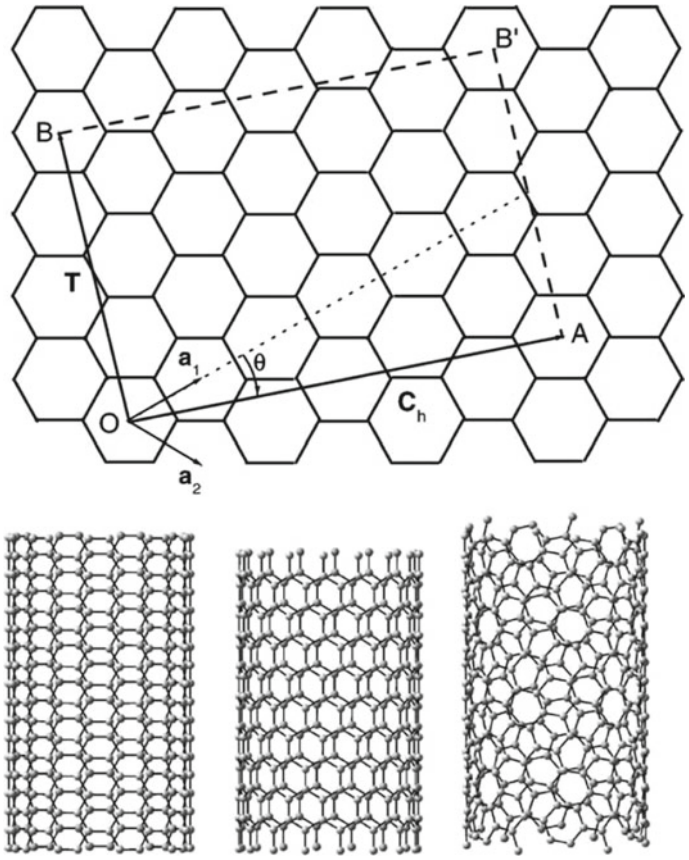

Fig. 1 Chiral vectors and the different CNT structures: zig zag; chiral and armchair. Reproduced from Popov [2] Copyright 2004, with permission from Elsevier

the catalyst, where the carbon nanostructures grow. This process is carried out at temperatures between 750 and 950 °C. In addition to the hydrocarbon deposition on the catalyst; the hydrogen gas is used in the CVD technique as an activator for the catalyst to reduce the metallic particles that constitute the catalyst and eliminates possible residues from its surface [27].

The synthesis parameters such as temperature, type, and degree of crystallinity of the catalyst and gas flow have a decisive character in the type of CNT formed, the quality of the tubes and their orientation (production of aligned or disordered tubes).

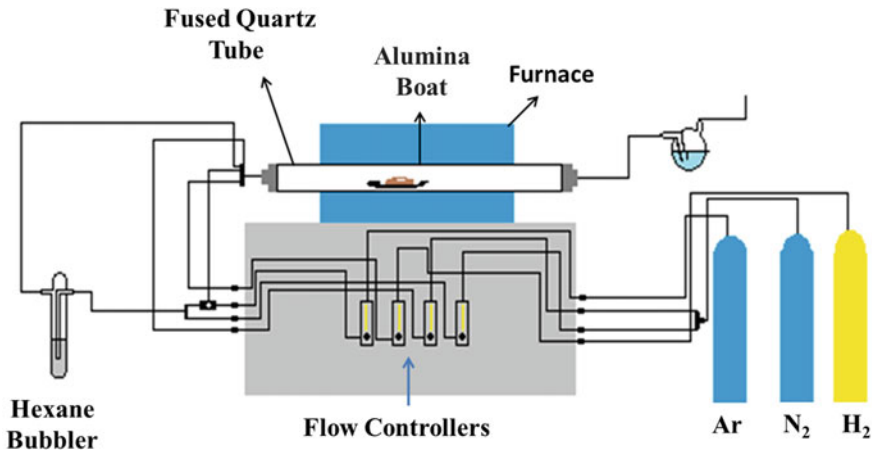

Fig. 2 Schematic drawing of a CVD reactor

4 CNT Three-Dimensional Structures

The three-dimensional structures of carbon nanotubes (S3DCNT) are arrangements formed basically by CNT and can be made by SWCNT and MWCNT. Figure 3 presents a photographic image of an S3DCNT and a possible schematic representation of these structures.

The detailed control of the synthesis parameters is directly related to the structural organization and dimensional arrangement of the CNT within the S3DCNT. Due to these factors, the electric arc and laser ablation techniques become inadequate to obtain S3DCNT because they do not present an adequate control of the synthesis parameters, resulting in disorganized and varied structures. However, using an adequate control of the synthesis parameters, it is possible to obtain materials composed

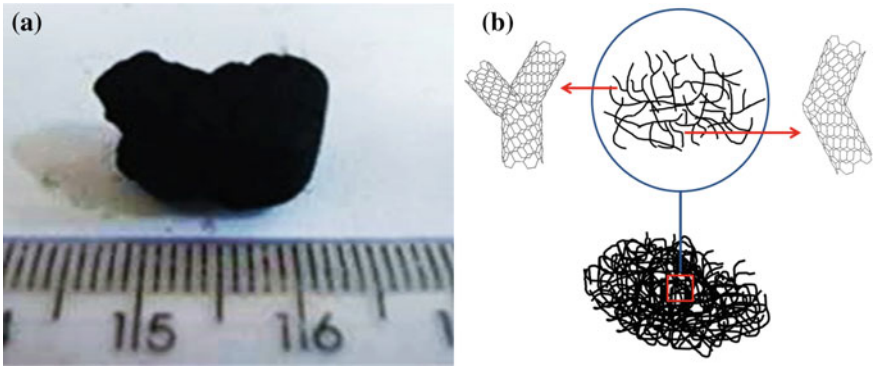

Fig. 3 Photographic image of S3DNTC (CNT sponge) and its schematic representation

of CNT with organized structures (CNT forests) and disorganized and misaligned (CNT sponges).

The CNT organized structures (CNT forests) are also known as vertically aligned CNT, consisting of CNT with nanometric diameters and with lengths of micrometers, millimeters and even centimeters. This control of orientation and height allows a wide range of future applications in the areas of electronics, electrochemistry, gas sensors, and environmental applications, among others.

In the other hand, S3DCNTs that present disorganized structures, it is now called CNT sponges and show unusual properties as low density, high porosity, and large surface area. Due to these properties, CNT sponges have a raising interest in the environmental area, because of its high capacity of adsorption, separation, and absorption of oils and reactive chemicals as organic solvents [10, 15]. Moreover, according to the literature, the disorganized three-dimensional structures have excellent thermal and mechanical stability, flexibility and a remarkable ability to absorb oils. Additionally, the low density of these structures allows a low light refraction index, potentially being the darkest material ever developed by man [15, 28].

4.1 CNT Forests

Since the study of Iijima on CNT, the research is focused on the production of CNT systems with high quality, with well-ordered typology (SWCNT or MWCNT) and organized forms (aligned and defined direction), searching future fields to these materials. The CNT forest is a result of this search. These structures present CNT with controlled diameter, length, and typology controlled, usually obtained by a CVD method or its variations.

In the study conducted by, Lepro et al. [29] NTC forests were produced by CVD using as a substrate for catalyst a flexible stainless-steel rod coated with thin films (Al, Al_2O_3, Si or SiOx) instead of conventionally used silicon pellets. The gases chosen in their study were hydrogen and argon, as an activator and inert gas, respectively. A comparison of acetylene (C_2H_2 > 99.6%) and ethylene (C_2H_4, 99.995%) was made using a temperature of 760 °C and dwell time of 10 min. The authors concluded that the aligned growth and homogeneity of CNT forests correlates directly with the substrate (thin film) at which the catalyst is deposited. The H_2 insertion had also emphasized before the synthesis temperature was reached. According to this study, hydrogen is critical for the production of denser, higher-sized NTC forests. For the percussive carbon gases (ethylene and acetylene), it was noted that both gases are indicated for the synthesis of NTC forests. However, acetylene resulted in forests with higher heights and more homogeneous than those produced by ethylene.

Kao et al. [30] obtained MWCNT forests coated with thin films of titanium nitride for possible applications as supercapacitors. These titanium-coated NTC forests had a significant surface area (about 81 m^2/g) and thus a 400-fold increase in their electrical capacity (capacitance) compared to unlined forests. Xiao et al. [31] carried out another study concerning the application of MWCNT forests, in which NTC forests

were produced on a tungsten tip. These tips are commonly used in the Atomic Force Microscope (AFM) and Scanning Tunneling Microscope (STM). The study indicated that the coating of the tungsten tip with NTCPM forests reduced tip shaking and improved conductivity. Although the results presented in the article were preliminary, they already demonstrate possible future applications of NTC forests in electron microscopes.

4.2 CNT Sponges

Gui et al. [9] reported one of the first three-dimensional structures of CNT with macroscopic size, which they called "CNT sponge" (dimensions: 4 cm long × 3 cm high × 0.8 cm wide). This sponge is constituted by multiple wall CNTs arranged in a porous structural conformation and interconnected three-dimensionally in the form of a frame. In their study, the synthesis of this sponge was performed using the CCVD method. The catalyst chosen was ferrocene, the carbon precursor was 1,2-dichlorobenzene, and the atmosphere was a combination of hydrogen (300 mL/min) and argon (2000 mL/min). The synthesis process lasted 4 h at a temperature of 860 °C. The authors concluded that material is homogeneous in composition and structure using scanning electron micrographs (SEM) and transmission (TEM). An absorption test showed that structure has a high capacity of absorption of oils and possibly of chemical residues.

A three-dimensional CNT structure also was produced in another study, by the authors Hashim et al. [10]. The structure was similar to a sponge but different from the sponge reported by Gui et al. [9] for containing boron in its three-dimensional network. This structure was obtained by a variation of the CVD method called the aerosol-assisted chemical vapor deposition method (AACVD). This method works similarly to CCVD. The difference consists in the form that catalyst is dispersed into the synthesis reactor. The catalyst used was a mixture of toluene (anhydrous), ferrocene (25 mg/mL) and triethylborane in Fe:B ratio of 5:1. The authors clarify two particular aspects of the synthesis of CNT sponges: (1) the importance of the formation of branches (joints) to obtain CNT networks; (2) the significant difference induced by the introduction of boron in the synthesis process of these structures. Boron is directly connected to the formation of branches and "elbows" or "knees" that are folded in the CNT (Fig. 4). According to this study, these "elbows" have a considerable covalent molecular energy, facilitating the formation of S3DCNT structures because they form covalent nano-junctions between the CNT. Furthermore, the sponge produced has a cyclic mechanical resistance, where it can be submitted to more than 100 cycles of loading and remain stable and unchanged.

Erbay et al. [32] fabricated MWCNT sponges by the CVD method using a commercial ferrocene catalyst and a furnace with different temperatures. The interesting detail of this synthesis process is that ferrocene was in the solid state and not in solution as in previous works. This catalyst was placed inside a silica boat in a lower temperature region of the furnace (120 °C) and was entrained by the gases during the

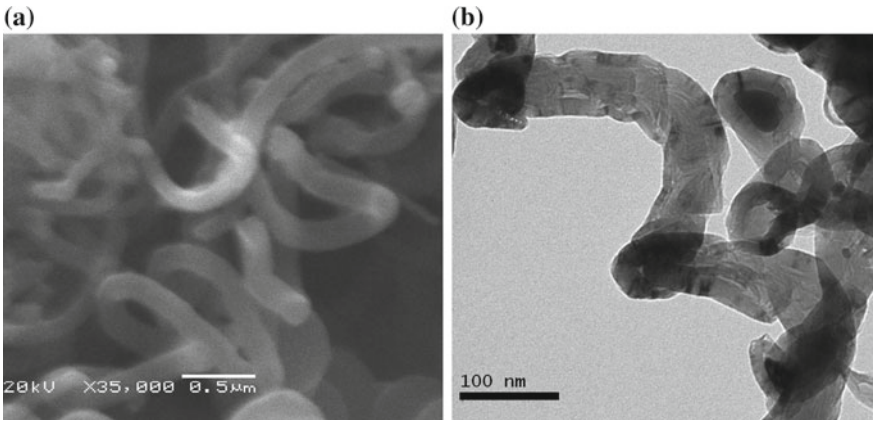

Fig. 4 SEM (**a**) and TEM (**b**) micrographs of structures similar to "elbows" or "knees"

synthesis. The sponge was formed on the quartz tube. The objective of the work was to produce electrodes for electrochemistry (high-performance anodes) or possible MWCNT batteries. The electrode produced generated high power, about 2150 W. According to the authors this power is higher than that presented by commercial pure graphite electrodes, and that these results are tied to the large surface area of the NTCPM sponge.

Yang et al. [33] performed another study using a similar CVD synthesis method. In this work, the authors aimed at the production of N-doped CNT sponges for application as electrocapacitors. The CNT sponges were posteriorly treated with a mixture of sulfuric acid and nitric acid for 5 h, then washed with deionized water and dried at room temperature. The next step was the submerged in a solution containing hydrochloric acid and aniline and sonicated for 30 min. Finally, dried and heat-treated at 900 °C for four hours. The result was CNT sponges doped with nitrogen with high electrical conductivity and high resistance to corrosion.

In the study reported by Li et al. [34], the authors obtained a CNT/nickel ferrite sponge by the ice modeling method, to use these sponges as glucose biosensors. The CNTPMs used in this research were commercially acquired (purity of 95%, mean diameter between 10–30 nm and length of 5–15 μm). The results of this study indicate that CNT/$NiFe_2O_4$ sponges present promising catalytic properties.

Siddiqa et al. [12] produced CNT sponges also using nickel as a catalyst. In this study, the authors used a Ni/Cu particle silica layer as a substrate. The sponge was produced by CVD, and the growth of the CNT occurred on both sides of the silica sheet, i.e., the blade was found inside the CNT sponge. The authors tested the absorption of CNT sponges for different solvents and mineral oils, showing a degree of absorption between 128 and 1885% of their mass. The highest value was obtained for the absorption of ethylene glycol. The oil absorption values were not higher than 600 wt%. This study demonstrated the large capacity of absorbing oils and solvents of the CNT sponges and that these structures are hydrophobic. However,

the synthesis process described in the study requires an extended time, about eight hours. This time of synthesis is the unfavorable aspect of industrial production.

Muñoz-Sandoval et al. [13] produced CNT sponges constituted by carbon-nanofibers and MWCNT doped with nitrogen using the aerosol-assisted chemical vapor deposition method (AACVD). A mixture of ferrocene, benzylamine (precursor of C and N), thiophene and ethanol was employed. The arresting gas was argon, and the activator gas was hydrogen. The synthesis temperature was 1020 °C with two hours of dwell. Vis-à-vis the absorption of solvents and fuels by the sponge, the structure presents an excellent absorption results, similar to previous studies. The great hydrophobic character of these sponges are results of the presence of MWCNT and carbon nanofibers on the surface of the material, according to the authors. However, the conclusion is not final, and new studies are necessary to describe this high hydrophobic behavior.

Recently, our research group (Laboratory of Ceramic Materials (LACER)—Federal University of Rio Grande do Sul (UFRGS), Brazil) presented the development of CNT sponges from a nanoscale powdered catalyst [14]. The synthetic route used to produce the sponge was that of classical CVD, which proved to be effective at low cost and high reproducibility. Mechanical compression tests indicated that the sponges produced have excellent mechanical resistance to cyclic tests around ~0.4 MPa. This result indicates that sponges have sufficient mechanical strength for application in operations that require some traction or compression.

According to the kerosene immersion test, 54% of the sponge volume is related to pores, presenting a low density of 0.227 g/cm^3. Herewith, the CNT sponge has a high liquid absorption capacity. Absorption tests of commercial fuels (Fig. 5a–c) indicated that in less than 1 min the sponge is capable of absorbing about 1603% of its weight in fuel and after 10 min, the value increases to 1675%. After each absorption test, the sponge was burnt (~300 °C) to remove the fuel from its structure. Figure 5d shows the burning process.

Figure 6 shows the absorption test performed with commercial gasoline and methylene blue as an indicator of alcohol. An essential factor to consider in this test is that commercial gasoline contains alcohol in its composition. The gasoline analyzed in this work is 27% ethyl alcohol. Complete absorption of gasoline (10 mL) was observed as part of the alcohol remaining on the plate. After the sponge reaches its maximum absorption capacity, 1.5 mL of alcohol remained unabsorbed. As 27% (2.7 mL) of the Brazilian gasoline composition is alcohol, it was calculated that 100% of the gasoline and 44.4% of the alcohol were absorbed. The sponge absorbs both fuels, but the velocity and the preference for absorption are highly related to the polarity of the fluid.

The CNT sponge (3D) has a strong apolar character having a contact angle of 146°. This angulation is probably related to the structural defects of the CNT and the presence of functional groups such as OH, CHO, COOH on the surface [35]. The above results show that CNT sponges synthesized with magnesium ferrite present promising properties for future environmental applications in marine disasters, for example.

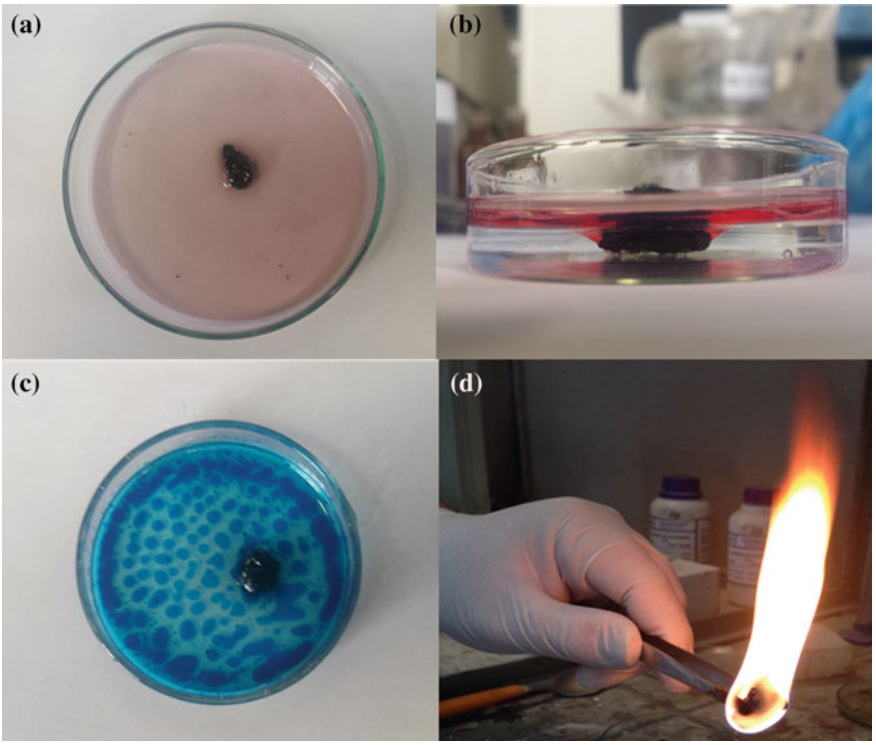

Fig. 5 Sponge in contact with **a** diesel oil; **b** diesel oil and water; **c** gasoline and methylene blue; **d** sponge burning

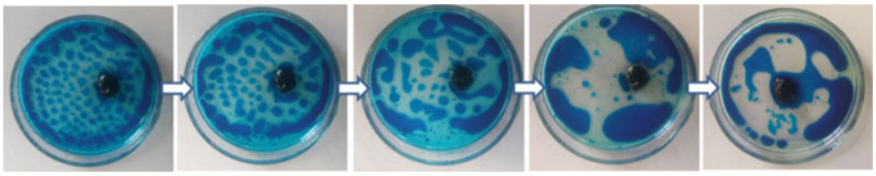

Fig. 6 Absorption test of Brazilian commercial gasoline (dyed with methylene blue)

5 Conclusion

CNT sponges are materials having a high non-polar character, a high absorption capacity of non-organic compounds, a high mechanical resistance to tensile and compression tests, and a high porosity. The sponges showed a high hydrophobic character and a rapid (about one minute) absorption of apolar fuels. All these properties indicate that CNT sponges are strong candidates for environmental applications.

These materials would be practical tools to prevent and control industrial chemical leaks, recover fluid resources contaminated by oily substances, and many other applications.

References

1. Salvetat J-P, Bonard J-M, Thomson NH (1999) Mechanical properties of carbon nanotubes. Appl Phys A 69:255–260. https://doi.org/10.1007/s003390050999
2. Popov VN (2004) Carbon nanotubes: properties and application. Mater Sci Eng R Rep 43:61–102. https://doi.org/10.1016/j.mser.2003.10.001
3. Zampiva RYS et al (2017) 3D CNT macrostructure synthesis catalyzed by $MgFe_2O_4$ nanoparticles—a study of surface area and spinel inversion influence. Appl Surf Sci 422:321–330. https://doi.org/10.1016/j.apsusc.2017.06.020
4. Kong J et al (1998) Chemical vapor deposition of methane for single-walled carbon nanotubes. Chem Phys Lett 292:567–574. https://doi.org/10.1016/S0009-2614(98)00745-3
5. Richter H et al (1996) Formation of nanotubes in low pressure hydrocarbon flames. Carbon N Y 34:427–429. https://doi.org/10.1016/0008-6223(96)87612-3
6. Ehbrecht M et al (1993) CO_2-laser-driven production of carbon clusters and fullerenes from the gas phase. Chem Phys Lett 214:34–38. https://doi.org/10.1016/0009-2614(93)85451-S
7. Biró LP et al (2003) Continuous carbon nanotube production in underwater AC electric arc. Chem Phys Lett 372:399–402. https://doi.org/10.1016/S0009-2614(03)00417-2
8. Bai H et al (2015) Multi-functional CNT/ZnO/TiO_2 nanocomposite membrane for concurrent filtration and photocatalytic degradation. Sep Purif Technol 156:922–930. https://doi.org/10.1016/j.seppur.2015.10.016
9. Gui X et al (2010) Carbon nanotube sponges. Adv Mater 22:617–621. https://doi.org/10.1002/adma.200902986
10. Hashim DP et al (2012) Covalently bonded three-dimensional carbon nanotube solids via boron induced nanojunctions. Sci Rep 2:1–8. https://doi.org/10.1038/srep00363
11. Ozden S et al (2015) 3D macroporous solids from chemically cross-linked carbon nanotubes. Small 11:688–693. https://doi.org/10.1002/smll.201402127
12. Siddiqa A et al (2015) Silica decorated CNTs sponge for selective removal of toxic contaminants and oil spills from water. J Environ Chem Eng 3:892–897. https://doi.org/10.1016/j.jece.2015.02.026
13. Muñoz-Sandoval E et al (2017) Carbon sponge-type nanostructures based on coaxial nitrogen-doped multiwalled carbon nanotubes grown by CVD using benzylamine as precursor. Carbon N Y 115:409–421. https://doi.org/10.1016/j.carbon.2017.01.010
14. Zampiva RYS et al (2017) 3D CNT macrostructure synthesis catalyzed by $MgFe_2O_4$ nanoparticles—a study of surface area and spinel inversion influence. Appl Surf Sci 422:321–330. https://doi.org/10.1016/j.apsusc.2017.06.020
15. Gui X et al (2011) Recyclable carbon nanotube sponges for oil absorption. Acta Mater 59:4798–4804. https://doi.org/10.1016/j.actamat.2011.04.022
16. Iqbal N et al (2016) Highly flexible $NiCo_2O_4$/CNTs doped carbon nanofibers for CO_2 adsorption and supercapacitor electrodes. J Colloid Interface Sci 476:87–93. https://doi.org/10.1016/j.jcis.2016.05.010
17. Fan X et al (2017) Synthesis of ordered mesoporous TiO_2-Carbon-CNTs nanocomposite and its efficient photoelectrocatalytic methanol oxidation performance. Microporous Mesoporous Mater 240:1–8. https://doi.org/10.1016/j.micromeso.2016.10.049
18. Serrano MC et al (2014) Role of polymers in the design of 3D carbon nanotube-based scaffolds for biomedical applications. Prog Polym Sci 39:1448–1471. https://doi.org/10.1016/j.progpolymsci.2014.02.004

19. Peng Y et al (2017) An optimized process for in situ formation of multi-walled carbon nanotubes in templated pores of polymer-derived silicon oxycarbide. Ceram Int 43:3854–3860. https://doi.org/10.1016/j.ceramint.2016.12.045
20. Liu Q et al (2007) Synthesis and characterization of 3D double branched K junction carbon nanotubes and nanorods. Carbon N Y 45:268–273. https://doi.org/10.1016/j.carbon.2006.09.029
21. Katsnelson MI (2007) Graphene: carbon in two dimensions. Mater Today 10:20–27. https://doi.org/10.1016/S1369-7021(06)71788-6
22. Kroto HW et al (1985) C60: Buckminsterfullerene. Nature 318:162–163. https://doi.org/10.1038/318162a0
23. Iijima S (1991) Helical microtubules of graphitic carbon. Nature 353:737–740. https://doi.org/10.1038/354056a0
24. Jorio A et al (2008) Carbon nanotubes. Springer, Berlin, Heidelberg
25. Walker PL et al (1959) Carbon formation from carbon monoxide-hydrogen mixtures over iron catalysts. I. Properties of carbon formed. J Phys Chem 63:133–140. https://doi.org/10.1021/j150572a002
26. José-Yacamán M et al (1993) Catalytic growth of carbon microtubules with fullerene structure. Appl Phys Lett 62:202–204. https://doi.org/10.1063/1.109315
27. Zhu J et al (2012) Synthesis of bamboo-like carbon nanotubes on a copper foil by catalytic chemical vapor deposition from ethanol. Carbon N Y 50:2504–2512. https://doi.org/10.1016/j.carbon.2012.01.073
28. Liu L et al (2011) Macroscopic carbon nanotube assemblies: preparation, properties, and potential applications. Small 7:1504–1520. https://doi.org/10.1002/smll.201002198
29. Lepró X et al (2010) Spinnable carbon nanotube forests grown on thin, flexible metallic substrates. Carbon N Y 48:3621–3627. https://doi.org/10.1016/j.carbon.2010.06.016
30. Kao E et al (2016) ALD titanium nitride on vertically aligned carbon nanotube forests for electrochemical supercapacitors. Sens Actuators A Phys 240:160–166. https://doi.org/10.1016/j.sna.2016.01.044
31. Xiao Y et al (2016) Transition metal carbide-based materials: synthesis and applications in electrochemical energy storage. J Mater Chem A 4:10379–10393. https://doi.org/10.1039/C6TA03832H
32. Erbay C et al (2015) Three-dimensional porous carbon nanotube sponges for high-performance anodes of microbial fuel cells. J Power Sources 298:177–183. https://doi.org/10.1016/j.jpowsour.2015.08.021
33. Yang G et al (2015) Scalable synthesis of bi-functional high-performance carbon nanotube sponge catalysts and electrodes with optimum C–N–Fe coordination for oxygen reduction reaction. Energy Environ Sci 8:1799–1807. https://doi.org/10.1039/C5EE00682A
34. Li Y et al (2016) Self-assembled $NiFe_2O_4$/carbon nanotubes sponge for enhanced glucose biosensing application. Appl Surf Sci 362:115–120. https://doi.org/10.1016/j.apsusc.2015.11.220
35. Narlikar AV, Fu YY (2017) Oxford handbook of nanoscience and technology. Oxford University Press, Oxford

Electrolytic Conversion of CO_2 to Carbon Nanostructures

Sabrina Arcaro

Abstract Different technologies are being developed to reduce emissions, and capture or store CO_2 emitted into the atmosphere. However, despite efforts, CO_2 capture methodologies continue to be a challenge to transform it into a stable, non-polluting product. In this context, the electrolytic conversion of CO_2 to carbon in molten salts has excellent possibilities for the production of large numbers of carbonaceous materials. Carbon nanostructures can be easily obtained by changing process parameters such as electrolytes, electrodes, and atmosphere. The final materials (carbon nanotubes, carbon spheres, carbon fibers) can have exceptional performance in energy conversion and storage, as well as electrocatalysis and merit future research.

Keywords Carbon nanostructures · Carbon dioxide · Electrolytic conversion CO_2

1 Introduction

Greenhouse gases are compounds capable of absorbing reflected or emitted infrared radiation from the surface of the Earth. These gases are of fundamental importance for the maintenance of life on the planet, because without them an average temperature of 33 °C would be estimated, lower than those observed today. Natural causes like volcanic eruptions can alter the concentration of these gases in the atmosphere, burned or even by the action of the man (anthropogenic). Also, the increase in CO_2 concentration is attributed mainly to the use of fossil fuels. In the case of CH_4 and N_2O, the increase in the level of these gases is related to agriculture.

It should be noted that CO_2 is the effect gas studied produced in greater quantity in anthropogenic emissions. Since the establishment of the industrial revolution, the average concentration of CO_2 has increased by 40% and it is currently around 400 ppm. The forecasts indicate that by the year 2100 this concentration should reach 650 ppm, according to the Intergovernmental Panel on Climate Change—IPCC [1]. The accumulation of these gases results in changes in the climate and brings severe consequences for the planet and the different forms of life. It is believed

S. Arcaro (✉)
Universidade do Extremo Sul Catarinense, Criciúma, Brazil
e-mail: sabrinarcaro@yahoo.com.br

A. Kopp Alves (ed.), *Nanomaterials for Eco-friendly Applications*,
Engineering Materials, https://doi.org/10.1007/978-3-030-26810-7_2

that climate change is one of the most critical issues in this century. While renewable and sustainable energy can significantly contribute to reducing CO_2 emissions. It will take a long time for them to be easily exploited and widely used. Therefore, fossil fuels will continue to be used since they are relatively abundant. The use of fossil fuels is not sustainable because of their limited reserves, and their combustion leads to the production of greenhouse gases (CO_2, N_2O, CH_4). Different technologies are being considered, developed or employed to reduce emissions, and capture and store CO_2 emitted into the atmosphere. Nonetheless, despite efforts, large-scale CO_2 capture methodologies continue to be a challenge to transform it economically into a stable, non-polluting product, providing an incentive to consume atmospheric CO_2 and possibly mitigate climate change [2].

Different approaches to reduce CO_2 emissions have been created over the years. These methodologies include better energy efficiency and conservation of energy, greater use of low-carbon fuels or better capture and storage of CO_2 [3, 4]. It is worth pointing out that renewable energy technologies (wind, solar, water, biomass or hydroelectric) have received universal acceptance as sources of clean energy, but their development is slow mainly due to significant cost, unsafe availability, intermittence, and geopolitical issues. Dependence on fossil fuel as the primary source of energy is likely to continue for several decades [5].

However, despite efforts, CO_2 capture remains a significant challenge to transform it economically into a stable, non-polluting product that will provide an incentive to consume atmospheric CO_2 and mitigate climate change. Carbon capture and storage techniques are promising, but some of the challenges for the future are their acceptance by populations and improved research and development.

An interesting method for converting CO_2 into a useful product is to reduce it to solid carbon using the electrochemical reduction in molten alkali metal carbonates. In the 1960s [6–8], researchers established that carbon can be electrodeposited from fused salts containing carbonate and lithium ions (CO_3^{2-} and Li^+). Subsequently, it was proposed that this process could be used for the indirect conversion of CO_2 to carbon [9–12] using the electroreduction of ions CO_3^{2-} in the molten salt electrolyte for carbon ions and solid oxide. The oxide ions formed from the reaction can react with the CO_2 in the atmosphere above the molten salt to regenerate the ions CO_3^{2-} [7, 9, 13–15].

The electrochemical conversion of CO_2 into carbon can occur through two types of mechanisms: direct reduction and indirect reduction. Direct reduction occurs in molten salts under high CO_2 pressures. The indirect reduction, on the other hand, occurs in salts of fused carbonate using the decrease in carbonate ions to carbon and oxygen ions. The oxygen ions, in turn, react with the available CO_2 from the molten salt atmosphere to regenerate the CO_3^{2-} ions.

2 Mechanism of Direct CO_2 Reduction for Carbon

In the direct electrochemical mechanism, the CO_2 dissolved in a molten salt electrolyte is reduced to elemental carbon at the negative electrode (cathode). The direct electrolysis of CO_2 in elemental carbon and oxygen is shown by Reaction 1 and can be achieved at a pressure of 0.203 MPa [13, 16].

$$CO_2 + 4e^- \rightarrow C + 2O^{2-} \tag{1}$$

A three-step mechanism was proposed [17, 18]. In this mechanism, the CO_2, besides being reduced, acts as an acceptor of oxide ions (O_2^-) and, as such, CO_2 ions are generated. The first step (Reaction 2) corresponds to the almost reversible reduction of CO_2 to a CO_2^{2-} radical.

$$CO_2 + 2e^- \rightleftharpoons CO_2^{2-} \tag{2}$$

In the second stage (Reaction 3) the chemical formation of CO occurs.

$$CO_2^{2-} \rightarrow CO + O^{2-} \tag{3}$$

In the third stage (Reaction 4) the irreversible electroreduction of CO to carbon occurs.

$$CO + 2e^- \rightarrow C + O^{2-} \tag{4}$$

The overall reaction (Reaction 5) is, therefore, the reduction of CO_2 for carbon and CO_3^{2-}.

$$3CO_2 + 4e^- \rightarrow C + 2CO_3^- \tag{5}$$

Evidence for this mechanism was obtained from cyclic voltammetric curves recorded in a fused NaCl–KCl mixture (1:1 molar ratio at 750 °C under a CO_2 pressure of 1.0 MPa reported in works of Novoelova and collaborators [19].

3 Mechanism of Indirect CO_2 Reduction for Carbon

Indirect reduction of CO_2 to carbon in molten carbonates, is possible due to the equilibrium reaction given in Reaction (6) (where M represents any of the corresponding metals).

$$M_xCO_3M_xO + CO_2 \quad (x = 1, 2) \tag{6}$$

The reduction of CO_3^{2-} ions to carbon can occur through three different reaction paths. Firstly, a direct electrochemical reduction of the CO_3^{2-} ion occurs through Reaction (7), and including the transfer of four electrons [7, 9, 14, 15, 20].

$$CO_3^{2-} + 4e^- \rightarrow C + 3O^{2-} \tag{7}$$

Then, the CO_3^{2-} ion can be reduced by a two-step process involving the hypothetical CO_2^{2-} ion (Reaction 8 and 9). This CO_2^{2-} ion is formed by combining a CO molecule and ion O^{2-}.

$$CO_3^{2-} + 2e^- \rightarrow CO_2^{2-} + O^{2-} \tag{8}$$

$$CO_2^{2-} + 2e^- \rightarrow C + 2O^{2-} \tag{9}$$

In the third, the CO_3^{2-} ions can also be reduced indirectly through the prior reduction of alkali metal ions to the metal (Reactions 10 and 11) [21]. Cyclic voltammetry performed on a LiF–NaF–KF–K_2CO_3 platinum electrode at 500 °C showed the absence of a CO_3^{2-} ions reduction peak before the cathode limit, suggesting that the ions were not directly reduced [21]. It was therefore proposed that CO_3^{2-} ions are not electrochemically reduced but are expressively reduced in a chemical reaction after alkali metal formation.

$$M^+ + xe^- \rightarrow M \tag{10}$$

$$2xM + M_xCO_3 \rightarrow C + 3M_xO \tag{11}$$

Of the three reaction routes, the most accepted is that the reduction of ions CO_3^{2-} occurs through the reaction (Reaction 7) and the corresponding products are carbon ions and oxygen [7, 14, 15]. The O^{2-} ions produced during the reduction process can react with the CO_2 present in the atmosphere above the molten carbonates to regenerate more CO_2 ions according to the reaction (Reaction 12). CO_2 can, thus, be indirectly converted to solid carbon using molten carbonate electrolysis.

$$CO_2 + O^{2-} \rightarrow CO_3^{2-} \tag{12}$$

During the electrolysis, the reduction of ions CO_3^{2-} to CO through the reaction (13) is also possible. However, the main anodic reaction is the ions oxidation CO_3^{2-} to CO_2 and O_2 using Reaction (Reaction 14) [15, 18, 20, 22, 23].

$$CO_3^{2-} + 2e^- \rightarrow CO + 2O^{2-} \tag{13}$$

$$2CO_3^{2-} \rightarrow 2CO_2 + O_2 + 4e^- \tag{14}$$

Besides the production of O_2 in the anode by Reaction (14), the ions produced at the cathode can migrate to the anode, where they can be oxidized to O_2 according to the reaction (15)

$$2O^{2-} \rightarrow O_2 + 4e^- \tag{15}$$

Results obtained by gas chromatography from the gases emitted at the anode during the electrolysis in Li_2CO_3–Na_2CO_3–K_2CO_3 at 500 °C under air atmosphere showed that O_2 and CO_2 were present during electrolysis. Furthermore, the ratio CO_2/O_2 increases with increasing current density, implying that the reaction (Reaction 14) held at high current densities and more positive potential [23].

The production capacity of an electrolysis system was analyzed using molten carbonates based on Faraday's law [24], and usually, one h generates 0.1 g of carbon materials and consumes about 0.4 g CO_2. However, the attempt to scalling up this system is still vague and requires further studies, although some studies have demonstrated electrolysis configuration to 10 A (50 cm^2 cathode area anode area 100 cm^2), where 24 g of carbon materials are prepared with 96 g of CO_2 consumed per day [25].

4 Influence of Electrolyte Composition

Researches on CO_2 capture and conversion into carbon products via electrolysis in molten salts have made considerable progress, where appropriate electrode materials, electrolyte, and reaction conditions are demonstrated to be of vital significance [13]. Molten salts, and in specific molten carbonates, used as the electrolyte for this electrochemical conversion is due to their natural properties, including great heat and ion conduction, fast reaction kinetics as well as a full electrochemical window, among others [26, 27]. The composition of the molten salt is one of the main factors affecting the cathodic and anodic processes in the reduction of CO_2 to carbon. Among the main observations is the fact that the carbon electrodeposition of the CO_3^{2-} ions under atmospheric CO_2 occurs only when Li^+ ions are present [7]. This is why the potential of molten Li_2CO_3 to deposit carbon (E°C) is more positive than that of Li^+ ion reduction for the Li metal (E°M), suggesting a favorite for carbon deposition. Nevertheless, in molten Na_2CO_3 or K_2CO_3, E°C is similar or more negative than E°M, which means that the reduction of the Na^+ or K^+ ion is preferential. It is noteworthy that at temperatures below 700 °C, the E°C of the Na_2CO_3 or the molten K_2CO_3 is slightly more positive than E°M, although no carbon deposit can be obtained. This can be attributed to the kinetics, and the high potential required for carbon deposition. Moreover, the increase of the electrolysis temperature favors the formation of CO and therefore the efficiency for the deposition of carbon decreases according to the reaction (Reaction 16) [23].

$$C + CO_2 \rightleftharpoons 2CO \tag{16}$$

Several papers show the effects of different electrolyte compositions on carbon deposition. Li_2CO_3 is the most widely used electrolyte in most of the work; however, due mainly to the high cost of Li_2CO_3, some work has been developed to use eutectic mixtures of Li_2CO_3 and other carbonates. Wu and collaborates, [28] evaluated the effects of electrolysis in Li–Na and Li–K, Li–Na–K on cathodic carbon deposition (morphology and structure) as well as coulomb efficiency for carbon generation. Moreover carbon flake with diverse thickness, is a potential to be used as elastomer filler and are formed during electrolysis in Li–Na electrolyte mixed by 50:50 wt% at 100 mA cm^{-2} (Fig. 1). Moreover, carbon nanotube, a valuable chemical, is obtained at cathode in the same electrolyte, but higher electrolytic temperature of 750 °C. Furthermore, molten carbonates composition could influence anode corrosion powerfully, and then recorded cell voltage and calculated coulomb efficiency (the ideal ability approaching 94.9% in Li–K electrolyte at 100 mA cm^{-2}) are indirectly affected.

Researchers [29] evaluated the influence of $CaCO_3$, $SrCO_3$ and $BaCO_3$ dissolved electrolytes in Li_2CO_3. The results demonstrate that the alkaline earth carbonate additives sustain continuous CO_2 electrolysis and carbon electro-deposition. However, the micromorphology and microstructure of the carbon deposits are found to be significantly changed mainly because of the interface modification induced by the alkaline earth carbonate additives. In addition, a high yield of carbon nanotubes is observed in the cathodic carbon products by optimizing the electrolytic conditions. Compared to pure Li_2CO_3, alkaline earth carbonate additives provide carbon nanotubes with a thicker diameter and more prominent hollow structure as seen in Fig. 2.

Li et al. [27] used different electrolyte composites to produce carbon spheres and carbon nanotubes. The results reveal that Li–Ca–Na and Li–Ca–K carbonate electrolytes support carbon sphere deposition rather than carbon nanotube deposition, and in particular, K_2CO_3 shows enhanced interference with carbon nanotube growth. It is also proved that K_2CO_3 exhibits stronger interference with one-dimensional carbon nanotubes growth as only 50% of carbon nanotubes are observed in the Li–K mixture, lower than >80% carbon nanotubes in either Li–Na (90:10, wt%) or Li–Na (50:50, wt%) carbonate systems. Carbon spheres were formed due to the presence of Na+ and K+ as well as the interface modification of CaO. On the other hand, Li–Ca–Ba and Li–Ba carbonate composites present an increase in the carbon nanotube fraction.

Additionally, carbon nanotubes generated from Li–K, Li–Ba and Li–Ca–Ba present a different diameter. In this way, the CO_2-derived carbon nanostructures could be alternatively synthesized through the appropriate regulation of the electrolyte composition.

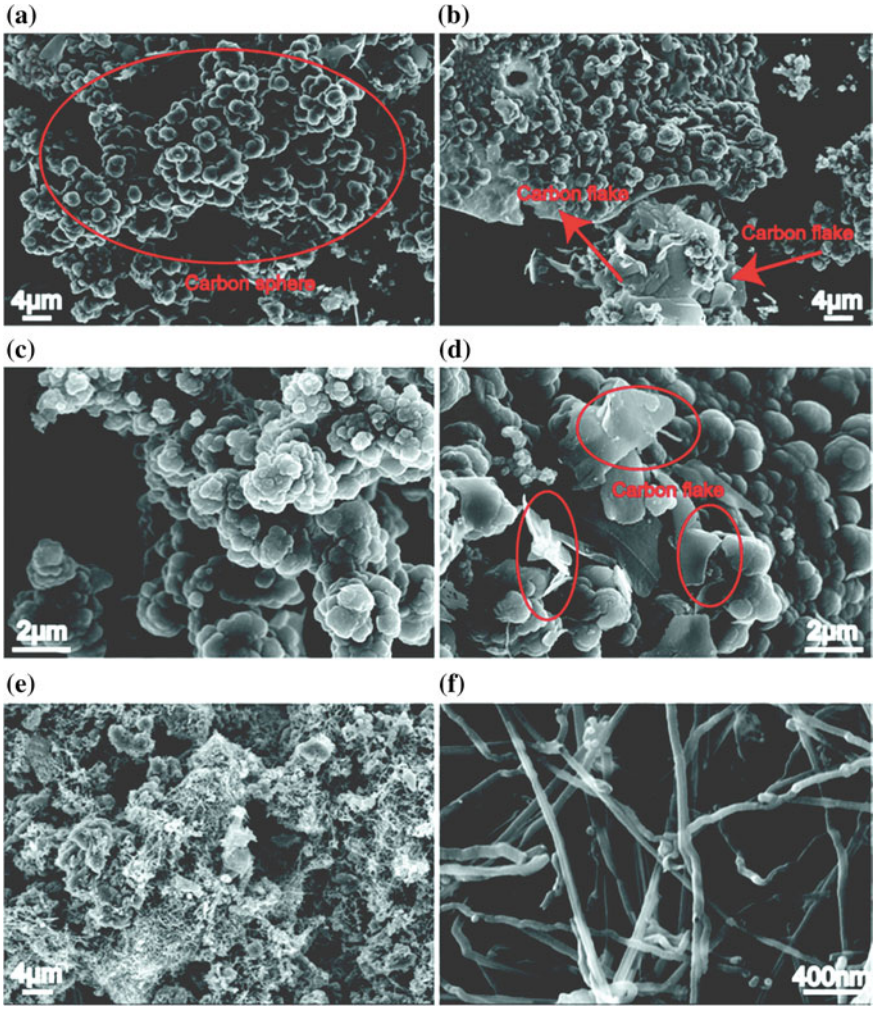

Fig. 1 **a**–**d** are lower magnification SEM images of carbon spheres obtained at Li–Na, 600 °C; **e** and **f** are carbon products synthesized at Li–Na, 750 °C [28]. Reprinted with permission of Wu et al. [28]. Published by The Royal Society of Chemistry

5 Effect of Atmospheric Composition

Carbon deposition can occur in the atmospheres of N_2, CO_2, and Ar, as well to mixtures of N_2 and CO_2 or Ar and CO_2 with greater or less efficiency. Moreover, the use of CO_2 not only limits the decomposition of the molten salt, but also aids in the regeneration of CO_3^{2-} ions and, thus, the deposition of carbon [13].

The effect of the static absorption curves of CO_2 by different molten salts at 450 °C under the CO_2 partial pressure of 50 kPa was evaluated by Deng and collaborators

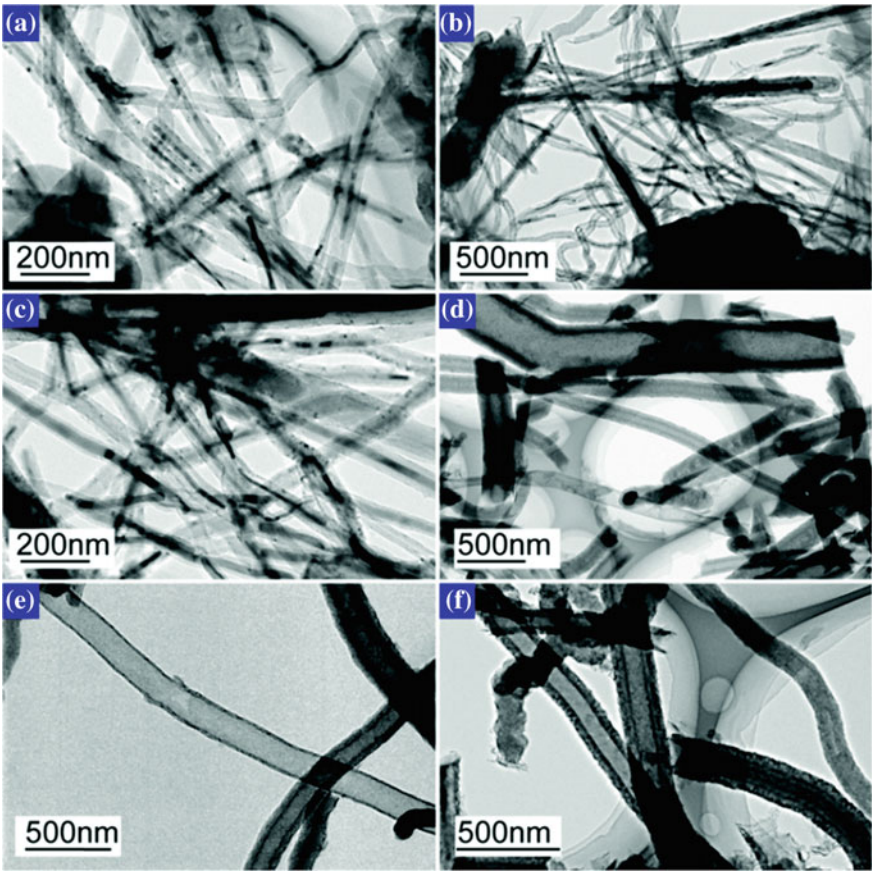

Fig. 2 Carbon nanotubes prepared in pure Li_2CO_3 at **a** 730 °C, **b** 750 °C and **c** 770 °C. Carbon nanotubes prepared in 750 °C alkaline-earth-carbonate-included electrolyte **d** Li_2CO_3–$CaCO_3$, **e** Li_2CO_3–$SrCO_3$ and **f** Li_2CO_3–$BaCO_3$ [29]. Reproduced from Ref. [29] with permission from The Royal Society of Chemistry

and are shown in Fig. 3. They observed that absorption of CO_2 in blank molten LiCl–KCl is negligible, while CO_2 solubility in oxide-free molten ternary carbonates was much higher, approximately 6 mmol CO_2 was absorbed by 100 g blank Li–Na–K carbonates. Furthermore, with the same mole amount of alkali/alkali earth oxide, CaO containing LiCl–KCl melt has the fastest absorption kinetics of CO_2, but the electrochemical kinetics in the melt is more sluggish and complicated. For the constant current electrolysis in a two-electrode system, the cell voltage in the ternary carbonates is the lowest with the highest current efficiency, demonstrating the best energy efficiency in molten carbonate [30].

Gao et al. proposed bubbling gas through a hollow electrode which to enhance the mass transfer of O_2^- by forced convection. The effect of CO_2 bubbling on the cathodic reaction kinetics was evaluated by electrochemical experiments. They observed that

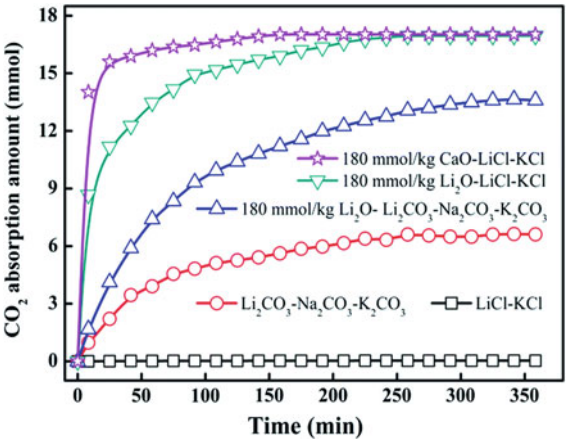

Fig. 3 CO_2 absorption curves in different salts (100 g) at 450 °C under a CO_2 partial pressure of 50 kPa [30]

the current for the reduction of CO_3^{2-} increases significantly on CO_2 bubbling, which can be ascribed to forced convection of CO_2 flow, enhances mass transfer and chemical depolarization through the reaction between CO_2 and O_2^- (Li_2O). The CO_2 bubbling might increase the amount of adsorbed CO_2 in the diffusion layer, contributing to the direct reduction of CO_2. Nevertheless, the chemical reaction between CO_2 and O_2^- (Li_2O) is thermodynamically favorable and should be the primary reaction. The physical dissolution of CO_2 gas in a high-temperature molten salt under normal pressure is relatively low. Therefore, CO_2 reduction in molten carbonates or oxides/carbonates containing molten salts is more likely following a carbonate-mediated indirect reduction mechanism [10, 24]. If all the CO_2 were electrochemically converted to carbon with 100% current efficiency, the current density would be as high as 45.5 A/cm^2, but the measured current density was only ~250 mA/cm^2. This is much lower than the theoretical value, confirming that most of the CO_2 is not captured and electrochemically reduced under the experimental conditions. However, CO_2 increased the cathodic reaction kinetics [31].

6 Influence of Electrodes

The selection of electrodes is also a crucial factor for carbon deposition. For example, the choice of the anode (a counter electrode in cyclic voltammetry) is critical because it needs to be able to withstand high temperatures, have satisfactory conductivity and stability, be inert and do not undergo any form of dissolution chemistry in the molten salt. Unlike the cathode (or working electrode) in which carbon deposits occur, the surface of the anode is always exposed to the molten salts.

Countless papers report studies aimed at understanding the phenomena and the limitations that occur in the electrodes. Carbon deposition was reported on Ni electrodes [13, 15, 20, 32]. Reduction peaks were observed in cyclic voltamme-

try at −2.0 and −2.4 V versus Ag in a eutectic mixture of fused carbonates at Li_2CO_3–$Na_2CO_3K_2CO_3$ a 450 °C. These peaks were qualified to the reduction of CO_3^{2-} ions to carbon and the deposition of alkali metals, respectively. In addition, carbon was deposited electrochemically on cathodes of Al [14], Ti [33], W, [34], Ag [35], Cu [9] and vitreous carbon electrodes [20].

Anodic materials (Ni, Fe, Cu, Pt, Ir, SnO_2) were compared in studies performed in a eutectic mixture of Li_2CO_3–Na_2CO_3–K_2CO_3 at 500 °C. It was observed that a dissolution of the Fe and Ni electrodes occurs, besides, for Cu electrodes, and CuO formation was observed at the surface. However, no apparent change in diameter was seen in any of the electrodes [11].

The mechanism of deposition of electrolytic carbon from molten carbonate salts is independent of the electrode in which deposition takes place provided the electrode is stable in molten salt. However, the potential for carbon deposition and the shape of the cyclic voltammogram for a system depend on the nature of the working electrode study [7, 36, 37].

Some researches [38, 39], have evaluated the effects of the initial microstructure of carbon anodes on the physical properties of carbon deposited electrochemically on carbon cathodes. It was verified that planar grains present in the anode led to the formation of tubular carbonaceous deposits and that when anodes with irregular grain structures were used, deposited carbon formed spherical nanostructures. When titanium electrodes with different surface conditions were used, different morphologies and carbon porosities were obtained. Also, hybrid sp^2 carbon, amorphous phase, and graphitized carbon were found. These studies demonstrate that although the deposition mechanism is the same in all cases, the nature of the electrode affects the physical properties of the carbon deposit.

Recently, it was observed that with the adjustment of the process parameters, the interaction between cathode surfaces and mainly electrode adjustment. It was possible to obtain carbon nanotubes or long carbon nanotubes (>100 nm) [40]. In this case, the electrolysis occurred using a Ni anode and a steel cathode. Also, there was a positive effect on the formation of tubular nanostructures when in the system there is Ni and Zn [41]. In this system, it is assumed that Ni corrosion is the basis for the metal catalyst without an apparent control for the formation and growth of carbon nanotubes [40, 41]. It is noteworthy that carbon nanotubes growth processes depend on the decomposition of the carbon-containing precursor on the surface of a metal catalyst. The most used catalysts are Fe, Ni, Co, Mo and spinel [42–44]. Three different cathodes and anodes were studied to evaluate the effect of the electrode on the carbon nanotubes growth process, [45]. The three anodes studied included untreated Ni, thermally oxidized semi-passive Ni and fully passivated Al_2O_3-coated Ni. The three cathodes include galvanized steel (ZnO coated, Fe > 95%), stainless steel (Cr_2O_3 coated, 72% Fe) and 1010 steel (99% Fe). In the case of untreated Ni, the growth results mainly in carbon fibers with some small minor carbon nanotubes species of large diameter. When Ni is thermally oxidized, the products formed are carbon nanotubes with large diameters (~100 nm) and moving surfaces which are indicative of a high sp^3 (defect) content. Finally, when the atomic layer deposition (ALD) is used to produce a moderately thick (50 nm) and a dense barrier layer

on the surface of the Ni anode, straight carbon nanotubes with smaller diameters are observed. The addition of Zn, as occurs in a galvanized steel coating, further reduces the activation energy for carbon nanotubes formation. The electrochemically produced carbon nanotubes are multi-walled, highly crystalline, with an average diameter of 27.5 nm and a high degree of crystallinity. These characteristics were only achieved due to the use of the ALD to produce a passive coating of alumina on the surface of the Ni anode to inhibit the mass transfer and to isolate the Fe as a kind of primary catalyst in the carbon nanotubes. In this way, it was possible to assess that catalysts inherent to anodic materials can be activated or deactivated, based on the properties of the projected surface in order to obtain carbon nanotubes as-deposited carbon products.

Other recent work [46], has demonstrated that the diameters, crystallinity, and concentration of carbon nanotubes defects, can be controlled from the distribution and growth of catalyst particles. Carbon nanotubes of 23 to 33 nm thickness were obtained by varying the thickness of the Fe deposited by ALD at the cathode. Galvanostatic electrolysis indicates the electrochemical reduction of Fe catalyst particles, followed by deposition of carbon to produce carbon nanotubes.

Arcaro and collaborators [47] evaluated the influence of the type of the electrodes (nickel–chrome and galvanized steel), the applied current, time of electrolysis and the atmosphere of reaction on the characteristics of formed nanostructures. When using steel and nickel chrome as a cathode, the products have lower levels of defects and are partially filled with a metal phase when 1 A and 4 h of electrolytic synthesis were used. Nevertheless, after electrolysis of 4 h, these products was 90% carbon nanotubes. The carbon nanotubes growth on the galvanized steel or nickel–chrome cathodes were similar to an average external diameter of 100–125 nm and internal diameter is 25–40 nm. Though, when grown in nickel–chrome cathode, the nanotubes have better quality and smaller walls. Figure 4 shows the carbon nanotubes produced using nickel–chrome cathode and 1 and 4 h using galvanized steel cathode.

7 Applications Carbon Deposited by Electrolysis in Molten Carbonates

7.1 Amorphous Carbon

In most electrolysis processes, the carbon obtained is mostly amorphous and has sp^2 hybridization mainly with some surface carbon having sp^3 hybridization. The existence of graphite domains was also reported with an interplanar spacing of approximately 0.34 nm [11, 14, 15, 48]. Depending on the process variables, carbon nanoparticles with high specific surface areas can be obtained, reaching 1315 $m^2\ g^{-1}$ when activated at 600 °C under vacuum [15], or an average specific surface area in the range of 200–700 $m^2\ g^{-1}$ without any activation [20].

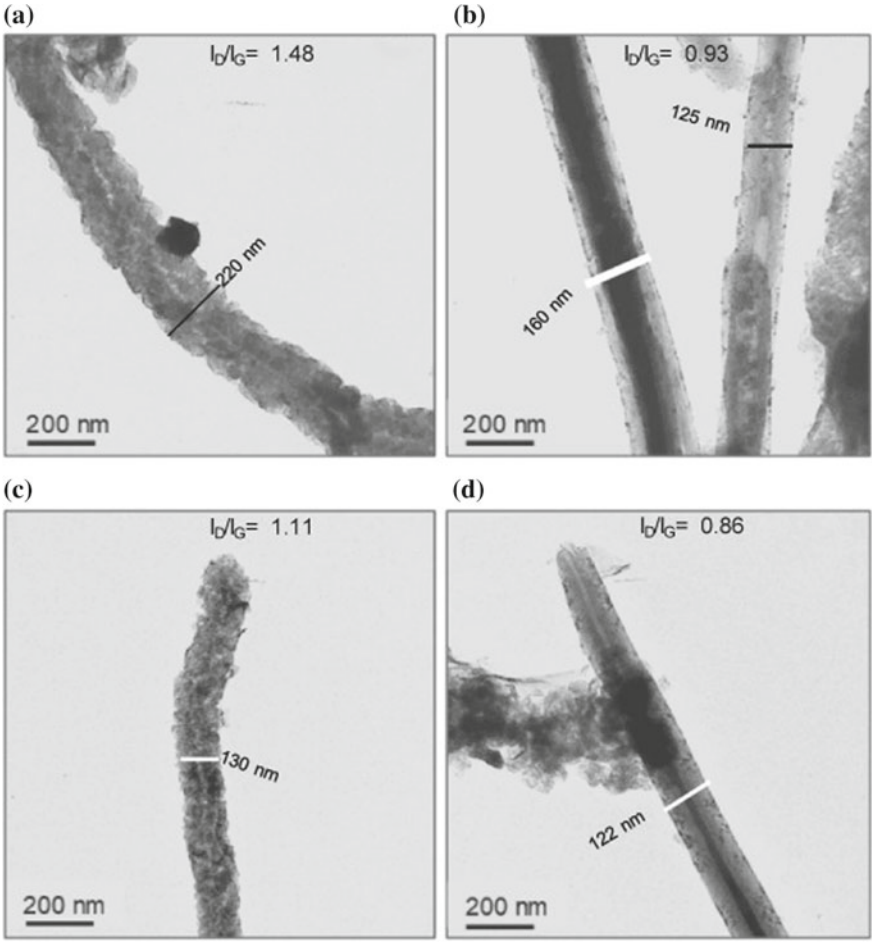

Fig. 4 TEM images after electrolysis at a temperature of 770 °C with 1.0 A for 1 (**a**) and 4 h (**b**) using nickel-chrome cathode and 1 (**c**) and 4 h (**d**) using galvanized steel cathode. Reproduced from Ref. [47] with permission from Elsevier

Electrolytic conditions, such as electrode potential, choice of molten salt and temperature, contribute to the properties of the carbon produced. The increase of molten salt temperature leads to significant and elongated particles with lower carbon surface areas, while more negative potentials increase the surface area [15]. Different morphologies and properties of electrodeposited carbon were obtained from the temperature variation and composition of the molten salt.

Flake-like particles, aggregated and flat, were obtained at 550 and 700 °C in 4 V Li_2CO_3–N_2CO_3. The more aggregated quasi-spherical carbon particles were electrodeposited from Li_2CO_3–K_2CO_3, indicating effects of the composition of salt melted on the properties of deposited carbon [11, 14, 15, 48] as show in Fig. 5.

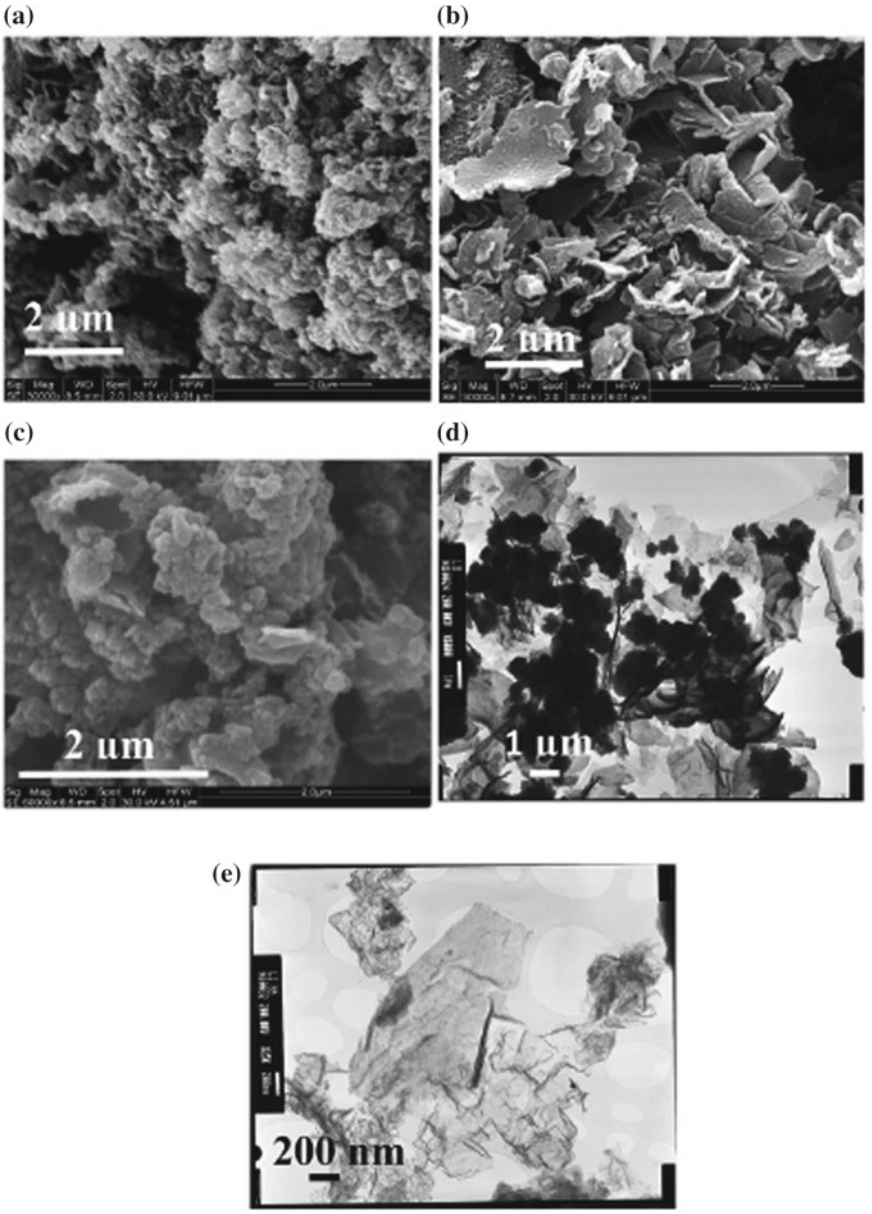

Fig. 5 Examples of electrodeposited carbon morphologies [13]. Reproduced from Ref. [13] with permission from The Royal Society of Chemistry

Due to the moderate to high specific surface areas and the presence of surface functional groups, electrodeposited carbon has shown promising results in electrochemical energy storage devices such as lithium-ion batteries [49, 50] and supercapacitors [11].

Low combustion temperatures ranging from 310 to 450 °C have also been reported for deposited carbon of Li_2CO_3–K_2CO_3 at various temperatures and voltages [36]. This unusual thermal behavior was attributed to the nanomorphology of the electrolytic carbon and the catalytic effects of the metal oxide impurities present on the carbon. These factors suggest that the carbon produced can be used as a solid fuel for high-tech applications. An example could involve using deposited carbon to make suspensions that can be used in internal combustion engines. While it is possible that the deposited carbon can be converted to electricity by combustion, the highest efficiency is in feeding the carbon into a direct carbon fuel cell [36].

On the other hand, the electrocatalytic property and heavy metal adsorption ability of the carbon materials obtained by electrolysis in molten carbonates process was also investigated. Researches [51] found that electrodeposited carbon was passive for oxygen reduction reaction. Nevertheless, after doping with S and Co by molten salt treatment, its catalytic activity for oxygen reduction reaction increased significantly. Due to a porous structure and high specific surface area, the derived carbon materials by the electrolysis in molten carbonates process also show a very high adsorption capacity for Cu^{2+},methylene and Cr^{6+} in aqueous solution, of 29.9 mg g^{-1}, 302.5 mg g^{-1} and 49.5 mg g^{-1} [51–53]. The above results indicated that the carbon materials derived from CO_2 also show good potential as the electro-catalysis and decontamination materials.

7.2 Carbon Nanotubes

Carbon nanotubes formed from CO_2 as the reactant can contribute to the reduction of greenhouse gases by storing the carbon in a compact, stable and valuable form. Despite its interesting mechanical, thermal and electronic properties, the applications of carbon nanotubes have been limited until now by the high cost of their conventional synthesis, which has a mean price in the Brazilian market of approximately R$ 30,000.00 each 100 g [54].

The carbon nanotubes obtained from the electrodeposition are being studied in a little more than 5 years. So, currently, most studies still focus on understanding the mechanisms of formation and growth. More recent studies are already achieving control of the diameter and chirality of the carbon nanotubes, maintaining the economic versatility and sustainability on which this electrochemical technique is based.

A broad portfolio of carbon nanotubes can be produced by controlling the electrolysis conditions [55]. Figure 6 shows examples of these morphologies as well as electrical conductivity results obtained by monitoring the electrolysis conditions. Carbon nanotubes were synthesized from Li_2CO_3, and also from eutectic mixtures

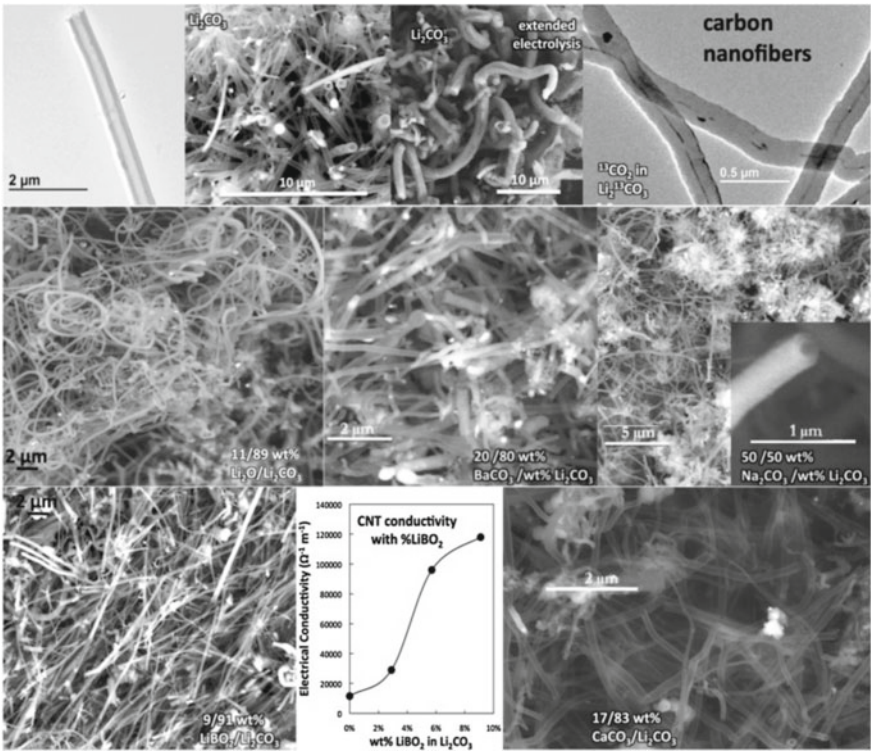

Fig. 6 Carbon nanotubes portfolio produced by Ren et al. [55] controlling the electrolysis conditions. Reproduced from Ref. [55] with permission from Elsevier

of other carbonates. Ni nucleation points are evidenced as bright spots at the carbon nanotubes ends, indicating that these were the catalysts of the reaction.

When Li_2O was dissolved in Li_2CO_3, they gave tangled carbon nanotubes instead of straight ones. These defective matched carbon nanotubes structures can significantly improve the Li and Na rechargeable battery and higher charge storage capacities [56]. Tangled carbon nanotubes result from sp^3 and sp^2 defects and can lead to nobler applications such as better storage capacity in rechargeable batteries. The tests showed that the carbon nanotubes for use in batteries have excellent performance and durability, without loss of capacity measured in more than 2.5 months of continuous cycles, corresponding to more than 200 cycles and 600 cycles for ion devices lithium and sodium, respectively.

In addition, it was explored the possibility of doping carbon nanotubes, with boron or calcium, since doped carbon nanotubes doped at different concentrations, alter their physical and chemical properties [57]. Doping with calcium demonstrate the possibility of obtaining carbon nanotubes with very thin walls. When carbon nanotubes are doped with boron, an increase in electrical conductivity is very evident. This suggests similar routes and opportunity for the synthesis of carbon nanotubes

doped with nitrogen, phosphorus or sulfur. Carbon nanotubes have a range of potential applications, including heterogeneous catalysis, adsorption and conversion, and energy storage. N-doped carbons have a variety of potential applications, including oxidation and reduction of O_2, fuel cell catalysts, supercapacitors and sensors [55, 58–60]. Likewise, carbon–phosphorus doping can significantly affect the properties and applications of carbon nanotubes, including aerobic oxidation catalysts, ultra-sensitive batteries and sensors [61, 62].

8 Conclusions

The CO_2 capture process in molten salts and the electrochemical conversion provides a new way to close the current loop and carbon mitigate global climate change, making the greenhouse gas CO_2 on different carbon nanostructures. Carbon nanostructures can be easily obtained by changing process parameters such as electrolytes, electrodes, and atmosphere. These materials can have exceptional performance in energy conversion and storage, as well as electrocatalysis and merit future research.

References

1. IPCC WG I (2013) Introduction. Clim Chang 2013 Phys Sci Basis Contrib Work Gr I to Fifth Assess Rep Intergov Panel Clim Chang 119–158. https://doi.org/10.1017/cbo9781107415324.007
2. Ren J, Licht S (2016) Tracking airborne CO_2 mitigation and low cost transformation into valuable carbon nanotubes. Sci Rep 6:27760. https://doi.org/10.1038/srep27760
3. Lewis NS (2016) Aspects of science and technology in support of legal and policy frameworks associated with a global carbon emissions-control regime. Energy Environ Sci 9:2172–2176. https://doi.org/10.1039/c6ee00272b
4. McNutt M (2015) Climate warning, 50 years later. Science 350(80):721. https://doi.org/10.1126/science.aad7927
5. Chery D et al (2016) Mechanistic approach of the electrochemical reduction of CO_2 into CO at a gold electrode in molten carbonates by cyclic voltammetry. Int J Hydrogen Energy 41:18706–18712. https://doi.org/10.1016/J.IJHYDENE.2016.06.094
6. Chandler HW Oser W (1962) Study of electrolytic reduction of carbon dioxide. ISOMET Corporation, Oakland NJ
7. Ingram MD et al (1966) The electrolytic deposition of carbon from fused carbonates. Electrochim Acta 11:1629–1639. https://doi.org/10.1016/0013-4686(66)80076-2
8. Delimarskii YK et al (1971) Constancy of the electrochemical impedance phase in molten salt cells. Theor Exp Chem 4:355–357. https://doi.org/10.1007/BF00524135
9. Massot L et al (2002) Electrodeposition of carbon films from molten alkaline fluoride media. Electrochim Acta 47:1949–1957. https://doi.org/10.1016/S0013-4686(02)00047-6
10. Licht S (2011) Efficient solar-driven synthesis, carbon capture, and desalinization, STEP: solar thermal electrochemical production of fuels, metals, bleach. Adv Mater 23:5592–5612. https://doi.org/10.1002/adma.201103198
11. Yin H et al (2013) Capture and electrochemical conversion of CO_2 to value-added carbon and oxygen by molten salt electrolysis. Energy Environ Sci 6:1538–1545. https://doi.org/10.1039/c3ee24132g

12. Tang D et al (2013) Effects of applied voltage and temperature on the electrochemical production of carbon powders from CO_2 in molten salt with an inert anode. Electrochim Acta 114:567–573. https://doi.org/10.1016/j.electacta.2013.10.109
13. Ijije HV et al (2014) Carbon electrodeposition in molten salts: Electrode reactions and applications. RSC Adv 4:35808–35817. https://doi.org/10.1039/c4ra04629c
14. Kawamura H, Ito Y (2000) Electrodeposition of cohesive carbon films on aluminum in a LiCl-KCl-K_2CO_3 melt. J Appl Electrochem 30:571–574. https://doi.org/10.1023/A:1003927100308
15. Le Van K et al (2009) Electrochemical formation of carbon nano-powders with various porosities in molten alkali carbonates. Electrochim Acta 54:4566–4573. https://doi.org/10.1016/j.electacta.2009.03.049
16. Delimarskii YK (1985) Some peculiarities of the electrolysis of ionic melts. Electrochim Acta 30:1007–1010. https://doi.org/10.1016/0013-4686(85)80164-X
17. Novoselova IA et al (2003) High temperature electrochemical synthesis of carbon-containing inorganic compounds under excessive carbon dioxide pressure. J Min Met 39:281–293
18. Novoselova IA et al (2007) Electrolytic production of carbon nano-tubes in chloride-oxide melts under carbon dioxide pressure. Hydrogen materials science and chemistry of carbon nanomaterials. Springer, Dordrecht, Netherlands, pp 459–465
19. Novoselova IA et al (2008) Electrolytic generation of nano-scale carbon phases with framework structures in molten salts on metal cathodes. Zeitschrift für Naturforsch A 63:467–474. https://doi.org/10.1515/ZNA-2008-7-814
20. Kaplan B et al (2002) Synthesis and structural characterization of carbon powder by electrolytic reduction of molten Li_2CO_3-Na_2CO_3-K_2CO_3. J Electrochem Soc 149:D72. https://doi.org/10.1149/1.1464884
21. Deanhardt ML et al (1986) Thermal decomposition and reduction of carbonate ion in fluoride melts. J Electrochem Soc 133:1148. https://doi.org/10.1149/1.2108802
22. Delimarskii YK et al (1964) Cathode liberation of carbon from molten carbonates Доклады Академии наук СССР. Dokl Akad Nauk SSSR 156:650–651
23. Lorenz PK, Janz GJ (1970) Electrolysis of molten carbonates: anodic and cathodic gas-evolving reactions. Electrochim Acta 15:1025–1035. https://doi.org/10.1016/0013-4686(70)80042-1
24. Wu H et al (2017) Effect of molten carbonate composition on the generation of carbon material. RSC Adv 7:8467–8473. https://doi.org/10.1039/C6RA25229J
25. Li Z et al (2018) A novel route to synthesize carbon spheres and carbon nanotubes from carbon dioxide in a molten carbonate electrolyzer. Inorg Chem Front 5:208–216. https://doi.org/10.1039/c7qi00479f
26. Kanai Y et al (2013) Mass transfer in molten salt and suspended molten salt in bubble column. Chem Eng Sci 100:153–159. https://doi.org/10.1016/J.CES.2012.11.029
27. Shi Z et al (2016) Solubility of carbon dioxide in LiF-Li_2CO_3 molten salt system. J Chem Eng Data 61:3020–3026. https://doi.org/10.1021/acs.jced.6b00043
28. Wu H et al (2017) Effect of molten carbonate composition on the generation of carbon material. RSC Adv 7:8467–8473. https://doi.org/10.1039/C6RA25229J
29. Li Z et al (2018) Carbon dioxide electrolysis and carbon deposition in alkaline-earth-carbonate-included molten salts electrolyzer. New J Chem 42:15663–15670. https://doi.org/10.1039/C8NJ02965B
30. Deng B et al (2016) Molten salt CO_2 capture and electro-transformation (MSCC-ET) into capacitive carbon at medium temperature: effect of the electrolyte composition. Faraday Discuss 190:241–258. https://doi.org/10.1039/C5FD00234F
31. Gao M et al (2019) Enhanced kinetics of CO_2 electro-reduction on a hollow gas bubbling electrode in molten ternary carbonates. Electrochem Commun 100:81–84. https://doi.org/10.1016/J.ELECOM.2019.01.026
32. Licht S et al (2010) A new solar carbon capture process: solar thermal electrochemical photo (STEP) carbon capture. J Phys Chem Lett 1:2363–2368. https://doi.org/10.1021/jz100829s
33. Kaplan V et al (2010) Conversion of CO_2 to CO by electrolysis of molten lithium carbonate. J Electrochem Soc 157:B552. https://doi.org/10.1149/1.3308596

34. Chen G et al (2010) Research on electro-deposition of carbon from LiF-NaF-Na_2CO_3 molten salt system. In: 2010 World non-grid-connected wind power and energy conference. IEEE, pp 1–3
35. Janz GJ, Conte A (1964) Potentiostatic polarization studies in fused carbonates—I. The noble metals, silver and nickel. Electrochim Acta 9:1269–1278. https://doi.org/10.1016/0013-4686(64)87003-1
36. Ijije HV et al (2014) Indirect electrochemical reduction of carbon dioxide to carbon nanopowders in molten alkali carbonates: process variables and product properties. Carbon 73:163–174. https://doi.org/10.1016/j.carbon.2014.02.052
37. Ijije HV et al (2014) Electro-deposition and re-oxidation of carbon in carbonate-containing molten salts. Faraday Discuss 172:105–116. https://doi.org/10.1039/C4FD00046C
38. Kamali AR et al (2011) Effect of the graphite electrode material on the characteristics of molten salt electrolytically produced carbon nanomaterials. Mater Charact 62:987–994. https://doi.org/10.1016/J.MATCHAR.2011.06.010
39. Song Q et al (2012) Electrochemical deposition of carbon films on titanium in molten LiCl–KCl–K_2CO_3. Thin Solid Films 520:6856–6863. https://doi.org/10.1016/J.TSF.2012.07.056
40. Licht S et al (2016) Carbon nanotubes produced from ambient carbon dioxide for environmentally sustainable lithium-ion and sodium-ion battery anodes. ACS Cent Sci 2:162–168. https://doi.org/10.1021/acscentsci.5b00400
41. Ren J et al (2015) One-pot synthesis of carbon nanofibers from CO_2. Nano Lett 15:6142–6148. https://doi.org/10.1021/acs.nanolett.5b02427
42. Grüneis A et al (2006) High quality double wall carbon nanotubes with a defined diameter distribution by chemical vapor deposition from alcohol. Carbon 44:3177–3182. https://doi.org/10.1016/j.carbon.2006.07.003
43. Wang Yao et al (2002) The large-scale production of carbon nanotubes in a nano-agglomerate fluidized-bed reactor. Chem Phys Lett 364:568–572. https://doi.org/10.1016/S0008-6223(02)00244-0
44. Zampiva RYS et al (2017) 3D CNT macrostructure synthesis catalyzed by $MgFe_2O_4$ nanoparticles—a study of surface area and spinel inversion influence. Appl Surf Sci 422:321–330. https://doi.org/10.1016/j.apsusc.2017.06.020
45. Douglas A et al (2017) Iron catalyzed growth of crystalline multi-walled carbon nanotubes from ambient carbon dioxide mediated by molten carbonates. Carbon 116:572–578. https://doi.org/10.1016/J.CARBON.2017.02.032
46. Douglas A et al (2018) Toward small-diameter carbon nanotubes synthesized from captured carbon dioxide: critical role of catalyst coarsening. ACS Appl Mater Interfaces. https://doi.org/10.1021/acsami.8b02834
47. Arcaro S et al (2018) MWCNTs produced by electrolysis of molten carbonate: characteristics of the cathodic products grown on galvanized steel and nickel chrome electrodes. Appl Surf Sci 466:367–374. https://doi.org/10.1016/j.apsusc.2018.10.055
48. Bartlett HE, Johnson KE (1967) Electrochemical studies in molten Li_2CO_3-Na_2CO_3. J Electrochem Soc 114:457. https://doi.org/10.1149/1.2426627
49. Groult H et al (2003) Lithium insertion into carbonaceous anode materials prepared by electrolysis of molten Li-K-Na carbonates. J Electrochem Soc 150:G67. https://doi.org/10.1149/1.1531490
50. Groult H et al (2006) Preparation of carbon nanoparticles from electrolysis of molten carbonates and use as anode materials in lithium-ion batteries. Solid State Ionics 177:869–875. https://doi.org/10.1016/J.SSI.2006.01.051
51. Chen Z et al (2017) Enhanced electrocatalysis performance of amorphous electrolytic carbon from CO_2 for oxygen reduction by surface modification in molten salt. Electrochim Acta 253:248–256. https://doi.org/10.1016/J.ELECTACTA.2017.09.053
52. Mao X et al (2017) Characterization and adsorption properties of the electrolytic carbon derived from CO_2 conversion in molten salts. Carbon 111:162–172. https://doi.org/10.1016/J.CARBON.2016.09.035

53. Yin H et al (2013) Capture and electrochemical conversion of CO_2 to value-added carbon and oxygen by molten salt electrolysis. Energy Environ Sci 6:1538. https://doi.org/10.1039/c3ee24132g
54. MWCNT | Sigma-Aldrich. https://www.sigmaaldrich.com/catalog/search?term=MWCNT&interface=All&N=0&mode=matchpartialmax&lang=pt&region=BR&focus=product. Accessed 6 Jun 2018
55. Ren J, et al. (2017) Transformation of the greenhouse gas CO_2 by molten electrolysis into a wide controlled selection of carbon nanotubes. J CO_2 Util 18:335–344. https://doi.org/10.1016/j.jcou.2017.02.005
56. Licht S et al (2016) Carbon nanotubes produced from ambient carbon dioxide for environmentally sustainable lithium-ion and sodium-ion battery anodes. ACS Cent Sci 2:162–168. https://doi.org/10.1021/acscentsci.5b00400
57. Paraknowitsch JP, Thomas A (2013) Doping carbons beyond nitrogen: an overview of advanced heteroatom doped carbons with boron, sulphur and phosphorus for energy applications. Energy Environ Sci 6:2839. https://doi.org/10.1039/c3ee41444b
58. Guo D et al (2016) Active sites of nitrogen-doped carbon materials for oxygen reduction reaction clarified using model catalysts. Science 351(80):361–365. https://doi.org/10.1126/science.aad0832
59. Wang Z et al (2013) Functionalized N-doped interconnected carbon nanofibers as an anode material for sodium-ion storage with excellent performance. Carbon 55:328–334. https://doi.org/10.1016/j.carbon.2012.12.072
60. Deng Y et al (2016) Review on recent advances in nitrogen-doped carbons: preparations and applications in supercapacitors. J Mater Chem A 4:1144–1173. https://doi.org/10.1039/C5TA08620E
61. Patel MA et al (2016) P-doped porous carbon as metal free catalysts for selective aerobic oxidation with an unexpected mechanism. ACS Nano 10:2305–2315. https://doi.org/10.1021/acsnano.5b07054
62. Maciel IO et al (2009) Synthesis, electronic structure, and raman scattering of phosphorus-doped single-wall carbon nanotubes. Nano Lett 9:2267–2272. https://doi.org/10.1021/nl9004207

TiO_2/CNT Nanocomposites for Water Splitting Applications

Waleska Campos Guaglianoni

Abstract The need for replacing fossil fuels by renewable energy sources has been growing over the last years due to the increasing demand for energy worldwide and environmental issues. One of the main compounds studied for future application as fuel is hydrogen gas (H_2). Extensive research has been performed on H_2 production via water splitting using solar light since Honda and Fujishima report in 1972. One of the most utilized materials for water splitting applications is titanium dioxide (TiO_2). TiO_2 is abundant, inexpensive, non-corrosive, stable and environment-friendly. However, its large band gap and rapid electron-hole recombination hinders the hydrogen production efficiency. In order to improve the efficiency in photoconversion, TiO_2 has been modified with several materials, including carbon nanotubes (CNT). A variety of different structural forms of CNT/TiO_2 composites have been studied. In this chapter, we review morphologies and methods of synthesis of CNT/TiO_2 nanocomposites, parameters employed at electrochemical tests and results of H_2 evolution.

Keywords TiO_2 · CNT · Water splitting · Hydrogen

Abbreviations

CNT	Carbon nanotube
CVD	Chemical Vapor Deposition
FESEM	Field Emission Scanning Electron Microscopy
H_2	Hydrogen gas
HRTEM	High Resolution Transmission Microscopy
MWCNT	Multi wall carbon nanotube
PEC	Photo-electrochemical cell
SWCNT	Single wall carbon nanotube
TiO_2	Titanium dioxide

W. C. Guaglianoni (✉)
Universidade Federal do Rio Grande do Sul, Porto Alegre, Brazil
e-mail: waleskacg88@hotmail.com

A. Kopp Alves (ed.), *Nanomaterials for Eco-friendly Applications*,
Engineering Materials, https://doi.org/10.1007/978-3-030-26810-7_3

1 Introduction

Currently, 80% of global energy depends on fossil fuel. The progressive depletion of oil reserves and the increasing demand for energy made the use of oil as the main energy source uncertain in the long term. In parallel, this kind of energy damages the planet climate, since pollutants such as Co_x, NO_x, SO_x, C_xH_x, ash, organic compounds, and others are thrown into the atmosphere as a result of the combustion of fossil fuels [1].

The impact caused on the community and environment by the atmospheric emissions made by fossil fuels is evident. In this context, the search for alternative sources of energy, which are clean and renewable and have a low impact such as the eolic, solar, biomass and hydrogen, is an important topic of investigation. The hydrogen gas (H_2) is one of the main compounds studied for future application as fuel. The H_2 gas may be easily produced from the water splitting reaction. However, this process is very intensive from an energetic point of view. Thus, the production of H_2 for its use as a sustainable and environment-friendly fuel must be powered by renewable sources, such as solar energy.

Since its first application as a photocatalyst for water-splitting in 1972 [2], the titanium dioxide (TiO_2) has been extensively studied for the evolution of hydrogen and oxygen gases from water. The TiO_2 crystalline phases have bandgap values that make them applicable to the conversion of high energy photons into electric energy. Despite the high photoactivity, the wide bandgap and the high charge recombination limit the TiO_2 efficiency for solar light conversion. Many researches have been carried out to enhance the properties of the TiO_2, for instance: synthesis of nanostructures, doping, functionalization, decoration with metallic particles, and preparation of composites with carbonaceous materials [3].

In this chapter, we review the water splitting reaction, some researches about the synthesis of TiO_2 and carbon nanotubes composites, and their application for hydrogen production by water splitting.

2 Hydrogen Production by Water Splitting

Water splitting using solar energy has been studied for a long time since the Honda and Fujishima report [2]. The reaction for splitting the water molecule requires a change of free energy (ΔG) of 237 kJ mol^{-1}, which corresponds to an electrolysis cell voltage ($\Delta E°$) of 1.23 V. Electrochemical water splitting consists of the following cathodic (Eq. 2) and anodic (Eq. 3) half-reactions:

$$H_2O(l) \rightarrow H_2(g) + 1/2O_2(g) \tag{1}$$

$$2H^+ + 2e^- \rightarrow H_2(g) \tag{2}$$

$$H_2O(l) \rightarrow 2e^- + 2H^+ + 1/2O_2(g) \quad (3)$$

Generally, photocatalytic H_2 production by water splitting can be classified into photochemical and photo-electrochemical reactions. The difference between these two types is that, in the photo-electrochemical cell (PEC), an external circuit is applied to direct the photogenerated electrons from the anode to the cathode.

Figure 1 illustrates a typical PEC cell, which consists of a semiconductor photoanode where oxygen is evolved and a photocathode (Pt sheet) where hydrogen is evolved. H_2 production using a PEC cell can be summarized into the following steps:

(1) The photoanode absorbs radiant light that has to possess energy greater than the bandgap of the photoactive material;
(2) Electrons of the valence band are excited into the conduction band and the holes remain in the valence band;
(3) The photo-generated electrons reach the cathode and react with protons (H^+), forming H_2;
(4) The holes at the photoanode oxidize the H_2O molecule and produce O_2.

In the last years, several materials have been employed as photocatalysts to split water into H_2 and O_2. Oxides, sulfides and nitrides of transition metal such as TiO_2, CdSe, CdS, GaP, $SrTiO_3$, Nb_2O_5, WO_3, and Fe_2O_3 have been most widely used [5]. Among the employed materials, the TiO_2 is one of the most studied and was the first material described as a photochemical water splitting catalyst.

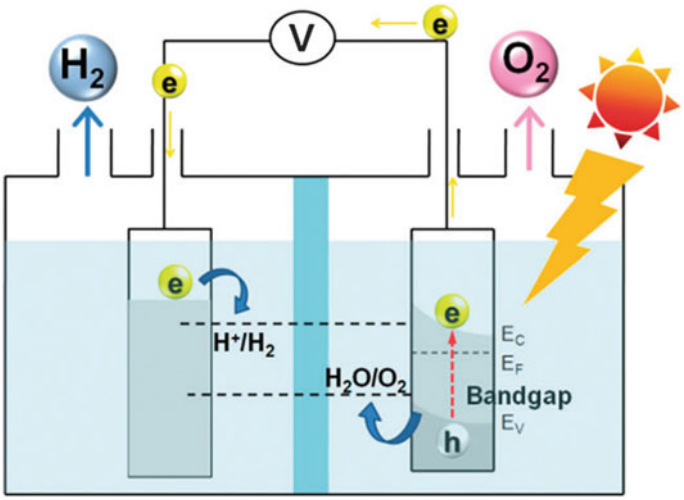

Fig. 1 Diagram of a photoelectrochemical cell for H_2 evolution by water splitting. Reproduced with permission of [4]

3 Titanium Dioxide

The titanium dioxide (TiO_2) is a transition metal that has been extensively investigated. TiO_2 is insoluble in aqueous medium, chemically and biologically inert, photo stable, non-toxic, and inexpensive. Due to these interesting attributes, the TiO_2 has many applications, such as pollutant [6] and bacterial [7] degradation, generation of hydrogen by water splitting [8], CO_2 conversion [9], dye-sensitized solar cells [10], sensors [11], and drug delivery systems [12].

Titanium dioxide mainly crystallizes in three structures: rutile, brookite and anatase. The rutile and anatase phases are the most relevant for photocatalytic applications. These polymorphs present a wide band gap: 3.0 and 3.2 eV for the rutile and anatase phases [13], respectively. For this reason, the radiation absorption by the TiO_2 occurs in the ultraviolet (UV) region of the electromagnetic spectrum, which corresponds to only 4% of the solar spectrum. Conversely, the visible light corresponds to 46% of the solar spectrum [14]. Thus, the use of TiO_2 to convert solar light becomes inefficient. Other factors that limit the TiO_2 efficiency are the fast recombination of photo-excited electron-hole pairs and the rapid rearrangement of H_2 and O_2 into water. Many researches have been carried out to improve the oxide properties. Some of the strategies researched are listed below:

(1) *Synthesis of nanostructures*: several works have shown that the nanostructured TiO_2 is more effective as photocatalyst than the bulk TiO_2. This occurs as the nanostructured shape has elevated surface area, higher efficiency in electrons transport, and reduced recombination of photogenerated electron-holes [15–17]. In this context, several TiO_2 nanostructures have been synthesized, such as nanoparticles [18, 19], nanospheres [20], nanosheets [21, 22], nanofibers [23, 24], nanorods [25, 26], and nanotubes [27–29]. Figure 2 shows SEM images of some synthesized nanostructures.

(2) *Doping*: the insertion of dopants in the TiO_2 structure improves the conductivity, diminishes the band gap energy and enhances the optical absorption of the semiconductor. Various nonmetal elements, such as B [30], C [31], N [32], and S [33], have been successfully doped into TiO_2. Transition metals such as Mn [34], Fe [35], Co [36], Ni [37], and Mo [38] have also been used as dopants.

(3) *Composites with carbonaceous nanomaterials*: graphene, fullerenes (C_{60}), and carbon nanotubes (CNTs) were already applied to enhance the photochemical behavior of the TiO_2 [3, 39–43]. Among these structures, CNTs are widely used due to their unique properties, such as their interesting electrical behavior and higher surface area. Furthermore, CNTs have played an important role in the effective charge separation in TiO_2 in electron harvesting processes [44, 45].

Next section reviews recent works about TiO_2/CNT composites.

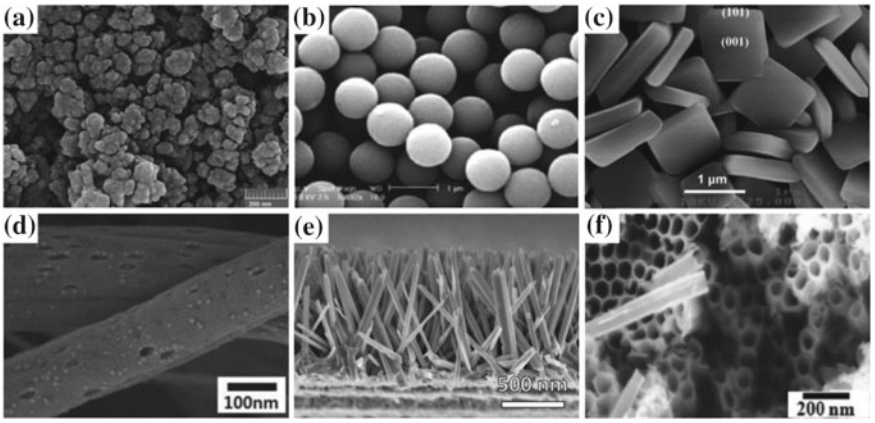

Fig. 2 SEM images of TiO_2 nanostructures synthesized as **a** particles, **b** spheres, **c** sheets, **d** fibers, **e** rods and **f** tubes. Reprinted with permission of (**a**) [18]; (**b**) [20]; (**c**) [21]; (**d**) [23]; (**e**) [26]; (**f**) [27]

4 TiO_2/Carbon Composites

Carbon nanotubes (CNTs) have proved to improve the photocatalytic activity of TiO_2 under ultraviolet (UV) and visible light irradiations for H_2 production. In this context, researchers have carried out extensive investigation about composites of TiO_2 and single-walled carbon nanotubes (SWCNT) or multi-walled carbon nanotubes (MWCNT).

Reddy et al. [46] synthesized MWCNTs/TiO_2 nanocomposites by hydrothermal method and evaluated the H_2 production under UV-visible light. The authors obtained the nanocomposite through treatment in autoclave of a mixture of TiO_2 powder and multi-walled carbon nanotubes. Figure 3a shows the TEM images of the MWCNT/TiO_2 nanocomposites synthesized. The influence of the MWCNT amount

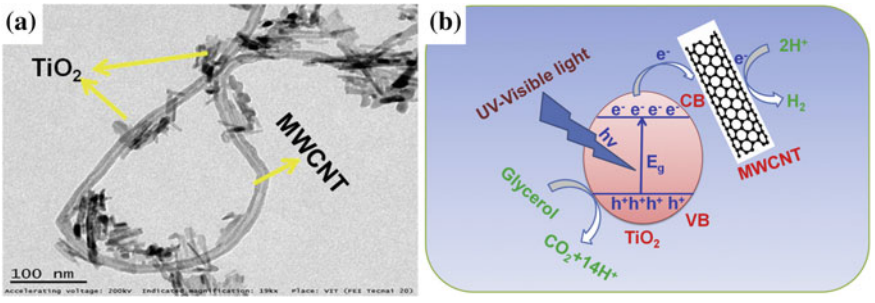

Fig. 3 **a** TEM images of MWCNT/TiO_2 nanocomposites synthesized by Reddy et al. [46]. **b** The mechanism proposed for the photocatalytic activity of MWCNTs/TiO_2 nanocomposite. Reprinted with permission [46]

in the composite and the treatment temperatures on the H_2 production were evaluated. The highest H_2 production rate (8.8 mmol $h^{-1}g^{-1}$) was observed for the sample with the addition of 0.1 wt% MWCNT and treated thermally at 450 °C. The amount of H_2 produced by the nanocomposite is roughly nine-fold higher than that of the pure TiO_2.

Figure 3b presents the mechanism proposed by Reddy et al. [46] for the photocatalytic activity of MWCNTs/TiO_2 nanocomposite under UV-Visible light irradiation. The authors affirm that the increase in the catalytic activity may be explained by the formation of Ti-O-C bonds on the interface of the TiO_2 and MWCNT. The formation of these bonds favored the charge transfer between the two materials. The MWCNTs worked as electron sinks and allowed only uni-directional flow of electrons, which limited the electron-hole recombination in the TiO_2. When the nanocomposite was irradiated with UV-Visible light, electron-hole pairs were formed in the conduction and valance bands of TiO_2. The electrons of the TiO_2 conduction band were transferred to MWCNTs, leaving holes in the valance band that oxide the water or glycerol (sacrifice agent) present in the solution.

TiO_2/MWCNT nanofibers were synthesized by a combination of sol-gel and electrospinning by Moya et al. [47]. Figure 4a shows a scheme of the steps of the TiO_2/MWCNT nanofibers synthesis. The TiO_2 was prepared through the sol-gel method from an alcoholic solution of titanium ethoxide and acetic acid. The formed sol was mixed with a polyvinyl pyrrolidone solution and the MWCNTs. Then, the mixture was used in the electrospinning. After electrospinning, the samples were treated thermally to remove the polymer. In order to crystallize the titania, a sec-

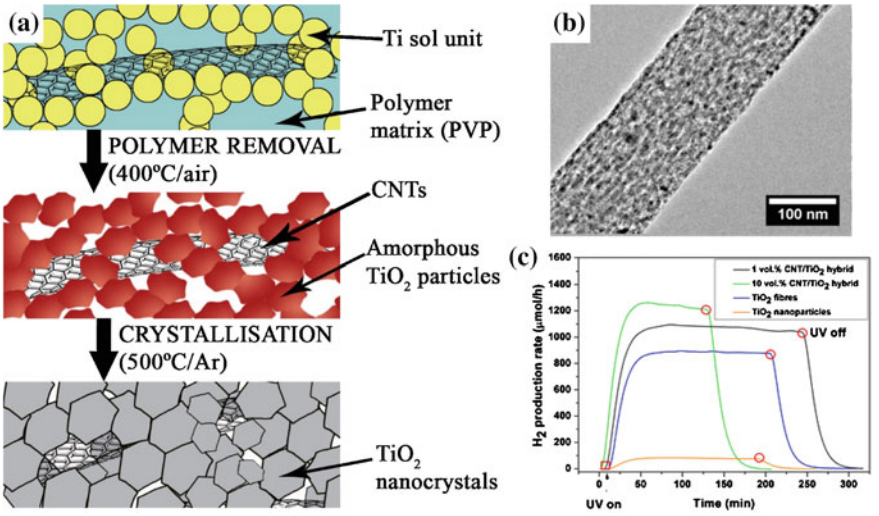

Fig. 4 **a** Scheme of the steps of the MWCNT/TiO_2 nanofibers synthesis. **b** TEM image of the MWCNT/TiO_2 nanofibers obtained. **c** Photocatalytic H_2 production of 1 and 10 vol% MWCNT/TiO_2 hybrid and TiO_2 reference samples. Reprinted with permission [47]

ond thermal treatment was realized. Figure 4b present TEM image of the structure formed.

The photocatalytic activity for H_2 production of the CNT/TiO_2 nanofibers was compared with electrospun TiO_2 nanofibers and TiO_2 nanoparticles. The experiments employed the photocatalysts dispersed in a reaction mixture of water and methanol. The reactor was irradiated with a UV–vis light source equipped with a 200 W Hg lamp.

Figure 4c shows the hydrogen production rate of the CNT/TiO_2 hybrids, TiO_2 nanoparticles and nanofibers. TiO_2 nanoparticles and nanofibers produced 2.94 and 27.66 $\mu mol\ h^{-1}\ g^{-1}$ of hydrogen, respectively. The formation of the CNT/TiO_2 hybrids increased even more the H_2 production rate. The hybrids with 1 and 10 vol% of MWCNT increased the H_2 production rate to 34.02 and 40.6 $\mu mol\ h^{-1}\ g^{-1}$, respectively. The authors affirm that the large gain in the photocatalytic performance with the use of nanofibers is due to the synergistic effect of the TiO_2 nanoparticle network in the fiber. The continuous and highly porous nanostructure aided the interfacial charge transfer and improved the adsorption and desorption of water photoreduction reactants and products. The introduction of the CNTs in the structure led to an additional gain in the photocatalytic H_2 production since it aided, even more, the electron transfer and mobility.

Similar to Reddy et al. [46], Chai et al. [48] employed the hydrothermal method to synthesize fullerene (C_{60}) decorated SWCNTs/TiO_2 nanocomposites (C_{60}-d-CNTs/TiO_2). The synthesis of the composite consisted of mixing C_{60} decorated SWCNTs and titanium sulfate ($Ti(SO_4)_2$). The mixture was kept in autoclave at 100 °C for 72 h. Figure 5a shows a high resolution transmission electronic microscopy (HRTEM) image of the nanocomposite obtained. We can see that the TiO_2 nanoparticles are intimately bound to C_{60}-d-CNTs surfaces.

The photoelectrochemical behavior of the materials was evaluated via linear voltammetry. Figure 5b shows the current density developed by the pure TiO_2, 5 wt% SWCNTs/TiO_2 and 5 wt% C_{60}-d-CNTs/TiO_2. The C_{60}-d-CNTs/TiO_2 nanocomposite presented a photocurrent approximately 10 and 2.5 times higher than the pure TiO_2 and SWCNTs/TiO_2, respectively. The increase of the current density indicates smaller recombination and more efficient carrier separation at the C60-d-CNTs and TiO_2 interface.

Figure 5c presents a comparison of the photocatalytic H_2 evolution rates of the pure TiO_2, C_{60}-d-CNTs, and carbon/TiO_2 nanocomposites with 5 wt% carbon-loading. The C_{60}-d-CNTs/TiO_2 presented the highest photocatalytic H_2 production rate, ca. 651 $\mu mol\ h^{-1}$. The authors proposed that the enhancement in the hydrogen production is due to a smooth transfer of photogenerated electrons from TiO_2 to CNTs, and then to C_{60} under UV-light irradiation, thereby effectively inhibiting the carrier recombination. The proposed photocatalytic H_2 evolution mechanism over the C_{60}-d-CNTs/TiO_2 is shown in Fig. 5d.

In order to enhance the photoelectrochemical (PEC) water splitting performance of TiO_2/CNT composites, some works investigated the formation of ternary nanocomposites. To accomplish this, noble metals and rare earth metal nanoparticles are added to the composites [14, 49]. Chaudhary et al. [14] obtained a

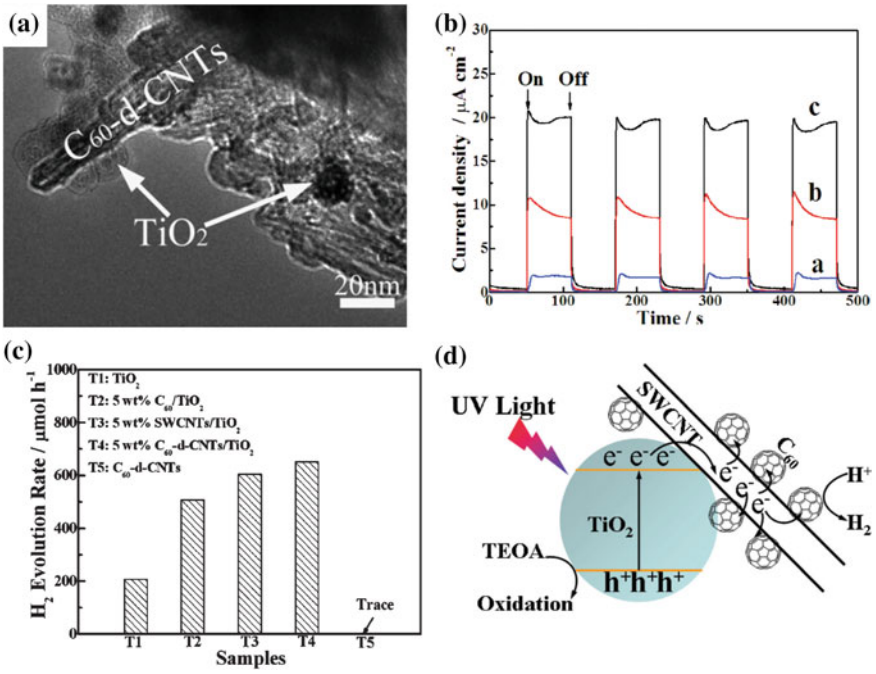

Fig. 5 **a** HRTEM images of C_{60}-d-CNTs/TiO_2 nanocomposites synthesized. **b** The transient photocurrent responses of [a] the pure TiO_2, [b] 5 wt% SWCNTs/TiO_2 and [c] 5 wt% C_{60}-d-CNTs/TiO_2. **c** Comparison of the photocatalytic H_2 evolution rates of the pure TiO_2, C_{60}-d-CNTs, and carbon/TiO_2 nanocomposites with 5 wt% carbon-loading. **d** The proposed photocatalytic H_2 evolution mechanism over the C_{60}-d-CNTs/TiO_2. Reprinted with permission [48]

ternary Ag/TiO_2/CNT nanocomposite with improved visible light photo-response and PEC performance. The TiO_2/CNT nanocomposite was prepared by hydrothermal method and chemically decorated with Ag nanoparticles. The TEM image of the Ag/TiO_2/CNT nanocomposite (Fig. 6a) shows the TiO_2 and Ag nanoparticles over the MWCNT surface.

The optical properties of the materials were studied by diffuse reflectance spectra. The TiO_2, TiO_2/CNT and Ag/TiO_2/CNT samples presented optical band gap values of 3.2, 3.1 and 2.8 eV, respectively. The lowest bandgap of the Ag/TiO_2/CNT nanocomposite is explained by the surface plasmon resonance (SPR) effect of Ag nanoparticles. It is known that plasmonic metal nanoparticles absorb visible light irradiation and inject charge carriers into the adjacent semiconductor. Therefore, this combination of Ag with TiO_2 is promising to be applied for water splitting.

The PEC water splitting of TiO_2, TiO_2/CNT, and Ag/TiO_2/CNT samples were investigated by linear voltammetry under dark and visible light irradiation (Fig. 6b). The Ag/TiO_2/CNT ternary nanocomposite exhibits a photocurrent density of 0.91 mA/cm^2, which is four-fold higher than that developed by the TiO_2/CNT composite (0.23 mA/cm^2). The results showed that the synergy of the Ag nanoparti-

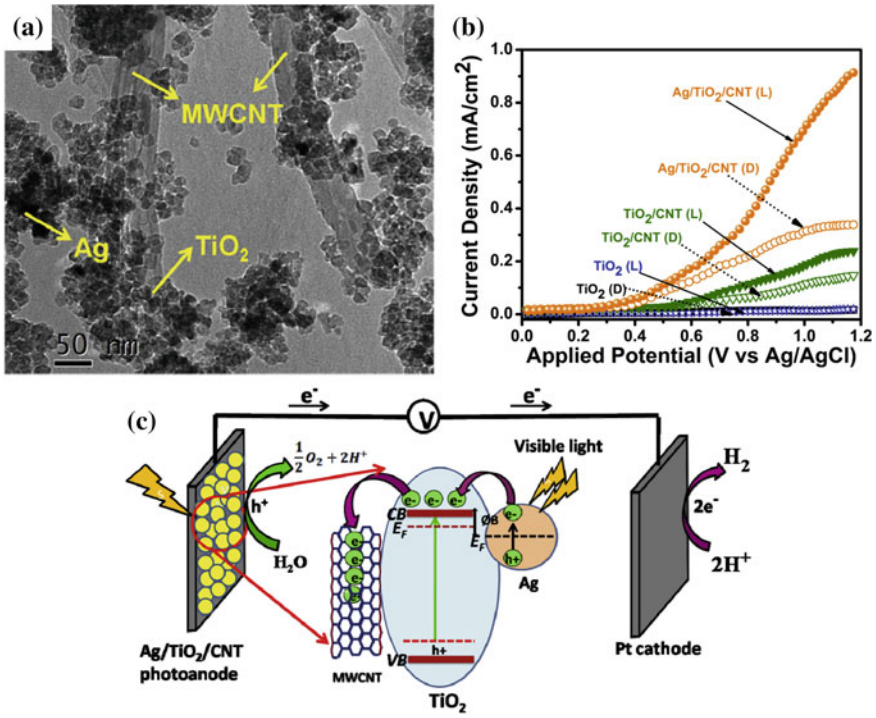

Fig. 6 **a** TEM images of Ag/TiO_2/CNT nanocomposites. **b** Linear voltammetry curves of TiO_2, TiO_2/CNT and Ag/TiO_2/CNT electrodes under dark (D) and visible illumination (L). **c** Schematic representation of the mechanism of PEC water splitting for Ag/TiO_2/CNT nanocomposite under visible light irradiation. Reprinted with permission [14]

cles and CNT at the Ag/TiO_2/CNT nanocomposite resulted in stronger visible light absorption, lower recombination of charge carriers and higher charge carrier density than those of the binary TiO_2/CNT and pure TiO_2. Figure 6c demonstrates a possible mechanism of PEC water splitting for Ag/TiO_2/CNT nanocomposite.

The synthesis of a ternary nanocomposite was also reported by Tahir [49]. The ternary was formed by the addition of the rare earth metal Lanthanum (La) to the CNTs/TiO_2 composites. Figure 7a, b show the SEM and HRTEM images of the La-modified CNTs/TiO_2 composite, respectively. The photocatalytic hydrogen evolution from glycerol-water mixture was investigated. The 7% La–5% CNT/TiO_2 nanocomposite produced the highest H_2 evolution rate, of 17265 ppm g^{-1} h^{-1}. On the other hand, the pure TiO_2 and 5%CNT/TiO_2 nanocomposite showed values of 4253 and 9225 ppm g^{-1} h^{-1}, respectively. The authors attribute the significant improvement in the photo-activity to the synergistic effect between La and CNTs, larger surface area, cleavage of glycerol by La, appropriate band structure, and hindered charges recombination rate. The mechanism proposed for the photocatalytic hydrogen production from a glycerol-water mixture over La-CNTs/TiO_2 composite is presented in Fig. 7c.

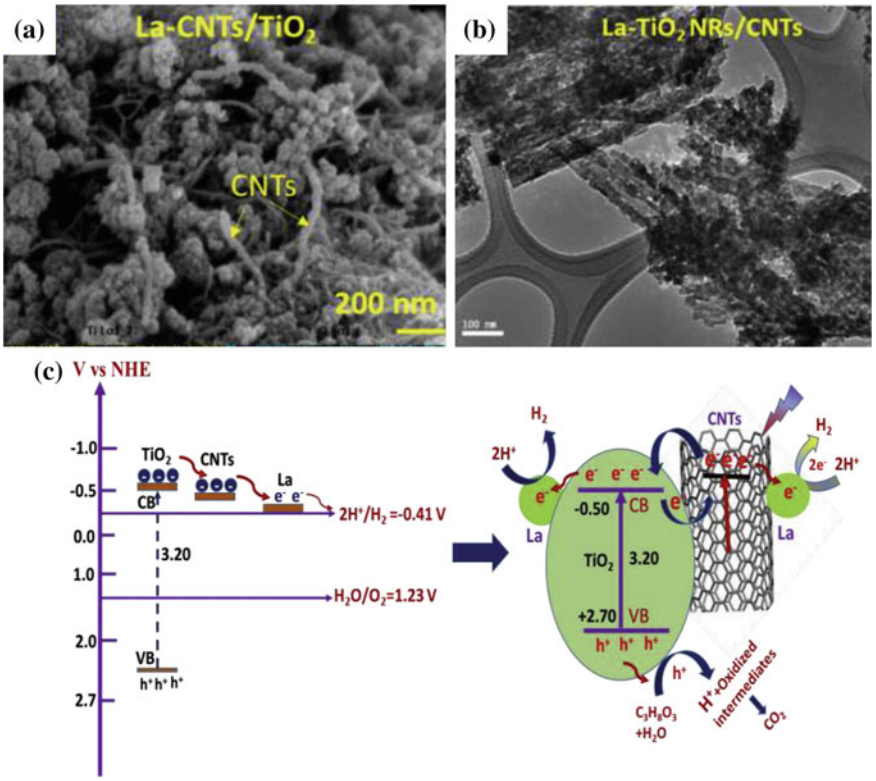

Fig. 7 **a** SEM and **b** HRTEM images of La-modified CNTs/TiO_2 composite. **c** The mechanism proposed for photocatalytic hydrogen production from glycerol-water mixture over La-CNTs/TiO_2 composite under UV-visible light irradiations. Reprinted with permission [49]

The main difference, compared to the CNT/TiO_2 nanocomposite, is that La captures the photogenerated electrons and enables them to prevent charges recombination.

As observed, most researches employ TiO_2 nanoparticles to form nanocomposites with CNTs. One-dimensional (1D) nanomaterials, such as the nanotubes, have in general enhanced chemical, optical, thermal, and electrical properties when compared to nanoparticles [50]. To verify whether the combination of TiO_2 with CNTs improves the photoelectric properties of the nanocomposites, Guaglianoni et al. [43] deposited CNTs on the surface of nanotubes of TiO_2 doped with cobalt. The nanotubes of TiO_2 doped with cobalt were synthesized by electrochemical anodization and applied as a substrate for the growth of CNTs via Chemical Vapor Deposition (CVD). Images of MEV and MET of the materials obtained are shown in Fig. 8a–d.

The linear voltammetry tests (Fig. 8e) show that the photocurrent developed by the CNTs/Co-TiO_2 nanotubes is much higher than that reported in the literature for CNTs nanocomposites and TiO_2 nanoparticles [14]. Thus, the synergic effect of the two nanomaterials on the photocurrent is evident. This result indicates that the materials

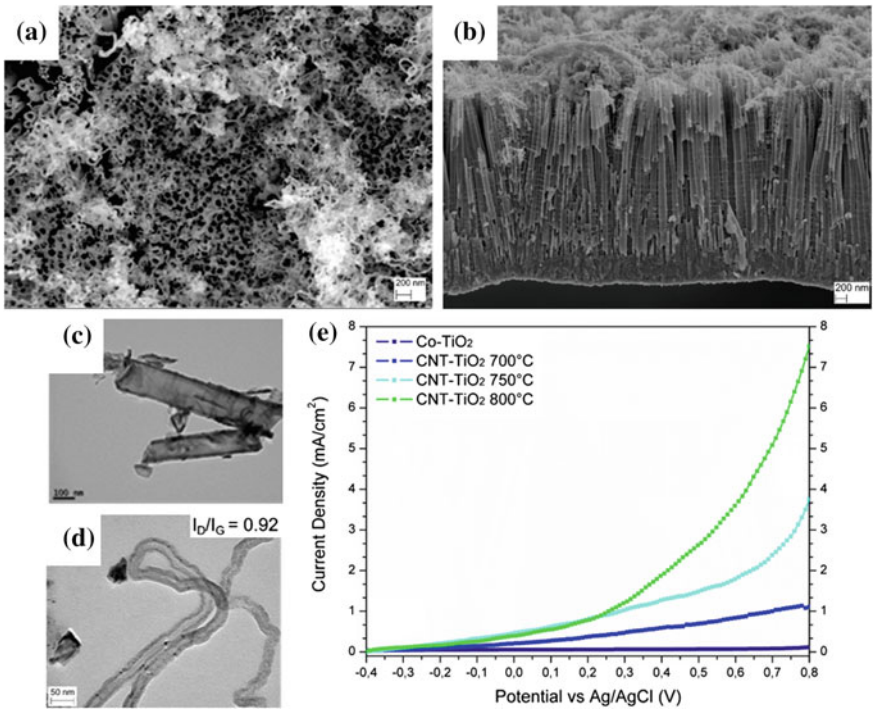

Fig. 8 SEM images of the CNTs/Co-TiO_2 nanotubes: **a** top view and **b** lateral view. TEM images of **c** Co-TiO_2 nanotubes and **d** carbon nanotubes. **e** Linear voltammetry curves of the CNTs/Co-TiO_2 nanotubes

obtained are promising candidates for the application of hydrogen production from the water using solar light.

Based on works presented and the growing number of publications about the topic, it is clear that the formation of CNT/TiO_2 nanocomposites is effective to improve the photoresponse of TiO_2 for H_2 production from water splitting. Researches covering different morphologies as well as the synthesis of ternary materials have not been thoroughly explored yet.

References

1. Das D, Veziroğlu TN (2001) Hydrogen production by biological processes: a survey of literature. Int J Hydrogen Energy 26:13–28. https://doi.org/10.1016/S0360-3199(00)00058-6
2. Fujishima A, Honda K (1972) TiO_2 photoelectrochemistry and photocatalysis. Nature 213:8656
3. Leary R, Westwood A (2011) Carbonaceous nanomaterials for the enhancement of TiO_2 photocatalysis. Carbon N. Y. 49:741–772. https://doi.org/10.1016/j.carbon.2010.10.010

4. Jafari T, Moharreri E, Amin AS, Miao R, Song W, Suib SL (2016) Photocatalytic water splitting—the untamed dream: a review of recent advances. Molecules 21:5654–5671. https://doi.org/10.3390/molecules21070900
5. Ge M, Cai J, Iocozzia J, Cao C, Huang J, Zhang X, Shen J, Wang S, Zhang S, Zhang KQ, Lai Y, Lin Z (2017) A review of TiO_2 nanostructured catalysts for sustainable H_2 generation. Int J Hydrogen Energy 42:8418–8449. https://doi.org/10.1016/j.ijhydene.2016.12.052
6. Xu T, Zheng H, Zhang P, Lin W (2016) Photocatalytic degradation of a low concentration pharmaceutical pollutant by nanoporous TiO_2 film with exposed 001 facets. RSC Adv. 6:95818–95824. https://doi.org/10.1039/c6ra22011h
7. Yañez D, Guerrero S, Lieberwirth I, Ulloa MT, Gomez T, Rabagliati FM, Zapata PA (2015) Photocatalytic inhibition of bacteria by TiO_2 nanotubes-doped polyethylene composites. Appl Catal A Gen 489:255–261. https://doi.org/10.1016/J.APCATA.2014.10.051
8. Gong J, Lai Y, Lin C (2010) Electrochemically multi-anodized TiO_2 nanotube arrays for enhancing hydrogen generation by photoelectrocatalytic water splitting. Electrochim Acta 55:4776–4782. https://doi.org/10.1016/J.ELECTACTA.2010.03.055
9. Lee CW, Antoniou Kourounioti R, Wu JCS, Murchie E, Maroto-Valer M, Jensen OE, Huang CW, Ruban A (2014) Photocatalytic conversion of CO_2 to hydrocarbons by light-harvesting complex assisted Rh-doped TiO_2 photocatalyst. J CO_2 Util 5:33–40. https://doi.org/10.1016/j.jcou.2013.12.002
10. B.X. Lei, J.Y. Liao, R. Zhang, J. Wang, C.Y. Su, D. Bin Kuang, Ordered crystalline tio2 nanotube arrays on transparent FTO glass for efficient dye-sensitized solar cells, J. Phys. Chem. C. 114 (2010) 15228–15233. https://doi.org/10.1021/jp105780v
11. Zhang L, Wang S, Yuan Z, Lu C (2016) A controllable selective cataluminescence sensor for diethyl ether using mesoporous TiO_2 nanoparticles. Sens Actuators B Chem 230:242–249. https://doi.org/10.1016/j.snb.2016.02.055
12. Kunrath MF, Hubler R, Shinkai RSA, Teixeira ER (2018) Application of TiO_2 nanotubes as a drug delivery system for biomedical implants: a critical overview. ChemistrySelect 3:11180–11189. https://doi.org/10.1002/slct.201801459
13. Gupta SM, Tripathi M (2011) A review of TiO_2 nanoparticles. Chin Sci Bull 56:1639–1657. https://doi.org/10.1007/s11434-011-4476-1
14. Chaudhary D, Singh S, Vankar VD, Khare N (2017) A ternary Ag/TiO_2/CNT photoanode for efficient photoelectrochemical water splitting under visible light irradiation. Int J Hydrogen Energy 42:7826–7835. https://doi.org/10.1016/j.ijhydene.2016.12.036
15. Wang Y, He Y, Lai Q, Fan M (2014) Review of the progress in preparing nano TiO_2: an important environmental engineering material. J Environ Sci (China) 26:2139–2177. https://doi.org/10.1016/j.jes.2014.09.023
16. Roy P, Berger S, Schmuki P (2011) TiO_2 nanotubes: synthesis and applications. Angew Chemie Int Ed 50:2904–2939. https://doi.org/10.1002/anie.201001374
17. Singh R, Dutta S (2018) Synthesis and characterization of solar photoactive TiO_2 nanoparticles with enhanced structural and optical properties. Adv Powder Technol 29:211–219. https://doi.org/10.1016/j.apt.2017.11.005
18. Kardanzadeh M, Kazeminezhad I, Mosivand S (2018) Electro-synthesis and characterization of TiO_2 nanoparticles and their application in removal of congo red from water without UV radiation. Ceram Int 44:5652–5659. https://doi.org/10.1016/j.ceramint.2017.12.214
19. Garcia AP et al (2018) Facile synthesis by peroxide method and microwave-assisted hydrothermal treatment of TiO_2 with high photocatalytic efficiency for dye degradation and hydrogen production. ChemistrySelect 3:11454–11459. https://doi.org/10.1002/slct.201802188
20. Eiden-Assmann S et al (2004) Synthesis and characterization of porous and nonporous monodisperse colloidal TiO_2 particles. Chem Mater 16:6–11. https://doi.org/10.1021/cm0348949
21. H.G. Yang, et al., Solvothermal synthesis and photoreactivity of anatase TiO_2 nanosheets with dominant {001} facets. J Am Chem Soc 4078–4083
22. Lin H et al (2012) Synthesis of high-quality brookite TiO_2 single-crystalline nanosheets with specific facets exposed: tuning catalysts from inert to highly reactive. J Am Chem Soc 134:8328–8331. https://doi.org/10.1021/ja3014049

23. Choi K et al (2015) Synthesis of hierarchical hollow electrospun TiO_2 nanofibers. Mater Lett 158:36–39. https://doi.org/10.1016/j.matlet.2015.05.066
24. Zhang J et al (2017) Fabrication of hierarchical TiO_2 nanofibers by microemulsion electrospinning for photocatalysis applications. Ceram Int 43:15911–15917. https://doi.org/10.1016/j.ceramint.2017.08.166
25. Zhang S et al (2017) Controlled synthesis of TiO_2 nanorod arrays immobilized on ceramic membranes with enhanced photocatalytic performance. Ceram Int 43:7261–7270. https://doi.org/10.1016/j.ceramint.2017.03.019
26. Chen Y et al (2018) Design and construction of hierarchical TiO_2 nanorod arrays by combining layer-by-layer and hydrothermal crystallization techniques for electrochromic application. Appl Surf Sci 440:217–223. https://doi.org/10.1016/j.apsusc.2018.01.115
27. Indira K et al (2015) A review on TiO_2 nanotubes: influence of anodization parameters, formation mechanism, properties, corrosion behavior, and biomedical applications. J Bio-Tribo-Corrosion 1:1–22. https://doi.org/10.1007/s40735-015-0024-x
28. Manique MC et al (2016) Application of hydrothermally produced TiO_2 nanotubes in photocatalytic esterification of oleic acid, Mater. Sci Eng B Solid-State Mater Adv Technol 206:17–21. https://doi.org/10.1016/j.mseb.2016.01.001
29. Tenkyong T et al (2018) Structural modulation and band gap optimisation of electrochemically anodised TiO_2 nanotubes. Mater Sci Semicond Process 83:150–158. https://doi.org/10.1016/j.mssp.2018.04.032
30. Bessegato GG et al (2015) Enhanced photoelectrocatalytic degradation of an acid dye with boron-doped TiO_2 nanotube anodes. Catal Today 240:100–106. https://doi.org/10.1016/j.cattod.2014.03.073
31. Wu Z et al (2009) The fabrication and characterization of novel carbon doped TiO_2 nanotubes, nanowires and nanorods with high visible light photocatalytic activity. Nanotechnology 20. https://doi.org/10.1088/0957-4484/20/23/235701
32. Yuan B et al (2013) Nitrogen doped TiO_2 nanotube arrays with high photoelectrochemical activity for photocatalytic applications. Appl Surf Sci 280:523–529. https://doi.org/10.1016/j.apsusc.2013.05.021
33. Ni J et al (2016) Self-supported nanotube arrays of sulfur-doped tio2enabling ultrastable and robust sodium storage. Adv Mater 28:2259–2265. https://doi.org/10.1002/adma.201504412
34. Ning X et al (2016) Preparation and capacitance properties of Mn-doped TiO_2 nanotube arrays by anodisation of Ti-Mn alloy. J Alloys Compd 658:177–182. https://doi.org/10.1016/j.jallcom.2015.10.204
35. Fan X et al (2014) Preparation and characterization of Ag deposited and Fe doped TiO_2 nanotube arrays for photocatalytic hydrogen production by water splitting. Ceram Int 40:15907–15917. https://doi.org/10.1016/j.ceramint.2014.07.119
36. Venturini J et al (2019) Cobalt-doped titanium oxide nanotubes grown via one-step anodization for water splitting applications. Appl Surf Sci 464:351–359. https://doi.org/10.1016/j.apsusc.2018.09.093
37. Dong Z et al (2018) Ni-doped TiO_2 nanotubes photoanode for enhanced photoelectrochemical water splitting. Appl Surf Sci 443:321–328. https://doi.org/10.1016/J.APSUSC.2018.03.031
38. Zhang T et al (2015) Molybdenum-doped and anatase/rutile mixed-phase TiO_2 nanotube photoelectrode for high photoelectrochemical performance. J Power Sources 281:411–416. https://doi.org/10.1016/j.jpowsour.2015.02.017
39. Nguyen Van C et al (2018) Preparation and photoelectrochemical performance of porous TiO_2/graphene nanocomposite films. Mater Lett 213:109–113. https://doi.org/10.1016/j.matlet.2017.11.008
40. Cho E et al (2015) Fullerene C 70 decorated TiO_2 nanowires for visible-light-responsive photocatalyst. Appl Surf Sci 355:536–546. https://doi.org/10.1016/j.apsusc.2015.07.062
41. Cao K et al (2016) Enhanced photocatalytic activity of nanohybrids TiO_2/CNTs materials. Mater Lett 165:247–251
42. Cendrowski K et al (2014) Preliminary study towards photoactivity enhancement using a biocompatible titanium dioxide/carbon nanotubes composite. J Alloys Compd 605:173–178. https://doi.org/10.1016/j.jallcom.2014.03.112

43. Guaglianoni WC et al (2018) Novel nanoarchitectured cobalt-doped TiO_2 and carbon nanotube arrays: synthesis and photocurrent performance. Ceram Int (2018). https://doi.org/10.1016/j.ceramint.2018.10.169
44. Kho YK et al (2010) Photocatalytic H_2 evolution over TiO_2 nanoparticles. the synergistic effect of anatase and rutile. J Phys Chem C 114:2821–2829
45. Woan K et al (2009) Photocatalytic Carbon nanotube-TiO_2 composites. Adv Mater 21:2233–2239. https://doi.org/10.1002/adma.200802738
46. Reddy NR et al (2018) Enhanced photocatalytic hydrogen production activity of noble metal free MWCNT-TiO_2 nanocomposites. Int J Hydrogen Energy 43:4036–4043. https://doi.org/10.1016/j.ijhydene.2018.01.011
47. Moya A et al (2015) Oxygen vacancies and interfaces enhancing photocatalytic hydrogen production in mesoporous CNT/TiO_2 hybrids. Appl Catal B Environ 179:574–582. https://doi.org/10.1016/J.APCATB.2015.05.052
48. Chai B et al (2013) Synthesis of C60-decorated SWCNTs (C60-d-CNTs) and its TiO_2-based nanocomposite with enhanced photocatalytic activity for hydrogen production. Dalt Trans 42:3402–3409. https://doi.org/10.1039/c2dt32458j
49. Tahir M (2019) La-modified TiO_2/carbon nanotubes assembly nanocomposite for efficient photocatalytic hydrogen evolution from glycerol-water mixture. Int J Hydrogen Energy 44:3711–3725. https://doi.org/10.1016/j.ijhydene.2018.12.095
50. Chen C et al (2018) One-dimensional nanomaterials for energy storage. J Phys D Appl Phys 51. https://doi.org/10.1088/1361-6463/aaa98d

TiO_2 Nanotubes as Photocatalyst for Biodiesel Production

Marcia Cardoso Manique

Abstract The use of semiconductors as catalysts in photocatalytic reactions is an alternative for the synthesis of esters with the potential to simplify the production process by enabling the use of ambient temperature and pressure. Photocatalysis is a process involving the use of a light source to trigger oxidation and reduction reactions through the formation of electrons and holes by excitation of the semiconductor. The use of photocatalysts with a high surface area such as TiO_2 nanotubes (TNTs) can offer better photocatalytic performance. They have a higher surface area and a high number of hydroxyl groups versus oxide precursors (TiO_2). The hydrothermal mechanism is a simple and effective method to synthesize TNTs, wherein the TiO_2 reacts with a concentrated NaOH solution at high pressure. In the related esterification experiments with TNTs as a photocatalyst, the lowest band gap energy sample exhibited the highest rate of oleic acid esterification among all the investigated TNTs. In addition to the band gap, other factors such as the TNT crystalline phase and surface area were important in photocatalytic performance.

Keywords TiO_2 nanotubes · Photocatalysis · Biodiesel

Abbreviations

CH	Conventional Hydrothermal
FFA	Free Fatty Acid
MAH	Microwave-Assisted Hydrothermal
TEM	Transmission Electron Microscopy
TNT	TiO_2 Nanotubes
UV	Ultraviolet
XRD	X-ray Diffraction

M. C. Manique (✉)
Universidade Federal Do Rio Grande Do Sul, Porto Alegre, Brazil
e-mail: marciamanique@yahoo.com.br

A. Kopp Alves (ed.), *Nanomaterials for Eco-friendly Applications*,
Engineering Materials, https://doi.org/10.1007/978-3-030-26810-7_4

1 Introduction

Heterogeneous photocatalysis has been studied mainly concerning its application in renewable fuel production. One of the methods studied is artificial photosynthesis, which is carried out from the catalytic CO_2 photoreduction. This method produces hydrocarbons of high commercial value such as methane and methanol [1–3]. Another widely studied method is hydrogen production by photocatalysis, which uses photocleavage of the water molecule. In this system, different electron donors are employed to prevent recombination of the electron/hole pair. This process reduces water to H2 on the semiconductor surface [4–6]. Another promising utilization of a heterogeneous photocatalytic is the esterification of free fatty acid (FFA) into methyl ester for biodiesel production.

Is widely known that conventional base-catalyzed process is susceptible to high FFA contents, which lead to soap formation and lower biodiesel yields [7, 8]. The conversion of FFAs into esters via an esterification reaction is required to avoid saponification. Acids catalysts, such as sulfuric acid (H_2SO_4), are commonly used to convert FFA in a pretreatment process [9]. However, the use of an acid catalyst requires excessive quantities of methanol, resulting in high costs related to both waste treatment and the necessary stainless-steel equipment [7, 10].

Thus, a heterogeneous photocatalytic process may be employed for the efficient esterification of fatty acids. A first study was related by Corro et al. [11]. The authors used the photocatalyst ZnO/SiO_2 for the esterification of FFAs present in the crude oil of Jatropha Curcas. The photocatalyst was highly active for this esterification process, and it was reusable because the catalytic activity remains virtually unchanged even after 10 cycles of use. They are obtained 96% ester content with 4 h of reaction using a mass ratio of catalyst: oil and a 15% molar ratio; methanol: oil was 12:1.

The use of photocatalysts with a high surface area such as TNTs can offer better photocatalytic performance. They have a higher surface area and a high number of hydroxyl groups versus oxide precursors (TiO_2) [12, 13]. The hydrothermal mechanism is a simple and effective method to synthesize TNTs, wherein the TiO_2 reacts with a concentrated NaOH solution at high pressure [14–16]. Macak et al. [17] showed in their study that the nanotubes provide a greater geometric optimization with significantly lower diffusion transport paths in the tube walls, in which it allows smaller occurrences of entrapment or recombination of the photogenerated electron-gap pairs compared to P25. Furthermore, this chapter describes the hydrothermal reaction for formation of TNTs, their characterization and their performance as a photocatalyst for biodiesel production in the esterification step.

2 TiO_2 Nanotubes

TNTs are some of the more interesting designs for electrochemical applications due to their unidirectional electron transport properties and elevated available specific surface. The first synthesis of TNTs reported was in 1996, by Hoyer [18] via electrochemical deposition in an aluminum oxide mold. Then, TNTs were produced

by the hydrothermal method (1998) by Kasuga et al. [14], and by the anodizing method (1999) by Zwilling et al. [19]. Table 1 compares the principal advantage, disadvantage, and characteristic of nanotubes obtained from each method.

The hydrothermal synthesis is one of the techniques most used by the researchers to obtain the TNTs. The reaction under high pressures allows the solvent to remain in the liquid state at temperatures higher than its boiling point. In this way, there is a considerable increase in the solubility of the precursor [22].

Kasuga et al. [14] used TiO_2 to react with a concentrated solution of NaOH (10 mol L^{-1}) at high pressures. According to the technique, some grams of TiO_2 powder can be converted into nanotubes with an efficiency of about 100%, at a temperature of 110–150 °C, followed by a wash with water and a dilute solution of 0.1 mol L^{-1} HCl. After some reproducibility tests, they noticed the persistent formation of nanotubes with a mean diameter ranging from 8 nm to 100 nm, predicting that the various sizes depended on the preparation conditions. This work was a starting point for a series of subsequent productions, allowing a review and investigation on the steps of the formation of TNTs.

Zhang et al. [13] have proposed a formation mechanism in which the hydrothermal method produces a disordered phase when TiO_2 reacts with NaOH. This phase recrystallizes in layers, forming sheets of titanates, with $H_2Ti_3O_7$ composition. The deficiency of H in the upper surface of the layers becomes responsible for the asymmetry that leads to the folding of the layer, forming the nanotube. In this way, the nanotubes have lower energy than in the flat form, since in this format the outstanding connections of the edge are eliminated, which ends up with the superficial tension of the outer layer. In the same work, the hydrothermal reactions were paused every two hours in an attempt to prove the steps of the formation of the nanotubes. After a few hours of reaction, the presence of nano-foils was identified, proving that they are intermediates in the formation of nanotubes. The recrystallization of the disordered phase in nano-foils has also been reported by other authors [24–28], mainly in incomplete conversions, some even captured in full winding process. Most authors suggest the formation of nanotubes by winding the sheets or lamellae. Already in

Table 1 Comparison of typical synthesis of TNTs

Method	Advantage	Disadvantage	Characteristic
Template method [9, 20]	Obtain TNTs in a regular and controlled manner	High cost due to mold loss at the end of the process	Ordered structures (powder)
Anodic oxidation [17, 21]	Ordered alignment with high length-to-diameter ratio	Use of toxic HF solutions	Oriented structures (films)
Hydrothermal method [12, 15, 16, 22, 23]	Simple route to obtain nanotube	Long reaction time	Alignment to chance (powder)

the works of Bavykin et al. [29] and Kukovecz et al. [30] considered another type of mechanism, that of folding overlapping layers or sheets.

Unlike the carbon nanotubes, where they have a perfectly concentric distribution of the multilayers, a same TiO_2 nanotube shows a variation in the wall thickness on opposite sides [29]. Most of the papers that deal with the subject adopt a model where the tubes are formed either by the winding of a single sheet (Fig. 1a), by the bending of a set of stacked sheets (Fig. 1b) or, by connecting sheets by the edges (Fig. 1c).

An evidence for these phenomena is exemplify in the electron microscopy images of the transverse sections of nanotubes, as shown in Fig. 2a. In the first case, the cross-section of the tubes forms a spiral, as shown in Fig. 2b. In the second, the cross-section of the tubes has the appearance of an onion, Fig. 2c. Figure 2d indicates that there are different thicknesses on the nanotube walls.

It is important to highlight that the characteristics of the nanotubes formed (surface area, crystalline phases, and morphology) depend on the synthesis conditions and the treatments applied after the hydrothermal synthesis.

The main disadvantage of the hydrothermal method is the long period that this mechanism of formation of TNTs requires, from 24 to 72 h of reaction [15]. An

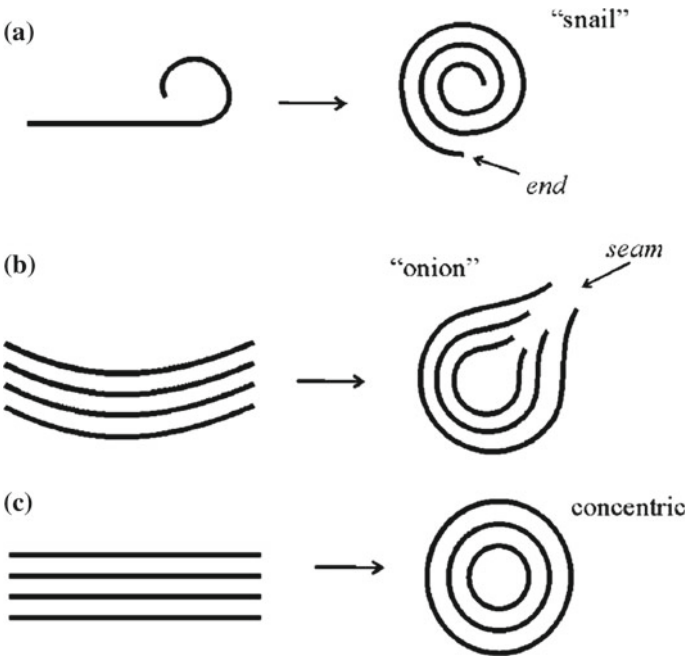

Fig. 1 A scheme demonstrates the possible mechanisms for the formation of nanotubes with multiple walls. **a** Winding a single sheet, **b** winding a set of stacked sheets and **c** sheets connected by the edge. Reproduced from Ref. [29] with permission from The Royal Society of Chemistry

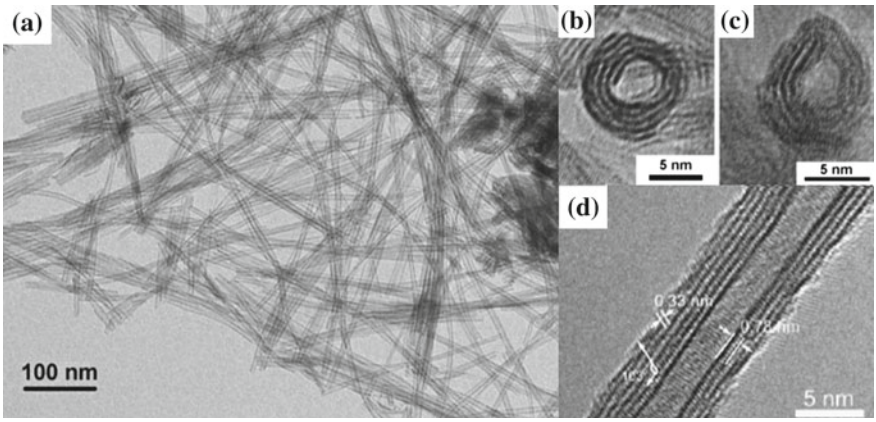

Fig. 2 TEM images of TNTs: **a** typical distribution of nanotubes, adapted from Ref. [29] with permission from The Royal Society of Chemistry; **b** spiral-shaped cross-section and **c** onion-shaped, adapted with permission from Kukovecz et al. [30]. Copyright 2005 American Chemical Society; **d** detail showing the different thicknesses on the nanotube wall, adapted with permission from Wu et al. [28]. Copyright 2006 American Chemical Society

alternative is the use of microwave as the heat source, been able to reduce the reaction time of 1–3 h, depending on the equipment and the temperature applied [31].

3 Hydrothermal Methods

The use of the microwave-assisted hydrothermal method or hydrothermal method irradiated by microwave has aroused particular interest in the synthesis of organic and inorganic compounds and the heat treatment of many materials. The use of microwave energy has great potential because it offers advantages in reducing processing time and saving energy [15, 32, 33].

Another important advantage of microwave synthesis is the small temperature variation in the reaction medium, where the heating of the solution and the processing of the materials is direct and homogeneous. In conventional heating synthesis, the solvent is heated indirectly by energy transmission, providing a temperature gradient in the system [34, 35]. Figure 3a and b shows the conventional hydrothermal heating system, where energy is transferred by conduction, convection, and radiate heat processes from the surface of the material.

In the hydrothermal system irradiated by microwave (Fig. 4a), the thermal gradient almost does not exist (Fig. 4b). Microwaves energy is transmitted directly through molecular interactions with the electromagnetic field, with homogeneous nucleation and uniform particle growth occurring. Electromagnetic radiation interacts with the induced and/or permanent dipoles of the water molecules and the dispersed particles. The dipoles of the molecules of the reaction medium interact with the electromagnetic

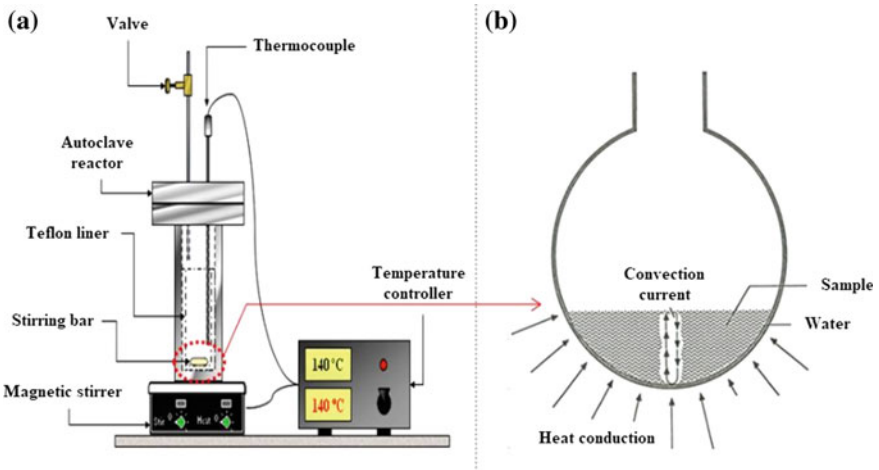

Fig. 3 Schematic representation (**a**) of the conventional hydrothermal system and **b** the reaction medium. Adapted with permission from Kingston and Jassie [35]. Copyright 1989 American Chemical Society

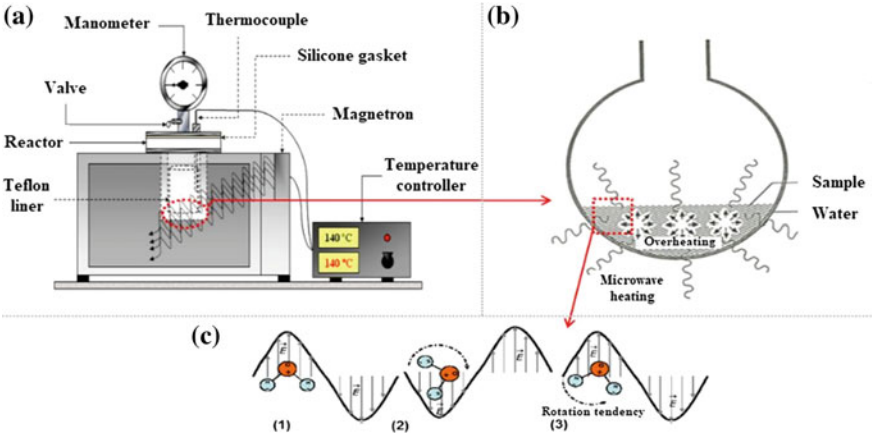

Fig. 4 Schematic representation (**a**) of the microwave-irradiated hydrothermal system, **b** the microwave-heated reaction medium, and **c** the interaction of water molecules with microwave waves. Adapted with permission from Kingston and Jassie [35]. Copyright 1989 American Chemical Society

radiation, where the molecules are oriented in the same direction of the electric field of these waves (Fig. 4c), resulting in the rotation of the particles and rapid heating of the reaction medium [35].

Many studies have used the microwave-assisted hydrothermal method for the synthesis of TNTs [15, 31–33]. The results indicate the formation of nanotubes with excellent morphologies, with significant reductions in reaction time and energy consumption. In addition, the technique showed greater reproducibility compared to the conventional method [15].

3.1 Hydrothermal Synthesis of TNTs

It will be reported here, results obtained from previous work on the synthesis and use of TNTs for the oleic acid esterification step to study the feasibility of photocatalysis for biodiesel production.

The conventional hydrothermal (CH) method is based on the work of Kasuga et al. [14] in which a solution is prepared with TiO_2 nanoparticles precursor and 10 M NaOH. This solution is transferred to a stainless-steel autoclave using a Teflon bottle. The solution is heated in temperatures of 110–150 °C for 20–72 h. After the reaction, the material is washed with deionized water and 0.1 M HCl to adjust the pH. The material is then dried and heat-treated at 450 °C.

In the synthesis by the microwave-assisted hydrothermal (MAH) method, the samples are prepared with a microwave digestion system in Teflon-lined bottles. The reactions are programmed to 400 W of power in the range of 110–150 °C for 1.5–3 h. The post-reaction processing is the same as above.

3.2 Morphology

Figure 5 shows TEM images of some TNTs samples. For CH 110-20 (TNTs produced by the conventional method sintered at 110 °C for 20 h), it can be observed a tubular titania morphology with diameters between 20 and 80 nm (Fig. 5a). This result shows that these conditions (110 °C–20 h) are sufficient to form nanotubes. It can also be observed the formation of filaments with diameters smaller than the nanotubes. These also show the presence of unreacted TiO_2 nanoparticles. For CH 130-48, we noted the presence of non-tubular or nanoribbon structures (Fig. 5b). According to this result, higher reaction times favor the formation of nanoribbons, probably due to the dissolution of the nanotube by precipitation of Ti (IV) in the inner and outer surface of the nanotubes, which fills the tube and pores.

The MAH synthesis (Figs. 5c and d) offered homogeneous nanotubes. The tubular structures were similar in all samples even after varying the time and temperature of synthesis. In contrast to the CH method, higher temperatures did not affect the tubular structures including samples synthesized at 150 °C. The nanotubes had diameters

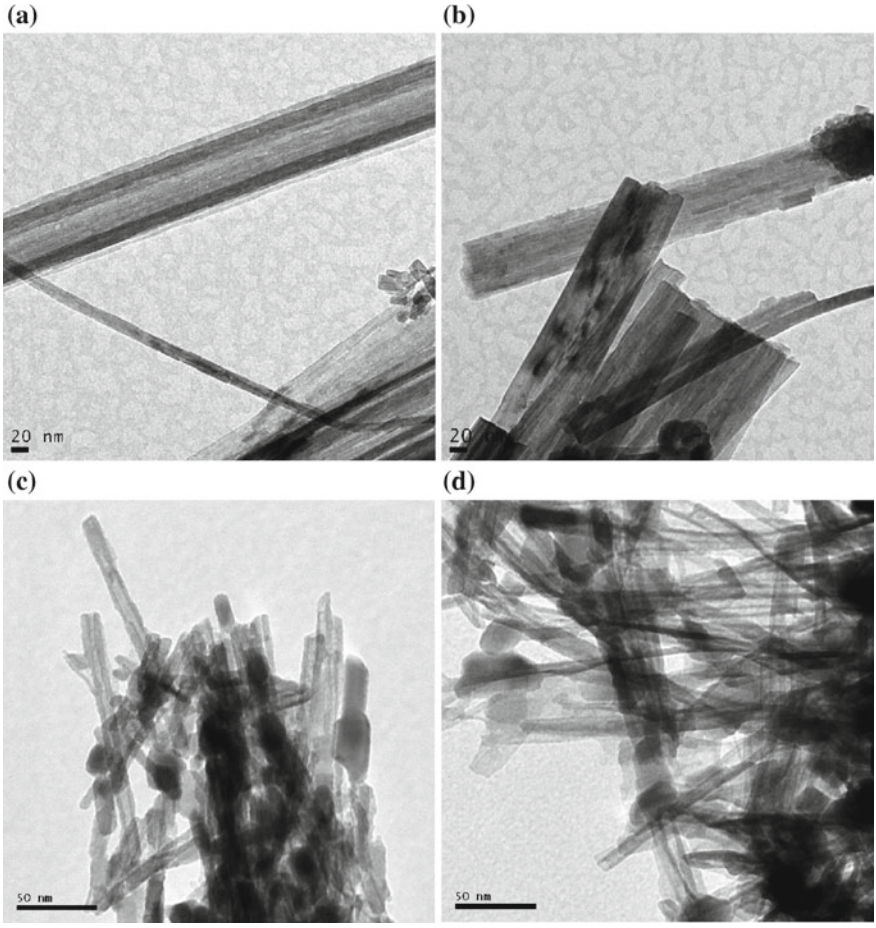

Fig. 5 TEM images of the samples: **a** CH 110-20, **b** CH 130-48, **c** MAH 130-1.5 and **d** MAH 150-3

around 10–12 nm—much smaller than those obtained with the CH method (20 to 80 nm).

This difference in diameter of the nanotubes may be related to the growth of the nano-foils resulting from the dissolution of the TiO_2 precursor. The dissolution rate of these particles corresponds to the number of titania species per unit time in the reaction medium. This rate directly influences the growth velocity of the nanostructure, which may occur preferentially by multi-lamellar stacking and by lateral bonds of these species, forming the nano-sheets. Then there is the thermodynamically favorable process, which is the bending and winding of the nano-foils. Thus, the final morphology of TNTs depends on a balance between (i) the rate of dissolution and subsequent recrystallization and (ii) the speed of bending of the nano-foils. If the rate of dissolution/recrystallization is high, the formation of a nanostructure with

a more significant number of lamellae is obtained quickly, making them more rigid and consequently reducing the bending speed, generating the nanotube with larger diameter and walls with multiple lamellae (thick). In the opposite case, the growth of the nano-foils occurs gradually with the curvature process, leading to the formation of nanotubes of smaller diameter and with few lamellae [29].

3.3 Crystallography

From the crystallographic database and spectra shown by Fig. 6, it can be concluded that the nanotubes have a crystal anatase phase and there is no evidence of a rutile phase. However, for the samples synthesized at 110 °C with the MAH method, it is observed the presence of the rutile phase, attributed to the incomplete amorphization of samples at this lower temperature, causing this crystalline phase to remain in the

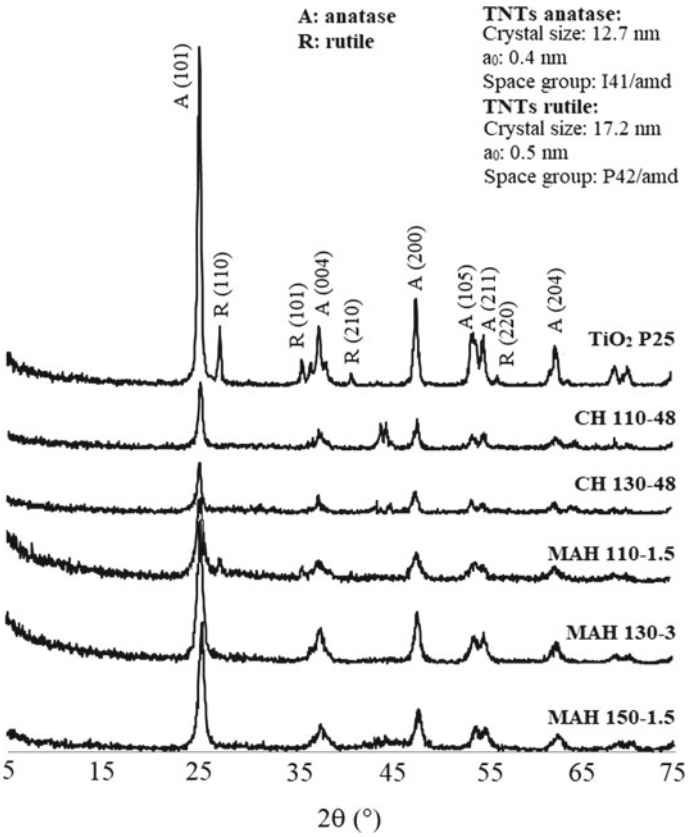

Fig. 6 XRD patterns of TiO_2 P25 and TNTs synthesized by the CH and MAH methods

material. The photocatalytic properties of TiO_2 nanoparticles are strongly dependent on the nature of the crystalline phase. The anatase phase generally exhibits higher photocatalytic activity than the rutile phase; therefore, this is a desirable step in obtaining nanotubes.

3.4 Photocatalytic Efficiency

For the photocatalytic tests of nanotubes using the methyl orange, the samples were kept in the dark for 20 min before the start of photocatalysis which is attributed to the adsorption phenomenon (Fig. 7).

Note that the reaction does not proceed before dye adsorption and photocatalysis. All nanotubes, regardless of the method and conditions of synthesis, showed photocatalytic activity. Nanoribbons showed lower performance and only degraded 16% of the dye in one hour. The TiO_2 P25 showed slightly faster methyl orange degradation (60% in 60 min). The nanotubes synthesized at 150 °C by the MAH method were better and degraded 50% of the dye.

The photocatalytic activity data can be directly related to the synthesis temperature and surface area of the samples. The samples synthesized at higher temperatures (150 °C) had a higher surface area and therefore degraded most of the dye molecules. This sample showed the best results in the photocatalytic tests. Based on these results it is possible to affirm that the larger surface area of the nanotubes promotes their better photocatalytic performance. In addition to the considerable reduction in syn-

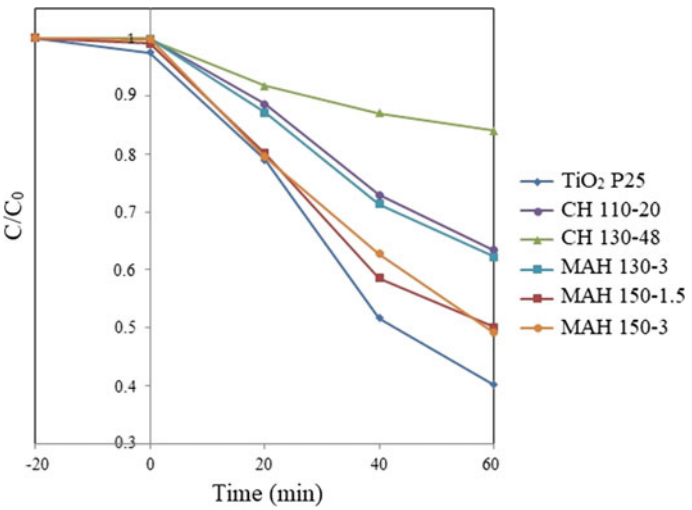

Fig. 7 Photocatalysis results with TNTs and TiO_2 P25 for the removal of methyl orange

thesis time, the MAH method presented advantages such as the uniform formation of nanotubes, higher temperatures of synthesis, and high surface area nanotubes.

3.5 Band Gap Energy

The UV-visible diffuse-reflectance spectrum of TiO_2 P25 (Fig. 8) shows a strong absorption band at around 375 nm. This phenomenon is associated with the transition of an electron from the valence band to the conduction band of a semiconductor. Thus, TiO_2 showed photocatalytic activity in the UV region.

The TNTs exhibited a band gap energy in the UV light absorption region, which did not differ from that of TiO_2 P25. However, the absorption onset of sample CH 110-48 shifted slightly towards a longer wavelength range, reaching an absorption in the visible light region (>400 nm). Band gap energies of the samples were estimated from the variation of the Kubelka-Munk function with photon energy. The results are shown in Table 2. The inset in Fig. 8 shows the Kubelka-Munk plots for the CH 110-48 sample. The estimated band gap value was slightly lower (3.08 eV) than that of P25 (3.28 eV).

Another sample that presented lower band gap energy ($E_g = 3.11$ eV) was MAH 150-3. This sample was highlighted by the best photocatalytic efficiency for the degradation of methyl orange dye.

According to the data presented, it can be concluded that as lower the band gap energy is, greater is the photocatalytic potential of the material since it required less energy to activate it.

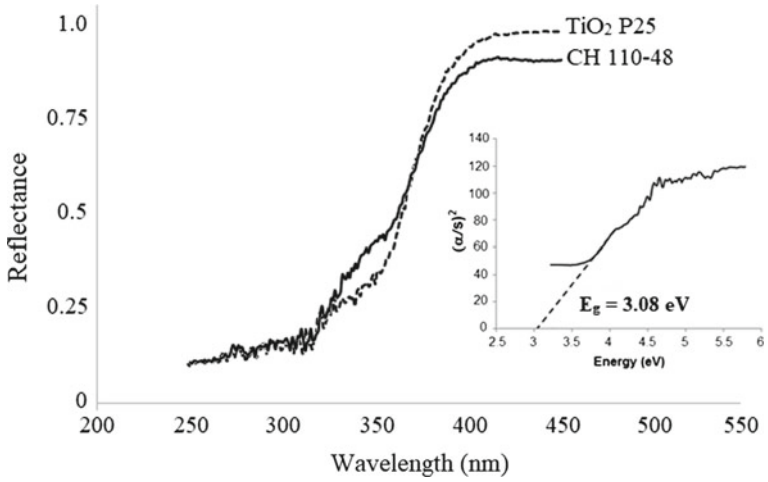

Fig. 8 UV-visible diffuse reflectance spectra of TiO_2 P25 and CH 110-48. Inset: Kubelka-Munk plots for the CH 110-48

Table 2 Absorption band (λ) and band gap (E_g) of TiO_2 P25 and TNTs

Sample	λ (nm)	E_g (eV)
TiO_2 P25	378	3.28
CH 110-20	350	3.54
CH 110-48	402	3.08
CH 130-20	383	3.24
MAH 110-3	370	3.35
MAH 130-1.5	346	3.58
MAH 130-3	386	3.21
MAH 150-1.5	384	3.23
MAH 150-3	399	3.11

4 Application of TNTs in Photocatalytic Esterification of Oleic Acid

For the esterification tests and a better understanding of the studies and reaction mechanisms, oleic acid was used as a reagent. Such a fatty acid was chosen because of its frequent presence in the major vegetable oils used for biodiesel production. The reaction of esterification of oleic acid with methanol, initially tested with the TiO_2 P25 catalyst, was carried out through the photocatalysis process, forming at the end of the reaction methyl oleate and water. Solutions were prepared with methanol: oleic acid molar ratios of 3:1, 6:1, 9:1 and 12:1. The catalyst concentrations were 5, 10, 15 and 20% (w/w oleic acid). Each solution was transferred to the photocatalytic reactor and subjected to UV irradiation at 30 °C with constant stirring. After the reaction, the samples were centrifuged to separate the catalyst from the solution. The samples were analyzed by gas, and the results are shown in Fig. 9.

Optimal ester yield was achieved at 86% with a 3:1 molar ratio and 15% P25 loading. Thus, it was not necessary to use a large stoichiometric excess of methanol to produce the esterification reaction. Stoichiometrically, the methanol: fatty acid reaction is 1:1. A solution with a 1:1 molar ratio and with 15% P25 was prepared for yield comparison. The results were 41.04 wt% and showed that the 1:1 sample produced half the methyl oleate content achieved by the system with a 3:1 ratio. For efficient biodiesel production, an excess of the alcohol must be present to drive the chemical equilibrium in favor of the ester. The esterification reaction is reversible, and its efficiency is dependent on factors such as agitation of the reaction medium, reaction temperature, and catalyst concentration.

In general, samples using 20% of the P25 catalyst showed the lowest methyl oleate conversion. Such a high catalyst concentration may result in saturation of the solution decreasing the UV light available for photocatalysis and prevents excitation and the subsequent reactions of fatty acids and methanol. As the catalyst concentration increases, there is a growth of irradiated particles until a critical concentration is reached where all the particles are illuminated. From this point, a higher concentration

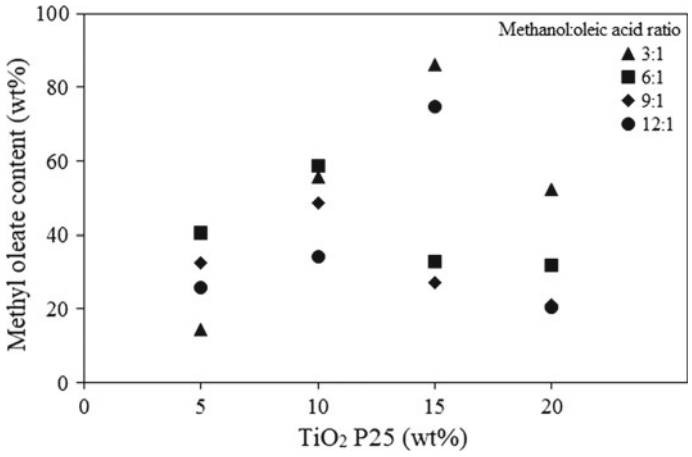

Fig. 9 Methyl oleate results after the photocatalysis reaction with varying concentrations of TiO_2 P25 and methanol

of catalyst increases the opacity of the reaction system, causing a decrease in light penetration into the solution, leading to a decrease in process efficiency.

The blank sample, prepared with neither UV light nor catalyst, obtained an ester conversion of 3.4%. The sample prepared without UV light, but with 15% catalyst loading, achieved a conversion rate of 10.6%. In conclusion, it may be assumed that all factors must be optimized for the desired achievement of esterification by photocatalysis.

The sample prepared without catalyst (0%) in the presence of UV light showed a methyl ester content of 32.6%. The significant difference between this sample and the sample reacted in the absence of UV light (3.4%) was noted. Apparently, the esterification reaction in the absence of catalyst occurs, but with a lower yield than experiments in the presence of the catalyst. The true photolytic nature of the reaction was proven by the fact that the reaction occurs only through the effects of UV radiation.

The results for a collection of samples irradiated with UV light for various intervals are shown in Fig. 10. The tested sample was prepared with a 3:1 methanol ratio and with 15% catalyst. Through data analysis, it can be concluded that the esterification reaction is achieved after a minimum of two hours of photocatalysis. Nevertheless, esterification with real oils may alter this conversion rate, which can be influenced by the presence of water, salts and other organic molecules. However, this result allows us to evaluate the feasibility of photocatalytic processes resulting in the esterification of fatty acids.

The chromatographic profile of oleic acid (fatty acid) and methyl oleate (ester) was obtained for characterization of the peaks by their retention time. As shown in the chromatogram given in Fig. 11, the conversion of oleic acid into methyl oleate is the only reaction that occurs during photocatalysis. The presence of only two chromatographic peaks corresponding to methyl oleate and unreacted oleic acid is

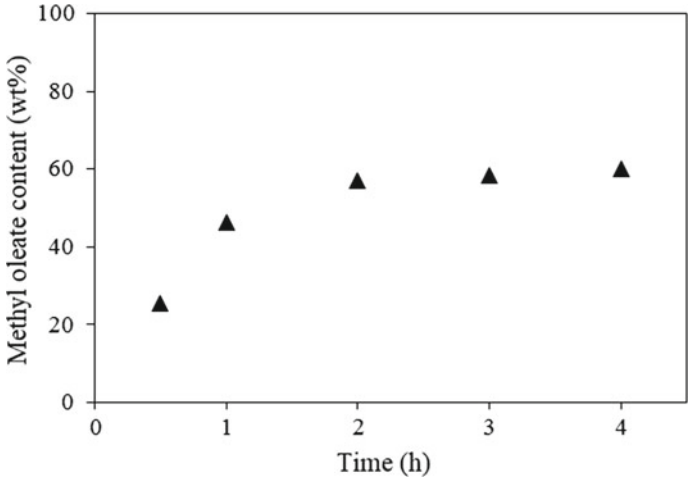

Fig. 10 Variation of the content of methyl oleate as a function of the reaction time

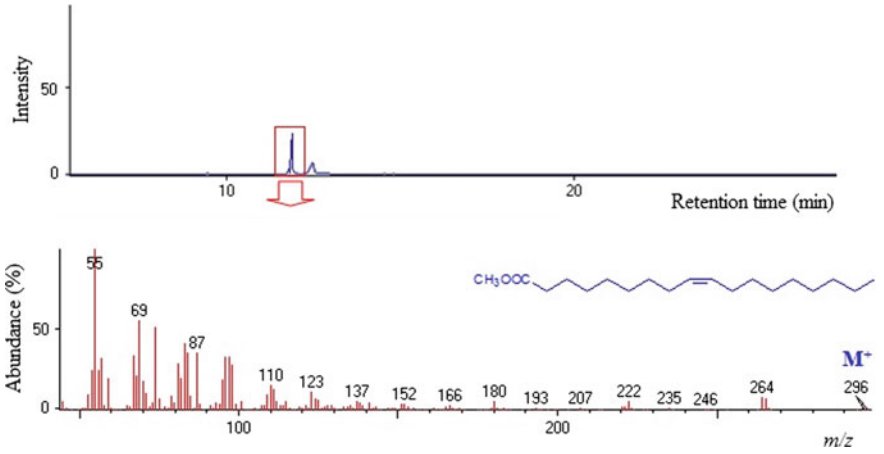

Fig. 11 Chromatogram of a sample after the esterification reaction showing the presence of the peaks of methyl oleate and oleic acid. Inset: the mass spectrum for methyl oleate

observed. The retention time of methyl oleate was 11.91 min, and that of oleic acid was 12.50 min. In the spectrum, the molecular ion (m/z = 296) indicates that it is the molecular mass of the methyl oleate. It is possible to observe the abundance of hydrocarbon ions, a common characteristic for unsaturated fatty acids, having the general formula $[CnH_{2n-1}]^+$, giving m/z = 55 as the base peak of the spectrum. However, analyses of reaction intermediates will be fundamentally important in understanding the real mechanism of esterification during photocatalysis.

Table 3 Methyl oleate content using TNTs at a concentration of 15% and methanol at a ratio of 3:1

Sample	Methyl oleate (%)
CH 110-20	48.49
CH 110-48	59.33
CH 130-20	25.32
CH 130-48	22.65
MAH 130-3	29.53
MAH 130-1.5	23.80
MAH 150-3	38.52
MAH 150-1.5	25.78

The TNTs were used for esterification assays, and the best results were obtained with P25, i.e., a molar ratio of 3:1 and 15% catalyst. Table 3 presents the results of the methyl oleate content for TNTs after esterification.

The production of esters in photocatalysis using the TNTs had lower values than those obtained with P25. The best result was almost 60%, which was produced with CH 110-48, and this sample had the lowest band gap. Among the synthesized samples, the nanoribbons (CH 130-48) showed lower photocatalytic efficiency, directly related to their lowest surface area.

What differentiates the P25 from the TNTs is that it has a more significant number of hydroxyl groups (OH^-) on its surface. Due to its high surface area, the adsorption of a substrate becomes very favorable on the surface of the TNTs. This mechanism may have occurred during photocatalysis. The oleic acid can interact in two ways with the surface of the TiO_2. First, the oxygen carboxylate (R-COO) interacts with the Ti^{+4} cation on the surface of the TNTs. The other adsorption is the formation of a hydrogen bond between the carbonyl group (C=O) and the hydroxyl group of the TiO_2 nanotubes. Thus, the higher number of hydroxyl groups may have contributed to a low yield of ester versus P25. To avoid the adsorption of fatty acid and increase the production of ester, new procedures should be adopted for TNT synthesis.

The photocatalytic esterification of oleic acid with methanol under UV irradiation has been studied for better understanding their reaction mechanism. The catalytic route and derivatives of reaction are still poorly understood. Knowledge of the photocatalytic route is required to achieve good yields and meet the variables that affect negatively or positively in the methyl oleate production.

The usually accepted mechanism of photocatalytic oxidation for TiO_2 is as follows:

$$TiO_2 + h\nu \rightarrow e^- + h^+ \quad (1)$$

$$e^- + h^+ \rightarrow \text{heat} \quad (2)$$

$$e^- + O_2 \rightarrow O_2^- \quad (3)$$

$$h^+ + OH \rightarrow \cdot OH \tag{4}$$

Adsorbed molecular oxygen acts as a photogenerated electron acceptor (O_2^-), and the hydroxyl group reacts with the photogenerated hole to produce hydroxyl radical (·OH).

Based on the photocatalytic process of methanol proposed by Micic et al. [36], ·OH react with adsorbed CH_3OH, which is further oxidized to $CH_3O\cdot$. After that, the electron reacts with $CH_3O\cdot$, releasing the radical $\cdot CH_3$. The O^- remaining trapped on the site by Ti^{+4}.

$$CH_3OH + \cdot OH \rightarrow CH_3O\cdot + H_2O \tag{5}$$

$$CH_3O\cdot + e^- \rightarrow \cdot CH_3 + O^- \tag{6}$$

In the case of oleic acid, direct oxidation by holes or attack by hydroxyl radicals produces hydrogen abstraction, leading to a carboxyl radical as the oxidation product [37]:

$$RCOOH + h^+(\cdot OH) \rightarrow RCOO\cdot + H^+(H_2O) \tag{7}$$

The generated $\cdot CH_3$ and RCOO· subsequently would react to form the methyl oleate product. This step is favored by the strong stirring conditions in the reactor:

$$RCOO\cdot + \cdot CH_3 \rightarrow RCOOCH_3 \tag{8}$$

The reactions through the formation of electrons and holes by excitation of the semiconductor proving that it acts as a true photocatalyst. Further complementary investigations are needed to test the photocatalytic activity.

5 Conclusion

The photocatalysis was presented as a promising alternative for the esterification step in the biodiesel production. The use of an heterogeneous photocatalyst is a cleaner alternative compared to the traditional reaction in which it uses an acid homogeneous catalyst. The synthesis at 150 °C via MAH showed the best results in the photocatalytic tests with methyl orange. Moreover, the lowest band gap energy was obtained with the sample CH 110-48 ($E_g = 3.08$ eV), which also exhibited the highest rate of oleic acid esterification (59.3%). It can be concluded that the band gap, the crystalline phase of the TNTs and their surface area were significant in photocatalytic performance.

References

1. Liu Y et al (2009) Selective ethanol formation from photocatalytic reduction of carbon dioxide in water with $BiVO_4$ photocatalyst. Catal Commun 11:210–213. https://doi.org/10.1016/j.catcom.2009.10.010
2. Qin S et al (2011) Photocatalytic reduction of CO_2 in methanol to methyl formate over CuO–TiO_2 composite catalysts. J Colloid Interf Sci 356:257–261. https://doi.org/10.1016/j.jcis.2010.12.034
3. Slamet S et al (2005) Photocatalytic reduction of CO_2 on copper-doped Titania catalysts prepared by improved-impregnation method. Catal Commun 6:313–319. https://doi.org/10.1016/j.catcom.2005.01.011
4. Lin CH et al (2004) Photocatalytic generation of H_2 gas from neat ethanol over Pt/TiO_2 nanotube catalysts. Catal Lett 98:61–66. https://doi.org/10.1007/s10562-004-6450-x
5. Wu NL, Lee MS (2004) Enhanced TiO_2 photocatalysis by Cu in hydrogen production from aqueous methanol solution. Int J Hydrogen Energy 29:1601–1605. https://doi.org/10.1016/j.ijhydene.2004.02.013
6. Yu J et al (2011) Photocatalytic hydrogen production over CuO-modified titania. J Colloid Interf Sci 357:223–228. https://doi.org/10.1016/j.jcis.2011.01.101
7. Canakci M, Van Gerpen J (2001) Biodiesel production from oils and fats with high free fatty acids. Trans ASAE 44:1429–1439
8. Aranda DAG et al (2008) Acid-catalyzed homogeneous esterification reaction for biodiesel production from palm fatty acids. Catal Lett 122:20–25. https://doi.org/10.1007/s10562-007-9318-z
9. Bavykin DV et al (2006) Protonated titanates and TiO_2 nanostructured materials: synthesis, properties and applications. Adv Mater 18:2807–2824. https://doi.org/10.1002/adma.200502696
10. Zhen B et al (2012) $SiW_{12}O_{40}$-based ionic liquid catalysts: catalytic esterification of oleic acid for biodiesel production. Ind Eng Chem Res 51:10374–10380. https://doi.org/10.1021/ie301453c
11. Corro G et al (2013) Biodiesel production from Jatropha curcas crude oil using ZnO/SiO_2 photocatalyst for free fatty acids esterification. Appl Cat B-Env 129:39–47. https://doi.org/10.1016/j.apcatb.2012.09.004
12. Li W et al (2007) The multi-staged formation process of titanium oxide nanotubes and its thermal stability. Mater Lett 61:730–735. https://doi.org/10.1016/j.matlet.2006.05.053
13. Zhang S et al (2003) Formation mechanism of $H_2Ti_3O_7$ nanotubes. Phys Rev Lett 91:256103–1–256103-4. https://doi.org/10.1103/PhysRevLett.91.256103
14. Kasuga T et al (1998) Formation of titanium oxide nanotube. Langmuir 14:3160–3163. https://doi.org/10.1021/la9713816
15. Cui L et al (2012) Facile microwave-assisted hydrothermal synthesis of TiO_2 nanotubes. Mater Lett 75:175–178. https://doi.org/10.1016/j.matlet.2012.02.004
16. Liu N et al (2014) A review on TiO_2-based nanotubes synthesized via hydrothermal method: Formation mechanism, structure modification, and photocatalytic applications. Catal Today 225:34–51. https://doi.org/10.1016/j.cattod.2013.10.090
17. Macak JM et al (2007) Self-organized TiO_2 nanotube layers as highly efficient photocatalysts. Small 3:300–304. https://doi.org/10.1002/smll.200600426
18. Hoyer P (1996) Formation of a titanium dioxide nanotube array. Langmuir 12:1411–1413. https://doi.org/10.1021/la9507803
19. Zwilling V et al (1999) Structure and physicochemistry of anodic oxide films on titanium and TA6V alloy. Surf Interface Anal 27:629–637. https://doi.org/10.1002/(SICI)1096-9918(199907)27:7%3c629:AID-SIA551%3e3.0.CO;2-0
20. Ku SJ et al (2013) Highly ordered freestanding titanium oxide nanotube arrays using Si-containing block copolymer lithography and atomic layer deposition. Nanotechnol 24:1–8. https://doi.org/10.1088/0957-4484/24/8/085301

21. Brammer KS et al (2011) Biomaterials and biotechnology schemes utilizing TiO_2 nanotube arrays. Biomater Sci Eng In: Pignatello R (ed) InTech, pp 193–210 (Chapter 9). https://doi.org/10.5772/23320
22. Feng SH, Xu RR (2001) New materials in hydrothermal synthesis. Acc Chem Res 34:239–247. https://doi.org/10.1021/ar0000105
23. Chen XB, Mao SS (2007) Titanium dioxide nanomaterials: synthesis, properties, modifications, and applications. Chem Rev 107:2891–2959. https://doi.org/10.1021/cr0500535
24. Ma R et al (2005) Structural features of titanate nanotubes/nanobelts revealed by Raman, X-ray absorption fine structure and electron diffraction characterizations. J Phys Chem B 109:6210–6214. https://doi.org/10.1021/jp044282r
25. Yao BD et al (2003) Formation mechanism of TiO_2 nanotubes. Appl Phys Lett 82:281–283. https://doi.org/10.1021/la400586r
26. Yuan ZY, Su BL (2004) Titanium oxide nanotubes, nanofibers and nanowires. Coll Surf A 241:173–183. https://doi.org/10.1016/j.colsurfa.2004.04.030
27. Wang W et al (2004) A study on the growth and structure of titania nanotubes. J Mater Res 19:417–422. https://doi.org/10.1557/jmr.2004.0048
28. Wu D et al (2006) Sequence of events for the formation of titanate nanotubes, nanofibers, nanowires and nanobelts. Chem Mater 18:547–553
29. Bavykin DV et al (2004) The effect of hydrothermal conditions on the mesoporous structure of TiO_2 nanotubes. J Mater Chem 14:3370–3377. https://doi.org/10.1039/B406378C
30. Kukovecz K et al (2005) Oriented crystal growth model explain the formation of titania nanotubes. J Phys Chem 109:17781–17783. https://doi.org/10.1021/jp054320m
31. Manfroi DC et al (2014) Titanate nanotubes produced from microwave-assisted hydrothermal synthesis: photocatalytic and structural properties. Ceram Int 40:14483–14491. https://doi.org/10.1016/j.ceramint.2014.07.007
32. Peng YP et al (2010) Microwave-assisted hydrothermal synthesis of N-doped titanate nanotubes for visible-light-responsive photocatalysis. J Haz Mat 183:754–758. https://doi.org/10.1016/j.jhazmat.2010.07.090
33. Li L et al (2011) Synthesis of anatase TiO_2 nanowires by modifying TiO_2 nanoparticles using the microwave heating method. Appl Surf Sci 257:8006–8011. https://doi.org/10.1016/j.apsusc.2011.04.073
34. Sczancoski JC et al (2009) Synthesis, growth process and photoluminescence properties of $SrWO_4$ powders. J Colloid Interf Sci 330:227–236. https://doi.org/10.1016/j.jcis.2008.10.034
35. Kingston HM, Jassie LB (1988) Introduction to microwave sample preparation—theory and practice. ACS Professional Reference Book, Washington
36. Micic OI et al (1993) Trapped holes on titania colloids studied by electron paramagnetic resonance. J Phys Chem 97:7277–7283. https://doi.org/10.1021/j100130a026
37. Testa JJ et al (2001) Experimental evidence in favor of an initial one-electron-transfer process in the heterogeneous photocatalytic reduction of chromium(vi) over TiO_2. Langmuir 17:3515–3517. https://doi.org/10.1021/la010100y

Metal Decoration of TiO_2 Nanotubes for Photocatalytic and Water Splitting Applications

Gisele Inês Selli, Maria Luisa Puga and Fernando Bonatto

Abstract TiO_2 materials, especially nanostructures, must not only be cost-effective, but they must also meet many other requirements: high photocatalytic activity, large active superficial area, chemical resistance, ease of manufacture, and fast synthesis route. However, it is commonly recurrent that TiO_2 nanostructures, nanoparticles or nanotubes, still have a high deficiency to collect a large part of the light spectrum. Nevertheless, anatase/rutile superficial defects, which increases considerably charge carrier recombination, can be circumvented by the addition of transition/noble metals, to intentionally increase the material photocatalytic properties and extend applications, in the field of H_2 generation.

Keywords TiO_2 · Photocatalysis · H_2 production · Metal decoration

Abbreviations

AO7	Acid Orange 7
BET	Brunauer–Emmett–Teller
EDX	Energy Dispersive X-ray
FESEM	Field Emission Scanning Electron Microscopy
FT-IR	Fourier Transformer Infrared
MB	Methylene Blue
PO	Heterogeneous Photocatalytic Oxidation
TNT	Titanium dioxide Nanotubes

G. I. Selli (✉) · M. L. Puga · F. Bonatto
Universidade Federal do Rio Grande do Sul, Porto Alegre, Brazil
e-mail: gisele.selli@ufrgs.br

F. Bonatto
e-mail: bonatto02@yahoo.com.br

A. Kopp Alves (ed.), *Nanomaterials for Eco-friendly Applications*,
Engineering Materials, https://doi.org/10.1007/978-3-030-26810-7_5

1 Introduction

With the advent of industries that produce a large number of pollutants in effluents, including pharmaceuticals, textiles, and chemicals, the amount of pollutants has grown almost exponentially in the last 30 years according to the UN survey in 2018. For this reason, in the context of reducing the number of emerging pollutants in industrial effluents. In this idea, titanium dioxide has become a highly researched material with high potential for commercial and industrial applicability. However, one of the major drawbacks is the fact that the material has a gap within the UV light spectrum and is considered a high bandgap semiconductor, which restricts its applications. Although this characteristic represents a depreciation of the material, since this part of the spectrum is smaller when compared to the whole spectrum available, the fact that the TiO_2 is low cost, with high physical-chemical stability and easy to manufacture makes it an attractive material for photocatalytic applications.

To increase the industrial use and applicability of nanostructured TiO_2, as a base element in the decomposition of pollutants, processes such as doping and decoration are widely used because of the ease of synthesis in conjunction with titanium dioxide. One of the most successful approaches is the use of transition and noble metals together with TiO_2 nanostructures. In addition to allowing access to a more significant portion of the available light spectrum, thereby increasing the photocatalytic activity, the presence of these metals still allows an improvement of yield and applicability in the decomposition of different chemical compounds present in effluents. This chapter presents a condensation of the primary metals used together with TiO_2.

This chapter aims to show the latest advances in the application of photocatalytic processes for the decomposition of pollutants and H_2 production using metals such as Fe, Cu, Ag, and Au together with TiO_2 nanostructures for their simplicity of synthesis and low cost for direct application.

2 Iron-Doped TiO_2

Although having wide application potential, titanium dioxide nanotubes (TNTs) face a major drawback regarding their large band gap, an aspect that limits photoresponse almost exclusively to the ultraviolet region [1]. Modifying TiO_2 with other narrow bandgap materials is a widely recognized method to minimize such drawback, as it causes a red shift of the absorption edge to the visible light region [2–4]. Moreover, selective metal ion doping, especially iron in its Fe^{3+} form [5, 6], significantly broadens light response range and inhibits charge-carrier recombination as the ions act as charge traps for the photogenerated electron-hole pairs [7–11]. Several studies also pointed out to an enhanced photocatalytic activity for Fe-doped catalysts both under UV [11–13] and visible light irradiation [14–17]. As demonstrated by Yu et al. [18], such high performance of Fe^{3+}/TiO_2 is attributed to the accumulation of photogen-

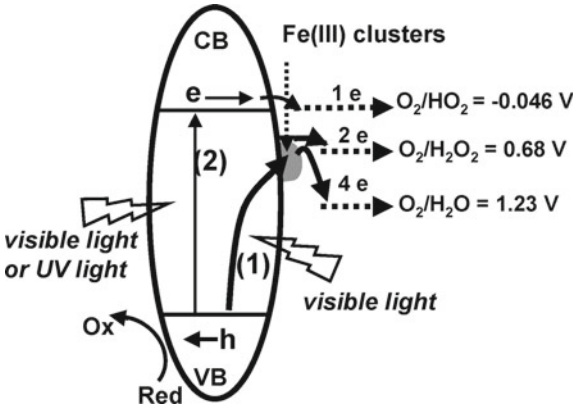

Fig. 1 Schematic diagram illustrating the possible photocatalytic mechanism of Fe^{3+}/TiO_2, involving interfacial charge transfer (arrow 1) and multielectron reduction processes. The band gap excitation is indicated by arrow 2. Reprinted with permission [18]

erated holes in the valence band (VB) of TiO_2 and the catalytic reduction of oxygen by photoreduced Fe^{2+} species on TiO_2 surface (Fig. 1).

Regarding Fe/TNTs, Asiltürk et al. [19] found that Fe^{3+} doping may prevent particle agglomeration due to the formation of well-defined crystalline nanoparticles (NPs) with high surface area, two key aspects to improving photocatalytic performance [19]. Compared to undoped, electrochemically anodized TNTs, Fe^{3+} doped nanotubes have shown a six-fold increase on photocurrent density and a doubled degradation rate measurement [1]. Using the crystal structure of TiO_2 as a matrix for fixating Fe^{3+} NPs is also presented as an alternative to having them dispersed in an aqueous suspension, thus avoiding the detrimental nanoparticle aggregation where many particles are hidden from light absorption [5].

Fe_2O_3 has been pointed out as another strong candidate for being a low cost, nontoxic and highly stable form of iron oxide [20, 21]. Concerning morphology, aggregating Fe NPs in adequate amounts to TNTs does not affect the highly ordered nanotube construction, as demonstrated by Zhang et al. [1] in Fig. 2, where SEM images compare undoped two-step anodized TiO_2 NTs with Fe^{3+}-doped TiO_2 NTs, also fabricated via a two-step anodization process. Xie et al. [22] reinforce this conclusion by successfully electrodepositing $ZnFe_2O_4$ nanoparticles within self-organized and highly ordered TiO_2 nanotube arrays while minimizing the clogging of the tube entrances (Fig. 3).

Cong et al. [23] studied the performance of α-Fe_2O_3/TNTs composites for photoelectro-Fenton degradation using phenol, a compound usually found in wastewater discharged from a variety of industries [24, 25], as a model pollutant with an initial concentration of 10 mg/L. The α-Fe_2O_3/TNT complex was synthesized over anodized nanotubes by two different techniques, a dipping method in aqueous suspension of α-Fe_2O_3 NPs (fixed-Fe_2O_3 system 1) and an electrochemical deposition (fixed-Fe_2O_3 system 2), for which the electrodes fabricated via the second one pre-

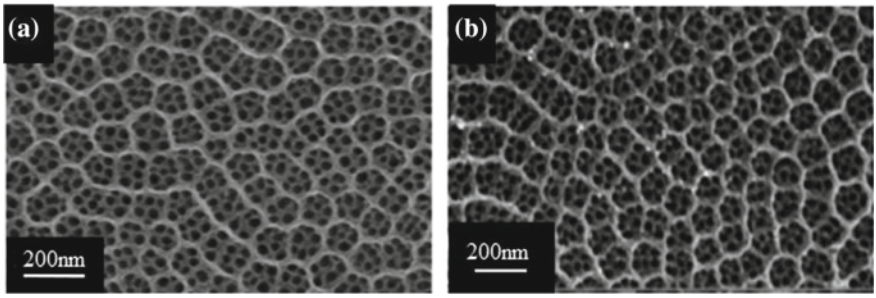

Fig. 2 SEM images of: **a** TiO_2 NTs in the two-step anodization. **b** Fe^{3+}/TiO_2 NTs. Reprinted with permission [1]

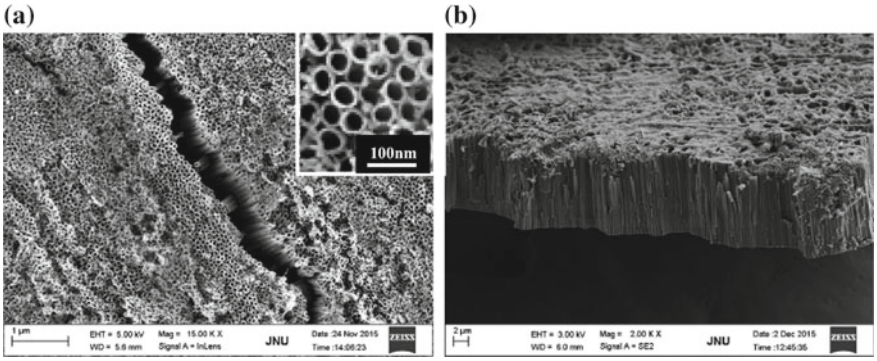

Fig. 3 **a** Top-view and **b** side-view SEM images of the TiO_2 nanotube arrays. The inset shows the images of TNTs at high magnification. Reprinted with permission [22]

sented higher removal efficiency of phenol and stronger photoresponse under visible light irradiation due to the uniform fixation of Fe NPs on TNTs. To further investigate the role of α-Fe_2O_3 NPs, phenol degradation was also carried in a dispersed system, where α-Fe_2O_3 NPs were added into the aqueous phenol solution instead of being attached to TNT electrodes. Responses to three different Fenton-related processes, electro-Fenton, visible light photoelectro-Fenton, and UV-visible light photoelectro-Fenton, are depicted in Fig. 4. After a 60 min treatment, electrochemically deposited α-Fe_2O_3/TNT electrodes presented 100% phenol removal efficiency in the UV-visible light photoelectro-Fenton process, whereas the dispersed system required double the amount of time to reach similar rates. The increased performance of Fe_2O_3 modified TNTs could be linked to the fact that incorporating α-Fe_2O_3 NPs effectively suppressed the recombination of electron-hole pairs, thus allowing them to act as heterogeneous catalysts for phenol degradation [23].

$ZnFe_2O_4$ appears as an opportunity to harvest most of the visible portion of the solar spectrum [26], also presenting an alternative to overcome the separation and recycling process of the powdered $ZnFe_2O_4$ and improving the energy conversion

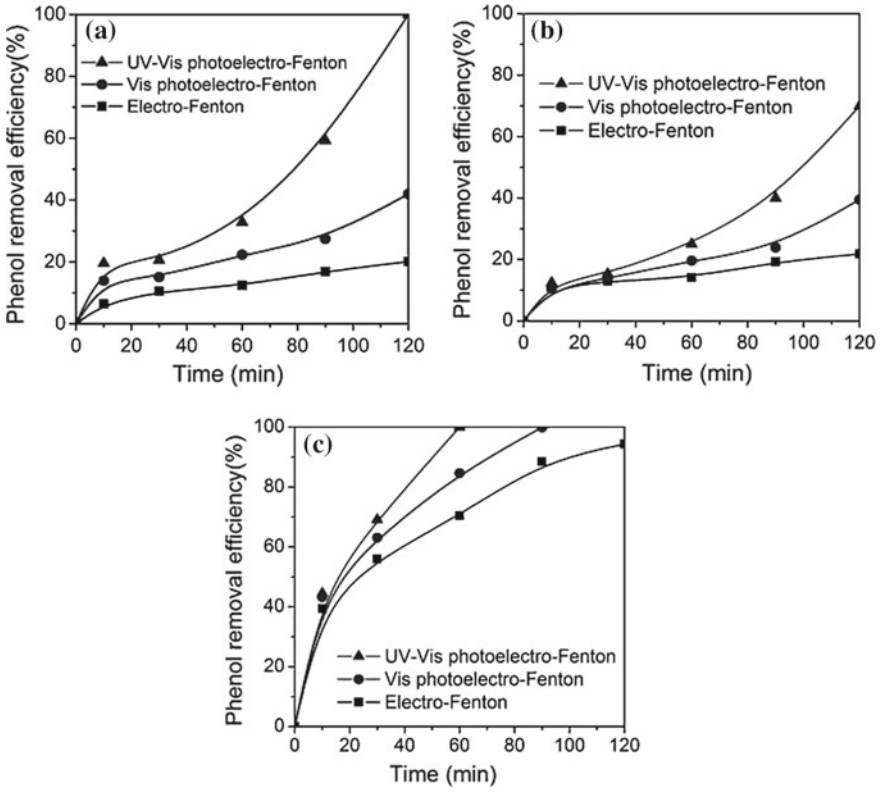

Fig. 4 Phenol degradation in **a** dispersed system, **b** fixed-Fe_2O_3 system 1, and **c** fixed-Fe_2O_3 system 2. Reprinted with permission [23]

efficiency when aggregated to TiO_2 in a $ZnFe_2O_4$/TNT composite [27]. Loading highly ordered TiO_2 nanotube arrays with $ZnFe_2O_4$ NPs enhances absorption in both UV and visible light regions promotes greater separation of photoinduced electron-hole pairs and presents a more effective photoconversion capability than undoped TNTs [22, 27]. Moreover, Xie et al. [22] demonstrated that the photocurrent density of the composite $ZnFe_2O_4$/TNT (Z-TNT) electrode was more than 5.5 times higher than that of the TNT electrode alone (Fig. 5), implying that $ZnFe_2O_4$ can be effectively used to sensitize TiO_2 nanotube array electrodes. Regarding its applicability, the synthesized electrode was found to possess excellent photoelectro-catalytic activity for degradation of 4-chlorophenol, a toxic and non-biodegradable pollutant present in wastewater of industrial activities [28, 29] under UV light illumination, presenting 100% efficiency with an applied potential bias of 0.8 V, 16% higher than the degradation efficiency measured for the unloaded TNT electrode [27].

Titanium nanotube composites are also attractive photocatalysts for photoelectrochemical (PEC) solar water splitting applications due to their high-efficiency energy conversion, good chemical stability, and corrosion resistance in aqueous envi-

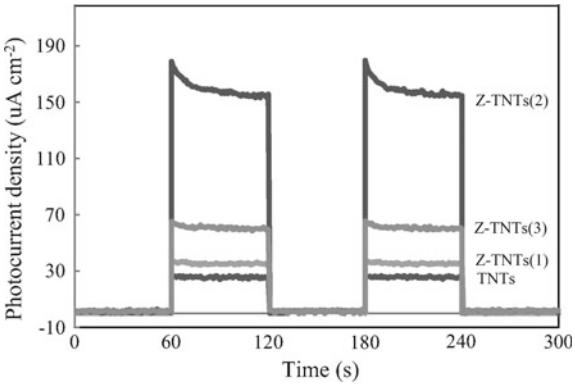

Fig. 5 **a** Transient photocurrent responses of the TNTs and the Z-TNTs samples under the bias potential of 0.8 V versus SCE. Three $ZnFe_2O_4$/TNT samples were analyzed, each containing a distinct concentration of $Fe(NO_3)_3$ and $Zn(NO_3)_2$: (1) 0.5 M and 0.25 M; (2) 1.0 M and 0.5 M; (3) 2.0 M and 1.0 M, respectively. Reprinted with permission [22]

ronments [30–33]. PEC splitting of water is an ideal, low-cost renewable method of hydrogen (H_2) production that integrates solar energy collection and water electrolysis in a single photocell [30, 34, 35]. Figure 6 presents the principle of photocatalytic water splitting reactions.

Moreover, H_2 has been considered an attractive energy carrier, achieving much higher conversion efficiency than the conventional fossil fuels, while offering a more sustainable [33], environmentally benign energy source with lesser emissions [36]. Unfortunately, large-scale application of most photocatalytic systems is restricted by the fact that noble metal-based co-catalysts are still the first option for achieving reasonable activity rates. Therefore, seeking cheap, earth-abundant and high-performance alternative materials is indispensable to achieve cost-effective, highly efficient water splitting process [32]. Momeni and Ghayeb [37] produced Fe/TNTs composites for water splitting applications with varying amounts of the iron source

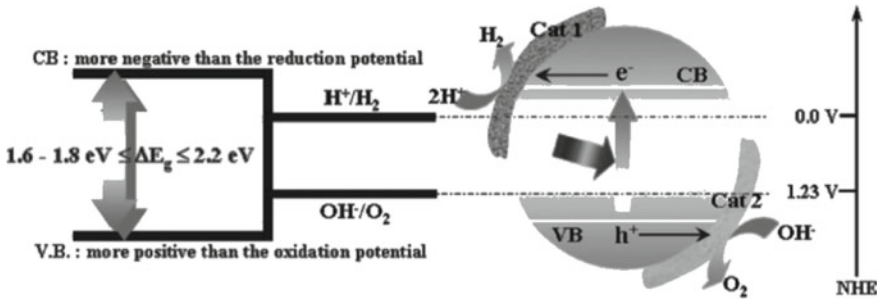

Fig. 6 The general principle of photocatalytic water splitting reactions. Reprinted with permission [35]

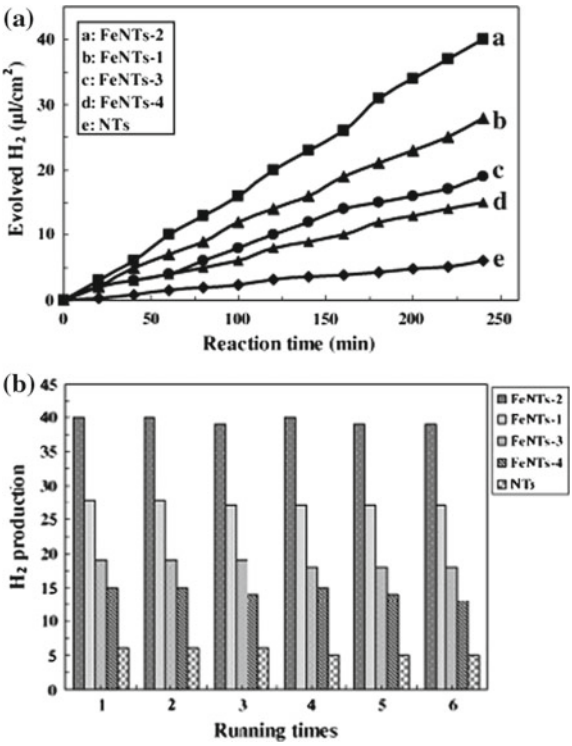

Fig. 7 **a** Photocatalytic H_2 production of different samples over irradiation, with applied external voltage [1.50 V (vs. Ag/AgCl)]. **b** H_2 evolution for different samples as a function of running times (reusability test of samples). Reprinted with permission [37]

potassium ferricyanide ($K_3Fe(CN)_6$), for which the ideal concentration was found to be 9 mM. Compared to undoped TNTs, the samples exhibited a red-shift of absorption edge and a band gap decrease, as well as a dramatic increase in photocurrent at the ideal Fe concentration. Regarding composite efficiency, Fig. 7a illustrates that the amount of H_2 evolved on the 9 mM Fe/TNTs sample (named FeNTs-2), after 240 min was more than 6,5 times the one verified on the undoped TiO_2 sample (NTs), and the hydrogen production showed no obvious decay after 6 continuous runs of photocatalytic reaction, as seen in Fig. 7b, thus proving the recyclability of the system.

3 Copper-Doped TiO_2

Exhibiting great potential for applications in the fields of solar energy conversion [38–40], photocatalytic hydrogen (H_2) production [32, 41, 42] and degradation of hazardous components [2, 43], earth-abundant and low-cost transitional metals such as cobalt (Co), nickel (Ni) and copper (Cu) [44, 45] have been successfully loaded on semiconductors in order to improve photocatalytic processes. According to Ran

et al. [32], applying such metals as cocatalysts promote charge separation due to the Schottky barrier formed at the metal/semiconductor interface.

Regarding solar water splitting, hydrogen not only is vital for many industrial processes but also is thought to be an attractive, clean energy vector when combined with efficient fuel cells. The overall photocatalytic water splitting reaction involves three major steps, those being light absorption by a semiconductor to generate electron-hole pairs, charge separation and migration to the surface of the semiconductor and finally surface reactions for H_2 or O_2 evolution [32] (Fig. 8). However, solar photocatalytic water splitting is still a challenging promise for sustainable H_2 production, mostly because the ideally described use of platinum (Pt) as cocatalyst endures a series of limitations linked to its high-cost and relatively low availability [32, 41].

In this context arises an increasing interest in the aforementioned transition metals, especially Cu species, for the narrow band-gap characteristic of both CuO and Cu_2O extends the photoresponse of TiO_2 into the visible light region [2, 38–40, 43, 46], making them a sustainable candidate for TiO_2 doping to enhance hydrogen production [44, 47]. On that note, Xu et al. [48] reported that CuO-loaded TiO_2 exhibited a photocatalytic H_2 production rate in methanol aqueous solution about 3 times higher than that of some Pt/TiO_2 electrodes (18,500 $\mu mol\, h^{-1}\, g^{-1}{}_{catalyst}$ to 6000 [49] and 6900 [50] $\mu mol\, h^{-1}\, g^{-1}{}_{catalyst}$, respectively). Furthermore, it was found that Cu-doping process does not influence the morphology of TiO_2 samples [43, 51], and different chemical states of Cu species, as well as their distribution ratio over

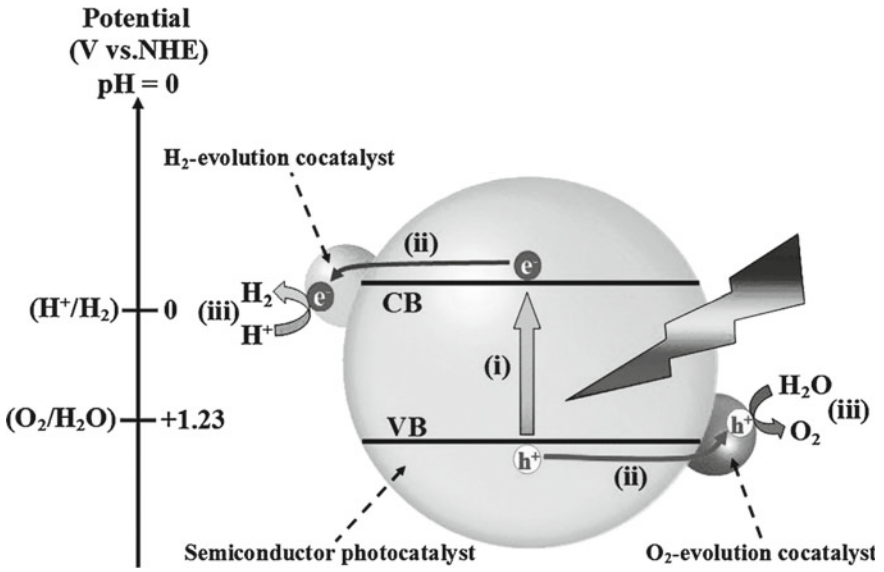

Fig. 8 Schematic illustration of photocatalytic water splitting over a semiconductor photocatalyst loaded with H_2^- and O_2^- evolution cocatalysts. Reprinted with permission [32]

TiO_2 notably influence H_2 production activities, with Cu species aggregated to its surface promoting charge transfer more efficiently than those in TiO_2 lattice [42].

The stability of the system is also to be observed, for leaching of non-metals is one of the main reasons for catalyst deactivation in liquid media [41]. Gombac et al. [41] tested copper leaching during and after photocatalytic reactions carried with a Cu/TiO_2 electrode both under reducing and oxidizing conditions, those being argon flow and inert atmosphere and exposure to air, respectively. Results indicated that under reducing conditions Cu leaching is marginal and, if operative, can be minimized by UV irradiation. On the other hand, dramatic leaching is observed under oxidized conditions.

Coupling Cu NPs with self-organized, highly ordered TiO_2 nanotube arrays (Cu/TNTs) creates an even more efficient opportunity to harvest sunlight when compared to randomly oriented TiO_2 nanoparticles [2]. Cu/TNTs heterojunction also favors the separation of photogenerated electron-hole pairs, ultimately improving photoelectrical conversion ability under solar light irradiation [40, 43]. Hua et al. [43] confirmed such aspect by varying deposition time of Cu NPs over TNTs, for which the increase in deposition time also meant an increase in the transient photocurrent response (Fig. 9). Moreover, uniformly dispersed Cu NPs ensured the electron migration by forming a strong interaction with TNTs, thereby improving charge transfer and separation.

In the same study, Hua et al. [43] evaluated the catalytic efficiency of Cu/TNTs electrodes for degrading of diclofenac (DCF), a non-steroidal anti-inflammatory drug vastly researched for its endocrine disrupting and adverse effects and also one of the most frequently detected pharmaceuticals in municipal wastewater [52]. Among the

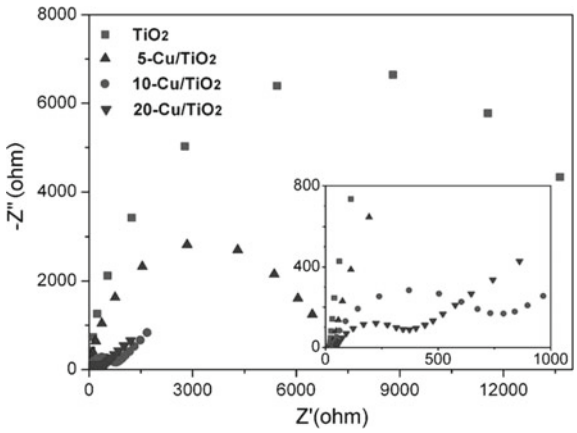

Fig. 9 Electrochemical impedance spectroscopy (EIS) spectra of Cu/TNTs electrodes, recorded at the open circuit potential under simulated solar light irradiation. The semicircle diameter of EIS, related to charge transfer resistance and separation efficiency at the contact interface between the electrode and electrolyte, was substantially decreased with increasing the deposition time, which could be attributed to Cu_2O and CuO improving the harvesting of visible light and reducing the transfer impedance of electrons. Reprinted with permission [43]

four processes tested, electrochemical (EC), direct photolysis (DP), photocatalysis (PC) and photoelectrocatalysis (PEC), the PEC process was found to be the most efficient with a DCF degradation efficiency of 71.9%, pointing to the important role played by an applied potential bias of 0.5 V in effectively separating electron-hole pairs and prolonging lifetime of the photogenerated charge carriers (Fig. 10).

Similar research utilizing the previously mentioned catalytic processes (EC, DP, PC, and PEC) was carried by Hou et al. [2] for 4-chlorophenol (4-CP) decomposition under UV light irradiation. As depicted in Fig. 11 the photocurrent density of the

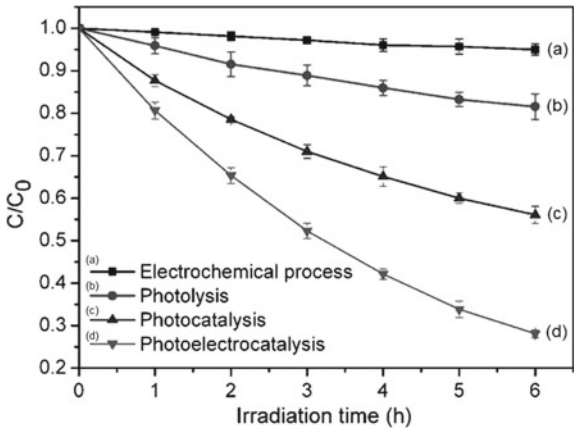

Fig. 10 Degrading DCF by electrochemical process (curve A), photolysis (curve B), photocatalysis (curve C) and photoelectrocatalysis (curve D) over Cu/TNTs electrode. Reprinted with permission [43]

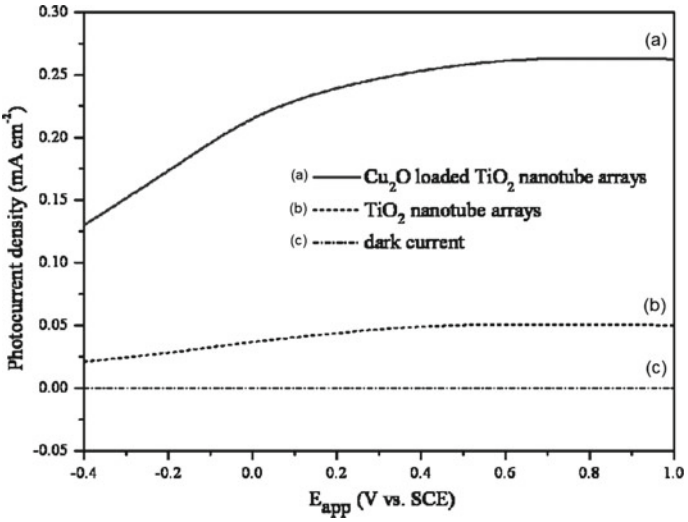

Fig. 11 Variation of photocurrent density versus bias potential (vs. SCE) in 0.01 M Na_2SO_4 solution for the Cu_2O-loaded TiO_2 nanotube array electrode and TiO_2 nanotube array electrode under Xe lamp (400–600 nm, 33 mW cm^{-2}) irradiation. Reprinted with permission [2]

Cu_2O/TNT electrode was measured to be more than 5 times the value for the non-loaded TNTs. Again, the PEC process utilizing a Cu_2O/TNT electrode was the fastest among the four alternatives, achieving nearly 100% of 4-CP degradation in 120 min, a value at least 20% higher than the one measured for the PEC process with a non-loaded TNT electrode (Fig. 12). Similarly, maximum photoconversion efficiency was observed at an applied bias of 0.1 V, corroborating the idea proposed by Hua et al. [43] that a potential bias inhibits the recombination of photogenerated electron-hole pairs.

Cu_2O appears yet in structures other than NPs. As an example, Yang et al. [46] incorporated both Cu^0 NPs on the inner walls (Fig. 13a) and Cu_2O nanowires onto the top surface of TNTs (Fig. 13b) for p-nitrophenol (PNP) degradation, creating an intercrossed network with extended absorption in the visible light range without blocking the nanotubes (Fig. 13c).

Used for drug, fungicide and dye manufacturing, the priority pollutant is generally degraded by strong oxidants only, thus impeding purification of PNP-contaminated wastewater due to its stability to chemical and biological degradation [53, 54]. However, the authors proved that under solar light PNP can be effectively degraded by the Cu_2O/TNT p-n junction network without the addition of oxidants, at a rate 2.3 times higher than the unmodified TiO_2 NTs (1.97 μg/min cm^2 versus 0.85 μg/min cm^2, respectively).

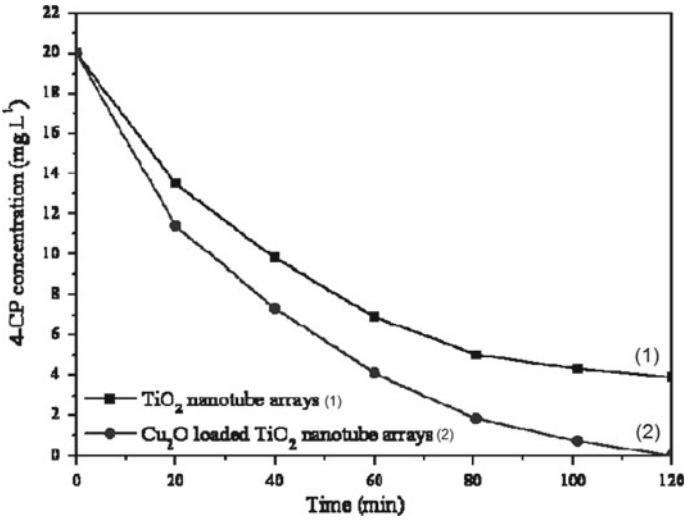

Fig. 12 Variation of 4-CP concentrations by photoelectrocatalytic (PEC) technology with TiO_2 nanotube array electrode and Cu_2O-loaded TiO_2 nanotube array electrode under UV light illumination (I_0 = 1.4 mW cm^{-2}, 0.2 V vs. SCE bias potential applied). Reprinted with permission [2]

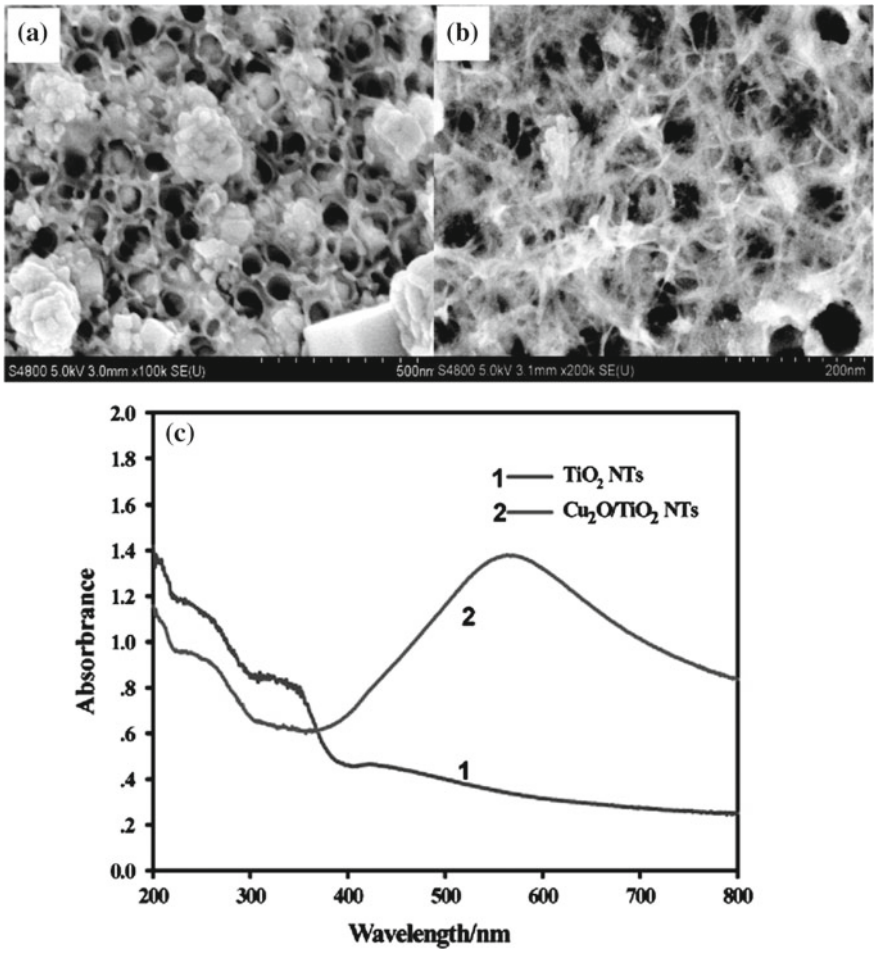

Fig. 13 SEM images of **a** Cu-loaded TiO_2 NTs and **b** Cu_2O ultrafine nanowires modified TiO_2 NTs. **c** UV-vis absorption spectra of TNTs (curve 1) and Cu_2O/TNTs (curve 2), demonstrating that the Cu_2O-modified TNTs have intense absorption in the visible light range. Reprinted with permission [46]

3.1 Silver/TiO_2 Nanostructures

The addition of nanostructured silver to titanium dioxide (Ag/TiO_2) has been thoroughly studied, mainly in terms of its photocatalytic properties [55–57]. Several studies [55, 58–60] demonstrate that silver is one of the most suitable materials for industrial application, due to the easy preparation and consequently low cost [58]. Because it is a noble metal, Ag presents characteristics that improve the photocatalytic activity of TiO_2 [61] as already mentioned (Fig. 14).

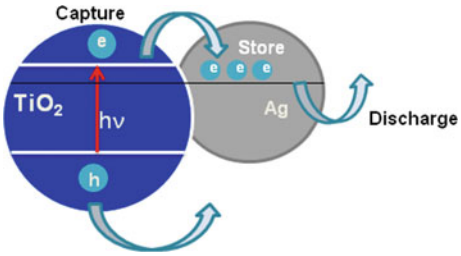

Fig. 14 Electron transfer mechanism in silver loaded TiO_2. Reprinted with permission [61]

Amongst the main properties directly linked to the addition of silver to the surface is the facility to dispose of photogenerated electrons on the TiO_2 surface, directly attached to the silver fermi energy being just below the conduction band of TiO_2, thus causing silver in this way function as a storage point of photogenerated load. Besides, the nanostructure of silver facilitates the photoabsorption process, due to the effects of SPR, which depend directly on the geometry and size of the nanostructures. Plasmon resonance effects can amplify the discharge effect for photoactive surfaces.

The Ag loaded TiO_2 (Ag/TiO_2), recently have been used in applications that aim pollutants and dyes degradation of wastewater. Seery [62] evaluated the rate of degradation of a model dye, rhodamine (R6G), and samples produced by different methods (irradiation and calcination) and the amount of silver doping. The author [62] relates that the degradation rate of the calcinated sample presented the most efficient catalytic properties (6–50% improvement in catalytic efficiency), that can be attributed to the silver is homogeneously dispersed throughout the material. The degradation rate of (R6G) oscillates among 0.06 min^{-1} for TiO_2 to 0.34 min^{-1} for 5 mol% Ag–TiO_2, which is attributed to the increasingly visible absorption capacity by Ag presence [62].

Concerning the pollutant materials, Li [63] explored the degradation of toluene with TiO_2 nanotube powder doped with Ag nanoparticles and compared the photocatalytic efficiency with commercial TiO_2 (P25, Degussa). The TiO_2 nanotubes were produced from Titanium foils with potenciostatic anodization method. The anodization was performed in a two-electrode configuration, where the Ti foil was used as a working electrode, and platinum foil as the counter electrode. The Ag-doped TiO_2 were prepared employing an incipient wetness impregnation method. The Ag/TiO_2 powder photocatalytic activity was measured through photo-oxidation of gaseous toluene. The results indicated that achieved efficiency for toluene degradation was 98% after 4 h reaction, under UV-light, these values were better than with pure TiO_2, Ag-doping P25 or P25 [63].

Another application that has been extensively studied using Ag/TiO_2 is water splitting, to generate gaseous H_2 as an alternative energy source. To enhance the process efficiency, Fan [64] produced highly ordered Fe^{3+}-doped TiO_2 nanotube arrays (Fe/TiO_2 NTs), then Ag nanoparticles were assembled in Ag-Fe/TiO_2 NTs. The material assembly with iron was prepared by electrochemical anodic oxidation

and the Ag was loaded by microwave-assisted chemical reduction. The author related that Ag-Fe/TiO_2 NTs showed higher UV-Vis light absorption and lower electron-hole recombination rate than pure TiO_2 (Fig. 15). The photocatalytic

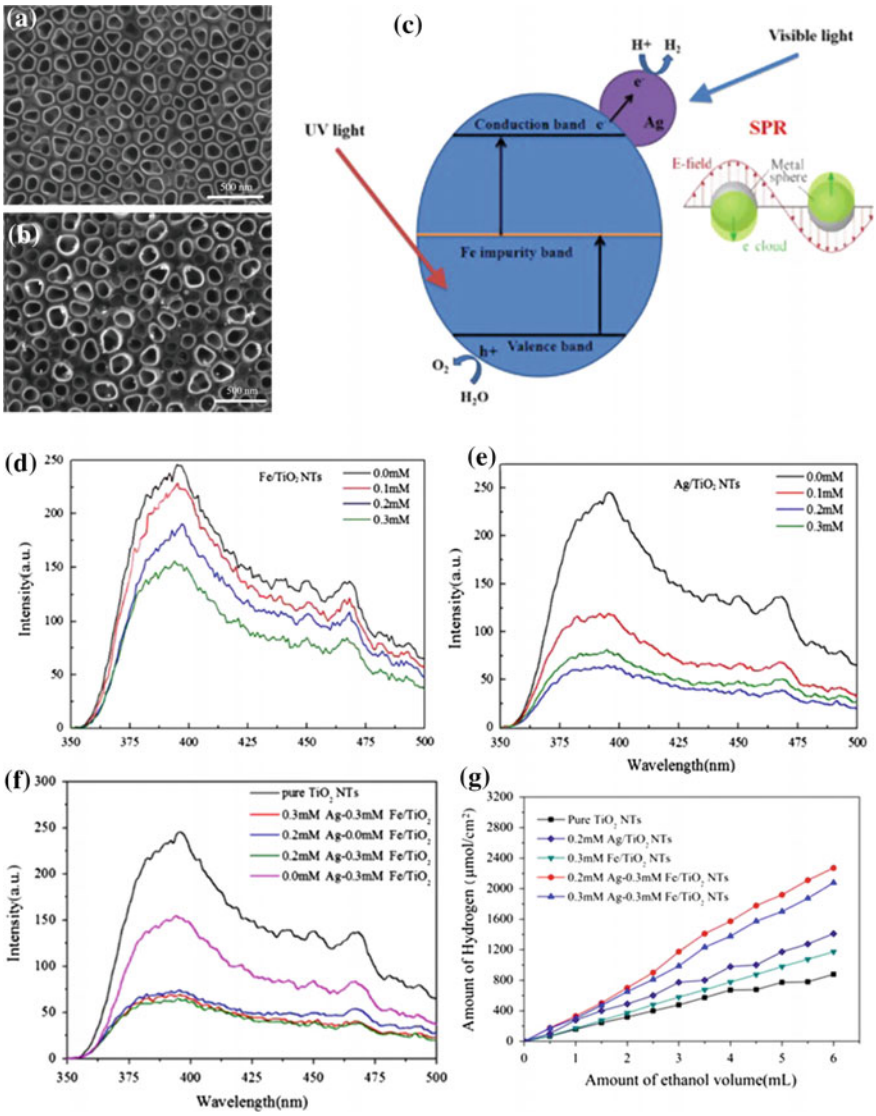

Fig. 15 **a** SEM images of pure TiO_2 NTs and **b** Fe doped and Ag NPs loaded on TiO_2 NT. **c** Mechanism of H_2 production by water splitting over Ag–Fe/TiO_2 NTs applying UV and visible light irradiation. **d** Photoluminescence spectra of TiO_2 NTs under the excitation of 250 nm Fe/TiO_2 NTs, **e** Ag/TiO_2 NTs and **f** Ag–Fe/TiO_2 NTs. **g** H_2 production by water splitting by TiO_2 catalysts. (*Ag/TiO_2–Ag-doped TiO_2). Reprinted with permission [64]

activity indicated a higher efficiency by 0.2 mM Ag-0.3 mM Fe/TiO_2 NTs samples. if compared with the pure TiO_2 catalyst. These results show the potential of photocatalytic material for energy and environment applications [64].

3.2 Gold

Gold is another noble metal that possesses singular electronic properties. Several researchers [65–67] relates that the presence of gold (Au) in nanoparticle form, or combined with other noble metals in TiO_2 supports, will improve the photocatalytic degradation of pollutants. In this regard, reports [68, 69], relate researches about the photocatalytic oxidation of pesticides and phenolic compounds applying TiO_2, furthermore, reviewed concerning the organic dyes degradation in effluents.

Sanabrina [66] has investigated the performance of Au and platinum (Pt) nanoparticles, and Au–Pt alloy on anodic TiO_2 nanotubes (TiO_2 NTs) for photocatalytic degradation. The materials were produced with a different method, that is, metal decoration intrinsically and extrinsically. The intrinsical decoration was obtained using a noble metal-containing titanium alloy for anodic tube growth, as the extrinsic decoration was realized by physical vapor deposition (PVD) method of the Ag and Pt on pure titania tubes (Fig. 16).

The results showed enhancement for decomposition of the model pollutant acid orange 7 (AO7) when the Au–Pt intrinsic decoration was evaluated, which can be attributed to the synergistic effect of both noble metals. This effect of Au- Pt intrinsic decoration has revealed to be a better option than the use of pure elements loaded on TiO_2 NTs. Sanabrina [66] relates the overall effect is due to the facilitated oxygen reduction reaction, which leads to higher production of reactive oxygen species on the conduction band, which provide an enhanced pollutant degradation rate [66].

Beyond the photocatalysis application, it is possible to cite the H_2 production using TiO_2 nanotubes (TiO_2 NTs) doped with Au. Choi [67] produced Au NP-decorated TiO_2 nanotube arrays (TNTs) to apply as photoelectrochemical (PEC) water splitting electrodes for H_2 production. To synthesize the TNTs, the author made use of a simple and low-cost method with two-step anodization process, and finally the deposition of a thin film of Au nanoparticles (Fig. 17) [67].

The TiO_2 NTs prepared using the two-step anodization process showed better photocurrent stability and efficiency. Furthermore, the Au presence on TNT array increases the photocurrent value in 67.2% to 1.02 mA/cm^2. The PEC process water splitting was enhanced and stabilized for charge separation and transport due to reduced cracking after second anodization and the annealing process [67].

Based on the context presented in this chapter, it is important to cite Paramasivam [70], that compared the photocatalytic activity of Au and Ag nanoparticles loaded TiO_2 nanotubes and the activity of the unloaded TiO_2 substrates. Paramasivam relates an enhancement of photocatalytic activity with TiO_2 nanotubular structures compared with a compact TiO_2 surface, which possesses higher performance due to SPR enhancement properties due to the presence of Au and Ag.

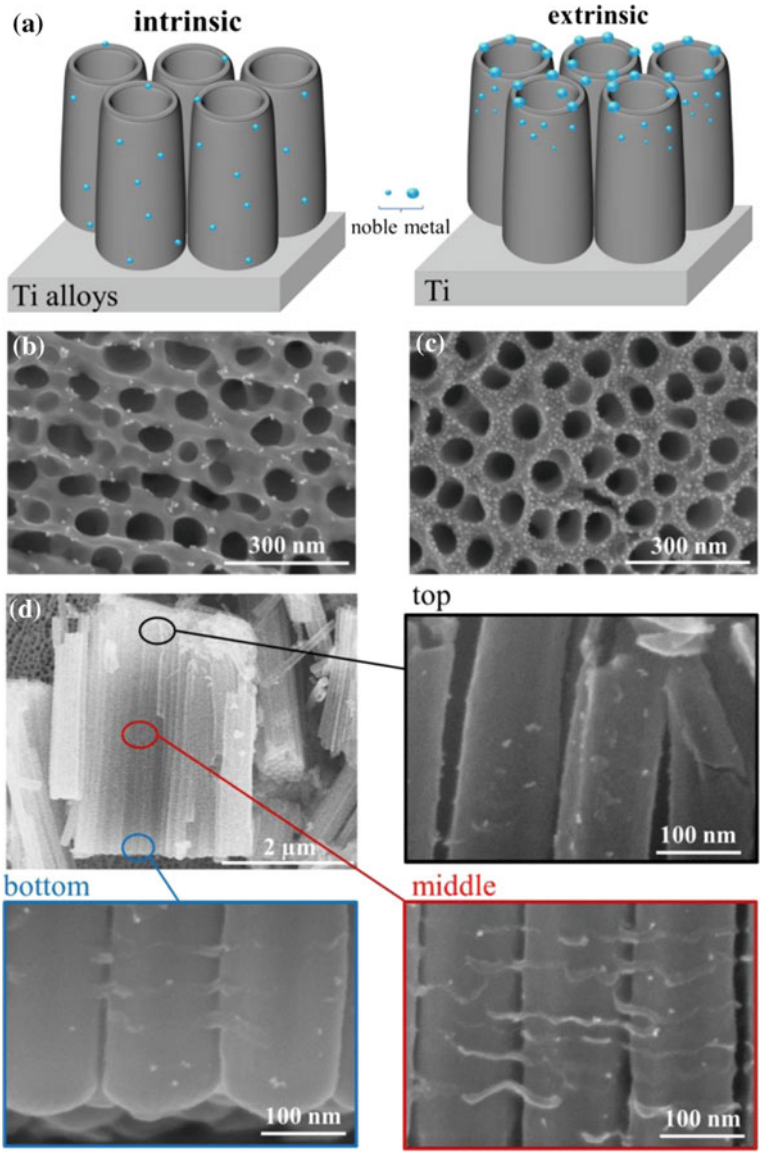

Fig. 16 **a** Representation of TiO_2 NTs intrinsically decorated by direct anodization of alloy (left) and extrinsically decorated by sputtering and dewetting a noble metal on the top of the NTs anodically growth on Ti foil (right); **b** top section of the NTs on TiAuPt alloy; **c** top section of the TiO_2 NTs with 1 nm of Au dewetted and **d** cross-section of the NTs on TiAuPt alloy with magnifications in the top, middle and bottom part identified by different colors black, blue and red. Reprinted with permission [66]

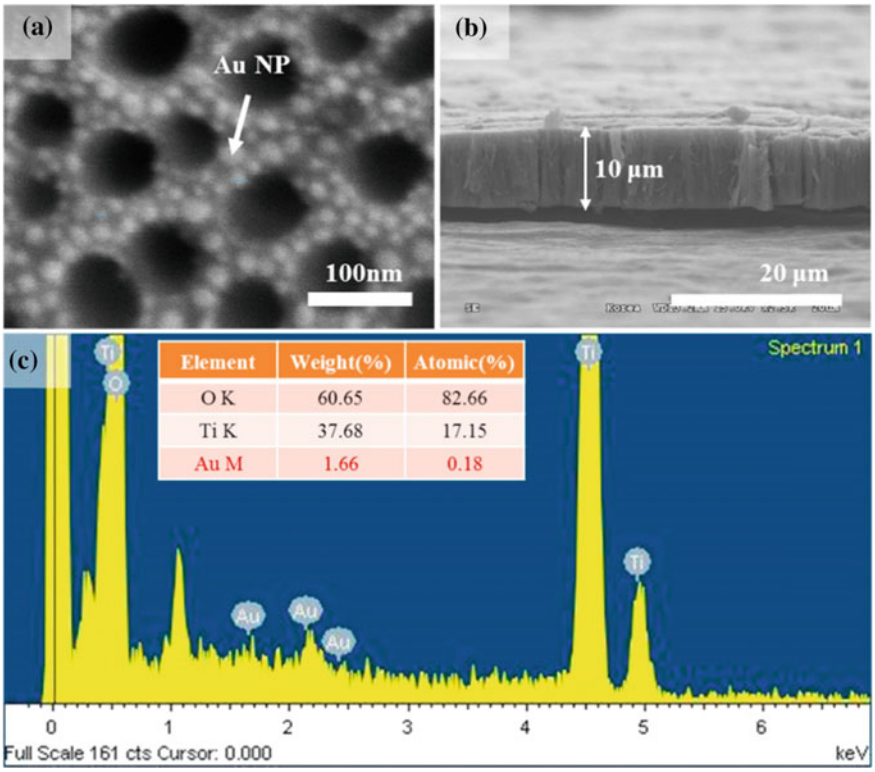

Fig. 17 SEM images of Au NP-decorated 2 nd anodized TNT arrays **a** top-view and **b** cross sectional view. **c** EDX analysis of Au NP-decorated 2 and anodized TNT arrays (TNT–Au NP-decorated TiO_2 nanotube). Reprinted with permission [67]

4 Conclusions

In summary, modifying TiO_2 with semiconductor materials, distinctly Fe and Cu ions, creates additional energy levels near the valence and conduction bands of TiO_2, thus minimizing the limitations associated with its large band gap via trapping of both electrons and holes. Consequently, it is highly recommended to dope TiO_2 with either Fe or Cu ions to obtain superior photocatalytic activity [6, 71]. Furthermore, the nanotubes loaded with Ag provide a doubled degradation when compared with pure nanotubes. The improvement of photocatalytic activity using Ag-TiO_2 can be explained considering the deposition method, which a thermal treatment step is recommended as an activation step, otherwise the addition of this metal may lead to decreased activity compared to pure TiO_2 NTs. Finally, the presence of the noble metal establish the formation of locally Schottky junctions with a high potential gradient, compared with TiO_2/electrolyte interface, established by Schottky barrier, which enables better charge tranfer between the materials. In view of the aforemen-

tioned results, it is possible to state that the addition of metallic structures, like Fe, Cu, Ag and Au, to TiO_2 NTs have a great potential to be used in photocatalytic reactions and water-splitting applications.

References

1. Zhang Y, Gu D, Zhu L, Wang B (2017) Highly ordered Fe^{3+}/TiO_2 nanotube arrays for efficient photocatalytic degradation of nitrobenzene. Appl Surf Sci 420:896–904. https://doi.org/10.1016/j.apsusc.2017.05.213
2. Hou Y, Li X, Zou X, Quan X, Chen G (2009) Photoeletrocatalytic activity of a Cu_2O-loaded self-organized highly oriented TiO_2 nanotube array electrode for 4-chlorophenol degradation. Environ Sci Technol 43:858–863. https://doi.org/10.1021/es802420u
3. Baker DR, Kamat PV (2009) Photosensitization of TiO_2 nanostructures with CdS quantum dots: particulate versus tubular support architectures. Adv Funct Mater 19:805–811. https://doi.org/10.1002/adfm.200801173
4. Teh CM, Mohamed AR (2011) Roles of titanium dioxide and ion-doped titanium dioxide on photocatalytic degradation of organic pollutants (phenolic compounds and dyes) in aqueous solutions. J Alloys Compd 509:1648–1660. https://doi.org/10.1016/j.jallcom.2010.10.181
5. Ambrus Z, Balázs N, Alapi T, Wittmann G, Sipos P, Dombi A, Mogyorósi K (2008) Synthesis structure and photocatalytic properties of Fe(III)-doped TiO_2 prepared from $TiCl_3$. Appl Catal B Environ 81:27–37. https://doi.org/10.1016/j.apcatb.2007.11.041
6. Choi W, Termin A, Hoffmann MR (1994) The role of metal ion dopants in quantum-sized TiO_2: correlation between photoreactivity and charge carrier recombination dynamics. J Phys Chem 98:13669–13679. https://doi.org/10.1021/j100102a038
7. Kraeutler B, Bard AJ (1978) Heterogeneous photocatalytic decomposition of saturated carboxylic acids on titanium dioxide powder. Decarboxylative route to alkanes. J Am Chem Soc 100:5985–5992. https://doi.org/10.1021/ja00487a001
8. Bard AJ (1979) Photoelectrochemistry and heterogeneous photo-catalysis at semiconductors. J Photochem 10:59–75. https://doi.org/10.1016/0047-2670(79)80037-4
9. Papp J, Soled S, Dwight K, Wold A (1994) Surface acidity and photocatalytic activity of and photocatalysts. Chem Mater 6:496–500. https://doi.org/10.1021/cm00040a026
10. Hoffmann MR, Martin ST, Choi W, Bahnemann DW (1995) Environmental applications of semiconductor photocatalysis. Chem Rev 95:69–96. https://doi.org/10.1021/cr00033a004
11. Zhang ZB, Wang CC, Zakaria R, Ying JY (1998) Role of particle size in nanocrystalline TiO_2-based photocatalysts. J Phys Chem Biol 102:10871–10878. https://doi.org/10.1021/jp982948+
12. Wang CY, Bahnemann DW, Dohrmann JK (2000) A novel preparation of iron-doped TiO_2 nanoparticles with enhanced photocatalytic activity. Chem Commun 0:1539–1540. https://doi.org/10.1039/b002988m
13. Adán C, Bahamonde A, Fernández-García M, Martínez-Arias A (2007) Photocatalytic degradation of ethidium bromide over titania in aqueous solutions. Appl Catal B Environ 72:11–17. https://doi.org/10.1016/j.apcatb.2006.09.018
14. Serpone N, Lawless D, Disdier J, Herrmann JM (1994) Spectroscopic, photoconductivity, and photocatalytic studies of TiO_2 colloids: naked and with the lattice doped with Cr^{3+}, Fe^{3+}, and V^{5+} cations. Langmuir 10:643–652. https://doi.org/10.1021/la00015a010
15. Zhu J, Zheng W, He B, Zhang J, Anpo M (2004) Characterization of Fe–TiO_2 photocatalysts synthesized by hydrothermal method and their photocatalytic reactivity for photodegradation of XRG dye diluted in water. J Mol Catal A Chem 216:35–43. https://doi.org/10.1016/j.molcata.2004.01.008
16. Zhu J, Chen F, Zhang J, Chen H, Anpo M (2006) Fe^{3+}–TiO_2 photocatalysts prepared by combining sol-gel method with hydrothermal treatment and their characterization. J Photochem Photobiol A Chem 180:196–204. https://doi.org/10.1016/j.jphotochem.2005.10.017

17. Wang XH, Li JG, Kamiyama H, Moriyoshi Y, Ishigaki T (2006) Wavelength-sensitive photocatalytic degradation of methyl orange in aqueous suspension over Iron(III)-doped TiO_2 nanopowders under UV and visible light irradiation. J Phys Chem B 110:6804–6809. https://doi.org/10.1021/jp060082z
18. Yu H, Irie H, Shimodaira Y, Hosogi Y, Kuroda Y, Miyauchi M, Hashimoto K (2010) An efficient visible-light-sensitive Fe(III)-grafted TiO_2 photocatalyst. J Phys Chem C 114:16481–16487. https://doi.org/10.1021/jp1071956
19. Asiltürk M, Sayilkan F, Arpaç E (2009) Effect of Fe^{3+} ion doping to TiO_2 on the photocatalytic degradation of Malachite Green dye under UV and vis-irradiation. J Photochem Photobiol A Chem 203:64–71. https://doi.org/10.1016/j.jphotochem.2008.12.021
20. Frandsen C, Bahl CRH, Lebech B, Lefmann K, Kuhn LT, Keller L, Andersen NH, Zimmermann MV, Johnson E, Klausen SN, Mørup S (2005) Oriented attachment and exchange coupling of $\alpha-Fe_2O_3$ nanoparticles. Phys Rev B Condens Matter Mater Phys 72:214406. https://doi.org/10.1103/physrevb.72.214406
21. Spray RL, McDonald KJ, Choi KS (2011) Enhancing photoresponse of nanoparticulate α-Fe_2O_3 electrodes by surface composition tuning. J Phys Chem C 115:3497–3506. https://doi.org/10.1021/jp1093433
22. Xie S, Ouyang K, Lao Y, He P, Wang Q (2017) Heterostructured $ZnFe_2O_4/TiO_2$ nanotube arrays with remarkable visible-light photoelectrocatalytic performance and stability. J Colloid Interface Sci 493:198–205. https://doi.org/10.1016/J.JCIS.2017.01.023
23. Cong Y, Li Z, Zhang Y, Wang Q, Xu Q (2012) Synthesis of α-Fe_2O_3/TiO_2 nanotube arrays for photoelectro-Fenton degradation of phenol. Chem Eng J 191:356–363. https://doi.org/10.1016/j.cej.2012.03.031
24. Yang X, Zou R, Huo F, Cai D, Xiao D (2009) Preparation and characterization of $Ti/SnO_2–Sb_2O_3–Nb_2O_5/PbO_2$ thin film as electrode material for the degradation of phenol. J Hazard Mater 164:367–373. https://doi.org/10.1016/j.jhazmat.2008.08.010
25. Li XY, Cui YH, Feng YJ, Xie ZM, Gu JD (2005) Reaction pathways and mechanisms of the electrochemical degradation of phenol on different electrodes. Water Res 39:1972–1981. https://doi.org/10.1016/j.watres.2005.02.021
26. Shihong X, Daolun F, Wenfeng S (2009) Preparations and photocatalytic properties of visible-light-active zinc ferrite-doped TiO_2 photocatalyst. J Phys Chem C 113:2463–2467. https://doi.org/10.1021/jp806704y
27. Hou Y, Li XY, Zhao QD, Quan X, Chen GH (2010) Electrochemical method for synthesis of a $ZnFe_2O_4/TiO_2$ composite nanotube array modified electrode with enhanced photoelectrochemical activity. Adv Funct Mater 20:2165–2174. https://doi.org/10.1002/adfm.200902390
28. Theurich J, Lindner M, Bahnemann DW (1996) Photocatalytic degradation of 4-Chlorophenol in aerated aqueous titanium dioxide suspensions: a kinetic and mechanistic study. Langmuir 12:6368–6376. https://doi.org/10.1021/la960228t
29. Venkatachalam N, Palanichamy M, Murugesan V (2007) Sol-gel preparation and characterization of alkaline earth metal doped nano TiO_2: efficient photocatalytic degradation of 4-chlorophenol. J Mol Catal A Chem 273:177–185. https://doi.org/10.1016/j.molcata.2007.03.077
30. Fujishima A, Honda K (1972) Electrochemical photolysis of water at a semiconductor electrode. Nature 238:37–38. https://doi.org/10.1038/238037a0
31. Momeni MM, Ghayeb Y, Davarzadeh M (2015) Single-step electrochemical anodization for synthesis of hierarchical $WO_3–TiO_2$ nanotube arrays on titanium foil as a good photoanode for water splitting with visible light. J Electroanal Chem 739:149–155. https://doi.org/10.1016/j.jelechem.2014.12.030
32. Ran J, Zhang J, Yu J, Jaroniec M, Qiao SZ (2014) Earth-abundant cocatalysts for semiconductor-based photocatalytic water splitting. Chem Soc Rev 43:7787–7812. https://doi.org/10.1039/c3cs60425j
33. Ahmad H, Kamarudin SK, Minggu LJ, Kassim M (2015) Hydrogen from photo-catalytic water splitting process: a review. Renew Sustain Energy Rev 43:599–610. https://doi.org/10.1016/j.rser.2014.10.101

34. Grätzel M (2001) Photoelectrochemical cells. Nature 414:338–344. https://doi.org/10.1038/35104607
35. Jang JS, Kim HG, Lee JS (2012) Heterojunction semiconductors: a strategy to develop efficient photocatalytic materials for visible light water splitting. Catal Today 185:270–277. https://doi.org/10.1016/j.cattod.2011.07.008
36. Meher LC, Vidya Sagar D, Naik SN (2006) Technical aspects of biodiesel production by transesterification—a review. Renew Sustain Energy Rev 10:248–268. https://doi.org/10.1016/j.rser.2004.09.002
37. Momeni MM, Ghayeb Y (2015) Fabrication, characterization and photoelectrochemical behavior of Fe–TiO_2 nanotubes composite photoanodes for solar water splitting. J Electroanal Chem 751:43–48. https://doi.org/10.1016/j.jelechem.2015.05.035
38. Siripala W, Ivanovskaya A, Jaramillo TF, Baeck SH, McFarland EW (2003) A Cu_2O/TiO_2 heterojunction thin film cathode for photoelectrocatalysis. Sol Energy Mater Sol Cells 77:229–237. https://doi.org/10.1016/S0927-0248(02)00343-4
39. Lu C, Qi L, Yang J, Wang X, Zhang D, Xie J, Ma J (2005) One-pot synthesis of octahedral Cu_2O nanocages via a catalytic solution route. Adv Mater 17:2562–2567. https://doi.org/10.1002/adma.200501128
40. Wang J, Ji G, Liu Y, Gondal MA, Chang X (2014) Cu_2O/TiO_2 heterostructure nanotube arrays prepared by an electrodeposition method exhibiting enhanced photocatalytic activity for CO_2 reduction to methanol. Catal Commun 46:17–21. https://doi.org/10.1016/j.catcom.2013.11.011
41. Gombac V, Sordelli L, Montini T, Delgado JJ, Adamski A, Adami G, Cargnello M, Bernai S, Fornasiero P (2010) CuO_x-TiO_2 photocatalysts for H_2 production from ethanol and glycerol solutions. J Phys Chem A 114:3916–3925. https://doi.org/10.1021/jp907242q
42. Xu S, Ng J, Zhang X, Bai H, Sun DD (2010) Fabrication and comparison of highly efficient Cu incorporated TiO_2 photocatalyst for hydrogen generation from water. Int J Hydrogen Energy 35:5254–5261. https://doi.org/10.1016/j.ijhydene.2010.02.129
43. Hua Z, Dai Z, Bai X, Ye Z, Wang P, Gu H, Huang X (2016) Copper nanoparticles sensitized TiO_2 nanotube arrays electrode with enhanced photoelectrocatalytic activity for diclofenac degradation. Chem Eng J 283:514–523. https://doi.org/10.1016/j.cej.2015.07.072
44. Wu NL, Lee MS (2004) Enhanced TiO_2 photocatalysis by Cu in hydrogen production from aqueous methanol solution. Int J Hydrogen Energy 29:1601–1605. https://doi.org/10.1016/j.ijhydene.2004.02.013
45. Foo WJ, Zhang C, Ho GW (2013) Non-noble metal Cu-loaded TiO_2 for enhanced photocatalytic H_2 production. Nanoscale. 5:759–764. https://doi.org/10.1039/c2nr33004k
46. Yang L, Luo S, Li Y, Xiao Y, Kang Q, Cai Q (2010) High efficient photocatalytic degradation of p-Nitrophenol on a unique Cu_2O/TiO_2 p-n heterojunction network catalyst. Environ Sci Technol 44:7641–7646. https://doi.org/10.1021/es101711k
47. Sakata Y, Yamamoto T, Okazaki T, Imamura H, Tsuchiya S (1998) Generation of visible light response on the photocatalyst of a copper ion containing TiO_2. Chem Lett 27:1253–1254. https://doi.org/10.1246/cl.1998.1253
48. Xu S, Sun DD (2009) Significant improvement of photocatalytic hydrogen generation rate over TiO_2 with deposited CuO. Int J Hydrogen Energy 34:6096–6104. https://doi.org/10.1016/j.ijhydene.2009.05.119
49. Yi H, Peng T, Ke D, Ke D, Zan L, Yan C (2008) Photocatalytic H_2 production from methanol aqueous solution over titania nanoparticles with mesostructures. Int J Hydrogen Energy 33:672–678. https://doi.org/10.1016/J.IJHYDENE.2007.10.034
50. Sreethawong T, Puangpetch T, Chavadej S, Yoshikawa S (2007) Quantifying influence of operational parameters on photocatalytic H_2 evolution over Pt-loaded nanocrystalline mesoporous TiO_2 prepared by single-step sol-gel process with surfactant template. J Power Sources 165:861–869. https://doi.org/10.1016/J.JPOWSOUR.2006.12.050
51. Momeni MM, Ghayeb Y, Ghonchegi Z (2015) Fabrication and characterization of copper doped TiO_2 nanotube arrays by in situ electrochemical method as efficient visible-light photocatalyst. Ceram Int 41:8735–8741. https://doi.org/10.1016/j.ceramint.2015.03.094

52. Hartmann J, Bartels P, Mau U, Witter M, Tümpling WV, Hofmann J, Nietzschmann E (2008) Degradation of the drug diclofenac in water by sonolysis in presence of catalysts. Chemosphere 70:453–461. https://doi.org/10.1016/j.chemosphere.2007.06.063
53. Yi S, Zhuang WQ, Wu B, Tay STL, Tay JH (2006) Biodegradation of p-nitrophenol by aerobic granules in a sequencing batch reactor. Environ Sci Technol 40:2396–2401. https://doi.org/10.1021/es0517771
54. Labana S, Pandey G, Paul D, Sharma NK, Basu A, Jain RK (2005) Pot and field studies on bioremediation of p-Nitrophenol contaminated soil using arthrobacter protophormiae RKJ100. Environ Sci Technol 39:3330–3337. https://doi.org/10.1021/es0489801
55. Daghrir R, Drogui P, Robert D (2013) Modified TiO_2 for environmental photocatalytic applications: a review. Ind Eng Chem Res 52:3581–3599. https://doi.org/10.1021/ie303468t
56. He C, Yu Y, Hu X (2002) Influence of silver doping on the photocatalytic activity of titania films. Appl Surf Sci 200:239–247. https://doi.org/10.1016/s0169-4332(02)00927-3
57. Hajjaji A, Elabidi M, Trabelsi K, Assadi AA, Bessais B, Rtimi S (2018) Bacterial adhesion and inactivation on Ag decorated TiO_2-nanotubes under visible light: effect of the nanotubes geometry on the photocatalytic activity. Colloids Surf B Biointer 170:92–98. https://doi.org/10.1016/j.colsurfb.2018.06.005
58. Sun L, Li J, Wang C, Li S, Lai Y, Chen H, Lin C (2009) Ultrasound aided photochemical synthesis of Ag loaded TiO_2 nanotube arrays to enhance photocatalytic activity. J Hazard Mater 171:1045–1050. https://doi.org/10.1016/j.jhazmat.2009.06.115
59. Roy P, Berger S, Schmuki P (2011) TiO_2 nanotubes: synthesis and applications. Angew Chemie Int Ed 50:2904–2939. https://doi.org/10.1002/anie.201001374
60. Zhang J, Li S, Ding H, Li Q, Wang B, Wang X, Wang H (2014) Transfer and assembly of large-area TiO_2 nanotube arrays onto conductive glass for dye sensitized solar cells. J Power Sources 247:807–812. https://doi.org/10.1016/J.JPOWSOUR.2013.08.124
61. Etacheri V, Di Valentin C, Schneider J, Bahnemann D, Pillai SC (2015) Visible-light activation of TiO_2 photocatalysts: advances in theory and experiments. J Photochem Photobiol C Photochem Rev 25:1–29. https://doi.org/10.1016/j.jphotochemrev.2015.08.003
62. Seery M, George R, Pillai S, Floris P (2007) Silver doped titanium dioxide nanomaterials for enhanced visible-light photocatalysis. J Photochem Photobiol A 189:258–263. https://doi.org/10.1016/j.jphotochem.2007.02.010
63. Li X, Zou X, Qu Z, Zhao Q, Wang L (2011) Photocatalytic degradation of gaseous toluene over Ag-doping TiO_2 nanotube powder prepared by anodization coupled with impregnation method. Chemosphere 83:674–679. https://doi.org/10.1016/j.chemosphere.2011.02.043
64. Fan X, Fan J, Hu X, Liu E, Kang L, Tang C, Ma Y, Wu H, Li Y (2014) Preparation and characterization of Ag deposited and Fe doped TiO_2 nanotube arrays for photocatalytic hydrogen production by water splitting. Ceram Int 40:15907–15917. https://doi.org/10.1016/j.ceramint.2014.07.119
65. Zhang G, Miao H, Hu X, Mu J, Liu X, Han T, Fan J, Liu E, Yin Y, Wan J (2017) A facile strategy to fabricate Au/TiO_2 nanotubes photoelectrode with excellent photoelectrocatalytic properties. Appl Surf Sci 391:345–352. https://doi.org/10.1016/j.apsusc.2016.03.042
66. Sanabria-Arenas BE, Mazare A, Yoo J, Nguyen NT, Hejazi S, Bian H, Diamanti MV, Pedeferri MP, Schmuki P (2018) Intrinsic AuPt-alloy particles decorated on TiO_2 nanotubes provide enhanced photocatalytic degradation. Electrochim Acta 292:865–870. https://doi.org/10.1016/j.electacta.2018.09.206
67. Choi J-Y, Hoon Sung Y, Choi H-J, Doo Kim Y, Huh D, Lee H (2017) Fabrication of Au nanoparticle-decorated TiO_2 nanotube arrays for stable photoelectrochemical water splitting by two-step anodization. Ceram Int 43:14063–14067. https://doi.org/10.1016/j.ceramint.2017.07.141
68. Ahmed S, Rasul MG, Brown R, Hashib MA (2011) Influence of parameters on the heterogeneous photocatalytic degradation of pesticides and phenolic contaminants in wastewater: a short review. J Environ Manage 92:311–330. https://doi.org/10.1016/j.jenvman.2010.08.028

69. Ayati A, Ahmadpour A, Bamoharram FF, Tanhaei B, Mänttäri M, Sillanpää M (2014) A review on catalytic applications of Au/TiO_2 nanoparticles in the removal of water pollutant. Chemosphere 107:163–174. https://doi.org/10.1016/j.chemosphere.2014.01.040
70. Paramasivam I, Macak JM, Schmuki P (2007) Photocatalytic activity of TiO_2 nanotube layers loaded with Ag and Au nanoparticles. Electrochem Commun 10:71–75. https://doi.org/10.1016/j.elecom.2007.11.001
71. Litter MI (1999) Heterogeneous photocatalysis: transition metal ions in photocatalytic systems. Appl Catal B Environ 23:89–114. https://doi.org/10.1016/S0926-3373(99)00069-7

Organic-Inorganic Hybrid Perovskites for Solar Cells Applications

Anne Esther Ribeiro Targino Pereira de Oliveira and Annelise Kopp Alves

Abstract The increasing efficiency of the organic-inorganic hybrid perovskite solar cells (PSCs), together with a series of advantages such as long carrier diffusion lengths, tunable bandgap, great light absorption potential and low-cost fabrication processes, have made this material the focus of attention of the solar cell researchers, despite the drawbacks such as device instability, J-V hysteresis and lead toxicity. This chapter will discuss the origin of perovskites and its application in solar cells, the structure of PSCs, how they are assembled, their obstacles and future perspectives.

Keywords Perovskite · Solar cells · Thin films · Stability · Toxicity

Abbreviation

DMA	Dimethyl acetamide
DMF	Dimethyl formamide
DMSO	Dimethyl sulfoxide
DSSC	Dye sensitive solar cell
FA	Formamidinium
FAI	Formamidinium iodide
FTO	Fluorine doped tin oxide
IPA	Isopropyl alcohol
ITO	Indium doped tin oxide
MA	Methylammonium
MAI	Methylammonium iodide
$MAPbBr_3$	Methylammonium lead bromide perovskite
mp-TiO_2	Mesoporous TiO_2
PET	Polyethylene terephthalate

A. E. R. T. P. de Oliveira · A. K. Alves (✉)
Universidade Federal do Rio Grande do Sul, Porto Alegre, Brazil
e-mail: annelise.alves@ufrgs.br

A. E. R. T. P. de Oliveira
e-mail: annetargino@gmail.com

A. Kopp Alves (ed.), *Nanomaterials for Eco-friendly Applications*,
Engineering Materials, https://doi.org/10.1007/978-3-030-26810-7_6

PSC	Perovskite solar cell
PV	Photovoltaic
PVc	Photovoltaic cell
TCO	Transparent conductive oxide
UV	Ultraviolet light

1 Introduction

The demand for alternative forms of clean energy generation is increasing worldwide mainly due to the depletion of non-renewable sources and the ever growing demands. There was a significant increase in the use of solar cells as a source of clean and sustainable energy. In such devices called photovoltaic cells (PVc), the energy from the sun is transformed into electrical energy.

The first-generation solar cell was based on silicon wafers, which are widely used nowadays due to their high performance (about 15–20%) and stability. The second-generation solar cells employed amorphous silicon or semiconducting materials, copper indium gallium selenide (CIGS) and cadmium telluride (CdTe), rather than silicon wafer, with an efficiency of 10–15%. The third-generation solar cells, the thin-film solar cells, uses organic materials (small molecules) or polymers as light harvesters that minimized production costs [1].

Among these different types of photovoltaic (PV) devices, perovskite solar cells (PSC) has been a focus of interest, mainly due to high conversion efficiency, up to 23.7%, measured in a certify institution [2]; high absorption coefficient, high mobility of charge carriers, high dielectric constant and low binding energy of the exciton [3].

Miyasaka et al. in 2009 were the first to use a hybrid perovskite material ($MAPbBr_3$) as a semiconductor sensitizers in liquid electrolyte dye sensitized solar cells (DSSCs) with an efficiency of only 3.1% [1].

2 Perovskites

Gustave Rose in 1839 was the first to identify a perovskite material in nature, the calcium titanate ($CaTiO_3$). He named this class of materials in honor of a mineralogist called Lev Perovski [4].

The materials known as organic-inorganic hybrid perovskites has a structure of an organometallic halide, whose general formula is ABX_3, composed of A and B cations and X as an anion, usually a halide (I, Br, Cl), as presented in Fig. 1.

The perovskite has a cubic unit cell in which the A-cation resides at the eight corners of the cube surrounded by twelve X-anions, while the B-cation is located at the body center which is surrounded by six X-anions (located at the face centers) in an octahedral $[BX_6]^{4-}$ cluster [5].

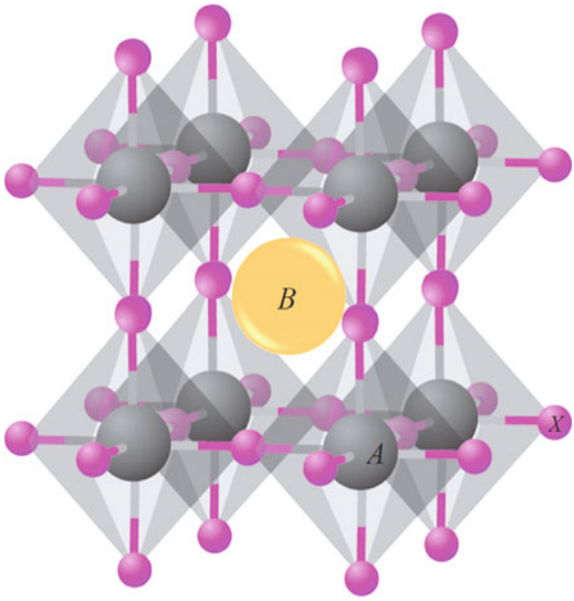

Fig. 1 Perovskite crystal structure. Edited and reprinted with permission from Cui et al. [5]

In organic-inorganic hybrid perovskites the *A*-cations are organic molecules, for example, methylammonium (MA) [$CH_3NH_3^+$] or formamidinium (FA) [$HC(NH_2)_2^+$], larger and more electropositive when compared to the *B*-cations, generally divalent metal ions such as Pb^{2+}, Sn^{2+}, Eu^{2+}, Cu^{2+}.

These halides hybrid structures have attracted the attention of the energy research field worldwide mainly due to (i) low-temperature solution processes; (ii) possibility of bandgap adjustment and; (iii) high charge transfer capability [6, 7]. These hybrid perovskites materials used in solar cells nowadays are variations on $CH_3NH_3PbX_3$ such as lead methylammonium iodide ($CH_3NH_3PbI_3$) and mixed halides such as $CH_3NH_3PbI_{3-x}Br_x$ and $CH_3NH_3PbI_{3-x}Cl_x$ [8].

3 PSC Structure

Typically, the perovskite solar cell consists of five parts, as shown in Fig. 2 [9].

There are two types of PSC device structure according to the arrangement of the electron transport layer (ETL) and hole transport layer (HTL): *n*–i–*p* or *p*–i–*n* structure, Fig. 3a, b, respectively.

Each one of these layers is adequately chosen to fulfill the requirements of bang-gaps positions that improve the light collection and transport of charges. Figure 4 exemplifies the band-gap values and energy level positions of the most common used materials in PSC devices [5].

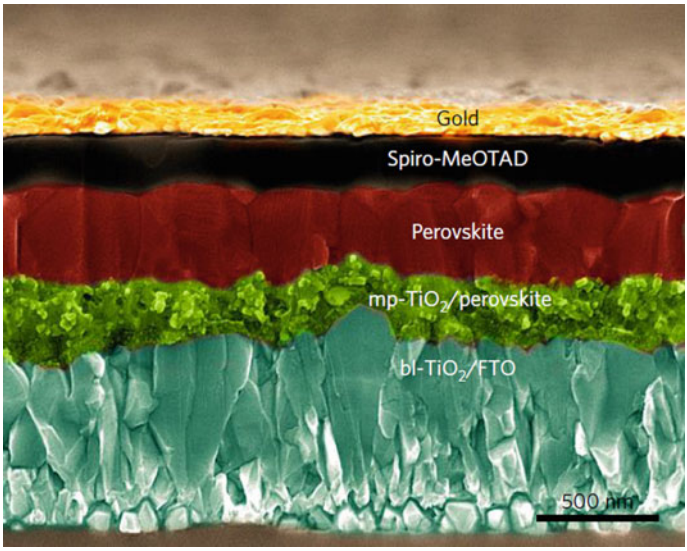

Fig. 2 Cross-sectional SEM image of perovskite solar cell. Reprinted with permission from [9]

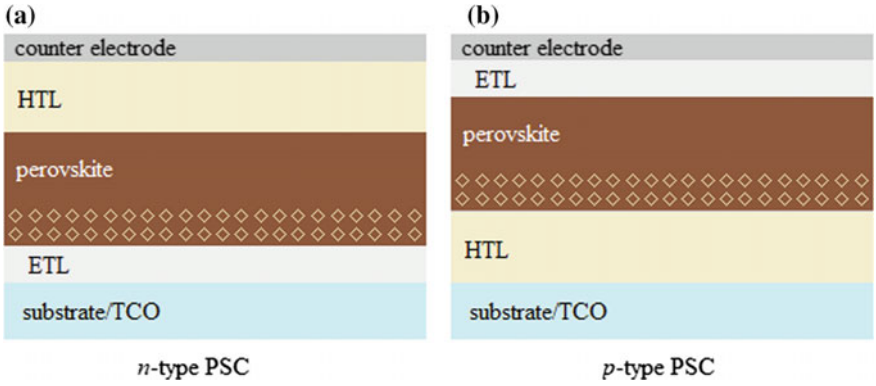

Fig. 3 PSC film configurations for **a** *n*-type and **b** *p*-type arrangements

3.1 Substrate

Most PSCs use a glass substrate, although PET (polyethylene terephthalate) [10], flexible invar metal foil [11], paper [12] and optically transparent wood [13] substrates have shown promising results for obtaining flexible solar cells. A thin electrical contact layer, transparent to UV radiation; must be deposited over the non-conductive substrate. A transparent conductive oxide (TCO) such as indium doped tin oxide (ITO) or fluorine doped tin oxide (FTO) is the selected material for the majority of researches.

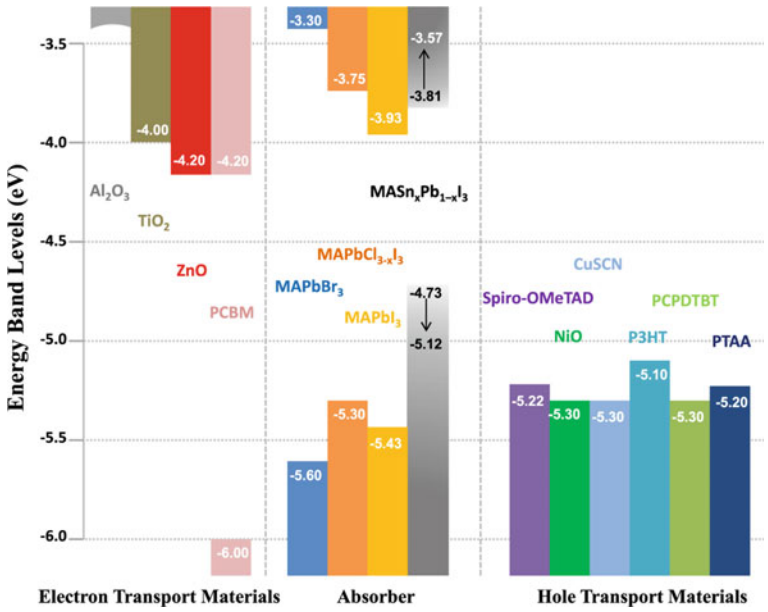

Fig. 4 Energy level diagram of the materials used in PSCs. Reprinted with permission of Cui et al. [5]

3.2 Electron Transport Layer

Although the early generation of PSC don't use an electron transport layer (ETL), the efficiency and stability of PSCs strongly depends on the type and morphology of the materials selected as the ETL [1]. The ETL is also called electron extraction layer (EEL) or electron selective layer (ESL) and the function of this layer is to enable efficient electron collection and transportation from the perovskite layer to its respective electrodes.

Traditionally, the ETL is composed of an *n*-type oxide semiconductor, most commonly TiO_2, that have a band alignment that favors the transfer of electrons and, at the same time, blocks the photogenerated holes. It also has the function of host the perovskite crystals, so a high surface area is of interest [2].

PSCs originate from DSSCs, but the architecture of the ETL in a PSC is completely different from its original device. In a DSSC, a thick (10 μm) mesoporous layer of dispersed TiO_2 nanoparticles is necessary to enable high dye loading. The optional mesoporous TiO_2 layer in the PSC, around 200 nm thick which is enough to generate a sufficient photocurrent, is employed to enhance the electron extraction and minimize the hysteresis effect [14, 15].

An example of the preparation of an TiO_2 ETL mesoporous layer is described in the work of Bi et al. [9]. Firstly, a 30 nm TiO_2 layer was deposited on a pre-cleaned glass/FTO by spray pyrolysis using O_2 as the carrying gas at 450 °C from

a precursor solution containing 0.6 mL of titanium diisopropoxide and 0.4 mL of bis(acetylacetonate) in 7 mL of anhydrous isopropanol. Then, a 150 nm mesoporous TiO_2 layer was deposited over this first layer by spin-coating at a speed of 4500 r.p.m. for 10 s, from a diluted 30 nm particle paste in ethanol (1:6, respectively). The substrate was sintered at 500 °C for 20 min.

Based on the arrangement of the electron transport layer (ETL) the *n*–i–*p* type PSC can be further categorized into planar or mesoporous.

The highest PSC efficiencies were achieved using a thin layer of mesoporous ETL TiO_2 layer (mp-TiO_2). In this architecture, the perovskite material permeates the mesoporous semiconductor layer, which is sandwiched between the HTL (typically Spiro- OMeTAD) and the ETL (typically TiO_2).

But soon it was realized that the perovskite transports both holes and electrons. This led to the investigation of a thin film perovskite configuration with a compact TiO_2 as the ETL. This PSC assemble is called planar configuration.

In the quest to increase photovoltaic properties and stability, other materials have been employed as an ETL layer, such as ZnO, SnO_2, ternary metal oxides, metal sulphides, and organic semiconductors such as fullerene, graphene, and ionic liquids [1].

3.3 Perovskite

The organo-metallic hybrid perovskite is the light-absorbing layer that creates exciton or free carriers [16]. In early history of DSSC, perovskites were an alternative sensitizer but their superior charge transport properties allowed thicker absorbing layers and perovskites stand apart as a new class of solar cells.

A hybrid perovskite is formed by combining two precursors, one organic and another one inorganic, which can be combined by different methods [17]. Most synthesis methods are based on the same principle: the combination of an organic component, for example methylammonium iodide (MAI) and an inorganic component, such as lead iodide or lead chloride (PbI_2 or $PbCl_2$) to form the hybrid perovskite, $MAPbI_3$ or $MAPbI_{3-x}Cl_x$, respectively [18]. Lead-halide perovskites have been largely produced by two methods: precipitation from solution and deposition from the vapor phase. A two-step processes in both methods have also been explored. More details on that methods on Sect. 4.

3.4 Hole Transport Layer

The hole transport layer (HTL), also called hole extraction layer (HEL), can be constituted of an oxide semiconductor, an organic (polymer) semiconductor or small molecules. The hole transport material infiltrates in the mesoporous structure of the ETL, guaranteeing a constant regeneration of oxidized molecules [19].

The most common hole transport material is Spiro-OMeTAD, also known as its scientific name: (2,20,7,70-tetrakis(N,N-di-pmethoxyphenylamine)-9,90-spirobifluorene) which have been used in high efficiency PSCs [20]. In fact, this was the first material used as a replacement of liquid electrolytes in solar cells [4].

An example of the process for obtaining a layer of about 250 nm thick of Spiro-OMeTAD layer is described by Bi, et al. [9]. In their work Spiro-OMeTAD was dissolved in chlorobenzene at a concentration of 60 mM, with the addition of 30 mM bis(trifluoromethanesulfonyl)imide from a stock solution in acetonitrile and 200 mM of tert-butylpyridine. This mixture was deposited on top of the perovskite layer by spin-coating, in a dry air flow in a glove box at a spin-coating speed of 3000 r.p.m. for 30 s.

Other materials such as graphene and derivatives (graphene oxide and reduced graphene oxide) [21–23], C60 [24], poly-triarylamine (PTAA) [25], poly(3,4-ethylenedioxythiophene) polystyrene sulfonate (PEDOT:PSS) [26], NiO [27], CuSCN [28], $CuGaO_2$ [29] was also been used to substitute the Spiro-OMeTAD because its high cost.

3.5 Counter Electrode

Finally, there is a counter electrode made of gold, silver or carbon to ensure an ohmic contact. This layer is most frequently deposited using thermal evaporation using a shadow mask to pattern the electrodes, leading to a layer of about 80 nm thick.

4 Assembling a PSC

The perovskites are commonly applied as a thin film over a substrate. The quality of the films that constitute a perovskite solar cell, which is also related to the obtaining method, are an essential factor in its final efficiency.

The PSC precursors may be deposited over a substrate simultaneously or independently, resulting in a variety of deposition techniques. Thus, considering the various perovskite film processing techniques documented so far, four are the most common ones.

4.1 One-Step Deposition

The one step deposition process is performed using a homogeneous solution precursor. A lead salt (PbX_2, X = I, Br, Cl) is dissolved in DMF (dimethyl formamide), DMSO (dimethyl sulfoxide) or DMA (dimethyl acetamide) and a methylammonium halide is added to this solution [5, 30]. This precursor solution can be deposited

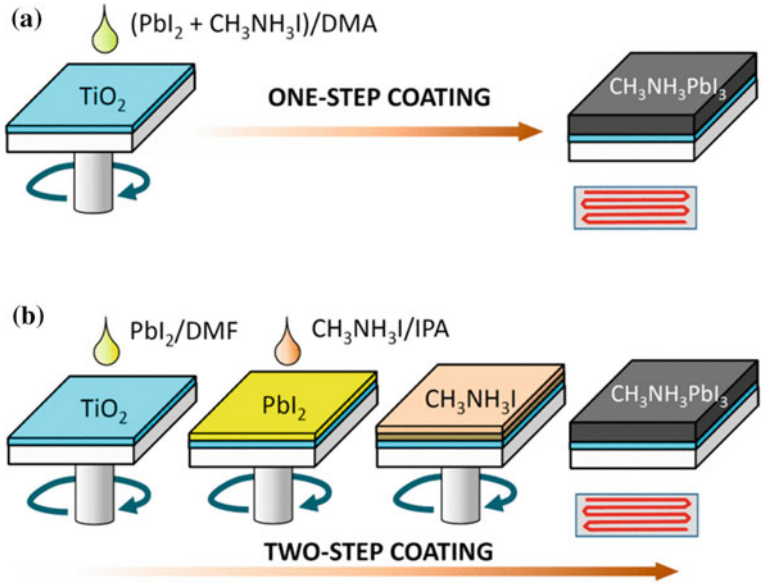

Fig. 5 Spin-coating process for $CH_3NH_3PbI_3$ formation: **a** one-step and **b** two-step. Adapted and reprinted with permission from Jeong-Hyeok et al. [30]

over the pre-prepared substrate by spin-coating, doctor blade, spray deposition. The obtained material is then submitted to a heat treatment at temperatures around 150 °C (Fig. 5a).

Although easily done, the one-step deposition is not so commonly used because it usually results in a non-homogenous morphology of the obtained film and their synthesis parameters and perovskite crystal development are sometimes difficult to precisely control (Fig. 6a).

4.2 Sequential Deposition

The first reported work of the sequential deposition of a hybrid perovskite film, describe a method in which the perovskite $CH_3NH_3PbI_3$ (methylammonium lead iodide) is formed by the contact between a film of PbI_2 and a solution of CH_3NH_3 (MA) through immersion [31] (Fig. 5b).

The current process that has been widely used is the one developed by Burchka et al. [32]. This method consists in obtaining the $CH_3NH_3PbI_3$ film using a lead halide solution (~1 M) in DMF or DMSO at 70 °C, which is deposited over the substrate. After drying, the film was dipped into a solution of CH_3NH_3I (methylammonium iodide—MAI) in isopropyl alcohol (IPA). Then, the sample is annealed at low temperature, to complete the crystallization and the formation of the perovskite

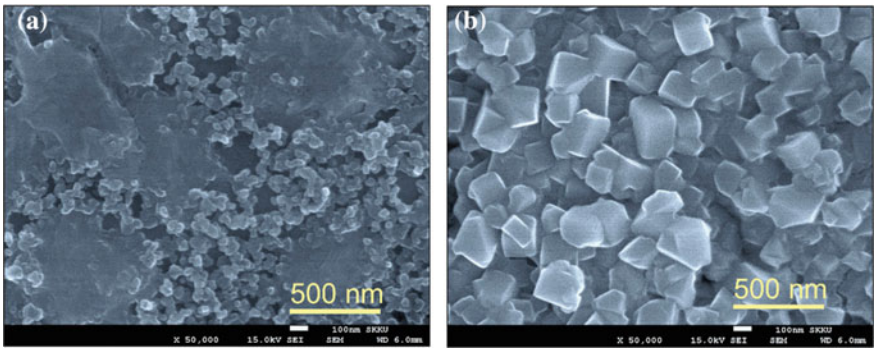

Fig. 6 Morphology of the PSC obtaining using **a** one-step deposition, where small TiO_2 particles are visible and islands of perovskite are formed; **b** two-step deposition formed a more homogeneous perovskite layer. Adapted and reprinted with permission from Jeong-Hyeok et al. [30]

(Fig. 6b). When in contact with the MAI solution, the color of the sample changed from yellow to dark brown, indicating the formation of $CH_3NH_3PbI_3$.

Several important parameters related to the formation of the perovskite film can be adjusted in order to further optimize the performance of the devices. Especially in planar solar cells, the perovskite layer requires optimization of parameters such as concentration and solvent of the precursor, perovskite layer thickness, temperature, rotational speed and post deposition process [33].

4.3 Vacuum/Vapor Deposition

The vacuum deposition method is a more controllable approach to obtain high-quality perovskite films compared to the solution process (Fig. 7). It is most commonly used to investigate the effects of perovskite layer thickness on the PSC properties [5]. One of the main advantages of the vacuum process in the capability to layered films over large areas [34].

Liu et al. [34] demonstrated efficient planar $CH_3NH_3PbI_{3-x}Cl_x$ solar cells formed by dual-source evaporation of $PbCl_2$ and MAI salts. In the dual-source evaporation procedure, these precursors were heated in ceramic crucibles to about 325 and 120 °C, respectively, then deposited simultaneously, ratio 4:1, under high vacuum (10^{-5} mbar) onto compact TiO_2 layer deposited over FTO glass. The compact TiO_2 and the spiro-OMeTAD layers were solution processed, as traditionally used. The deposited perovskite film was extremely uniform with a thickness of about 330 nm and the PSC efficiency was up to 15.4%.

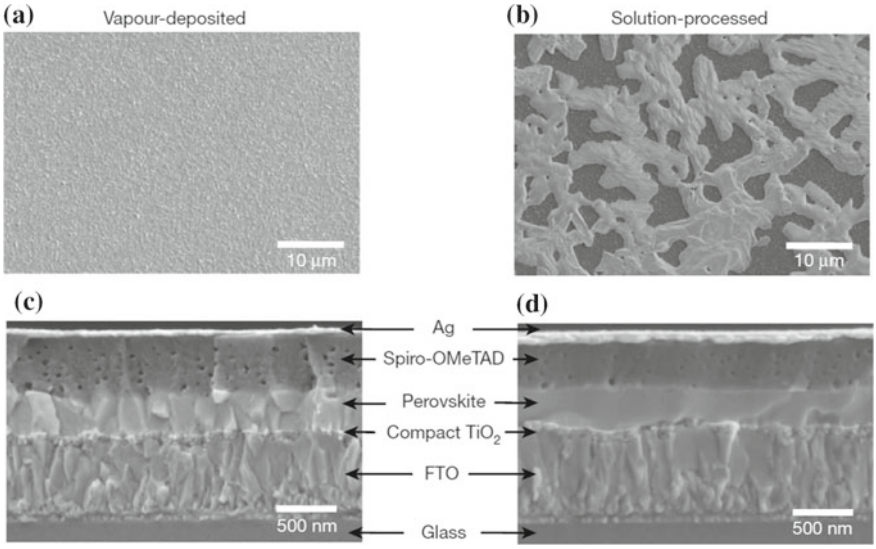

Fig. 7 SEM top views of a vapour-deposited perovskite film (**a**) and a solution-processed perovskite film (**b**). Cross-sectional SEM images of complete solar cells from a vapour-deposited (**c**) and solution-processed perovskite film (**d**). Adapted and reprinted by permission from Liu et al. [34]

5 Obstacles and Future Perspectives

Despite the progress in the efficiency of PSC, there are still many obstacles on their way towards popular commercialization and use. Among them, it is possible to highlight the low resistance to moisture, the low thermal stability, and the toxicity of lead [35].

The perovskites are organic-inorganic salts that easily absorbs water [36]. Light exposure can break weak bonds in the perovskite layer and in the other contact layers, generating halogen vacancy—halogen interstitial pairs that enable halogen migration [37] or, convert available oxygen into highly reactive superoxide [38]. The perovskite methylammonium lead iodide, slowly decomposes at the high temperatures that solar panels endure (65–85 °C) [39]. Also, perovskites react with many metals since heat volatilizes the halide species and light enhances halogen mobility [40]. Another difficulty presented by PSC is the thermal expansion coefficient of perovskites, that is about 10 times higher than that of the glass substrates or the TCO layer. Stress can build up during temperature changes causing breakage and possibly accelerate perovskite decomposition [41].

The lead toxicity drawback is starting to be tackled by using Sn perovskites, although they are instable at ambient condition. Doping strategies were evaluated to improve Sn-perovskite stability, but the efficiency of these devices is low. The same occurs to germanium perovskites. Sn-Ge and Pb-Sn perovskites have shown promising results on performance and stability. Bi and Sb perovskites show promising

stability against humidity, heat, and continuous light exposure but the efficiency of these devices is also limited [35].

To increase the thermal stability of PSC, a strategy to improve the chemical interaction between organic cations and the inorganic part must be developed. Recently, Gong et al. [42] reported high chemical stability of $MAPbI_3$ by doping it with selenium ions.

Because of it increasing performance and relatively low-cost, the PSC are the best alternative so far for solar cell applications, but in view of their drawbacks, new materials and synthesis methods need to be developed to overcome these difficulties.

References

1. Noh MFM et al (2018) The architecture of the electron transport layer for a perovskite solar cell. J Mater Chem C 6:682. https://doi.org/10.1039/c7tc04649a
2. Jena AK et al (2019) Halide perovskite photovoltaics: background, status, and future prospects. Chem Rev 119:3036–3103. https://doi.org/10.1021/acs.chemrev.8b00539
3. Yang X et al (2018) Progress in hole-transporting materials for perovskite solar cells. J Energy Chem 26:650–672. https://doi.org/10.1016/j.jechem.2017.12.017
4. Shi Z et al (2018) Perovkites-based solar cells: a review of recent progress, materials and processing methods. Materials 11:729. https://doi.org/10.3390/ma11050729
5. Cui J et al (2015) Recent progress in efficient hybrid lead halide perovskite solar cells. Sci Technol Adv Mater 16:036004. https://doi.org/10.1088/1468-6996/16/3/036004
6. Noh JH et al (2013) Chemical management for colorful, efficient, and stable inorganic-organic hybrid nanostructured solar cells. Nano Lett 13:1764–1769. https://doi.org/10.1021/nl400349b
7. Wang, J.T-W., et al.. Low-temperature processed electron collection layers of graphene/TiO_2 nanocomposites in thin film perovskite solar cells. Nano Lett 14:724–730. https://doi.org/10.1021/nl403997a
8. Song T-B et al (2015) Perovskite solar cells: film formation and properties. J Mater Chem A 3:9032. https://doi.org/10.1039/C4TA05246C
9. Bi D et al (2016) Polymer-templated nucleation and crystal growth of perovskite films for solar cells with efficiency greater than 21%. Nat Energy 1:16142. https://doi.org/10.1038/nenergy.2016.142
10. Jung HS et al (2015) Perovskite solar cells: from materials to devices. Small 11(1):10. https://doi.org/10.1002/smll.201402767
11. Seok H-J et al (2019) Study of sputtered ITO films on flexible invar metal foils for curved perovskite solar cells. Metals 9:120. https://doi.org/10.3390/met9020120
12. Castro-Hermosa S et al (2017) Perovskite solar cells on paper and the role of substrates and electrodes on performance. IEEE Electron Device Lett 38:9. https://doi.org/10.1109/LED.2017.2735178
13. Li Y et al (2019) Optically transparent wood substrate for perovskite solar cells. ACS Sustain Chem Eng 7:6061–6067. https://doi.org/10.1021/acssuschemeng.8b06248
14. Maçaira J et al (2013) Review on nanostructured photoelectrodes for next generation dye-sensitized solar cells. Renew Sustain Energy Rev 27:334–349. https://doi.org/10.1016/j.rser.2013.07.011
15. Ye M et al (2015) Recent advances in dye-sensitized solar cells: from photoanodes, sensitizers and electrolytes to counter electrodes. Mater Today 18:155–162. https://doi.org/10.1016/j.mattod.2014.09.001
16. Docampo P et al (2013) Efficient organometal trihalide perovskite planar-heterojunction solar cells on flexible polymer substrates. Nat Commun 4:1–6. https://doi.org/10.1038/ncomms3761

17. Matthews, P. D., et al.. Updating the road map to metal-halide perovskites for photovoltaics. J Mater Chem A 17135–17150. https://doi.org/10.1039/c7ta04544a
18. Stranks SD et al (2015) Formation of thin films of organic-inorganic perovskites for high-efficiency solar cells. Angew Chem Int Ed 54:3240. https://doi.org/10.1002/anie.201410214
19. Hong S et al (2015) A facile and low-cost fabrication of TiO_2 compact layer for efficient perovskite solar cells. Curr Appl Phys 15:574–579. https://doi.org/10.1016/j.cap.2015.01.028
20. Ma S et al (2015) Spiro-thiophene derivatives as hole-transport materials for perovskite solar cells. J Mater Chem A 3:12139. https://doi.org/10.1039/C5TA01155H
21. Acik M et al (2016) Graphene in perovskite solar cells: device design, characterization and implementation. J Mater Chem A 4:6185–6235. https://doi.org/10.1039/C5TA09911K
22. Zhang, x., et al.. Graphene oxide as an additive to improve perovskite film crystallization and morphology for high-efficiency solar cells. RSC Adv 8:987–993. https://doi.org/10.1039/c7ra12049d
23. Milić, J. V., et al.. Reduced graphene oxide as a stabilizing agent in perovskite solar cells. Adv Mater Interfaces 5(22):1800416. https://doi.org/10.1002/admi.201800416
24. Liu X et al (2018) Novel efficient C60-based inverted perovskite solar cells with negligible hysteresis. Electrochim Acta 288:115–125. https://doi.org/10.1016/j.electacta.2018.09.004
25. Kim Y et al (2018) Sequentially fluorinated PTAA polymers for enhancing V_{OC} of high-performance perovskite solar cells. Adv Energy Mater 8(29):1801668. https://doi.org/10.1002/aenm.201801668
26. Hu L et al (2018) PEDOT:PSS monolayers to enhance the hole extraction and stability of perovskite solar cells. J Mater Chem A 6:16583–16589. https://doi.org/10.1039/C8TA05234D
27. Tang J et al (2018) High-performance inverted planar perovskite solar cells based on efficient hole-transporting layers from well-crystalline NiO nanocrystals. Sol Energy 161:100–108. https://doi.org/10.1016/j.solener.2017.12.045
28. Arora N et al (2017) Perovskite solar cells with CuSCN hole extraction layers yield stabilized efficiencies greater than 20%. Science 358(6364):768–771. https://doi.org/10.1126/science.aam5655
29. Zhang H et al (2017) $CuGaO_2$: a promising inorganic hole-transporting material for highly efficient and stable perovskite solar cells. Adv Mater 29(8):1604984. https://doi.org/10.1002/adma.201604984
30. Jeong-Hyeok I et al (2014) Morphology-photovoltaic property correlation in perovskite solar cells: one-step versus two-step deposition of $CH_3NH_3PbI_3$. APL Mater 2:081510. https://doi.org/10.1063/1.4891275
31. Liang K et al (1998) Synthesis and characterization of organic-inorganic perovskite thin films prepared using a versatile two-step dipping technique. Chem Mater 10:403–411. https://doi.org/10.1021/cm970568f
32. Burschka J et al (2013) Sequential deposition as route to high-performance perovskite-sensitized solar cells. Nature 499(7458):316–319. https://doi.org/10.1038/nature12340
33. Kim H-S et al (2012) Lead iodide perovskite sensitized all-solid-state submicron thin film mesoscopic solar cell with efficiency exceeding 9%. Sci Rep 2:591. https://doi.org/10.1038/srep00591
34. Liu M et al (2013) Efficient planar heterojunction perovskite solar cells by vapour deposition. Nature 501:395–398. https://doi.org/10.1038/nature12509
35. Huang J et al (2017) Understanding the physical properties of hybrid perovskites for photovoltaic applications. Nat Rev Mat 2(17042):1–19. https://doi.org/10.1038/natrevmats.2017.42
36. Leguy AMA et al (2015) Reversible hydration of $CH_3NH_3PbI_3$ in films, single crystals, and solar cells. Chem Mater 27:3397–3407. https://doi.org/10.1021/acs.chemmater.5b00660
37. Kim GY et al (2018) Large tunable photoeffect on ion conduction in halide perovskites and implications for photodecomposition. Nat Mater 17:445–449. https://doi.org/10.1038/s41563-018-0038-0
38. Aristidou N et al (2017) Fast oxygen diffusion and iodide defects mediate oxygen-induced degradation of perovskite solar cells. Nat Commun 8:15218. https://doi.org/10.1038/ncomms15218

39. Conings B et al (2015) Intrinsic thermal instability of methylammonium lead trihalide perovskite. Adv Energy Mater 5:1500477. https://doi.org/10.1002/aenm.201500477
40. Boyd CC et al (2018) Barrier design to prevent metal-induced degradation and improve thermal stability in perovskite solar cells. ACS Energy Lett 3:1772–1778. https://doi.org/10.1021/acsenergylett.8b00926
41. Rolston N et al (2018) Engineering stress in perovskite solar cells to improve stability. Adv Energy Mater 8:1802139. https://doi.org/10.1002/aenm.201802139
42. Gong J et al (2018) Divalent anionic doping in perovskite solar cells for enhanced chemical stability. Adv Mater 30:1800973. https://doi.org/10.1002/adma.201800973

Rare-Earth Doped Forsterite: Anti-reflection Coating with Upconversion Properties as Solar Capture Solution

Rúbia Young Sun Zampiva

Abstract Solar energy is a renewable power source that is harnessable nearly everywhere in the world. The investments in solar devices increase each year. Silicon is the dominant material in the production of commercial solar cells. More than 80% of world production is based on monocrystalline and polycrystalline silicon. Efficiency record commercial silicon solar panels convert about 25% of the sunlight into energy while the vast majority of conventional panels convert between 15 and 16%. The main factors of energy loss are the loss by light reflection on the cell surface and the loss by the energy emitted in the ultraviolet (UV) and infrared (IR) ranges which is directly transmitted and converted to heat without being harnessed by the cell. To overcome these losses, usually anti-reflective materials are applied on solar devices. In this chapter, the use of forsterite (Mg_2SiO_4) as an anti-reflective coating (ARC) is explored. Besides the antireflection property, forsterite is easily doped with several rare-earths (REs). Some elements of these group are capable of upconverting energy from de IR to the visible (Vis) spectral range. The theory behind the upconversion (UC) phenomenon is also presented here. Studies indicate that the use of forsterite ARC doped with UC REs on commercial silicon solar cells might be a low-cost solution to increase the efficiency of commercial devices.

Keywords Anti-reflexive coatings · Forsterite · Rare-earths · Solar energy · Upconversion

Abbreviations

ARC	Anti-reflective Coating
CR	Cross-Relaxation
CUP	Cooperative Upconversion
ESA	Excited State Absorption
ETU	Energy Transfer Upconversion

R. Y. S. Zampiva (✉)
Universidade Federal do Rio Grande do Sul, Porto Alegre, Brazil
e-mail: rubiayoungsun@gmail.com

A. Kopp Alves (ed.), *Nanomaterials for Eco-friendly Applications*,
Engineering Materials, https://doi.org/10.1007/978-3-030-26810-7_7

GSA	Ground State Absorption
IR	Infrared
IUPAC	International Union of Pure and Applied Chemistry
J	Angular Orbital Momentum
NIR	Near-infrared
NREL	National Renewable Energy Laboratory
PA	Photons Avalanche
PV	Photovoltaic
RE	Rare-earth
UC	Upconversion
UV	Ultraviolet
Vis	Visible

1 Introduction

Solar energy is a clean, inexpensive, renewable power source that is harnessable nearly everywhere in the world. Any point where sunlight hits the surface of the earth is a potential location to generate solar power, and since solar energy comes from the sun, it represents a limitless source of power. Solar energy can contribute to reduced dependence on energy imports. As it entails no fuel price risk or constraints, it also improves the security of supply. Solar power enhances energy diversity and hedges against price volatility of fossil fuels, thus stabilizing the costs of electricity generation in the long term [1].

Solar photovoltaic (PV) entails no greenhouse gas emissions during operation and does not emit other pollutants (such as oxides of sulfur and nitrogen); additionally, it consumes no or little water. As local air pollution and extensive use of fresh water for cooling of thermal power plants are becoming severe concerns in hot or dry regions, these benefits of solar PV become increasingly important [2].

Solar PV was the top source of new power generating capacity in 2017, primarily due to strong growth in China, with more solar PV installed globally than the net additions of fossil fuels and nuclear power combined. Global capacity increased nearly one-third, to approximately 402 GWdc. Although solar PV capacity is concentrated in a short list of countries, by year's end every continent had installed at least 1 GW of capacity, and at least 29 countries had 1 GW or more. Solar PV is playing an increasingly important role in electricity generation, accounting for over 10% of generation in Honduras in 2017 and for significant shares in Italy, Greece, Germany and Japan [3].

Silicon is the dominant material in the production of commercial solar cells. More than 80% of world production is based on monocrystalline and polycrystalline silicon [4]. According to data provided in 2016 by US National Renewable Energy Laboratory (NREL), commercial silicon solar panels, with a record of efficiency,

convert about 25% of light (AM1.5 global spectrum, 1000 W/m^2 at 25 °C) while the vast majority of the panels convert between 15 and 16% [5].

The solar cells energy efficiency is affected by several factors such as recombination and bad contacts [6, 7] that occur at the solar device interfaces. Among these factors, the most relevant is the light capture conditions. The pure silicon in solar cells presents losses by surface reflection ranging from 31 to 51% between 1.1 and 0.40 μm respectively [8, 9]. A high amount of energy is lost by UV and IR solar emission that is transmitted directly without being harnessed by the cell [10] and also generating heat, which increases the losses due to thermalization process. Despite all technological innovation in the last years, there is still a lot to develop to solar cell devices reach their full potential [4, 11].

To overcome these losses different materials such as ARCs are used. The ARC can increase the efficiency of solar collection and therefore increase the efficiency of converting solar energy into electricity. As solar radiation occurs in a wide range of the spectrum, the ARCs for solar applications need to be effective over the entire solar spectrum that covers wavelengths from UV to IR [12, 13].

In this sense, forsterite (Mg_2SiO_4) appears as fascinating material for application as an ARC. Its refractive index (~1.6) allows the forsterite to be applied in different configurations of coatings composed of layers [14]. Also, forsterite is an excellent host for REs atoms due to the two non-equivalent crystallographic positions for the cations in the crystalline structure. Both sites can be replaced by various REs and other ions [15–18].

Some of the REs atoms present the photons UC property. In this process in which the sequential absorption of two or more photons leads to light emission at a shorter wavelength than the excitation wavelength [19]. An example is a conversion from IR to Vis range [20–23]. The application of UC REs doped hosts as solar cells coatings could allow the utilization of IR solar emission by the device.

Since this coating is extra the cell, the introduction of this system into commercial solar devices would not lead to significant changes in the industrial production line. Although the proposal is interesting, the number of scientific groups working in this line of research is small. There is still a long path to prove the efficiency and advantages of using ARC/UC systems. In this chapter, the theory behind the UC activity, as well as the most influence on this system will be discussed. In addition, works developed in this area, using forsterite as host, will be presented.

1.1 Forsterite (Mg_2SiO_4)

Forsterite is a ternary oxide that belongs to the olivine mineral group. Its empirical formula is Mg_2SiO_4, formed by the SiO_4^{4-} anion and the Mg^{2+} cation in a 1:2 molar ratio. Silicon is the central atom in the SiO_4^{4-} anion. Each oxygen atom is connected to the silicon by a covalent bond which causes a partial negative charge in the oxygen atoms. Therefore, the oxygen atoms must be distant from each other to reduce the repulsive forces between them. The best geometry to reduce repulsion is

the tetrahedral plane. The cations occupy two different octahedral sites indicated as M1 and M2 (Fig. 1) and form ionic bonds with the silicate anions. M1 and M2 are slightly different; the M2 site is larger and more regular than M1. Forsterite presents a dense packaging, and its crystallization occurs in an orthorhombic dipyramidal system (Pbnm space group) with cell parameters of 4.75 Å (0.475 nm), b 10.20 Å (1.020 nm) and c 5.98 Å (0.598 nm) [24–26].

The Mg atoms present in the forsterite structure can be replaced by a variety of transition metals due to the large M1 and M2 non-equivalent sites. For this reason, although forsterite is the main constituent of the earth's mantle, it is never found purely. Usually, fayalite (Fe_2SiO_4) is also found in the composition. Since it is too hard to find pure forsterite in nature, synthetic routes are required to produce high-quality material for technological application [15]. The presence of additional ions affects the electrical, mechanical and optical properties of the crystal [27–29].

1.1.1 Forsterite Physical and Chemical Properties

Mg_2SiO_4 exhibits high refractoriness with a melting point of 1890 °C. It is a good insulator with a thermal conductivity of 3.8 W/m °C. Forsterite is stable chemically, even at high temperatures [16, 30, 31]; therefore, it is applied as a coating for industrial furnaces. It presents hardness 7 on the Mohs scale and has a density of 3.28 g/cm^3. Recent studies have shown that forsterite is a biocompatible material, presenting an excellent ability to form apatite, in vivo biocompatibility and degradability. Due to these characteristics and the high mechanical properties (fracture strength, KIC = 2.4 MPa.m-1/2), when compared to the hydroxyapatite ceramics (0.6–1.0 MPa.m-1/2), forsterite has been used to produce nanocomposites to improve the mechanical strength of prostheses and bones [32].

Mg_2SiO_4 exhibits low dielectric constant ($\varepsilon r = 6.8$), high dielectric strength (250 V/mm) and electrical resistivity (>1 E14 ohms-cm) in addition to a high-quality factor (Q factor) (~241,500 GHz) [15]; making forsterite an ideal substrate for electronics.

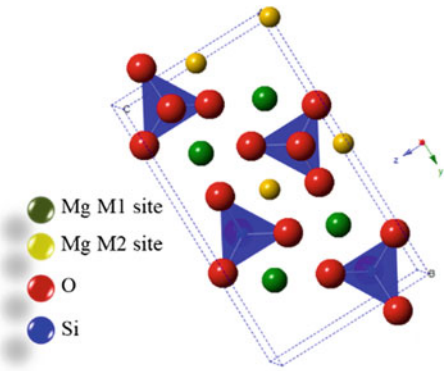

Fig. 1 Structure of the forsterite orthorhombic unitary cell (Mg_2SiO_4). Magnesium occupies the M1 and M2 sites, while silicon is in the center of the tetrahedra formed by oxygens forming the asymmetric unity

Studies about the increase of solar cells efficiency showed that thin films of MgO, SiO_2 and Mg_2SiO_4 alloys deposited on the glass and silicon surface presented a high mechanical resistance and high adhesion. These were not removed in tests with adhesive tape and steel needle scratch. According to transmittance and light reflectance analyzes for these films, a 10% reflection region covers a wavelength range of 0.47–0.9 μm. These films are transparent in the sensitivity range of solar cells and can be used as ARCs [33].

Although forsterite crystals have been utilized in several fields of science and technology, this mineral is currently getting more attention due to the properties showed when doped. Forsterite is an interesting host for photoluminescent phosphors1 since the crystal presents easily replaceable active sites and an elevated structural chemical and physical stability [29, 34].

The characteristics of these crystals emission depend very much on the type of doping agent. Each ion has its specific energy states and will provide energy for the emission of specific wavelengths. Each type of ion that is introduced in the structure presents a different application. The range of possibilities is immense: luminescent phosphors, tunable lasers, femtosecond pulsed lasers, optical transmission, biochemical tests, clinical diagnostics, solar energy applications, among others [27, 29, 34–36].

1.2 Phosphors

A luminescent material, also called phosphor, is a solid that converts energy (e.g., electromagnetic radiation, electron beam energy, mechanical energy, chemical reaction energy) into electromagnetic radiation in the Vis region [37]. Phosphors are usually transition metals or REs of various types. A material can emit light through incandescence when all atoms radiate energy, or by luminescence, when only a fraction of atoms, called emitting centers or luminescent centers, emit light. In inorganic phosphors, these heterogeneities in the crystalline structure are generally created by the addition of dopants, impurities called "activators". The wavelength emitted by the emission center is dependent on the atom, and the crystalline structure that surrounds it.

The scintillation process (light emission) in inorganic crystalline systems is a result of the electronic band structure found in these crystals (Fig. 2). The entrance of a particle in the crystal can excite an electron from the valence band to the conduction band or the exciton band (located just below the conduction band and separated from the valence band by an energy gap). This action leaves a hole associated back in the valence band. The dopants in the crystal create electronic levels in the forbidden band. The excitons have weaker bonds in the electron-gap pair and wander through the crystalline system until activation centers fully capture them. Once captured, they quickly relax, emitting scintillating light (fast component).

The holes associated with electrons in the conduction band do not participate in this process. These are captured successively by the centers of impurities by exciting

certain metastable levels that are not accessible to excitons. The delay in relaxation of these metastable levels of impurities, retarded by the low probability of forbidden transitions, again results in light emission (slow component).

Luminescent materials play a significant role in many technologic fields, being extremely useful in areas such as optical devices, biomedicine, and solar energy. Therefore, there is a great interest in the development and characterization of new luminescent materials that present new photophysical effects [35, 38, 39].

Most luminescent materials (e.g., organic dyes and quantum dots) exhibit luminescent emission with Stokes shift, i.e., the emission spectrum is always located at longer wavelengths compared to the absorption spectrum. It means that the energy of the excitation photon is higher than that of the emission photon. In some particular cases, the energy of the excitation photon is smaller (longer wavelength) than the energy of the emission photon, called emission with anti-Stokes shift (Fig. 3).

The anti-Stokes emission can occur in three ways: simultaneous absorption of two photons, second harmonic generation, and UC. Of these, the UC process is the most

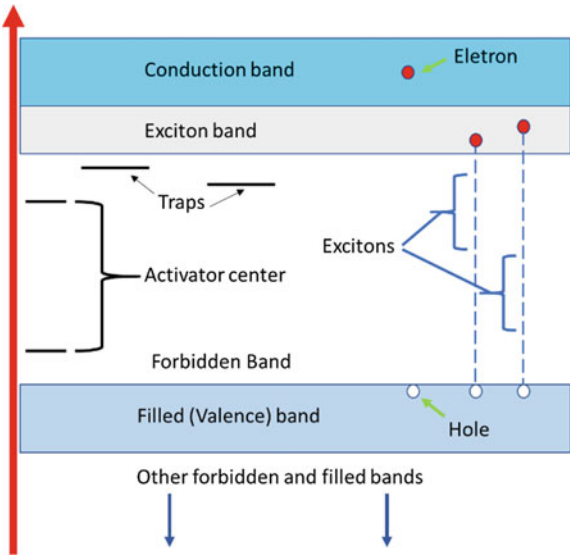

Fig. 2 Activity in the crystal/dopant band structure

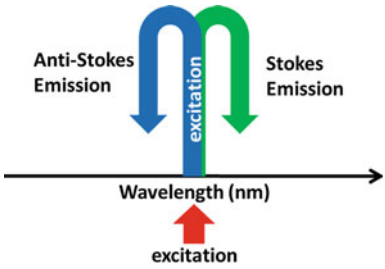

Fig. 3 Representation of the Stokes and Anti-Stokes effect. The emission at shorter wavelengths (with higher energy) than the excitation, is called emission Anti-stokes. The emission at longer wavelengths (lower energy) than the excitation, is called Stokes emission

efficient. However, a source of high intensity should be used in a continuous or pulsed way [40, 41]. UC can be obtained from low energy excitation via lanthanide ions such as Ln^{3+} or by the so-called triplet-triplet annihilation process. The crystalline systems doped with some lanthanides have unique UC luminescence properties, including high anti-Stokes shifts, narrow emission lines, high luminescence lifetime (~ms) and high photostability [41]. In the late 1990s, the field of nanoparticles for UC has widely expanded and has become one of the most active areas of research within nanoscience.

1.2.1 Upconversion (UC) Phenomenon

The upconversion UC phenomenon has been extensively studied in recent years, proving to be an effective method for the production of Vis light from IR radiation [23]. UC is a nonlinear optical process whereby the absorption of two or more photons, through intermediate long-life energy states, leads to the emission of radiation with higher energy than the absorbed, that is, it is an anti-Stokes mechanism [41].

The UC concept was initially conceived as a theoretical possibility by the physicist Nicolas Bloembergen in 1959 [42]. His idea was to develop an IR phonon detector using super excitation to count the IR phonons through the interaction of these with ions of REs and transition metals inserted as impurities in crystalline materials. In this way, the IR quantum wave was mainly counted through sequential absorptions at successive excited levels of the doping ion used. Although the idea of achieving phonon UC was promising, Bloembergen was not able to validate his idea due to the lack of coherent sources of pumping at that time. Nonetheless, because of his pioneering work in the field of nonlinear optics, Bloembergen was awarded a Nobel Prize in physics in 1981. With the advances on the laser field, around the 1960s, various research groups started to explore the UC optical signals of inorganic solids.

Although from the 1960s until now, several significant advances have been reached, the application of UC materials in the biomedicine and energy fields remains not well defined [43]. One of the principal challenges is to develop methods to produce materials with adjustable size and shape, in addition to desirable properties such as biocompatibility [44, 45], nontoxicity, chemical stability, high resistance to pH variations, as well as mechanical properties related to applications in energy conversion devices [41].

There are several mechanisms by which the UC process may occur, all of which are related to the sequential absorption of at least two photons and can occur isolated or combined [46]. These mechanisms are described below.

Excited state absorption (ESA)

ESA is a mechanism characterized by the absorption of at least two photons by a single ion and is the only UC process that occurs when the dopant concentration is low [47]. Figure 4 presents a schematic of the ESA mechanism. If the resonance conditions are met, there is the absorption of the first photon, which leads to the

promotion of the ion, which is in the ground state, E0, to the first excited state, E1. This transition is called ground state absorption (GSA). This meta-stable state is of long duration, which allows the absorption of the second photon and, consequently, the promotion of the ion to a more excited state, E2. This transition is called ESA. The UC emission results from the relaxation of the excited ion to the ground state [46, 48].

Energy Transfer UC (ETU)

The ETU mechanism is similar to ESA. Both processes resort to the successive absorption of two photons to fill the highest metastable excited state, E2. Figure 5 shows a schematic of the ETU activity. The main difference between the two mechanisms is that ETU involves the transfer of non-radiative energy between two neighboring ions. Initially, since the two ions are in the ground state, E0, each of them can absorb a photon and, therefore, be promoted to the first meta-stable excited state, E1, through GSA. One of the ions, the activator (ion II), can be excited to the metastable state E2, after the transfer of non-radiative energy from the neighboring ion, the sensitizer (ion I), which, therefore, returns to the ground state [46, 47]. The energy transfer between ions occurs before the sensitizer relaxes radiatively if the difference of energy between the sensitizer E0 and E1 states is resonant with the transition from the E1 state to the E2 state in the activator.

If there is a small energy difference between the transition pairs, from the same ion or different elements, the energy transfer must be assisted by phonons to obtain the optimal resonance conditions. The energy transfer is performed through dipole-dipole interactions (Coulombic mechanism, also known as resonant energy transfer) as a consequence of the electrostatic overlap between the electronic system of two ions [49]. The distance between the ions is determined by their concentration and has an essential influence on the efficiency of non-radiative energy transfer and consequently on the ETU mechanism. This is one of the most efficient mechanisms, which makes it one of the most used in the design of UC materials [46].

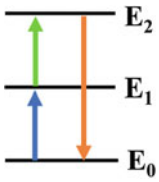

Fig. 4 Representation of the ESA mechanism

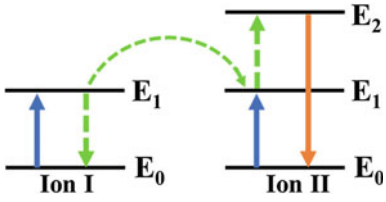

Fig. 5 Representation of the ETU mechanism

Cooperative UC (CUP)

CUP is a process that involves the interaction between three ions. As represented in Fig. 6, two of these ions (I and III) act as sensitizers in the UC process. The ions I and III are promoted to the first excited state, E1, via GSA. These two sensitizing ions interact simultaneously with the ion II (activator) promoting it to the excited state E2. The emission of the up-conversion photon is achieved due to the relaxation of ion II from the excited state E2 to the ground state [19, 47].

Photons avalanche (PA)

This mechanism starts with the promotion of ion II from the ground state to the excited state E1, and from that state to the excited state E2 through ESA, as represented in Fig. 7. At this point, the ion at the E2 interacts with a neighboring ion (ion I), which is in the ground state, and as a result of an efficient energy transfer, the two ions occupy the E1 state and can subsequently be excited to the E2 state by ESA. This process repeatedly occurs, exponentially increasing the ion population in the E2 excited state and producing a strong UC emission [47]. In this mechanism, the ion concentration must be high enough that the ion-ion interactions result in an efficient energy transfer, which allows the filling of the metastable state and the induction of ESA. The PA mechanism is responsible for the optical activity of solid-state lasers.

Cross-Relaxation (CR)

Cross-relaxation (also called self-quenching) occurs between two identical ions when the first ion initially in an excited state transfer energy to a second ion that was initially in the ground state. This energy transfer results in both ions simultaneously reaching excited states with intermediary energy when compared to the two initial states. The

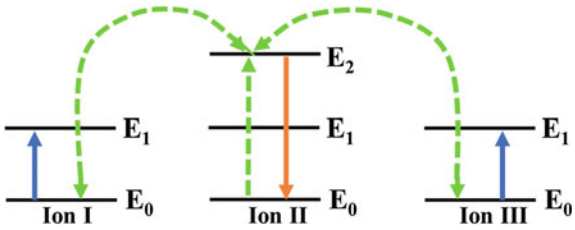

Fig. 6 Representation of the CUP mechanism

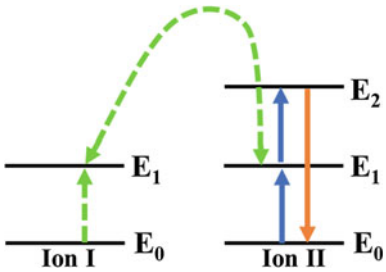

Fig. 7 Representation of the PA mechanism

energy drop of the first ion is equal to the energy increase of the second ion, thus conserving energy in the CR. The two ions intermediate states have the same energy and are energetically half the path between the initial excited state of the first ion and the ground state of the second ion [50].

The diagram in Fig. 8 shows two sets of energy states for two identical ions and the transformations of their current states under CR.

1.3 Rare-Earths (REs)

According to the IUPAC classification, the REs form a relatively abundant group of 17 chemical elements, of which 15 belong to the lanthanide group (elements with an atomic number between $Z = 57$ and $Z = 71$, i.e., from lanthanum to lutetium) in the periodic table. Scandium ($Z = 21$) and yttrium ($Z = 39$) are also part of this group since they are found in the same ores and present similar physicochemical properties. The primary economic sources of REs are the monazite, bastnaesite, xenotime, loparite minerals and the lateritic clays that absorb ions [51].

The electronic configuration of the REs elements is indicated in Table 1. Only scandium (Sc) and yttrium (Y) do not derive from the xenon noble gas configuration (Xe). All other elements have the basic configuration of xenon followed by the sequential filling of layer 4f. One of the most interesting feature of the REs elements is that, except for Sc, Y, La, Yb, and Lu elements, all present an incomplete 4f layer. This layer is internal, covered by layers 6s and 5d.

Additionally, the 5p and 5s orbitals are more external than the 4f since they have a greater radial extent. The layers that participate in element bindings are the outer layers 5d and 6 s. In this way, the 4f layer, although incomplete, is shielded by the outer ones [52].

The Yb and Lu elements are the only ones that present a complete 4f layer. In Sc, Y and La, the partially filled orbitals are respectively 3d, 4d and 5d which are internal to the layers $4s^2$, $5s^2$ and $6s^2$. In general, all lanthanides may present the 3+ oxidation state. However, some of these elements also appear in 2+ and 4+ states. The filled outer layers make the REs very similar chemically. The differences show up in the physical properties, as, for example, in the crystalline structures formed by a single element, in the magnetic properties coming from the mismatching of electrons in

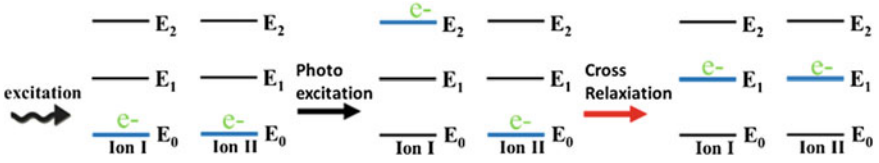

Fig. 8 Representation of the CR mechanism

Table 1 Electronic configuration of the REs elements

Element	Configuration
Sc (21)	$[Ar]3d^1 4s^2$
Y (39)	$[Kr]4d^1 5s^2$
La (57)	$[Xe]5d^1 6s^2$
Ce (58)	$[Xe]4f^1 5d^1 6s^2$
Sc (21)	$[Ar]3d^1 4s^2$
Y (39)	$[Kr]4d^1 5s^2$
La (57)	$[Xe]5d^1 6s^2$
Ce (58)	$[Xe]4f^1 5d^1 6s^2$
Pr (59)	$[Xe]4f^3 6s^2$
Nd (60)	$[Xe]4f^4 6s^2$
Pm (61)	$[Xe]4f^5 6s^2$
Sm (62)	$[Xe]4f^6 6s^2$
Eu (63)	$[Xe]4f^7 6s^2$
Gd (64)	$[Xe]4f^7 5d^1 6s^2$
Tb (65)	$[Xe]4f^9 6s^2$
Dy (66)	$[Xe]4f^{10} 6s^2$
Ho (67)	$[Xe]4f^{11} 6s^2$
Er (68)	$[Xe]4f^{12} 6s^2$
Tm (69)	$[Xe]4f^{13} 6s^2$
Yb (70)	$[Xe]4f^{14} 6s^2$
Lu (71)	$[Xe]4f^{14} d^1 6s^2$

The brackets indicate the electronic distribution of the correspondent noble gas

the 4f layer and mainly in the optical properties, which will be discussed in the next section [52].

1.3.1 REs^{3+} Optical Properties

As previously mentioned, the electrons in the REs 4f layer are strongly shielded by the electrons of the outer layers 5s and 5p. Due to this shielding, the REs are not significantly influenced by the structure present in the crystalline hosts or amorphous materials in which they are inserted. These ions are capable of keeping the atomic energy states in different chemical environments. Also, REs have a large number of energy levels that can provide emissions from IR to UV, with many in the Vis region. The absorption and emission bands of REs ions vary depending on the host and the interaction between the dopant and the host [53].

REs^{3+} transitions are often attributed to the electric dipole mechanism. To explain the experimental observation of electronic transitions between 4f states, Judd [54]

and Ofelt [55] working independently, concluded that the transitions in the REs are originated from a mixture of states from the 4f and 5d configurations. From this mixture emerges the concept of forced electric dipole transition and the transitions can be explained both qualitatively and quantitatively. This theory is known as the Judd-Ofelt theory [54]. In this chapter, it will not be necessary to study this theory deeply. Instead, the spectroscopic properties of these ions can be well described and understood by looking at what happens in the optical absorption and emission of these ions.

Absorption: Lanthanide ions absorb radiation in defined and very narrow bands (transitions f-f). According to the selection rules of the atomic spectrum, the f-f transitions of isolated lanthanide ions are prohibited. This rule states that in a centrosymmetric molecule or ion, the only permissible transitions are those accompanied by the parity exchange [49], for example, the f-d transition. Remember that the secondary quantum numbers p and f are odd and s and d are even. Thus, if the symmetry of the ion is removed with an external anti-symmetric field and with the blending of some different parity state, transitions such as, e.g. f-f, become allowed. The shielding of the electrons in the 4f orbital also indicates that the absorption spectrum of the lanthanide ions is weakly disturbed after the insertion of these ions into inorganic crystalline systems.

Luminescence: The REs emissions arise from radiative transitions between levels of the 4f electronic configurations. In the absence of any interaction between the electrons, the levels would degenerate. However, due to Coulomb interactions, the degeneracy is inhibited and the energy levels separated, reaching values close to 20,000 cm^{-1}. There are still some other interactions that can be taken into account, as is the case of spin-orbit interactions that can lead to separations in the order of 1000 cm^{-1}. The relatively large values of the spin-orbit coupling constants cause the angular orbital momentum (J) levels to be quite separated. Thus, approximately, each trivalent lanthanide ion is characterized by a ground state, with a single value of J, and by a first excited state in a kT energy many times above the ground state. Therefore, the first excited state is essentially electron depopulated, except at very high temperatures. However, the Sm^{3+} and Eu^{3+} ions are two exceptions: their first excited state is situated sufficiently close to the ground state, so they are populated by electrons still at room temperature [56].

As already mentioned, one of the ways to obtain UC luminescence is through the use of REs ions. For n electrons, in 14 available orbitals, there are 14/n possible configurations, and all configurations can have different energies, giving rise to a structure rich in energy levels in the NIR-Vis-UV regions. The emission of the lanthanides, unlike other emission processes, is not sensitive to quenching caused by oxygen, since the 4f electrons are protected by the layers 5s and 5p. In this way, they are not easily affected by the surroundings. Usually, the electronic transitions of Ln^{3+} ions are internal transitions in the 4f-4f (forbidden parity) and 4f-5d levels. As a result of the forbidden character of the f-f transitions, low absorption coefficients and long luminescence lifetimes are obtained, ranging from microseconds to several milliseconds [57].

Activators and Sensitizers

It is necessary to dope the host material with luminescent centers, called activators, to produce UC emission. Except for La^{3+}, Ce^{3+}, Yb^{3+}, and Lu^{3+}, the Ln^{3+} ions can be used as activators in the UC process, since they have more than one energy level 4f excited. However, to achieve more efficient UC emissions, the energy difference between the excited state and the ground state must be low enough to facilitate the absorption of photons. The Ln^{3+} ions used as activators are Er^{3+}, Tm^{3+}, and Ho^{3+}, since they have energy levels arranged in a ladder form [58], as presented in Fig. 9 for these ions in the structure of GdVO4:Ln^{3+} [59].

The UC luminescence efficiency of lanthanide-doped materials is strongly affected by the 4f-4f transitions. The 4f-4f parity-forbidden transition leads to low absorption of excitation energy. To improve this absorption, one can increase the concentration of Ln^{3+} ions in the host. However, because of the distance decrease between ions, the probability of non-radiative relaxation increases. Therefore, the range of activator concentrations that can be used is limited. Another way to increase the efficiency of the UC processes is the use of ETU mechanisms. The addition of a sensitizer ion, which has a higher absorption cross-section and which is capable of efficiently transfer the absorbed energy to the activator ion, can significantly increase the UC efficiency of lanthanide-doped materials [19].

The lanthanide ion Yb^{3+} has a single energy level 4f excited, as can be seen in Fig. 9. The electron transition energy between the ground state and the excited state of Yb^{3+} (2F7/2 → 2F5/2) is resonant with the radiation at 980 nm, and the absorption band of this transition has a higher absorption cross-section than other Ln^{3+} ions. In addition, the transition of the Yb^{3+} ion is resonant with many of the typical UC f-f transitions of Er^{3+}, Tm^{3+}, Ho^{3+} ions, facilitating the energy transfer between ions. These characteristics make the Yb^{3+} ion widely used as a sensitizer in UC materials. When the sensitizer-activator system is used, the concentration of the

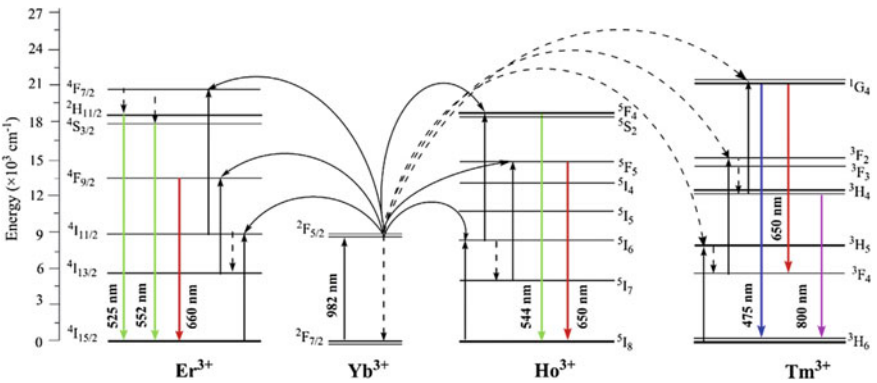

Fig. 9 Schematic energy level diagrams of Yb^{3+}, Er^{3+}, Ho^{3+} and Tm^{3+} and proposed UC mechanisms in the $GdVO_4$:Ln^{3+} nanorods. Reproduced from Gavrilović et al. [59], with permission from Elsevier

sensitizer ion (~20% molar) should be higher than the activator concentration (<2% molar) to avoid energy losses through cross relaxation [47].

1.4 Crystalline Hosts for Optical Applications

The 4f shielding in the REs also has effects on the emission lines of these ions, since it prevents the electrons of the 4f sublayer from undergoing strong influence of the crystalline field. It reduces the disturbances of their energy levels resulting in discrete electronic transitions in the 4f layer. Thus, the emission lines of the REs ions are not significantly altered when inserted in different host structures. However, when the emission lines are measured experimentally, the result presented is related not only to one but to several atoms interacting with each other and with their neighborhood, leading to an enlargement of the measured lines. The line's width directly increases with the increasing of atoms interacting and the non-uniformity of the crystalline field in the host. As an example, REs ions when inserted into an amorphous host show larger line widths than when inserted into a crystal lattice. In the amorphous network, each ion undergoes a perturbation produced by the different neighborhood in the disorientated crystalline field. Amorphous materials generally present emission in wide bands in the spectrum.

On the other hand, crystalline hosts generate narrow lines. The higher the asymmetry of the crystalline structure, the higher the probability of emissions. The choice of host material depends on the application [60].

Due to the particular characteristics of the emission and non-radiative relaxation processes in solid state materials, it is necessary to carefully select the pre-cursors used (the active ions and the host material). In addition, the dopants and doping states characteristics also play a crucial influence on the optical performance of solid-state materials. The effectiveness of doping is mainly determined by the degree of correspondence between the ionic radius of the doping ion and the substituted cation in the host. The efficiency of the substitution is also strongly related to the conditions of materials production and processing. As an example; the precursor's properties, synthesis methods, process parameters, among others.

The doping efficiency is also related to the dopant valences and the substituted ion. The difference in the valence requires compensation of charge, which is performed with the creation of defects in the network, such as vacancies or interstitial defects. Occasionally, a high concentration of dopant with significant valence difference may result in a drastic restructuring of the crystalline or a structural change in the phase. There are also other requirements for the host material, such as, mechanical strength, chemical stability, manufacturing processability and among others, which must be taken into consideration during the matrix selection. All precursor materials and procedures involved should have a favorable cost-benefit, especially for large-scale production; otherwise, it is industrially not acceptable [60].

The properties of the host material and its interaction with the dopant ions have an essential influence on the absorption and emission process. The host structure

determines the distance between the dopant ions, their relative spatial position, coordination number and kind of anions that surround them. The host preferably should be spectroscopically transparent in the range where it is applied, avoiding interferences in the dopant activity [61]. Therefore, the choice of suitable host material is essential to obtain materials with the desired optical properties.

The host materials must have a dense crystalline network that combines with the doping ions to guarantee high levels of doping and, consequently, high efficiency of luminescence [62]. In this sense, the ions of the host material must have an ionic radius similar to the doping ions. The up and down conversion processes and the optical properties of the nanoparticles are also strongly influenced by the crystalline phase of the host material. The influence of the crystalline phase on the optical properties is related to the different crystalline fields around the Ln^{3+} ions. For example, when using NaYF4 as a host material, it is possible to obtain two different phases; cubic (α-NaYF4) or hexagonal (β-NaYF4). The UC efficiency of the green emission in the NaYF4:Yb^{3+}/Er^{3+} hexagonal phase is approximately ten times higher than that of the NaYF4: Yb^{3+}/Er^{3+} cubic phase. The β-NaYF4 crystals have low symmetry and, therefore, exert a less symmetrical crystalline field around the dopant ions. This asymmetry leads to an increase in the probability of occurrence of 4f-4f electronic transitions [46].

Crystals can be doped using different methodologies. Through the post-doping, the dopant insertion is performed after the crystal has already been synthesized. Among post-doping techniques, the most known are ion implantation and diffusion methods. Another way is to insert a dopant, as a precursor, before starting the crystal synthesis. In this way, the crystal might grow already doped. This method ensures a better distribution of the dopant through the crystal lattice [63].

1.4.1 Fosterite as Host for Luminescent Ions

The dopant element, by definition, is a substance inserted in a host as a trace of impurity (very low concentration) to alter the properties of the host. In the case of crystalline hosts, the dopant usually replaces the atoms in the crystalline lattice of the host.

The crystalline structure of the forsterite is fascinating due to the two non-equivalent crystallographic positions for the Mg: The mirrored symmetry M1 and the inverse symmetry M2 (Fig. 10) present in its orthorhombic structure. Both sites can be replaced by various transition metal ions, such as Mn^{2+}, Fe^{2+}, Co^{2+}, Ni^{2+}, and Cr^{3+}. The insertion of REs such as Eu^{3+} has been shown in recent studies [55]. The incorporation of these ions directly affects the electrical, mechanical and optical properties of the structure [27, 28, 55, 64].

The Mg^{2+} at an octahedral site has an ionic radius around 0.72 Å while the Er^{3+} at an octahedral site has an ionic radius around 0.89 Å. These values represent an 18% difference between the radius of these ions [65]. Ions with a radium difference of about 15% can freely substitute one another. Above 30% difference, it becomes

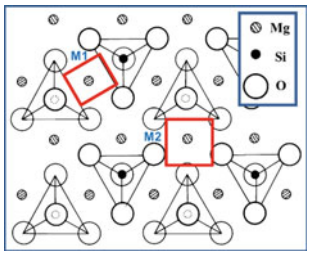

Fig. 10 Forsterite crystalline structure. Crystallographic positions of Mg: M1 site with mirror symmetry and M2 site with inverse symmetry

practically impossible to compete for the same site [66]. Thus, there are no significant difficulties for both Mg^{2+} and Er^{3+} ions to occupy the octahedral sites of forsterite.

Forsterite is composed of abundant elements in the Earth's crust, and although difficulties still exist for the pure phase production in nanoscale, large quantities of this mineral can be obtained by low-cost techniques. Due to its bio-compatibility, dielectric behavior, high physicochemical stability even in extreme conditions, such as high temperatures ($\geq$1800 °C) and pH, forsterite is attracting attention for its application in fields such as biomedicine, solar energy, and solid state lasers. Despite of the physical and chemical properties that it presents, and its commercial use as coating in industrial furnaces, as insulation in electronic devices and lasers when chromium doped [67–69], there are few reports about the production of REs doped forsterite and the exploration of its optical properties [28, 29, 70, 71].

1.5 Thin-Film Application

Nanostructures for up and down conversion are increasingly attracting interest from the scientific community. In this same way, the possible applications are also increasing. As cited in the prior section, the application of nanostructured optical materials in biomedicine, solar energy, and solid-state lasers is exponentially growing. Although these areas have already evolved a lot, there is still a long way to have full knowledge and control of the optical phenomena involved and the development of applied devices [41, 72]. Among the possible applications, in this chapter, just the thin-films will be explored since the main focus is to investigate the use of REs doped forsterite to improve solar cells efficiency.

Thin-film can be defined as a material that presents one of its dimensions much smaller than the other two. To be considered a thin-film, this layer may present a thickness in the range of angstroms up to several microns. The development of thin-film materials and its production techniques brings benefits to many important areas, such as Semiconductor electronics, optical coatings, barrier packaging, and surface treatments [61].

1.5.1 Forsterite Thin-Films and Silicon Solar Cells

Pure silicon in solar cells has surface reflectance losses ranging from 31 to 51% between 1100 and 400 nm respectively. The maximum light transmission is 70% of the IR and 50% of the UV emitted by the sun [8].

When losses are not counted in terms of reflection, about 35% of the energy incident is lost due to thermalization effects. The energy from the photons that exceed the silicon band gap is lost as heating. The best performing commercial cells absorb energy in a range of 390–1100 nm [73]. When comparing the absorption bands of these solar cells and the range of solar emission, it is observed that much of the energy emitted by the sun is not used. In terms of wavelengths, solar radiation occupies the spectral range from 100 to 3000 nm (3 μm), having a maximum spectral density around 550-600 nm [73].

The main factors of energy loss are the loss by reflection of the light on the surface of the cell, and loss by the energy emitted in the IR band that is directly transmitted and or converted to heat, without being harnessed by the cell [5, 74, 75].

Different materials such as ARCs are used to overcome these losses. ARC is a coating applied on the surface of materials to reduce light reflection, increasing its transmission. The ARCs applied to solar cells are similar to those used on other optical equipment such as camera lenses [12]. The coating can increase the efficiency of solar collection and therefore increase the efficiency of converting solar energy into electricity. As solar radiation occurs in a wide range of the spectrum, the ARCs for solar applications need to be effective over the entire solar spectrum that covers wavelengths from UV to IR [12, 13].

These coatings consist of thin layers of dielectric materials with a specially chosen thickness so that the interference effect on the coating causes the reflected wave at the top of the ARC to be out of phase with the wave reflected off the surface of the semiconductor. The out of phase reflected waves destructively interfere with each other, resulting in zero energy reflected by the system (Fig. 11). Since thin

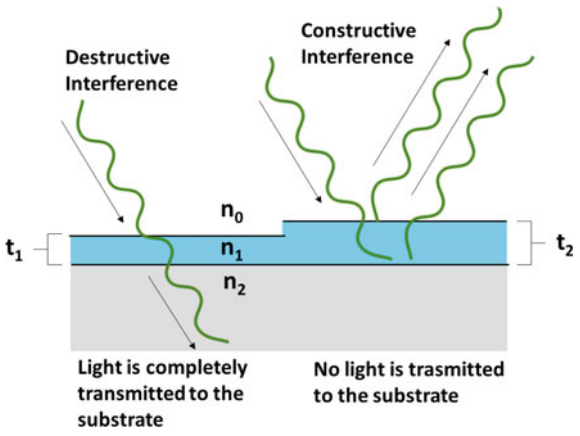

Fig. 11 Destructive and constructive interference of the ARC according to the coating thickness (t_1 and t_2). n_0, n_1 and n_2 represents the reflection index that light cross until reach the substrate

films in solar cells are usually exposed to environmental adversities, it is crucial that in addition to the anti-reflective properties, the dielectric materials used present good passivation and resistance to scratches besides being chemically stable at high temperatures [76].

In this sense, forsterite (Mg_2SiO_4) appears as interesting material for application as an ARC. Mg_2SiO_4 is the most abundant mineral of the Earth's mantle, and the presence of SiO in the structure allows a strong interaction with the substrates since these are generally formed of silicon. Its refractive index (~1.6) allows the forsterite to be applied in different configurations of coatings composed of layers [14]. According to S. Kh. Suleimanov et al., with a thickness of 86 nm, films of forsterite deposited on glass and silicon wafer presented high transparency between 500 and 900 nm [33]. Since this region represents the most important range of light absorption in solar devices, forsterite could be applied as a low-cost anti-reflective thin-film.

In addition to the anti-reflective properties, the forsterite doping capacity leads to another possibility to increase the efficiency of the cells. The doping of forsterite ARC thin-films with UC materials would allow the use of the solar energy range that is not harnessed by the solar device. As explained in Sect. 1.2.1, the UC of photons is a process in which the sequential absorption of two or more photons leads to light emission at a wavelength shorter than the excitation wavelength [19]. An example is the conversion from IR to Vis range [21, 23, 35, 77].

1.6 Er^{3+} Applied as a UC in Silicon Solar Cells

The use of UC materials might be a promising method to dislocate the energy emitted by the sun outside the absorption range of the solar device to an energy level where the cell can use that energy. By this method, it is possible to reduce the energy losses without interfering in the electronic properties of the silicon and the photovoltaic devices. The theoretical limit efficiency is increased from about 30% [78] to 40.2% [79] in solar cells with UC systems exposed to non-concentrated light.

Among the promising converters based on REs, the trivalent erbium (Er^{3+}) stands out. A representation of the Er^{3+} configuration is shown in Fig. 12. The absorption of photons at wavelengths around 1520 nm pumps the energy levels $^4I_{13/2}$, $^4I_{9/2}$ and $^4S_{3/2}$. These excited states decay to the next state (less energetic) or decay directly to the ground state emitting radiation ($^4I_{15/2}$). The photons emitted in the energy transition from level $^4I_{11/2}$ or more excited levels to the ground state present higher energy than the silicon band gap [61].

One of the technological advantages of the erbium ion is that the transition from its excited state to the ground state (1.54 μm) coincides with the maximum transmission wavelength of silica optical fibers that are used for telecommunications. The development of optical amplifiers doped with erbium was a significant technological contribution since it simplified the long-distance optical communication [18].

Likewise, the absorption range around 1500 nm is important in the solar devices field, since the silicon cells absorb up to a range of 1000 nm. With the use of erbium,

it is possible to absorb the solar energy that is emitted in the NIR around 1500 nm and reemit this energy in a smaller wavelength reaching the UV-Vis and thus being possible for the cell to take advantage of this energy that would be lost in the form of heat, among other forms.

Figure 13 shows a representation of a possible thin-film arrangement of $Mg_2SiO_4:Er^{3+}$ on the surface of a silicon-based solar cell. The energy of the NIR is absorbed by the dopant in the film and converted into energy in the UV-Vis which can be absorbed by the solar cell. Meanwhile, the sunlight that is emitted in the UV-Vis region directly pass through the forsterite anti-reflective film, being absorbed directly by the cell.

1.7 $Mg_2SiO_4:Er^{3+}$ UC/ARC System

There are few publications regarding the synthesis and use of RE-doped forsterite [28, 29, 70, 71]. Specifically, about erbium, we can cite two articles produced by Zampiva et al. The first one [80] presents the synthesis of nanostructured powders of $Mg_2SiO_4:Er^{3+}$ doped with different concentrations. The influence of erbium concentration on UC emission from NIR to Vis was studied. The powders were produced by reverse strike coprecipitation and showed a high degree of crystallinity, maintaining the single forsterite phase up to 10% erbium in the structure. The UC for the Vis

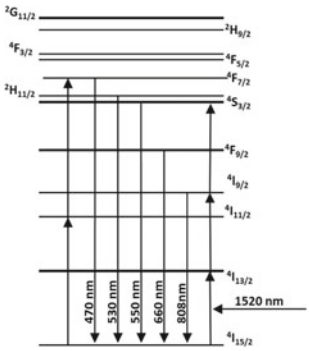

Fig. 12 Representation of the Er^{3+} configuration. The diagram indicates the energetic levels activity with excitation at 1520 nm

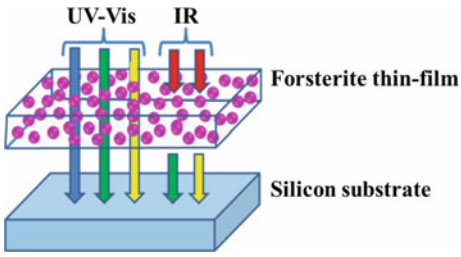

Fig. 13 Representation of a possible arrangement of $Mg_2SiO_4:Er^{3+}$ thin-film on the surface of a silicon-based solar cell

with excitation at 980 and 801 nm was evaluated. These wavelengths are essential for biological applications such as Photo Dynamic Therapy.

Figure 14a shows the emission in the visible spectra of Mg_2SiO_4 doped with different concentrations of erbium using an excitation source of 980 nm while Fig. 14b present the emission with an excitation source of 808 nm. When comparing the samples excited at 980 and 808 nm, it is interesting to observe that the emission intensity and the position of the bands changed with the excitation wavelength. The probable energy levels involved in the transitions of both sources have been described, and the discussion can be followed in the Ref. [80]. Among all samples, Mg_2SiO_4:Er^{3+} 7% presented the highest emission intensity in the visible with excitation at 980 nm.

Continuing the research on the Mg_2SiO_4:Er^{3+} system, the authors Zampiva et al. produced a second paper [81] presenting the Mg_2SiO_4: Er^{3+} optical behavior with excitation at ~1500 nm (NIR region). This wavelength lies outside the activity region of commercial solar devices, as described in Sect. 1.5.1, and so it is of interest in this chapter. Figure 15a shows the emission spectrum of Mg_2SiO_4: Er^{3+} 7% compared to pure forsterite. While pure Mg_2SiO_4 does not present any emission, the Mg_2SiO_4:Er^{3+} spectrum exhibits the characteristic Er^{3+} emission bands in a crystalline host. The Mg_2SiO_4:Er^{3+} system showed emissions at 488 nm ($^4F_{7/2} \rightarrow {}^4I_{15/2}$), 530 nm ($^4H_{11/2} \rightarrow {}^4I_{15/2}$), 554 nm ($^4S_{3/2} \rightarrow {}^4I_{15/2}$), 660 nm ($^4F_{9/2} \rightarrow {}^4I_{15/2}$) and 801 nm ($^4I_{9/2} \rightarrow {}^4I_{15/2}$). The possible UC processes that originate these emission bands are displayed in the schematic energy level diagram (Fig. 15b).

There are two main pathways for the excitation of erbium-doped materials, ESA and ETU [82, 83]. The first involves the absorption of a second photon by a previously excited atom, while the latter implies the energy transfer between two neighboring excited atoms, with one of them decaying in the process. Under pumping at 1470 nm, the first upper state is excited directly (4I15/2 → 4I13/2). From this level, ESA process occurs, populating two states; the $^4I_{9/2}$ and, via multiphoton, the $^4I_{11/2}$, promoting emission at around 801 and 980 nm, respectively. The lifetime of the $^4I_{11/2}$ state is longer than the other active levels [84], so photons from upper levels get through

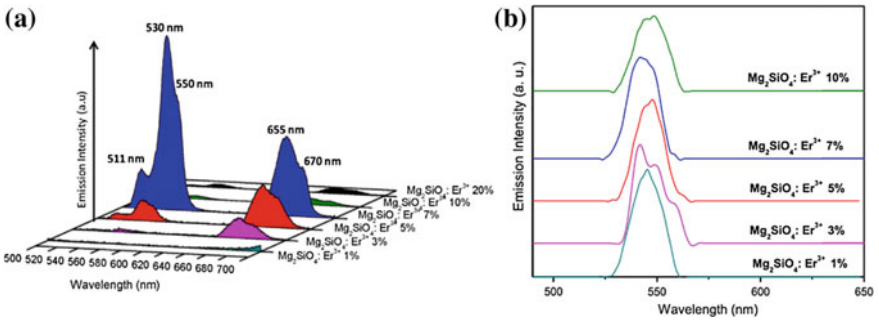

Fig. 14 **a** Photoluminescence UC spectra of the produced samples excited at 980 nm. A maximum in emission is observed for the Mg_2SiO_4:Er^{3+} 7%. **b** Photoluminescence UC spectra of the produced samples excited at 808 nm. Only the green emission was measured for all the samples. Adapted from Zampiva et al. [80], with permission from Elsevier

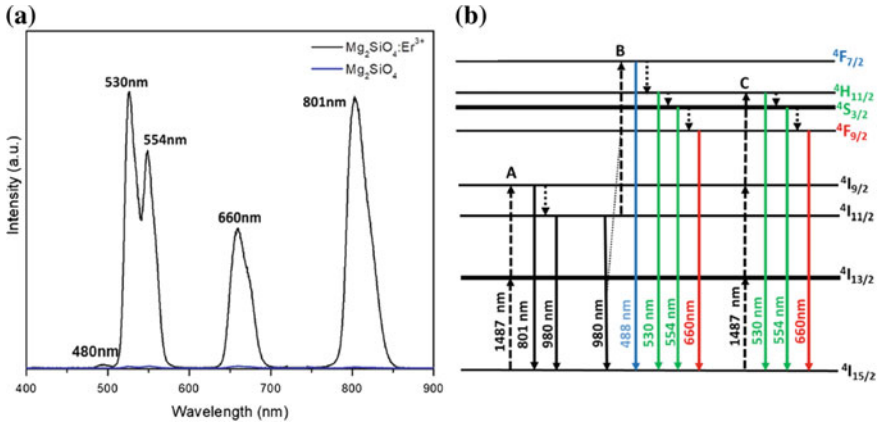

Fig. 15 **a** photoluminescence UC spectrum excited at 1470 nm of Mg_2SiO_4 and Mg_2SiO_4:Er^{3+} powders. **b** Schematic energy level diagram showing the possible UC processes A, B and C for Er^{3+} doped Mg_2SiO_4 host, under 1470 nm excitation. The dashed, dotted, and full arrows represent excitation, nonradiative relaxation, and emission processes, respectively Adapted Zampiva et al. [71], with permission from Elsevier

nonradiative relaxation and accumulate at $^4I_{11/2}$. Once the $^4I_{11/2}$ level is excited, ETU can occur between two neighbor atoms populating the $^4F_{7/2}$ state, from where emissions can occur at around 488 nm (blue), 530 nm (green), 554 nm (green) and 660 nm (red), as represented by the B set in Fig. 15b. At $^4F_{7/2}$, the photons lifetimes are much shorter than that of $^4S_{3/2}$, so most parts of the photons get through a rapid relaxation and accumulate at the 4S3/2 level. Another process that is possibly taking place, simultaneously, is the ESA of three photons (set C) triggering the emission of 530, 554 (green) and 660 (red) lights. Since more than one process may be responsible for the green and red emissions; and the photons lifetime is short for $^4F_{7/2}$ level, green and red bands (530, 554 and 660 nm) are more intense than that for blue emission (488 nm) [77, 84, 85].

As the optical behavior of the Mg_2SiO_4:Er^{3+} system proved efficient with excitation at ~1500 nm, other important properties for the use of this material as ARC in solar devices were investigated. Thin-films Mg_2SiO_4:Er^{3+} 7% were deposited by sputtering on a silicon wafer and its chemical and mechanical properties were evaluated.

Commercial solar cells are used in several environments, and the films might be exposed to external factors such as sand, powder, and dirt that may cause damage to the surface, decreasing the device efficiency [86]. To analyze the abrasion resistance, scratching tests were performed and as a result of five linear scratching applying 500 mN force, no delamination was observed on the film surface. For more in-depth data, it is recommended to read the paper [81].

Besides friction effects, solar modules are employed in many climates, some of which with unusually high humidity, as occurs in equatorial regions, or saline atmospheres, like coastal areas. The coatings used on all solar cell technologies must

be able to withstand high humidity and corrosive environments. High humidity and saline fog tests were performed on the pure forsterite and on the 7% Er^{3+} doped sample to evaluate the chemical stability of the films in such conditions. The surface analysis determined that the coatings remained constant after 1000 h test, for both salt fog and high humidity. These accelerated tests suggest-ed that humidity and saline fog have a minimum effect on the coating stability and it is unlikely to cause delamination or other types of damage. The high chemical stability and scratch resistance presented by forsterite films would allow their use as a protective layer on photovoltaic cells, or even on glass shields, usually present on commercial solar devices.

The use of forsterite was also evaluated by simulation of different configurations of ARC. Single layer and double layer models were built to determine the ideal ARC combination, remembering that forsterite presents a refractive index of ~1.6 at 600 nm (mainly region of commercial silicon solar cells activity). The results of all proposed models are discussed in the paper. Here, only the simulation data for the single layer model is presented. The single-layer theoretical model was built according to Eq. (1) [87]:

$$\mathbf{R} = \left|\left|r^2\right|\right| = ((r_1)^2 + (r_2)^2 + 2r_1r_2\cos 2\theta_1)/(1 + (r_1)^2 \cdot (r_2)^2 + 2r_1r_2\cos 2\theta_1) \quad (1)$$

where

$r_1 = (n_0 - n_1)/(n_0 + n_1)$

$\boldsymbol{r}_2 = (n_1 - n_2)/(n_1 + n_2)$

$\theta_1 = 2\pi\ n_1t_1/\lambda$

The surrounding region has a refractive index of n_0 (n air = 1), the thin film has a refractive index of n_1 (n forsterite = 1.6 at 600 nm), and a thickness of t_1 and the substrate has a refractive index of n_2 (n silicon wafer = 3.5). Through this equation, an ideal thickness (t_1) of 92 nm was settled.

Theoretical and experimental results were then compared through reflectance analysis. Pure and erbium-doped forsterite thin-films with different thicknesses were deposited by sputtering on a silicon wafer. The reflectance activity of the simulated ARC model and the experimental results were then compared in order to verify the correlation between the theoretical models and the experimental data. As presented in Fig. 16a, b, the optical activity of ARC films was also compared to the bare silicon. Both, doped and the non-doped films showed much higher transmittance values than the bare silicon wafer.

The application of Mg_2SiO_4 and Mg_2SiO_4:Er^{3+} coatings on the silicon wafer led to an improvement over 80% for MR (minimum reflectance) and spectral absorption gain. Furthermore, considering 600 nm as the central work wavelength for solar devices, the best results are obtained for Mg_2SiO_4 85 nm and Mg_2SiO_4: Er^{3+} 84 nm, presenting an absorption gain of 88.92 and 89.55% at MR and 76.59 and 75.54% of spectral gain respectively. The produced experimental data fit properly the simulations for the single layer films, and it was experimentally demonstrated that the forsterite coatings could expressively improve the silicon wafer light absorption. As indicated by the transmittance spectroscopy, the presence of Er^{3+} in the forsterite

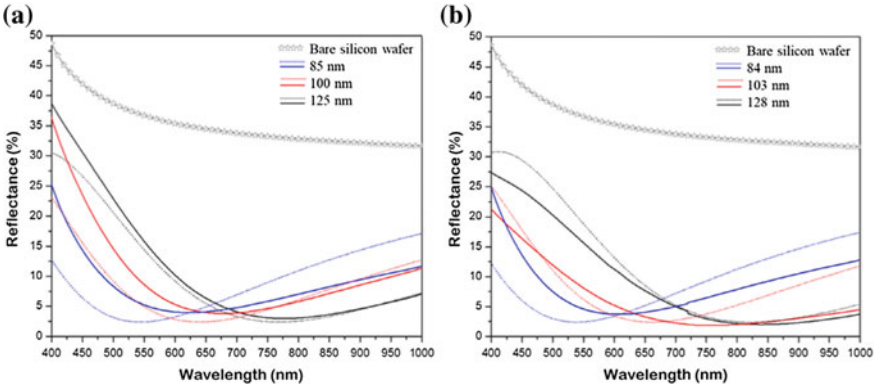

Fig. 16 **a** Pure Mg_2SiO_4 and **b** Mg_2SiO_4: Er^{3+} 7% coatings, the solid lines denote the experimental data, while the dotted lines represent the simulated data (Adapted from Zampiva et al. [81])

coating induced a small increase in the total absorbance in the Vis range. However, as observed in the reflectance spectra, it is still negligible facing the total anti-reflection improvement of the doped coatings when compared to the bare wafer.

The Mg_2SiO_4: Er^{3+} showed high-efficiency as a thin film for ARC. In addition, the material presented NIR to Vis UC that can lead to a significant increase on the commercial solar devices efficiency, without adding high costs to industrial production. Along with the erbium, it is possible to add other elements that can act as sensitizers. An example is the combination of ytterbium-erbium, already used in optical fibers. Other REs or transition metals may also exhibit such properties [70].

Among the REs there are elements with different absorption and emission lines that may present values even better than those observed for erbium. To this end, Zampiva et al. continue to explore the REs in the crystalline structure of forsterite. Not only sensitizers but also other activators such as Eu^{3+} are being studied. These elements may vary and or increase the activity range of these systems in the spectrum. Future works are focused on testing the energy conversion efficiency of commercial solar cells coated with thin forsterite films doped with different REs. As seen here, the preliminary results are quite encouraging.

2 Conclusion

Despite the importance of the UC materials in several areas, there is still a lot to be studied and developed. As presented in Sect. 1.2.1, less than 70 years ago, it was not even possible to prove the existence of the UC phenomenon. This chapter presented one of the possible applications of UC materials in the environmental field. The use of antireflection films with UC properties might considerably increase the efficiency of solar devices. These coatings may allow the increasing of commercial

devices efficiency without generating significant changes in industrial plants or product planning. Increasing efficiency while ensuring a low cost is the best way to keep rising the replacing of non-renewable energy sources with eco-friendly sources.

Although the scientific community devoted to the development of ARC/UC is small, the potential of this system was clearly noticed through the presented data. The ARC/UC system produced with erbium-doped forsterite presented very satisfactory results related to chemical and mechanical properties and also related to the optical behavior of the films. The films presented elevated anti-reflectivity in all UV-Vis spectra and UC activity from NIR to Vis. Likewise erbium, other REs ions might have interesting optical properties for application in ARC/UC systems. The next step in the development of these films is the doping of forsterite with different activating and sensitizers ions to increase the intensity and spectral range of activity. In addition, the study of the efficiency of commercial solar cells coated with these films is already being developed.

References

1. Technology roadmap—Solar Photovoltaic Energy (2014) International Energy Agency, France
2. World Energy Resources 2013 Survey (2013) World Energy Council, United Kingdom
3. Sawin JL, Rutovitz J, Sverrisson F (2018) Renewables 2018 Global Status Report, France
4. Global Market Outlook for Photovoltaics Until 2016 (2012) European Photovoltaic Industry Association, Belgium
5. Green MA, Emery K, Hishikawa Y et al (2016) Solar cell efficiency tables—version 47. Prog Photovoltaics 24:3–11. https://doi.org/10.1002/pip.2728
6. Ali K, Khan SA, Matjafri MZ, Sains U (2013) Co γ-irradiation effects on electrical characteristics of monocrystalline silicon solar cell. Int J Electrochem Sci 8:7831–7841
7. Minak G, Fragassa C, de Camargo FV (2017) A brief review on determinant aspects in energy efficient solar car design and manufacturing. Sustain Des Manuf 2017:847–856. https://doi.org/10.1007/978-3-319-57078-5_79
8. Ali K, Khan SA, Jafri MZ (2014) Structural and optical properties of ITO/TiO_2 anti-reflective films for solar cell applications. Nanoscale Res Lett 9:175. https://doi.org/10.1186/1556-276X-9-175
9. Ali K, Khan SA, Mat Jafri MZ (2014) Effect of double layer (SiO_2/TiO_2) anti-reflective coating on silicon solar cells. Int J Electrochem Sci 9:7865–7874
10. Fischer S, Goldschmidt JC, Löper P et al (2010) Enhancement of silicon solar cell efficiency by upconversion: Optical and electrical characterization. J Appl Phys 108. https://doi.org/10.1063/1.3478742
11. World Energy Resources—Full Report (2016) Energy Council 2016, United Kingdom
12. PV Education (2017) Antireflection coatings. https://www.pveducation.org/es/fotovoltaica/anti-reflection-coatings
13. Uzum A, Kuriyama M, Kanda H et al (2017) Sprayed and spin-coated multilayer antireflection coating films for nonvacuum processed crystalline silicon solar cells. Int J Photoenergy. https://doi.org/10.1155/2017/3436271
14. Rapp G (2009) Archaeomineralogy. Springer, Berlin, Heidelberg
15. Tsunooka T, Androu M, Higashida Y et al (2003) Effects of TiO_2 on sinterability and dielectric properties of high-Q forsterite ceramics. J Eur Ceram Soc 23:2573–2578. https://doi.org/10.1016/S0955-2219(03)00177-8

16. Abraham E, Bordenave E, Tsurumachi N et al (2000) Real-time two-dimensional imaging in scattering media by use of a femtosecond Cr($^{4+}$): forsterite laser. Opt Lett 25:929–931. https://doi.org/10.1364/OL.25.000929
17. Haase M, Schäfer H (2011) Upconverting nanoparticles. Angew Chemie Int Ed 50:5808–5829. https://doi.org/10.1002/anie.201005159
18. Chia S, Liu T, Ivanov AA et al (2010) A femtosecond Cr^{4+}: forsterite laser generating 1.4 W output power. Conference Lasers Electro-Optics 18:10–11. https://doi.org/10.1364/CLEO.2010.CMNN6
19. Zhang F (2015) Photon upconversion nanomaterials. Springer, Berlin, Heidelberg. https://doi.org/10.1007/978-3-662-45597-5
20. Jiang T, Xing M, Tian Y et al (2016) Up-conversion luminescence of Er 2 Mo_4O_{15} under 980 and 1550 nm excitation. RSC Adv 6:109278–109285. https://doi.org/10.1039/C6RA21580G
21. Han R, Yi H, Shi J et al (2016) pH-responsive drug release and NIR-triggered singlet oxygen generation based on a multifunctional core–shell–shell structure. Phys Chem Chem Phys 18:25497–25503. https://doi.org/10.1039/C6CP05308D
22. Liang P, Wang M, Liu Z (2017) Synthesis and spectroscopic studies of $Zn_4B_6O_{13}$ and Eu/Tb single-doped $Zn_4B_6O_{13}$ phosphors. J Rare Earths 35:441–445. https://doi.org/10.1016/S1002-0721(17)60931-1
23. Wang H, Han R, Yang L et al (2016) Design and synthesis of Core–Shell–Shell upconversion nanoparticles for NIR-induced drug release, photodynamic therapy, and cell imaging. ACS Appl Mater & Interfaces 8:4416–4423. https://doi.org/10.1021/acsami.5b11197
24. Figueiredo BR, Valente AA, Lin Z, Silva CM (2016) Photoluminescent porous and layered lanthanide silicates: a review. Microporous Mesoporous Mater 234:73–97. https://doi.org/10.1016/j.micromeso.2016.07.004
25. Selvasekarapandian S, Bhuvaneswari MS, Vijayakumar M et al (2005) A comparative study on ionic conductivity of Sr and Mg stabilized zirconia by impedance spectroscopy. J Eur Ceram Soc 25:2573–2575. https://doi.org/10.1016/j.jeurceramsoc.2005.03.104
26. Ringwood AE (1989) Significance of the terrestrial Mg/Si ratio. Earth Planet Sci Lett 95:1–7. https://doi.org/10.1016/0012-821X(89)90162-3
27. Ahmad HB, McKinnie IT (1995) Chromium doped forsterite ring laser. Opt Laser Technol 27:403–406. https://doi.org/10.1016/0030-3992(95)00031-3
28. El Hadri M, Ahamdane H, El Idrissi Raghni MA (2015) Sol gel synthesis of forsterite, M-doped forsterite (M=Ni, Co) solid solutions and their use as ceramic pigments. J Eur Ceram Soc 35:765–777. https://doi.org/10.1016/j.jeurceramsoc.2014.09.024
29. Yang H, Shi J, Gong M, Cheah KW (2006) Synthesis and photoluminescence of Eu^{3+}- or Tb^{3+}-doped Mg_2SiO_4 nanoparticles prepared by a combined novel approach. J Lumin 118:257–264. https://doi.org/10.1016/j.jlumin.2005.09.005
30. Yang H, Li S, Liang Z (2013) Anodized oxidative electrosynthesis of magnesium silicate whiskers. Int J Electrochem Sci 8:9332–9337
31. Shinno I, Nakamura T, Sekine T (2000) Deformation-sensitive luminescence of forsterite (Mg_2SiO_4) shocked up to 82 GPa. J Lumin 87–89:1292–1294. https://doi.org/10.1016/S0022-2313(99)00592-X
32. Choudhary R, Chatterjee A (2018) Antibacterial forsterite (Mg_2SiO_4) scaffold: a promising bioceramic forload bearing applications. Bioact Mater 3:218–224. https://doi.org/10.1016/j.bioactmat.2018.03.003
33. Suleimanov SK, Dyskin VG, Settarova ZS et al (2010) Antireflection coatings for solar cells based on an alloy of a mixture of MgO and SiO_2. Appl Sol Energy 46:296–297. https://doi.org/10.3103/S0003701X10040122
34. Mostafavi K, Ghahari M, Baghshahi S, Arabi AM (2013) Synthesis of Mg2SiO4:Eu^{3+} by combustion method and investigating its luminescence properties. J Alloys Compd 555:62–67. https://doi.org/10.1016/j.jallcom.2012.12.022
35. Chen S, Fan J, Pan L et al (2016) Synthesis of Yb:$Lu_3Al_5O_{12}$ nano powders with the reverse strike co-precipitation method: influence of decomposition of NH_4HCO_3. J Rare Earths 34:901–907. https://doi.org/10.1016/S1002-0721(16)60113-8

36. Padmanabhan P, Kumar A, Kumar S et al (2016) Nanoparticles in practice for molecular-imaging applications: an overview. Acta Biomater 41:1–16. https://doi.org/10.1016/j.actbio.2016.06.003
37. Blasse G, Grabmaier BC (1994) Luminescent Materials. Springer, Berlin, Heidelberg
38. Wang M, Abbineni G, Clevenger A et al (2011) Upconversion nanoparticles: synthesis, surface modification, and biological applications. NIH Public Access 7:710–729. https://doi.org/10.1016/j.nano.2011.02.013.Upconversion
39. Yu W, Tian Y, Xing M et al (2016) Up-conversion luminescence of $NaY(WO_4)_2$: Yb, Er under 1550 and 980 nm excitation. Mater Res Bull 80:223–229. https://doi.org/10.1016/j.materresbull.2016.03.013
40. Sathi ZM, Zhang J, Luo Y et al (2015) Improving broadband emission within Bi/Er doped silicate fibres with Yb co-doping. Opt Mater Express 5:2096. https://doi.org/10.1364/OME.5.002096
41. Zhou B, Shi B, Jin D, Liu X (2015) Controlling upconversion nanocrystals for emerging applications. Nat Publ Gr 10:924–936. https://doi.org/10.1038/nnano.2015.251
42. Bloembergen N (1959) Solid State Infrared Quantum Counters. Phys Rev Lett 2:84–85. https://doi.org/10.1103/PhysRevLett.2.84
43. Bünzli J-CG, Piguet C (2005) Taking advantage of luminescent lanthanide ions. Chem Soc Rev 34:1048. https://doi.org/10.1039/b406082m
44. Chen X, Xu W, Song H et al (2016) Highly efficient LiYF4:Yb^{3+}, Er^{3+} upconversion single crystal under solar cell spectrum excitation and photovoltaic application. ACS Appl Mater Interfaces 8:9071–9079. https://doi.org/10.1021/acsami.5b12528
45. Wang Q, Dahal R, Feng IW et al (2011) Emission and absorption cross-sections of an Er:GaN waveguide prepared with metal organic chemical vapor deposition. Appl Phys Lett 99:1–4. https://doi.org/10.1063/1.3636418
46. Gonçalves IMC (2016) Multifunctional nanocomplexes with a Fe_3O_4 superparamagnetic core and rare earth-doped upconversion fluorescent shell. Dissertacao, Universidade de Coimbra
47. Wang D, Lu J, Zhang Z et al (2011) Upconversion luminescence of Er^{3+}/Yb^{3+} Co-Doped Sb_2O_3–WO_3–LI_2O antimonate glasses. New J Glas Ceram 01:34–39. https://doi.org/10.4236/njgc.2011.12006
48. Wang M, Abbineni G, Clevenger A et al (2011) Upconversion nanoparticles: synthesis, surface modification and biological applications. Nanomed Nanotechnol Biol Med 7:710–729. https://doi.org/10.1016/j.nano.2011.02.013
49. Wardle B (2010) Principles and Applications Of Photochemistry. Wiley, Machester
50. Jackson SD (2004) Cross relaxation and energy transfer upconversion processes relevant to the functioning of 2 μm Tm^{3+}-doped silica fibre lasers. Opt Commun 230:197–203. https://doi.org/10.1016/j.optcom.2003.11.045
51. Connelly Ngrmhathtd (2005) Nomenclature of inorganic chemistry—IUPAC recommendations. The Royal Society of Chemistry, United Kingdom
52. Santos WQ (2011) Investigação de perdas por down-conversion e upconversion em materiais lasers dopados com Nd^{3+} usando a técnica de lente térmica. Dissertacao. Universidae Federal de Alagoas
53. Dieke GH, Crosswhite HM (1963) The spectra of the doubly and triply ionized rare earths. Appl Opt 2:675–686. https://doi.org/10.1364/AO.2.000675
54. Judd BR (1962) Optical absorption intensities of rare-earth ions. Phys Rev 127:750–761. https://doi.org/10.1103/PhysRev.127.750
55. Mondal K, Kumari P, Manam J (2016) Influence of doping and annealing temperature on the structural and optical properties of Mg_2SiO_4:Eu^{3+} synthesized by combustion method. Curr Appl Phys 16:707–719. https://doi.org/10.1016/j.cap.2016.04.001
56. Davidovich L (2015) Os quanta de luz e a ótica quântica. Rev Bras Ensino Física 37:1–12. https://doi.org/10.1590/S1806-11173732073
57. Lang JK, Baer Y, Cox PA (1981) Study of the 4f and valence band density of states in rare-earth metals. II. Experiment and results. J Phys F Met Phys 11:121. https://doi.org/10.1088/0305-4608/11/1/015

58. Schweizer T, Mobert PEA, Hector JR et al (1998) Optical measurement Of narrow band rare-earth 4f levels with energies greater than the bandgap of the host. Phys Rev Lett 80:1537–1540. https://doi.org/10.1103/PhysRevLett.80.1537
59. Gavrilović TV, Jovanović DJ, Smits K, Dramićanin MD (2016) Multicolor upconversion luminescence of $GdVO_4$:Ln^{3+}/Yb^{3+}(Ln^{3+}=Ho^{3+}, Er^{3+}, Tm^{3+}, Ho^{3+}/Er^{3+}/Tm^{3+}) nanorods. Dye Pigment 126:1–7. https://doi.org/10.1016/j.dyepig.2015.11.005
60. Bergmann CP (2015) Topics in mining, metallurgy and materials engineering. Springer, New York
61. Fischer S, Goldschmidt JC, Janz S et al (2008) Material characterization for advanced upconverter systems a potential setup for an. Sol Energy 4–7. https://doi.org/10.1117/2.1201312.005293
62. Zheng K, Wang L, Zhang D et al (2010) Power switched multiphoton upconversion emissions of Er^{3+} in Yb^{3+}/Er^{3+} codoped beta-$NaYF_4$ microcrystals induced by 980 nm excitation. Opt Express 18:2934–2939. https://doi.org/10.1364/OE.18.002934
63. Gatak Ajoy, Thygarajan K (1997) Introduction to fiber optics. Cambridge University Press, Manchester
64. Yang Q, Wang J, Zhang W et al (2017) Interface engineering of metal organic framework on graphene oxide with enhanced adsorption capacity for organophosphorus pesticide. Chem Eng J 313:19–26. https://doi.org/10.1016/j.cej.2016.12.041
65. Shannon RD (1976) Revised effective ionic radii and systematic studies of interatomic distances in halides and chalcogenides. Acta Crystallogr Sect A 32:751–767. https://doi.org/10.1107/S0567739476001551
66. Rafferty J (2012) Minerals. Britannica, New York
67. Mortensen JL, McWilliam A, Leburn CG et al (2006) Up to 30 mW of broadly tunable CW green-to-orange light, based on sum-frequency mixing of Cr^{4+} : forsterite and Nd:YVO_4 lasers. Opt Commun 260:637–640. https://doi.org/10.1016/j.optcom.2005.10.056
68. Naveed Hosseini S, Salimi Jazi H, Fathi M (2015) Novel electrophoretic deposited nanostructured forsterite coating on 316 L stainless steel implants for biocompatibility improvement. Mater Lett 143:16–19. https://doi.org/10.1016/j.matlet.2014.12.079
69. Tan CY, Singh R, Teh YC et al (2015) Sinterability of forsterite prepared via solid-state reaction. Int J Appl Ceram Technol 12:437–442. https://doi.org/10.1111/ijac.12172
70. Zampiva RYS, Alves AK, Bergmann CP (2017) Mg_2SiO_4: Er^{3+} coating for efficiency increase of silicon-based commercial solar cells. Sys Technol 68. https://doi.org/10.1007/978-3-319-57078-5_77
71. Zampiva RYS, Jr CGK, Acauan LH et al (2018) Luminescent anti-reflection coatings based on Er doped forsterite for commercial silicon solar cells applications. Solar Energy 170:752–761. https://doi.org/10.1016/j.solener.2018.05.097
72. Auzel F (2004) Upconversion and Anti-Stokes processes with f and d ions in solids. Chem Rev 104:139–173. https://doi.org/10.1021/cr020357g
73. Ronald B (2017) Solarquotes Blog. https://www.solarquotes.com.au/blog/uv-solar-panels/
74. Fathi MH, Kharaziha M (2008) Mechanically activated crystallization of phase pure nanocrystalline forsterite powders. Mater Lett 62:4306–4309. https://doi.org/10.1016/j.matlet.2008.07.015
75. Zhang L, Fang X, Ye C (2007) Controlled growth of nanomaterials. World Scientific. https://doi.org/10.1142/6066
76. Zhengjun S (2017) Antireflective coatings with enhanced adhesion strength. Nanoscale 9:11047–11054. https://doi.org/10.1039/c7nr02334k
77. Liang X, Fan J, Wang Y et al (2017) Synthesis of hollow and mesoporous structured NaYF4:Yb, Er upconversion luminescent nanoparticles for targeted drug delivery. J Rare Earths 35:419–429. https://doi.org/10.1016/S1002-0721(17)60929-3
78. Shockley W, Queisser HJ (1961) Detailed balance limit of efficiency of p-n junction solar cells. J Appl Phys 32:510–519. https://doi.org/10.1063/1.1736034
79. Shang Y, Hao S, Yang C, Chen G (2015) Enhancing solar cell efficiency using photon upconversion materials. Nanomaterials 5:1782–1809. https://doi.org/10.3390/nano5041782

80. Zampiva RYS, Acauan LH, Venturini J et al (2018) Tunable green/red luminescence by infrared upconversion in biocompatible forsterite nanoparticles with high erbium doping uptake. Opt Mater (Amst) 76:407–415. https://doi.org/10.1016/j.optmat.2018.01.004
81. Zampiva RYS, Kaufmann CG, Acauan LH et al (2018) Luminescent anti-reflection coatings based on Er^{3+} doped forsterite for commercial silicon solar cells applications. Sol Energy. https://doi.org/10.1016/j.solener.2018.05.097
82. Som T, Karmakar B (2009) Green and red fluorescence upconversion in neodymium-doped low phonon antimony glasses. J Alloys Compd 476:383–389. https://doi.org/10.1016/j.jallcom.2008.09.006
83. Vu K, Farahani S, Madden S (2015) 980 nm pumped erbium doped tellurium oxide planar rib waveguide laser and amplifier with gain in S, C and L band. Opt Express 23:747. https://doi.org/10.1364/OE.23.000747
84. Ye R, Xu C, Wang X et al (2016) Room-temperature near-infrared up-conversion lasing in single-crystal Er–Y chloride silicate nanowires. Nat Publ Gr 1–6. https://doi.org/10.1038/srep34407
85. Shang X, Chen P, Jia T et al (2015) Upconversion luminescence mechanisms of Er^{3+} ions under excitation of an 800 nm laser. Phys Chem Chem Phys 17:11481–11489. https://doi.org/10.1039/C5CP00057B
86. Kaltenbach T, Klimm E, Meier T et al (2014) Testing of components for solar thermal collectors in respect of saline atmospheres. Energy Procedia 48:731–738. https://doi.org/10.1016/j.egypro.2014.02.085
87. Lee CC (2015) Thin film optical coatings. Curr Trends Optics Photonics 129:3–33. https://doi.org/10.1007/978-94-017-9392-6

Chitin Adsorbents to Wastewater Treatment

Tania Maria Hubert Ribeiro and Márcia Cristina dos Santos

Abstract This chapter presents studies on the use of chitin and its chitosan derivative as adsorbents in effluent treatment. Initially the origin of chitin is addressed, which is predominantly obtained from fishing waste. The objective is to present an overview of the main results obtained during the effluent treatment using chitin, chitosan and its derivatives in the removal of different classes of dyes, metallic ions, that is, several pollutants.

Keywords Chitin · Chitosan · Adsorption · Dyes · Metals

Abbreviations

BET	Brunauer–Emmett–Teller
EDX	Dispersive energy x-Ray
FTIR	Fourier transformer infrared
MB	Methylene blue
RB198	Reactive blue 198 dye
RB4	Reactive blue 4 dye
RR120	Reactive red 120 dye
RB4	Reactive blue 4 dye
RR120	Reactive red 120 dye
SEM	Scanning electron microscopy
SEM	Scanning electron microscopy
TC-Chitosan	Thiocarbamoyl chitosan
XDR	X-Ray diffraction
XDR	X-Ray diffraction

T. M. Hubert Ribeiro (✉) · M. C. dos Santos
Universidade Federal do Rio Grande do Sul, Porto Alegre, Brazil
e-mail: tania.hubert@gmail.com

A. Kopp Alves (ed.), *Nanomaterials for Eco-friendly Applications*,
Engineering Materials, https://doi.org/10.1007/978-3-030-26810-7_8

1 Introduction

The need to control the quality of wastewater is an ever-present and urgent issue, as water resources are absolutely indispensable to human and animal life. It is important to be aware that water is a finite resource and that the environmental balance for present and future generations depends on its preservation. Treating effluents is essential.

The modes of water contamination are very diverse, from heavy metals, volatile organic compounds, to discharges containing excess nutrients, such as nitrogenous and phosphorous compounds. Synthetic dyes are an important class of organic pollutants, and a part of the total amount of dyes used in dyeing processes are discarded as effluents, which discharged into the environment have harmful effects on life. Removal of dyes by adsorption is an attractive method due to its effectiveness and economic viability.

The primary effluent treatment contemplates coarser aspects, which are the elimination of particulate solids of the most diverse sizes, turbidity, etc. There are deeper and often invisible issues, in this case the dissolved contaminants. Sorption of dissolved contaminants represents a desirable final effluent treatment.

Aspects to be considered in the use of these biosorbents are related to their origin. Chitin is a natural polymer like cellulose, which is more abundantly present in the exoskeleton of crustaceans, occurring also in insects and fungi. After extractive processes it is possible to isolate chitin, which by deacetylation produces chitosan, the object of numerous publications and patents in the last decades. Figure 1 shows the chitin and chitosan structures. Chitin is a linear polymer with 2-acetamido-2-deoxy-D-glucopyranose units linked by glycosidic bonds at 1, 4. It is the second most abundant natural fiber after cellulose. Chitosan is the partially N-deacetylated derivative of chitin, which has a primary amino group.

The source of this biomaterial is a residue of the fishing industry. This residue is most often used in animal feed, it is a highly degradable material if not properly fractionated. After its degradation the waste does not lend itself to any form of consumption and its disposal, often in collections of water, causes serious pollution. The extraction process of chitin consists in three chemical steps: demineralization, deproteinization and depigmentation. The characteristics of the obtained chitin depends on countless factors, like the crustacean species and the process conditions, for example [2]. The uses of chitosan and of chitin are very varied and interesting, but they do not occur with the intensity and with the expected frequency. Figure 2 shows the

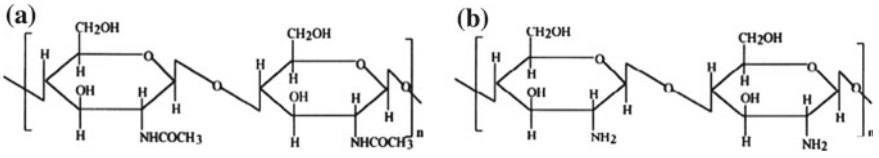

Fig. 1 Chemical structure of **a** chitin and **b** chitosan (Reprinted with permission [1])

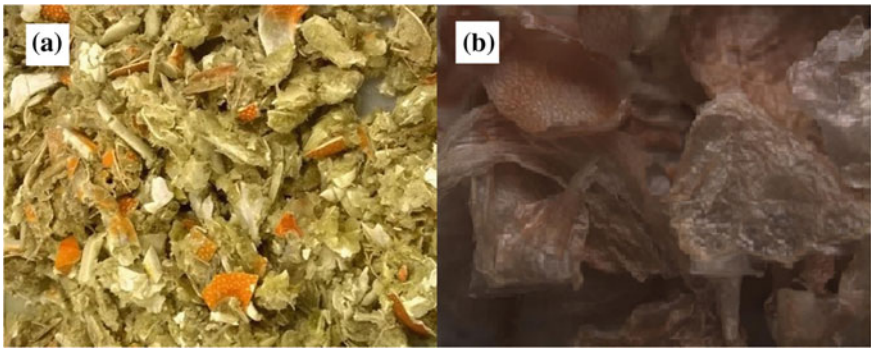

Fig. 2 Aspect of crustacean residue (A) before chitin isolation treatment and (B) after treatment

crustacean residue aspect before and after treatment for the isolation of chitin.

Disposal of shrimp waste poses a serious environmental problem because valuable natural resources are wasted. Populations of some species are in danger due to the ecological imbalance resulting from the environmental impact following the dumping of shrimp waste in coastal regions. Depending on the scale, resources used, and the nature of the practices adopted, coastal aquaculture may or may not cause serious environmental damage. The great problem of the valorization of shrimp as biomaterial is its high perishability. Under tropical climatic conditions, decomposition begins within one hour after processing with the production of amines responsible for extremely unpleasant odors. If this deterioration is not impeded, the biomaterial becomes a real waste, and, due to its high protein content, it becomes a significant threat to the environment with considerable consequences if not disposed of properly.

For environmental and economic reasons wherever possible, appropriate technology should be applied to prevent deterioration and to promote the conversion of biomaterial into higher value-added products. The technology must delay or prevent decomposition of the biomaterial by means of fractionation procedures. There is a significant interest in the recycling of shrimp waste.

Shrimp shells, which account for 40–48% of their weight, contain between 15–20% chitin, 25–40% protein and 40–55% calcium carbonate. They are usable products that normally have a not very noble destination since they do not receive the appropriate fractionation.

Thus, the use of shrimp waste for the production of chitin and its use contemplate the care of the environment in a very broad way, on the one hand prevents contamination by deterioration of the material with consequent risk to soil and water collections and the final product allows the decontamination of liquid effluents.

Figure 3 shows photomicrographs of chitin and chitosan obtained by SEM. This biopolymer has a crystalline nanostructure formed by nanofibers acetamide with strong hydrogen bonds that give it natural nanometric characteristics. The FTIR and XRD spectra of chitin and chitosan are shown in Fig. 4.

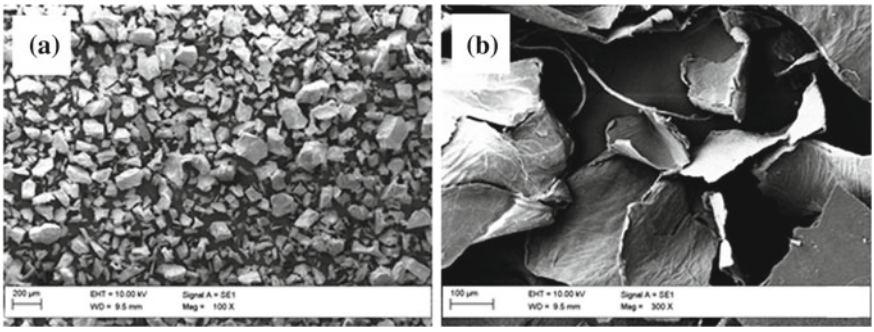

Fig. 3 SEM images of **a** chitin and **b** chitosan

2 Chitin as Sorbent for Dyes

Dotto et al. [3] compared several sorbents commonly employed in the removal of dyes contained in effluents with chitosan. Acid blue 9, food yellow 3 and FD&C yellow nº 5 were studied for aqueous solutions with different pH values in the range of 2 to 10. The equilibrium studies showed that chitosan at pH 3 was the best adsorbent for all the dyes, removing 50, 90 and 80% of the dyes bright blue, twilight yellow and tartrazine yellow, respectively. The Langmuir model presented the best fit with the experimental data and the maximum adsorption capacities in the monolayer were 1134, 1684 and 1977 mg g^{-1} for bright blue, dusky yellow and tartrazine yellow dyes obtained respectively at 298 K.

In other works, aiming to observe the behavior of chitin after surface modification Dotto et al. [4] submitted chitin samples to ultrasonic treatment (400 W, 24 kHz) for one hour. The purpose was to increase its surface area for the adsorption of methylene blue. The modified chitin was characterized as surface area (BET isotherms), FTIR spectroscopy, XRD and SEM. Compared with untreated chitin, there was a 25-fold increase in surface area. The adsorption tests with methylene blue solutions demonstrated that the system obeys the Langmuir model, the maximum adsorption capacity of MB was 26.69 mg g^{-1} and it is possible to reuse the chitin seven times with the same sorption power.

The different works for the use of chitin/chitosan also contemplate chemical modifications as observed by Fávere and collaborators [5]. These investigators modified the chitosan by reaction with glycidyl trimethylammonium chloride and the product was characterized by spectroscopic methods and conductometric titration. The obtained quaternary chitosan was tested for adsorption in aqueous solutions of two dyes, blue dye RB4 and red dye RR120. The results were compatible with the Langmuir isotherm model. In the case of the blue dye the sorption capacity was 637 mg g^{-1} of dye and for the red dye 415 mg.

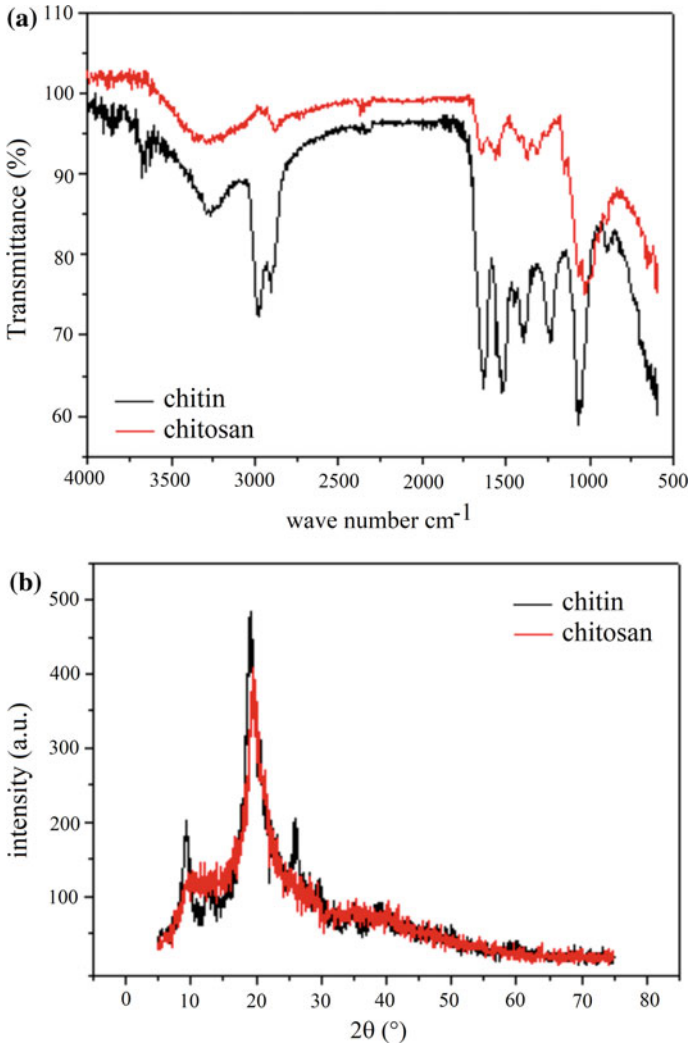

Fig. 4 **a** FTIR spectra and **b** XRD spectra of chitin and chitosan

Debrassi et al. [6] used chitosan to obtain carboxymethyl derivatives. These modified compounds were tested for the sorption of Congo red, an anionic dye. Studies have shown that the system obeys the Freundlich and Langmuir models. The maximum adsorption capacity at pH 7.0 was 281.97 mg g^{-1}. The process from the thermodynamic point of view is spontaneous.

The chemical modification by oxidizing agent was studied by Dassanayakea et al. [7]. These authors investigated the modification of chitin by the use of $KMnO_4$ and applied the hybrid product of manganese dioxide and chitin in the removal of methylene blue from aqueous solutions as a model for wastewater treatment. The hybrid

was characterized by several spectroscopic methods, by SEM and thermal analysis. About 300 mg of the product obtained in one liter of solution with concentration of 20 mg L^{-1} MB promotes complete discoloration in 2.5 min. In addition, the material presented the capacity to degrade 99% of MB after ten consecutive cycles.

In other studies, chitosan was used to modify the surface of a synthetic polymer. Centenaro et al. [8] produced a polyurethane foam and coated it with a chitosan layer to employ it as a sorbent for the organic dye RB198. This blue dye has an anionic character and is of use in textile industries. The foams were characterized by spectroscopic methods and by scanning electron microscopy. The studies concluded that the chitosan-coated polyurethane foam with respect to this dye in aqueous medium exhibits a good correlation with the Langmuir adsorption model with a dye adsorption capacity of 86.43 mg g^{-1} of adsorbent up to seven cycles with the same material.

3 Sorption of Metals by Chitinous Products

Chitin is an extremely versatile material. Dotto et al. [9] investigated the superficial alteration of chitin using ultrasound and supercritical CO_2 to remove cobalt from aqueous solutions. Chitin samples were characterized before and after treatment. BET, FTIR spectroscopy, XRD and SEM analyses revealed important surface changes and decreased crystallinity of the material. The adsorption studies were performed by equilibrium isotherms and kinetic curves. The results could be described by both Freundlich and Langmuir isotherms. And the maximum adsorption capacities found were 50.3 for untreated chitin, 83.94 for chitin modified by ultrasound and 63.8 for chitin modified by supercritical CO_2, results in milligram of cobalt per gram of adsorbent.

The adsorption of Al (III) and Fe (III) on chitosan films from individual and binary systems was investigated by Marques et al. [10]. The dosages of the films varied in the range of 100, 200 and 300 mg L^{-1} of chitosan and the pH values used were 3, 4.5 and 6. After the tests the films were analysed by XRD, SEM, thermal analysis and EDX spectroscopy. The most suitable conditions for all experiments corresponded to the film dosage of 100 mg L^{-1} and pH 4.5. In individual systems it was possible to obtain the following sorption values: 140.2 mg of Fe (III) and 665.5 mg of Al (III) per gram of film. In binary systems the values found for the Fe (III) and Al (III) were respectively 132.33 and 621.2 mg per gram of film. Using an actual effluent from a gas scrubber of aluminum sulfate process the amount of ferric ions sorbed was 66.3 and aluminum ions were 275.7 mg.

The thiocarbamoyl chitosan (TC-chitosan) is obtained by treatment of chitosan with thiourea and glutaraldehyde. This modified chitosan was prepared, characterized and evaluated for the removal of Cr (VI) and Cd (II) from electroplating effluents. TC-chitosan was characterized by several techniques such as SEM, EDX spectroscopy, BET and FTIR spectroscopy. It was observed that the adsorption of Cd (II) was maximal at pH (7.5) alkaline in contrast to acid pH (2.0) for Cr (VI). The

Langmuir isotherm model fitted better compared to the Freundlich model indicating monolayer adsorption. Equilibrium studies revealed a maximum adsorption capacity of 666.7 mg g^{-1} for Cd (II) and 434.8 mg g^{-1} for Cr (VI). The sorption process found followed a pseudo second order kinetics with a rate constant of 0.0498 and 0.028 g mg^{-1} h^{-1} for Cr (VI) and Cd (II), respectively. Thermodynamic parameters such as entropy, enthalpy and free energy of Gibbs indicated the suitability of TC-chitosan for the removal of Cr (VI) and cadmium. It was possible the simultaneous removal of Cr (VI) and Cd (II) and the results obtained allow to be applied to the removal of these heavy metals from electroplating waste water [11].

Humic acids have been investigated in the production of hybrids with chitin for the adsorption of metals, especially tanning effluents containing chromium are the targets of these works. Santosa et al. [12] tested the behavior of chitin hybrids with humic acid for the removal of Cr (III) from synthetic and real effluents. The system followed Freundlich model. The solutions were analyzed by atomic absorption spectrophotometry and the chitin hybrid and humic acid were evaluated by FTIR spectroscopy. The optimum pH value of 3.5 was reached with Cr (III) adsorption capacity of 35.57 mg g^{-1} of adsorbent. In the actual effluent the maximum amount obtained was 10.82 mg of Cr (III) per gram of hybrid.

The complexation of chitosan with Fe (III) ions forms an insoluble solid that has been shown to adsorb oxyanions. Fagundes et al. [13] prepared crosslinked chitosan and Fe (III) complexes and evaluated, according to the Langmuir model, the adsorption capacity by finding the maximum value of As (V) 127 mg per gram of adsorbent. The studies showed that the complex maintains its adsorption capacity practically unchanged in the pH range from 4.0 to 8.0. The percentage of arsenic removal in the ideal process conditions reached 94% of the initial concentration after the first 20 min, showing a very fast reaction kinetics.

Some of the advantages of the adsorption technique for the removal of metallic ions are the low amount of residue generated, the easy recovery of the metals and the possible reuse of the adsorbent. The use of adsorbents prepared by the microencapsulation of organic complexing agents allows easy substitution, and the same adsorbent can be used for different purposes in flexible working conditions. Chitosan, as already mentioned, is a biopolymer with interesting properties, such as biocompatibility, biodegradability and non-toxicity, and is commonly used for drug encapsulation. The chitosan molecule has amino groups that, when protonated, present a high density of positive charge, propitiating the ionic interaction with numerous anionic chelating agents. An organic compound having complexing properties is 8-hydroxyquinoline-5 sulfonic acid, better known as sulfoxine, an anionic chelator of high versatility and capable of reacting with a wide range of metal ions.

Various forms of presentation of chitosan for use as adsorbent material have as example the production of microspheres. Microspheres of glutaraldehyde-crosslinked chitosan were obtained by atomization via spray drying containing the sulfoxin chelating agent. As a result, a new chelating adsorbent was obtained. Vitali et al. [14] investigated their adsorbent properties with respect to Cu (II) ions. The adsorbent obtained in the form of microspheres was characterized by Raman Spectroscopy, SEM and EDX spectroscopy. To evaluate the adsorption experiments, the

concentrations of Cu (II) in the supernatant were determined by flame atomic absorption spectrophotometry. The adsorption process of Cu (II) by the new adsorbent material produced is dependent on the pH of the solution, with 6.0 being the optimum adsorption pH. The experimental data also indicated that the maximum adsorption capacity was 53.8 mg g^{-1}, which shows that the new adsorbent material could be tested in processes of separation and preconcentration of metallic ions in aqueous solutions and in natural waters.

In a work by Silva et al. [15] the synthesis of crosslinked chitosan microspheres is reported. Its application in Cr (VI) removal has been described as well as the parameters of Cr (VI) adsorption processes found using continuous isothermal calorimetry. The spectroscopic characterization of the synthesized chitosan beads showed significant chemical and structural differences, before and after crosslinking with epichlorohydrin.

4 Prospects of Biosorption

Pakdel and Peighambardoust [16] have published a review that provides a wealth of important information on the future prospects of chitosan-based hydrogels for wastewater application. Recently, chitosan has been used as a raw material for the synthesis of hydrogels in a wide range of potential and practical applications, such as waste water treatment. The potential of these chitosan-based hydrogels for effluent treatment is very promising. Chitosan-based hydrogels are physically and chemically modified through cross-linking, grafting, impregnation, incorporation of hard fillers, blending, interpenetration and ion printing methods to improve adsorption and mechanical properties. The understanding of these methods provides useful information on the design of efficient chitosan-based hydrogels and the selection of appropriate pollutants for the removal of pollutants.

Sarode et al. [17] in their review article discusses the mechanical and physicochemical characteristics of chitin and chitosan and their electrostatic interactions of functional groups responsible for their behavior in the removal of metal ions in wastewater. In their paper the authors describe the different technologies commonly used for wastewater treatment, their advantages and limitations. Efficient and effective treatment of wastewater is a need for environmental and public health. Special attention is given to chitin and chitosan, natural polymers that can adsorb heavy metal ions and dyes, for example. The primary amino and hydroxyl groups present on the surface of the chitosan provide a hydrophilic character. The biosorption of heavy metals allowing their removal of aqueous effluents is due to these groups, responsible for electrostatic interactions. In addition, a flexible polymer chain structure of chitosan allows to present suitable configurations in liquid medium.

5 Conclusion

Chitin and chitosan derivatives show good potential for the removal of various aquatic pollutants. Maximum adsorption capacities provide an idea of the sorbent efficacy for several types of pollutants and depend mainly on experimental conditions. Several gaps need to be filled with regard to the method of production of these sorbents. Mechanistic studies with organic and inorganic pollutants need to be carried out in detail to propose a model that describes the interactions of these pollutants with chitin, chitosan and derivatives. Initially there is a general impression that in most cases sorption follows the Langmuir model. However, it is still necessary to discover the practical utility of such adsorbents, to develop them on a commercial scale. For this purpose, it is necessary to establish the identification of a suitable form of chitin/chitosan to achieve the maximum removal or adsorption of specific type of pollutant depending on the characteristics of the adsorbate/adsorbent system.

The development of the adsorption process essentially requires further investigation using actual industrial effluents. These adsorbents may offer advantages over currently available commercial adsorbents, further contributing to overall waste minimization.

References

1. Knidri HE, Belaabed R, Addaou A et al (2018) Extraction, chemical modification and characterization of chitin and chitosan. Int J Biol Macromol 120:1181–1189. https://doi.org/10.1016/j.ijbiomac.2018.08.139
2. Campana-Filho SP, de Britto D, Curti E et al (2007) Extração, estruturas e propriedades de α- e β-quitina. Quim Nova 30:644–650
3. Dotto GL, Vieira MLG, Gonçalves JO et al (2011) Remoção dos corantes azul brilhante, amarelo crepúsculo e amarelo tartrazina de soluções aquosas utilizando carvão ativado, terra ativada, terra diatomácea, quitina e quitosana: estudos de equilíbrio e termodinâmica. Quim Nova 34:1193–1199
4. Dotto GL, Santos JMN, Rodrigues IL et al (2015) Adsorption of methylene blue by ultrasonic surface modified chitin. J Colloid Interface Sci 446:133–140. https://doi.org/10.1016/j.jcis.2015.01.046
5. Fávere VT, Riella HG, da Rosa S (2010) Cloreto de N-(2-hidroxil) propil-3-trimetil amônio quitosana como adsorvente de corantes reativos em solução aquosa. Quim Nova 33:1476–1481
6. Debrassi A, Largura MCT, Rodrigues CA (2011) Adsorção do corante vermelho congo por derivados da o-carboximetilquitosana hidrofobicamente modificados. Quim Nova 34:764–770
7. Dassanayake RS, Rajakaruna E, Moussa H et al (2016) One-pot synthesis of MnO_2–chitin hybrids for effective removal of methylene blue. Int J Biol Macromol 93:350–358. https://doi.org/10.1016/j.ijbiomac.2016.08.081
8. Centenaro GSNM, Facin BR, Valério A et al (2017) Application of polyurethane foam chitosan-coated as alow-cost adsorbent in the effluent treatment. J Water Process Eng 20:201–206. https://doi.org/10.1016/j.jwpe.2017.11.008
9. Dotto GL, Cunha JM, Calgaro CO et al (2015) Surface modification of chitin using ultrasound-assisted and supercritical CO_2 technologies for cobalt adsorption. J Hazard Mater 295:29–36. https://doi.org/10.1016/j.jhazmat.2015.04.009

10. Marques JL Jr, Lütke SF, Frantz TS et al (2018) Removal of Al (III) and Fe (III) from binary system and industrial effluent using chitosan films. Int J Biol Macromol 120:1667–1673. https://doi.org/10.1016/j.ijbiomac.2018.09.135
11. Chauhan D, Jaiswal M, Sankararamakrishnan N (2012) Removal of cadmium and hexavalent chromium from electroplating waste water using thiocarbamoyl chitosan. Carbohyd Polym 88:670–675. https://doi.org/10.1016/j.carbpol.2012.01.014
12. Santosa SJ, Siswanta D, Sudiono S et al (2008) Chitin-humic acid hybrid as adsorbent for Cr(III) in effluent of tannery wastewater treatment. Appl Surf Sci 254:7846–7850. https://doi.org/10.1016/j.apsusc.2008.02.102
13. Fagundes T, Bachmann AWL, Tomaz HSO et al (2008) Adsorção de arsênio(V) pela quitosana ferro—III reticulada. Quim Nova 31:1305–1309
14. Vitali L, Laranjeira MCM, de Fávere VT (2008) Microencapsulação do agente quelante sulfoxina em microesferas de quitosana preparadas por spray drying como novo adsorvente para íons metálicos. Quim Nova 31:1400–1404
15. Silva RC, Andrade MAS Jr, Cestari AR (2010) Adsorção de Cr (VI) em esferas reticuladas de quitosana—novas correlações cinéticas e termodinâmicas utilizando microcalorimetria isotérmica contínua. Quim Nova 33:880–884
16. Pakdel PM, Peighambardoust SJ (2018) Review on recent progress in chitosan-based hydrogels for wastewater treatment application. Carbohyd Polym 201:264–279. https://doi.org/10.1016/j.carbpol.2018.08.070
17. Sarode S, Upadhyay P, Khosa MA et al (2019) Overview of wastewater treatment methods with special focus on biopolymer chitin-chitosan. Int J Biol Macromol 121:1086–1100. https://doi.org/10.1016/j.ijbiomac.2018.10.089

Application of Ferrite Nanoparticles in Wastewater Treatment

Janio Venturini

Abstract This chapter describes aspects of the application of spinel ferrite nanoparticles (SFNPs) in the purification of water bodies and wastewater. The structural and magnetic properties of these ferrimagnetic systems are described. Several synthesis methods are illustrated, with special focus on green processes. Furthermore, the adsorption of inorganic and organic contaminants is discussed, and several recently published adsorbent/adsorbate systems are presented. The utilization of spinel ferrites in the photodegradation of organic materials is also examined. Finally, the recovery and recycling aspects of the utilization of ferrite nanoparticles in the purification of wastewater are also presented.

Keywords Ferrites · Spinel · Wastewater treatment · Adsorption

Abbreviations

CNT	Carbon nanotube
CR	Congo red
GO	Graphene oxide
MB	Methylene blue
rGO	Reduced graphene oxide
SFNP	Spinel ferrite nanoparticles
UV	Ultraviolet
XRD	X-ray diffraction

J. Venturini (✉)
Universidade Federal Do Rio Grande Do Sul, Porto Alegre, Brazil
e-mail: janio.venturini@ufrgs.br

A. Kopp Alves (ed.), *Nanomaterials for Eco-friendly Applications*,
Engineering Materials, https://doi.org/10.1007/978-3-030-26810-7_9

1 Introduction

Water is an essential element for life, as well as an economic resource of the utmost importance. Nevertheless, a large percentage of the water available on the surface of Earth is not suitable for human or industrial use. Furthermore, enormous quantities of wastewater are generated daily. Though modern water treatment facilities can remove most of the contaminants from these effluents, several harmful ions and emerging organic contaminants might remain in the water. Therefore, it may require a final polishing process for the removal of such compounds.

One of these polishing processes is the adsorption of the remaining contaminants. These pollutants are removed via their chemisorption or physisorption onto the surface of a solid. Owing to their naturally high specific surface area, nanoparticles are widely studied for their application in the adsorption of compounds. Nevertheless, the separation of these adsorbents from the purified liquid can be a painstaking process, given their minute dimensions. Furthermore, the effects of these nanoparticles on the environment and on human health are very poorly understood; therefore, their total removal from treated water is paramount.

In this regard, magnetic nanoparticles circumvent such a hurdle: their removal from water can be conducted via the simple application of a magnetic field on the system. Special attention has been paid to one particular family of nanoparticles: the spinel ferrites.

2 Spinel Ferrites

Spinel ferrites are a family of transition metal oxides with the chemical formula MFe_2O_4, where M is usually a divalent cation [1]. Such compounds are widely regarded as non-toxic and chemically and mechanically stable, and they display interesting magnetic properties. The prototypical example of this family is magnetite (Fe_3O_4), where divalent iron occupies the M site. These materials crystallize in the spinel space group ($Fd\bar{3}m$, no 227), with a face-centered cubic packing of oxygen ions and the divalent and trivalent cations populating the tetrahedral and octahedral voids, respectively. A representation of the spinel structure is displayed in Fig. 1. Such arrangement is commonly found in zinc ferrite ($ZnFe_2O_4$) [2] and manganese ferrite ($MnFe_2O_4$) [3].

The spinel structure is actually much more flexible than most other structures. The divalent and trivalent cations can occupy both tetrahedral and octahedral sublattices, adding much more room for the variation of the properties displayed by these materials. In the previously described arrangement, with the divalent and trivalent cations in the tetrahedral and octahedral sites, respectively, the material is said to be a normal spinel. On the other hand, if the divalent cations fill the octahedral sites, thus forcing half of the trivalent atoms into the tetrahedral void, the framework is

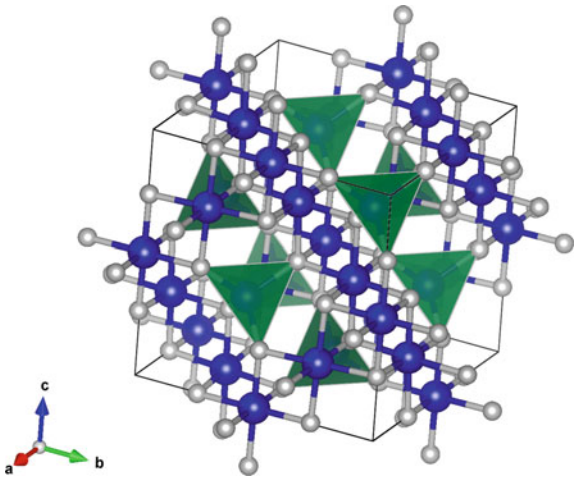

Fig. 1 Schematic representation of the crystal structure of spinel ferrites. Oxygen atoms are represented by white spheres, while the blue spheres represent the metal in the octahedral site. The tetrahedral position is highlighted as the green polyhedron

called an inverse spinel. This is usually the configuration of magnetite (Fe_3O_4) [4] and cobalt ferrite ($CoFe_2O_4$) [5].

In reality, most spinel ferrites can be found somewhere in between these two extremes; such configuration is known as a mixed spinel. The degree of inversion (x) of the spinel quantifies the extent of the cationic interchange: normal spinels display an inversion of zero, while inverse spinels have the maximum value of degree of inversion, namely one. The mathematical definition of the inversion degree is shown in Eq. (1), where M_{oct} and M_{tet} are the number of divalent cations in the tetrahedral and octahedral sublattices, respectively.

$$x = \frac{M_{oct}}{M_{tet} + M_{oct}} \tag{1}$$

The degree of inversion is an important parameter in wastewater treatment for several reasons. For one, it might determine the population of surface groups available for the adsorption of contaminants. Furthermore, the cationic arrangement dictates the electronic structure of ferrites and, therefore, the photocatalytic capacity of the systems [6]. Finally, the ferrimagnetism of spinel ferrites relies heavily on the AB interaction, which exhibits the largest exchange integral in spinel frameworks [7]. One can logically infer from this fact that the atoms in the A and B positions (tetrahedral and octahedral, respectively) and, hence, the inversion degree are of great importance in the definition of the magnetic properties of ferrites. Amongst several other methods, this configurational parameter is empirically assessed most usually via X-ray diffraction [8] and Raman [9] and Mössbauer spectroscopies [10].

The structural arrangement is usually dictated by the composition of the ferrites. Cations with larger radii have a natural tendency to populate the octahedral site, which, in comparison, is much larger than the tetrahedral position (0.414R against 0.255R) [11]. On the other hand, valence also plays a role in the determination of

the inversion degree of ferrite. Trivalent iron should be most stable in the octahedral position, where it coordinates to six oxygen anions—against only four in the tetrahedral site. Nevertheless, several other parameters play significant roles in the final cationic arrangement of ferrites. The synthesis conditions can strongly define the framework displayed by these spinels [12–14].

3 Synthesis

Several methods of synthesis of spinel ferrite nanoparticles (SFNPs) can be found in the literature. This section will enumerate a few of the most economically and environmentally interesting processes.

Sol-gel synthesis is one of the methods most commonly utilized in literature for the production of spinel ferrite nanoparticles, particularly via the citrate-nitrate method [15, 16]. The utilization of mostly non-toxic reagents and the decreased generation of effluents help explain the recent interest in this method. Furthermore, the large number of parameters that can be modified in the sol-gel synthesis adds flexibility to the production of nanoparticles. It is widely regarded as an interesting method for the preparation of crystalline, homogeneous, and high-purity materials [17].

Co-precipitation is also a very common method in the preparation of SFNPs. It allies cost-effectiveness to the production of very narrow size distributions [18, 19]. The method commonly consists in the dropwise addition of an alkali to acid solutions containing the precursor cations [20].

Another method that should be cited is the ferritization of metallic sludge. This method is even more environmentally-friendly than those cited previously, given the utilization of waste material in the production of SNFPs. Precursor cations can be leached from sludge and further reacted with iron to form the adsorbent ferrite, further reducing the economic cost of the synthesis. For instance, nanoferrites have recently been prepared from iron scale waste via the controlled crystallization of ferrites in a vitreous matrix [21].

After being prepared by the aforementioned processes, spinel ferrite nanoparticles can be further varied by surface modification. The attachment of different functional groups to the surface of the nanoparticles adds extra flexibility to these magnetic systems. The functional groups can be carefully chosen to ensure favorable interaction with the desired contaminant, guaranteeing increased removal capacities and rates. Some of the functional groups most commonly utilized in the modification of nanoferrites are depicted in Fig. 2.

Besides surface functionalization, another very common method in the utilization of spinel ferrites for wastewater recovery is the design of composites of these materials. For instance, the decoration of carbon nanotubes or graphene with SFNPs is a common strategy utilized to increase the adsorptive surface and to reach performances unattainable by spinel ferrites alone. A schematic representation of the most common composite strategies is shown in Fig. 3.

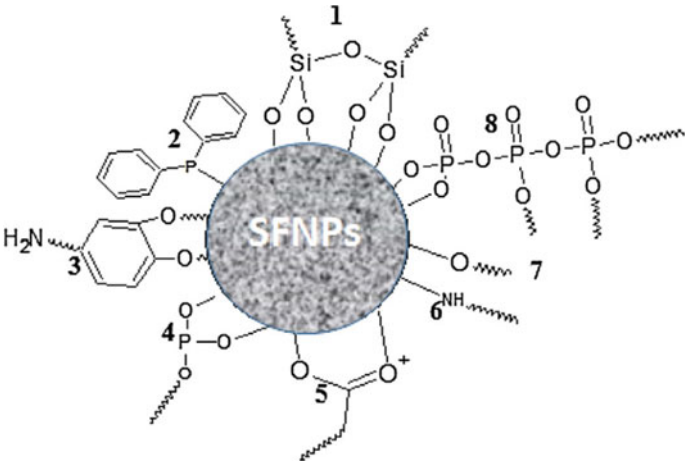

Fig. 2 Schematic representation of the groups most commonly utilized in the functionalization of spinel ferrite nanoparticles: 1. trimethoxy silane; 2. diphenyl phosphine; 3. dopamine 1,2-diol; 4. phosphoric acid; 5. carboxylic acids; 6. amines; 7. alcohols; and 8. triphosphines. Reproduced from Ref. [22] with permission from Elsevier

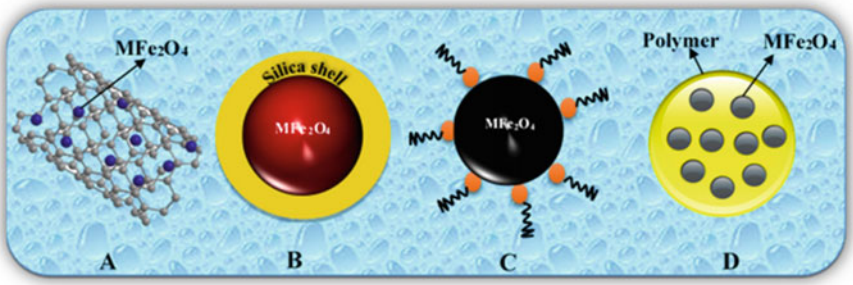

Fig. 3 Examples of the several possible spinel ferrite composites: **a** carbon nanotubes decorated with nanoparticles; **b** core-shell structures; **c** surfactant-coated nanoferrites; and **d** nanoparticles in a polymer matrix. Reproduced from Ref. [23] with permission from Elsevier

The materials synthesized by the methods described previously are utilized in the remediation of water bodies via two main strategies. The first of these processes is via the direct adsorption of contaminants.

4 Adsorption

Metallic ions are particularly concerning contaminants due to their possibly very deleterious effects on the human body. Nanometric spinel ferrites are especially

suited for the adsorption of these ions due to their inherent inorganic character, which facilitates the removal of metals when compared to carbonaceous structures, for instance. Furthermore, their applicability is also enhanced by the non-toxicity, recyclability and ease of separation of spinel ferrites.

SFNPs have already shown great promise in the removal of highly toxic metals from solutions. For instance, several radionuclides have been successfully removed from solution via their adsorption onto nickel ferrite/graphene oxide composites [24]. Table 1 shows some literature data on the adsorption performance of selected metals onto SFNPs.

Also, where organic contaminants are concerned, spinel ferrites show great promise as advanced adsorbents. For instance, nanoparticles of $CaFe_2O_4$ have been reported to display a very rapid and selective absorption of organic dyes [29]. Figure 4 depicts one such outstanding example of these systems, with the adsorption of Congo Red onto $CoFe_2O_4$ nanoparticles and the subsequent magnetic separation of the SFNPs. A plethora of literature on the adsorption of model organic dyes is currently available; some selected adsorbent/adsorbate systems and their performances are shown in Table 2.

Besides the aforementioned removal mechanisms, organic pollutants can also be removed from wastewater by spinel ferrites via another process: photodegradation.

Table 1 Selected examples of adsorption of inorganic ions onto spinel ferrite magnetic nanoparticles

Adsorbent	Size (nm)	Specific area (m^2/g)	Pollutant	Capacity (mg/g)	References
$CuFe_2O_4$/DC	17.91	16.96	Pb(II)	921.1	[25]
$MnFe_2O_4$/GO	20	67.5	As(V)	240.4	[26]
$CoFe_2O_4$	20	–	Cs(I)	75	[27]
Fe_3O_4	–	109.6	U(IV)	52.63	[28]
$NiFe_2O_4$/rGO	32.2	167.3	Th(IV)	100	[24]

Fig. 4 Adsorption of congo red dye onto $CoFe_2O_4$ nanoparticles, with posterior magnetic separation of the adsorbent. Reproduced from Ref. [30] with permission from Elsevier

Table 2 Selected examples of adsorption of organic compounds onto spinel ferrite magnetic nanoparticles

Adsorbent	Size (nm)	Specific area (m^2/g)	Dye	Capacity (mg/g)	References
$CoFe_2O_4$	9–21	31.2	RR195	91.7	[31]
$MnFe_2O_4$/GO	20	67.5	MB	177.3	[26]
$Ni_{0.5}Zn_{0.5}Fe_2O_4$	9	–	Alizarin	250	[32]
$CoFe_{1.9}Sm_{0.1}O_4$	11	–	CR	178.6	[33]
$CaFe_2O_4$	15–30	41.8	CR	40.9	[34]

5 Photodegradation

Fenton and photo-Fenton processes are commonplace in the current state of water treatment. The reagent comprises H_2O_2 and a ferrous ion (Fe^{2+}) source. In a simplified mechanism, the metal aids the decomposition of the peroxide into OH radicals, while generating a ferric ion (Fe^{3+}). The radicals, in turn, react with organic matter, decomposing it. Given the high rate of recombination of the said radicals, UV photons are also commonly utilized to accelerate the breakdown of the peroxide, in the thus-known photo-Fenton process.

Nevertheless, the iron ions remain in the liquid current, requiring a second unit operation in order to achieve full purification of the processed water. In this regard, the utilization of a magnetic heterogeneous catalyst containing iron—namely, ferrites—simplifies the treatment process. Despite the great majority of ferrites not containing the ferrous ion, the divalent cation present in their structure can also create hydroxyl ions; a possible mechanism is shown in Fig. 5.

Nowadays, a wide body of literature on the heterogeneous Fenton process utilizing SFNPs can be found. A selected number of such catalytic systems is displayed in Table 3.

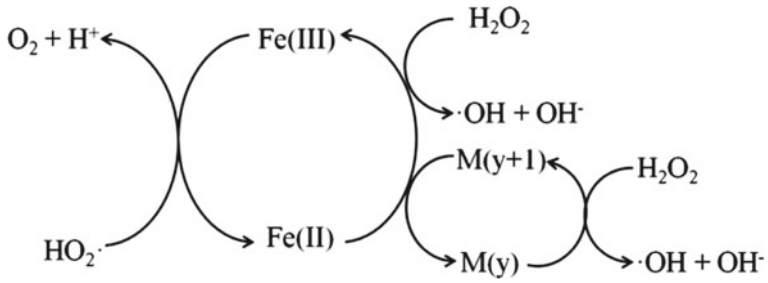

Fig. 5 Mechanism proposed by He et al. [35] for the participation of the M cation (where M is the divalent cation in the MFe_2O_4 spinel structure) in the heterogeneous Fenton process. Reproduced from Ref. [35] with permission from Elsevier

Table 3 Selected examples of heterogeneous Fenton processes utilizing spinel ferrite nanoparticles as catalyst

Adsorbent	Size (nm)	Specific area (m^2/g)	Decomposed compound	Apparent reaction rate (min^{-1})	References
$ZnFe_2O_4$	30.06	151	MB	0.267	[36]
$MgFe_2O_4$	20	14	MB	0.117	[37]
$NiFe_2O_4$/CNT	–	54	Amaranth	0.017	[38]
Doped $MgFe_2O_4$	52	141.5	RhB	0.0197	[39]
$CoFe_2O_4$	25.3	48.6	DCP	0.0273	[40]

6 Recycling

The most alluring characteristic of water decontamination via the utilization of spinel ferrites is the magnetic character of these particles. Usually, decontamination with non-magnetic materials involves a secondary purification or filtration process for the recovery of solid particles of the bed from the purified current. These additional unit operations incur in a large economic cost and do not guarantee that the catalyst/adsorbent is indeed removed from the processed liquid. This is a particularly difficult problem to overcome; despite being viable options in the recovery of wastewater, the direct health effects of most nanoparticles are still to be studied. The utilization of magnetic materials circumvents such hindrances; the application of a magnetic field ensures the successful separation of the solid particles from the exiting liquid current (Fig. 6).

After recovery, a desorption process can be applied to the solid and the SFNPs can be reutilized in the same process. Indeed, the number of cycles to which the

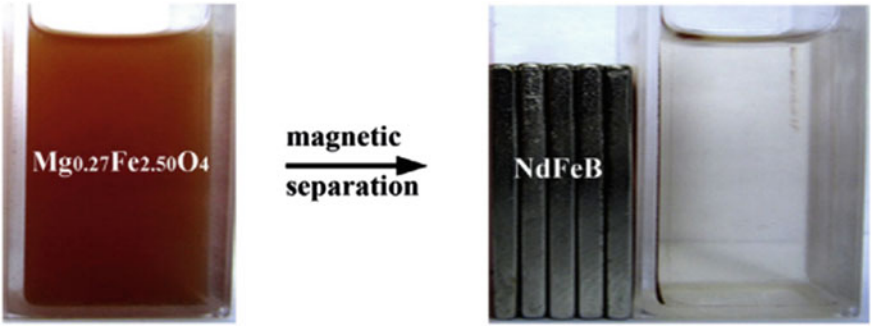

Fig. 6 Magnetic separation of superparamagnetic $Mg_{0.27}Fe_{2.50}O_4$ ferrite from test solution after arsenic adsorption essays. The left and right vessels show the behavior of the fine particles without and with the application of an external magnetic field, respectively. Reproduced from Ref. [41] with permission from Elsevier

spinel ferrites can be submitted depends mostly on the chemicals utilized in the desorption processes. These are usually strong acids or alkalis, which can react with the ferrite and thus diminish its adsorption capacity. Hao et al. reported adsorption stability over 15 cycles when applying modified Fe_3O_4 nanoparticles in the removal of Cu(II) [42].

7 Conclusion

The topics discussed in this chapter demonstrate the flexibility of spinel ferrites in the purification of contaminated water. Besides their inherent low toxicity and chemical stability, these materials are also economically interesting due to their ease of separation from the purified stream. Whether via adsorption or degradation processes, these nanoparticles show great promise for future application in water treatment systems.

References

1. Mathew DS, Juang RS (2007) An overview of the structure and magnetism of spinel ferrite nanoparticles and their synthesis in microemulsions. Chem Eng J 129:51–65
2. Hastings JM, Corliss LM (1953) Neutron diffraction studies of zinc ferrite and nickel ferrite. Rev Mod Phys 25:114–119. https://doi.org/10.1103/RevModPhys.25.114
3. Carta D, Casula MF, Falqui A et al (2009) A Structural and magnetic investigation of the inversion degree in ferrite nanocrystals mfe2o4 (M = Mn Co, Ni). J Phys Chem C 113:8606–8615. https://doi.org/10.1021/jp901077c
4. Torruella P, Ruiz-Caridad A, Walls M et al (2018) Atomic-Scale Determination of Cation Inversion in Spinel-Based Oxide Nanoparticles. Nano Lett 18:5854–5861. https://doi.org/10.1021/acs.nanolett.8b02524
5. Concas G, Spano G, Cannas C et al (2009) Inversion degree and saturation magnetization of different nanocrystalline cobalt ferrites. J Magn Magn Mater 321:1893–1897. https://doi.org/10.1016/J.JMMM.2008.12.001
6. Tiano AL, Papaefthymiou GC, Lewis CS et al (2015) Correlating size and composition-dependent effects with magnetic, mössbauer, and pair distribution function measurements in a family of catalytically active ferrite nanoparticles. Chem Mater 27:3572–3592. https://doi.org/10.1021/acs.chemmater.5b00767
7. Sawatzky GA, Van Der Woude F, Morrish AH (1969) Mössbauer study of several ferrimagnetic spinels. Phys Rev 187:747–757. https://doi.org/10.1103/PhysRev.187.747
8. Zampiva RYS, Kaufmann CG, Alves AK, Bergmann CP (2018) Influence of the fuel composition and the fuel/oxidizer ratio on the combustion solution synthesis of MgFe2O4 catalyst nanoparticles. FME Trans 46:157–164. https://doi.org/10.5937/fmet1802157Z
9. Venturini J, Tonelli AM, Wermuth TB et al (2019) Excess of cations in the sol-gel synthesis of cobalt ferrite (CoFe2O4): a pathway to switching the inversion degree of spinels. J Magn Magn Mater 482:1–8. https://doi.org/10.1016/j.jmmm.2019.03.057
10. Venturini J, Piva DH, da Cunha JBM, Bergmann CP (2016) Effect of the thermal treatment on the magnetic and structural properties of cobalt ferrite particles. Ceram Int. https://doi.org/10.1016/j.ceramint.2016.06.120

11. Hou YH, Zhao YJ, Liu ZW et al (2010) Structural, electronic and magnetic properties of partially inverse spinel CoFe2O4: A first-principles study. J Phys D Appl Phys 43. https://doi.org/10.1088/0022-3727/43/44/445003
12. Sawatzky GA, Van Der Woude F, Morrish AH (1968) Cation distributions in octahedral and tetrahedral sites of the ferrimagnetic spinel $CoFe_2O_4$. J Appl Phys 39:1204–1205. https://doi.org/10.1063/1.1656224
13. De Guire MR, O'Handley RC, Kalonji G (1989) The cooling rate dependence of cation distributions in cobalt ferrite ($CoFe_2O_4$). J Appl Phys 65:3167–3172. https://doi.org/10.1063/1.342667
14. Daffé N, Gavrilov V, Neveu S et al (2019) Small $CoFe_2O_4$ magnetic nanoparticles in ferrofluids, influence of the synthesis on the magnetic anisotropies. J Magn Magn Mater 477:226–231. https://doi.org/10.1016/J.JMMM.2019.01.048
15. Venturini J, Wermuth TB, Machado MC et al (2019) The influence of solvent composition in the sol-gel synthesis of cobalt ferrite ($CoFe_2O_4$): a route to tuning its magnetic and mechanical properties. J Eur Ceram Soc. https://doi.org/10.1016/j.jeurceramsoc.2019.01.030
16. Venturini J, Zampiva RYS, Piva DH et al (2018) Conductivity dynamics of metallic-to-insulator transition near room temperature in normal spinel $CoFe_2O_4$ nanoparticles. J Mater Chem C 6:4720–4726. https://doi.org/10.1039/C8TC00099A
17. Danks AE, Hall SR, Schnepp Z (2016) The evolution of 'sol–gel' chemistry as a technique for materials synthesis. Mater Horiz 3:91–112. https://doi.org/10.1039/C5MH00260E
18. Chinnasamy CN, Jeyadevan B, Perales-Perez O et al (2002) Growth dominant co-precipitation process to achieve high coercivity at room temperature in $CoFe_2O_4$ nanoparticles. IEEE Trans Magn 38:2640–2642. https://doi.org/10.1109/TMAG.2002.801972
19. Il Kim Y, Kim D, Lee CS (2003) Synthesis and characterization of CoFe2O4 magnetic nanoparticles prepared by temperature-controlled coprecipitation method. Phys B Condens Matter 337:42–51. https://doi.org/10.1016/S0921-4526(03)00322-3
20. Stein CR, Bezerra MTS, Holanda GHA et al (2017) Structural and magnetic properties of cobalt ferrite nanoparticles synthesized by co-precipitation at increasing temperatures. AIP Adv 8:56303. https://doi.org/10.1063/1.5006321
21. Avancini TG, Souza MT, de Oliveira APN et al (2019) Magnetic properties of magnetite-based nano-glass-ceramics obtained from a Fe-rich scale and borosilicate glass wastes. Ceram Int 45:4360–4367. https://doi.org/10.1016/J.CERAMINT.2018.11.111
22. Kefeni KK, Mamba BB, Msagati TAM (2017) Application of spinel ferrite nanoparticles in water and wastewater treatment: A review. Sep Purif Technol 188:399–422. https://doi.org/10.1016/J.SEPPUR.2017.07.015
23. Reddy DHK, Yun Y-S (2016) Spinel ferrite magnetic adsorbents: alternative future materials for water purification? Coord Chem Rev 315:90–111. https://doi.org/10.1016/J.CCR.2016.01.012
24. Lingamdinne LP, Choi Y-L, Kim I-S et al (2017) Preparation and characterization of porous reduced graphene oxide based inverse spinel nickel ferrite nanocomposite for adsorption removal of radionuclides. J Hazard Mater 326:145–156. https://doi.org/10.1016/J.JHAZMAT.2016.12.035
25. Khan MA, Otero M, Kazi M et al (2019) Unary and binary adsorption studies of lead and malachite green onto a nanomagnetic copper ferrite/drumstick pod biomass composite. J Hazard Mater 365:759–770. https://doi.org/10.1016/J.JHAZMAT.2018.11.072
26. Lan Huong PT, Tu N, Lan H et al (2018) Functional manganese ferrite/graphene oxide nanocomposites: effects of graphene oxide on the adsorption mechanisms of organic MB dye and inorganic As(v) ions from aqueous solution. RSC Adv 8:12376–12389. https://doi.org/10.1039/C8RA00270C
27. Hassan MR, Aly MI (2019) Adsorptive removal of cesium ions from aqueous solutions using synthesized Prussian blue/magnetic cobalt ferrite nanoparticles. Part Sci Technol 1–11. https://doi.org/10.1080/02726351.2018.1539799
28. Li M, Liu H, Chen T et al (2019) Synthesis of magnetic biochar composites for enhanced uranium(VI) adsorption. Sci Total Environ 651:1020–1028. https://doi.org/10.1016/J.SCITOTENV.2018.09.259

29. Liu X, An S, Wang Y et al (2015) Rapid selective separation and recovery of a specific target dye from mixture consisted of different dyes by magnetic Ca-ferrites nanoparticles. Chem Eng J 262:517–526. https://doi.org/10.1016/J.CEJ.2014.10.002
30. Ding Z, Wang W, Zhang Y et al (2015) Synthesis, characterization and adsorption capability for Congo red of $CoFe_2O_4$ ferrite nanoparticles. J Alloys Compd 640:362–370. https://doi.org/10.1016/J.JALLCOM.2015.04.020
31. Nassar MY, Khatab M (2016) Cobalt ferrite nanoparticles via a template-free hydrothermal route as an efficient nano-adsorbent for potential textile dye removal. RSC Adv 6:79688–79705. https://doi.org/10.1039/C6RA12852A
32. Afkhami A, Sayari S, Moosavi R, Madrakian T (2015) Magnetic nickel zinc ferrite nanocomposite as an efficient adsorbent for the removal of organic dyes from aqueous solutions. J Ind Eng Chem 21:920–924. https://doi.org/10.1016/J.JIEC.2014.04.033
33. Wu X, Ding Z, Song N et al (2016) Effect of the rare-earth substitution on the structural, magnetic and adsorption properties in cobalt ferrite nanoparticles. Ceram Int 42:4246–4255. https://doi.org/10.1016/J.CERAMINT.2015.11.100
34. An S, Liu X, Yang L, Zhang L (2015) Enhancement removal of crystal violet dye using magnetic calcium ferrite nanoparticle: Study in single- and binary-solute systems. Chem Eng Res Des 94:726–735. https://doi.org/10.1016/J.CHERD.2014.10.013
35. He J, Yang X, Men B, Wang D (2016) Interfacial mechanisms of heterogeneous Fenton reactions catalyzed by iron-based materials: a review. J Environ Sci 39:97–109. https://doi.org/10.1016/J.JES.2015.12.003
36. Sharma R, Bansal S, Singhal S (2015) Tailoring the photo-Fenton activity of spinel ferrites (MFe2O4) by incorporating different cations (M = Cu, Zn, Ni and Co) in the structure. RSC Adv 5:6006–6018. https://doi.org/10.1039/C4RA13692F
37. Ivanets A, Roshchina M, Srivastava V et al (2019) Effect of metal ions adsorption on the efficiency of methylene blue degradation onto $MgFe_2O_4$ as Fenton-like catalysts. Colloids Surfaces A Physicochem Eng Asp 571:17–26. https://doi.org/10.1016/J.COLSURFA.2019.03.071
38. Rigo C, Severo EDC, Mazutti MA et al (2017) Preparation of nickel ferrite/carbon nanotubes composite by microwave irradiation technique for use as catalyst in photo-fenton reaction. Mater. Res 20:311–316
39. Diao Y, Yan Z, Guo M, Wang X (2018) Magnetic multi-metal co-doped magnesium ferrite nanoparticles: An efficient visible light-assisted heterogeneous Fenton-like catalyst synthesized from saprolite laterite ore. J Hazard Mater 344:829–838. https://doi.org/10.1016/J.JHAZMAT.2017.11.029
40. Nair DS, Kurian M (2017) Heterogeneous catalytic oxidation of persistent chlorinated organics over cobalt substituted zinc ferrite nanoparticles at mild conditions: Reaction kinetics and catalyst reusability studies. J Environ Chem Eng 5:964–974. https://doi.org/10.1016/J.JECE.2017.01.021
41. Tang W, Su Y, Li Q et al (2013) Superparamagnetic magnesium ferrite nanoadsorbent for effective arsenic (III, V) removal and easy magnetic separation. Water Res 47:3624–3634. https://doi.org/10.1016/J.WATRES.2013.04.023
42. Hao Y-M, Man C, Hu Z-B (2010) Effective removal of Cu (II) ions from aqueous solution by amino-functionalized magnetic nanoparticles. J Hazard Mater 184:392–399. https://doi.org/10.1016/j.jhazmat.2010.08.048

Synthesis of Potassium Niobate ($KNbO_3$) for Environmental Applications

Tiago Bender Wermuth

Abstract In recent years, environmental issues have become increasingly significant, mainly due to the contamination of water resources by chemicals and pharmaceuticals, such as medicines, disinfectants, contrast media, detergents, pesticides, dyes, paints, preservatives. Advanced techniques, such as advanced oxidative processes (AOPs), are being studied and improved for the removal of these contaminants in wastewater. Among some AOPs we can mention the use of heterogeneous photocatalysis process using materials based on perovskite (e.g. $KNbO_3$) due to their different properties, such as ferroelectricity, optics and applications involving photocatalysis. The use of these materials has provided an improvement in photocatalytic activity through permanent internal polarization that can effectively separate the photoexcited charge carriers and effectively increase the efficiency of the degradation process.

Keywords Perovskite · Potassium niobate · Microwave-assisted hydrothermal method · Photocatalytic application

Abbreviations

AOPs	Advanced oxidative processes
COD	Chemical oxygen demand
DRAM	Dynamic randon acess memory
SEM	Scanning electron microscopy
T_C	Curie temperature
TEM	Transmission electron microscopy
UV irradiation	Ultraviolet irradiation

T. B. Wermuth (✉)
Universidade Federal do Rio Grande do Sul, Porto Alegre, Brazil
e-mail: tiago.wermuth@ufrgs.br

A. Kopp Alves (ed.), *Nanomaterials for Eco-friendly Applications*,
Engineering Materials, https://doi.org/10.1007/978-3-030-26810-7_10

1 Introduction

The contamination of water bodies with industrial effluents and wastewater has caused serious problems to the environment. Numerous treatment technologies have been developed for environmental remediation, among them the Advanced Oxidative Processe (AOPs) [1]. In this process, the mineralization of the great majority of organic contaminants occurs by their transformation into carbon dioxide, water and inorganic anions.

Among the (AOPs), the heterogeneous photocatalysis process has been widely used for the degradation of organic pollutants [2]. Among the various classes of materials studied, perovskite photocatalysts have begun to attract attention due to their unique photophysical properties that offer great advantages.

Niobium-based perovskites ($ANbO_3$, A = Na, K, Ag, Cu) have attracted great interest from the scientific community due to excellent non-linear optical properties, ferroelectricity, piezoelectricity, pyroelectricity and photocatalytic properties. Potassium niobate ($KNbO_3$), for example, has a band-gap value ranging from 3.08 to 3.15 eV [3]. Under UV irradiation, this material exhibits promising photocatalytic properties.

In addition, the modification of band-gap structure may improve photocatalytic activity under visible light [4]. It is a perovskite that exhibits low toxicity and high stability under light irradiation. Several methods of synthesis have been used to prepare and obtain $KNbO_3$, such as solid state method [5], sol-gel method [6], polymeric precursor method [7], conventional hydro/solvotermal method [8] and microwave-assisted hydrothermal [9]. In this context, the aim of this chapter is to describe materials with perovskite structure, mainly $KNbO_3$ and their different methods of production. It should be noted that the combination of different synthesis processes, such as the microwave-assisted hydrothermal method, with the modification of the synthesis parameters allows the preparation of different $KNbO_3$ morphologies for applications in processes involving photodegradation [10].

2 Materials with Perovskite Structure

Perovskite of type ABO_3 has a cubic crystalline structure. The ions that form part of this composition are the metal cations (A and B) and the non-metallic anion (O). The atoms of element A occupy the vertices of the octahedral, while the atoms of oxygen are located on the octahedron faces, forming an octahedral structure. For temperatures above the Curie temperature (Tc), the element B atom is located in the center of the octahedron. For such temperatures, there is no dipole moment formation in the material. For temperatures below the Curie temperature (Tc), the B atom undergoes displacement along the c-axis, generating charge densities in the extreme oxygens of the octahedron, giving the system a dipole moment, creating the property of ferroelectricity [11, 12]. Figure 1 shows the crystalline structure (ABO_3)

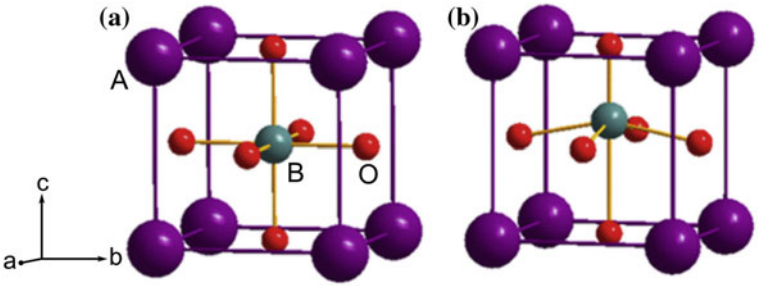

Fig. 1 Example of perovskite structure ABO_3 of **a** cubic symmetry and **b** tetragonal symmetry. Reprinted with permission from [13]

with cation A or B at the origin of the unit cell.

Among the compounds belonging to the perovskite family, there are potassium niobate ($KNbO_3$), lithium niobate ($LiNbO_3$) and sodium niobate ($NaNbO_3$), which are known as alkaline niobates and have presented interesting scientific and technological properties, for example, ferroelectricity, piezoelectricity, pyroelectricity, non-linear electro-optical behavior [25] and also photocatalytic properties [26] [1–5] (Table 1).

2.1 Potassium Niobate ($KNbO_3$)

Potassium niobate ($KNbO_3$) is a ferroelectric compound with a perovskite-like crystalline structure with temperature-dependent crystalline phases, including rhombohedral (−70 °C), orthorhombic (−10 °C), tetragonal (230 °C) and cubic (500 °C) [4]. The last two transitions occur above the room temperature, so the crystal loses its ferroelectricity in the transition from the tetragonal to the cubic phase (708 K), passing to a paraelectric phase [27]. Figure 2 shows the phase transitions of $KNbO_3$ with increasing temperature.

Due to their applications in different technological fields, such as optical, electro-optical and non-linear devices [9] the $KNbO_3$ has attracted significant attention from the scientific community. Also, it also has excellent photocatalytic properties under UV irradiation (band gap in the range of 3.08–3.14 eV).

The $KNbO_3$ can be synthesized by different methods, such as solid state reaction [5, 29], sol-gel, hydrothermal [30, 31] and hydrothermal microwave assisted [32, 22]. The $KNbO_3$ can be obtained with different morphologies and has received considerable attention because it presents attractive properties, mainly related to dimensional confinement. Anisotropic one-dimensional (1D) nanostructures, for example, can improve photocatalytic performance by adjusting the direction and path of photogenerated charge carriers through quantum confinement, minimizing recombination between electrons and holes [33, 34].

Table 1 Types of perovskites and some applications of the material

Oxides type—Perovskites (ABO_3)	Crystalline structure	Properties	Applications
$BaTiO_3$	Cubic	Dielectric	Ceramic capacitors, dynamic random access memory (DRAM), sensors and electro-optical devices [14–16]
$SrTiO_3$	Cubic	Dielectric	Accumulators, oxygen sensors and photocatalysts [17–19]
$KNbO_3$	Cubic, Orthorhombic, Rhombohedral, Tetragonal	Electro-optics ferroelectric photocatalytic	Waveguides, photocatalysts, sensors, actuators and holographic storage systems [20–22]
$LiNbO_3$	Rhombohedral	Dielectric	Non-linear optical devices, electro-optical modulators, capacitors and optical memories [23, 24]

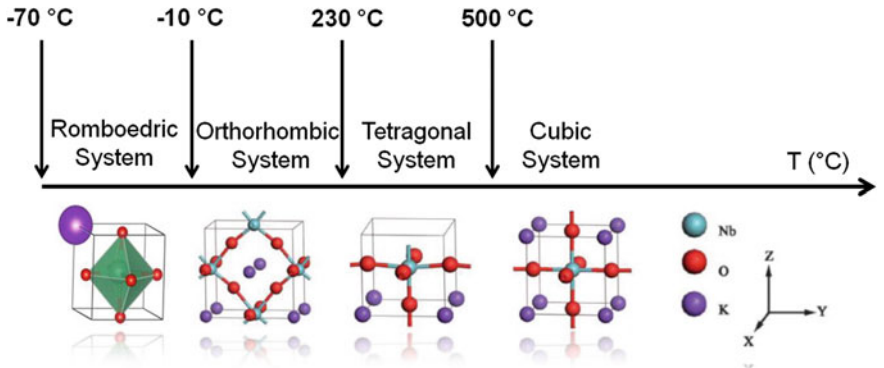

Fig. 2 Phase transitions of the $KNbO_3$ crystal structure with increasing temperature. Adapted from Hewat [28]. Reprinted with permission from Zhang et al. [3]

2.2 $KNbO_3$ Synthesis Methods

There are several techniques for the synthesis of perovskites (ABO_3). Among the different methods, it can be mention the most used for $KNbO_3$ production: solid-state reaction, sol-gel, hydrothermal and hydrothermal-assisted microwave method.

The solid-state reaction method is an essential method for the synthesis of inorganic ceramic powders. During a process, two or more compounds or elemental substances are mixed and react in the solid state at high temperatures, thereby generating new materials with bulk or powdered morphologies. Solid-state reactions have been widely used in various industries, such as high-temperature ceramics, electronic ceramics and even superconducting materials [35]. Chaiyo et al. [5] investigated the synthesis of $KNbO_3$ nanoparticles through the solid-state reaction method with a low reaction temperature using potassium oxalate as a precursor. The crystallite size ranged from 36 ± 8 to 58 ± 6 nm, and the particle size (SEM) was 278 ± 75 nm. Figure 3 shows the SEM images of heat treated $KNbO_3$ powders (a) 550 °C and (b) 700 °C, respectively.

The sol-gel method can be described as a chemical process used to synthesize inorganic oxides by the preparation of a sol. Sol can be well-defined as a colloidal dispersion, in which the dispersion medium is the liquid. The gel may, however, be characterized as a substance containing a solid-solid network formed by the establishment of bonds between the particles or between the molecular species of the sol which forms an interconnected three-dimensional structure which immobilizes the liquid phase at its interstices. When the liquid phase is removed by drying at atmospheric pressure, the wet gel is converted into a xerogel and, when the liquid phase is removed above a critical pressure, it is converted into an airgel [36].

In the polymeric sol-gel type method, the oxides which will give rise to the perovskites are formed from polymeric gels. After the choice of the polymer precursors, the sol-gel method follows with the crystalline particles obtained by polymerization

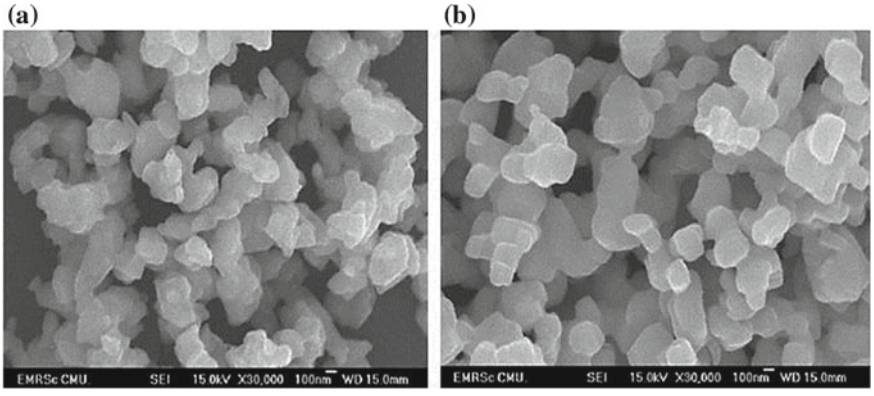

Fig. 3 Morphology of $KNbO_3$ powders synthesized by the solid-state reaction method and heat treated **a** 500 °C and **b** 700 °C. Reprinted with permission from Chaiyo et al. [5]

reactions based on the hydrolysis and condensation of these precursors. These reactions can be performed at lower temperatures (~25 °C) [37]. The gel is formed by the interaction between the polymer chains, resulting from the polymerization of the precursors. The decomposition of the precursor leads to the formation of particles, usually of an intermediate solid, forming a sol [38]. The next step is gelation, in which the formation of the gel is formed by the formation of bonds between the particles or between the molecular species of the sol. In the gelling step, gel molding can be made in structures close to the final shape of the product.

Cao et al. [6] investigated the synthesis of $KNbO_3$ by the sol-gel technique using a mixture of complexing agents (ethylene diamine tetraacetic acid- EDTA/citrate) with niobium and potassium precursors. The xerogel were heat treated at 700 and 850 °C. The authors obtained grain size (~60 nm) when $KNbO_3$ powders were thermally treated at 850 °C with a K/Nb molar ratio equals 1:2.

In addition to the sol-gel method, another technique that deserves to be highlighted about the synthesis of ferroelectric nanostructures, such as alkaline niobates [8], is the hydrothermal synthesis [39].

The method generally involves heterogeneous chemical reactions in aqueous medium above room temperature (greater than 100 °C) under pressure levels greater than 1 atm [35]. High pressure is required to maintain a solution phase (liquid phase with dissolved salts) at elevated temperatures. This phase in solution works as a medium for mass transport, promoting rapid kinetics of phase transformation. In this way, this technique is well indicated for the preparation of particles with high crystallinity [40].

The main difference between this method and traditional methods (oxide mixing) for the synthesis of ceramic materials is the non-use of high heat treatment temperatures. Another important factor is the absence of milling steps. The products are formed directly in the aqueous medium. Also, by varying specific reaction parameters (pH, temperature, time, pressure), it is possible to produce crystalline powders with particles of size, shape and controlled stoichiometry [40].

Wang et al. [32] investigated the effects of the KOH concentration (10–30 M) on the $KNbO_3$ morphology synthesized by the hydrothermal method at a temperature of 200 °C for 12 h. Nanoblasts with lengths ranging from 1.7 to 6.5 μm and diameter in the range of 90–230 nm were obtained with a concentration of 10 M KOH. When KOH concentration was increased to 30 M, $KNbO_3$ nanocubes having a size ranging from 150 to 450 nm were obtained. Figure 4 presents SEM images of the KOH concentration variation to obtain different $KNbO_3$ morphologies.

Although the hydrothermal technique is a consolidated method for the synthesis of materials, one of the main limitations is the long synthesis time (many hours or days) for the complete reaction of the system [41]. The chemical reactions in this method take approximately 12 to 48 h, leading to the nucleation and growth of homogeneous particles. The concentration of the precursor in the hydrothermal route plays a vital role in the formation of the phase and the morphology of the material to be obtained. That is why the concentration is an essential factor in the reaction kinetics, influencing the mobility of the suspended particles and the proportion of effective shocks [42].

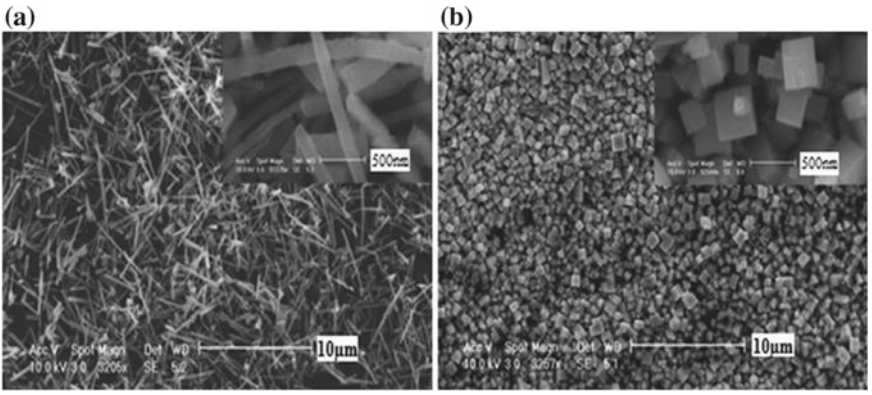

Fig. 4 SEM images of different $KNbO_3$ morphologies **a** concentration of 10 M KOH **b** concentration of 30 M KOH synthesized by hydrothermal method at 200 °C for 12 h. Reprinted with permission from Wang et al. [32]

The combination of the hydrothermal method with the microwave effect allows (i) a high heating rate; (ii) reduction in the time of synthesis; (iii) higher reaction rate as a function of a uniform microwave heating during the hydrothermal method [43]. This mechanism accelerates the crystallization process of the synthesized products by increasing the nucleation rate [44].

The microwaves are electromagnetic waves with frequencies between 0.3 and 300 GHz. One of the main characteristics is their ability to warm up rapidly the materials based on the interactions of the molecules with the electromagnetic field. This heating, unlike the conventional one, occurs from the core, that is, as the microwaves penetrate, the heat is generated from inside out, leading to faster and uniform heating. The heating mechanism involves two types of processes: dipolar polarization and ionic conduction. The irradiation of a sample with microwaves results in the alignment of the dipoles or ions in the electric field. As a consequence of the oscillating field produced by the electromagnetic radiation, the dipoles or ions try to align themselves with the electric field. If the dipole does not have enough time to realign (the frequency of the field is higher than the response time of the dipoles), or it easily keeps pace with the field changes (time change of direction of the electric field is higher than the response time of the dipoles), then no heating occurs [45].

In the case of ionic conduction, the dissolved charged particles oscillate back and forth under the influence of microwave irradiation, collide with neighboring molecules, thereby creating heat [45]. The creation of "hot spots" and the improved dissolution of the precursors can also promote the reactivity of the processes assisted by microwaves [46].

It is emphasized that the generated heating is dependent on the response of the material to the electric and magnetic field generated by the microwaves, that is, the ability of the materials to absorb and transform the electromagnetic energy into heat. The main properties that measure the response of a material to an electric field are

the dielectric constant and dielectric loss. The first determines the capacity of the material to store the electric energy, i.e., the polarization capacity of the molecules by the electric field; and the second, to determine the material ability to convert electrical power into heat [47, 48].

Compared to traditional methods, microwave heating is rapid volumetric heating without the process of conducting heat, in which it can achieve uniform heating in a short period [41]. It is further emphasized that the heating profile occurring in a conventional hydrothermal process is conduction and convection type [49].

The microwave-assisted hydrothermal synthesis begins with the homogeneous rapid heating process, caused by microwave dielectric heating, where the microwave energy is transmitted directly to the material (if it absorbs microwaves) or to the medium (H_2O), through molecule interactions with the electromagnetic field, generating molecular vibrations. These, by aligning and realigning with the oscillating field, cause, in some cases, effective shocks between the particles, leading to the formation of uniform and homogeneous nanoparticles [45, 47, 48, 50].

As a consequence, the precipitation of the particles from the solutions tends to be rapid and almost simultaneous, leading to the formation in the final product of small particles and of narrow size distribution [51].

Paula et al. [9] synthesized one-dimensional (1D) nanostructures of $KNbO_3$ through microwave-assisted hydrothermal synthesis. $KNbO_3$ powders with morphology in the form of nanofingers were obtained in a period of 1 to 12 h of reaction. The crystallization in the form of nanofingers was achieved after 1, 2 and 4 h of reaction. Longer reaction times caused the degradation of one-dimensional morphology (1D). Figure 5 presents SEM and TEM images of the $KNbO_3$ nanofingers synthesized by the microwave-assisted hydrothermal method.

Wermuth et al. [10] investigated the effects of the molar ratio of niobium and potassium precursors on the morphology and structure of potassium niobate powders prepared via microwave hydrothermal-assisted synthesis and their optical properties. It was possible to obtain nanostructured $KNbO_3$ using microwave-assisted hydrothermal synthesis, in reduced synthesis times (30–240 min), at a temperature of 200 °C. The time of synthesis directly influenced the crystallinity of the phases formed due to the crystallization kinetics increase caused by the microwaves. The morphology of $KNbO_3$ synthesized with orthorhombic symmetry is dependent on the time of synthesis and the molar ratio [Nb_2O_5: KOH] ([1:8] to [1:16] M). The band-gap energy for the different molar proportions presented similar values, ranging from 3.1 to 3.3 eV, which indicates potential use in different applications in processes involving photodegradation, for example. Figure 6 shows the SEM images of the $KNbO_3$ powders synthesized with different molar ratios of the precursors by the microwave-assisted hydrothermal method.

Figure 7 shows the TEM images of the powders of $KNbO_3$ synthesized at different molar ratios of [Nb_2O_5: KOH]. It can be verified that the longer synthesis time favored the ordered growth of the $KNbO_3$ structure.

The band-gap energies (Eg) of samples synthesized at 200 °C at different synthesis times in the [1:8], [1:12] and [1:16] molar ratios [Nb_2O_5: KOH] are shown in Table 2.

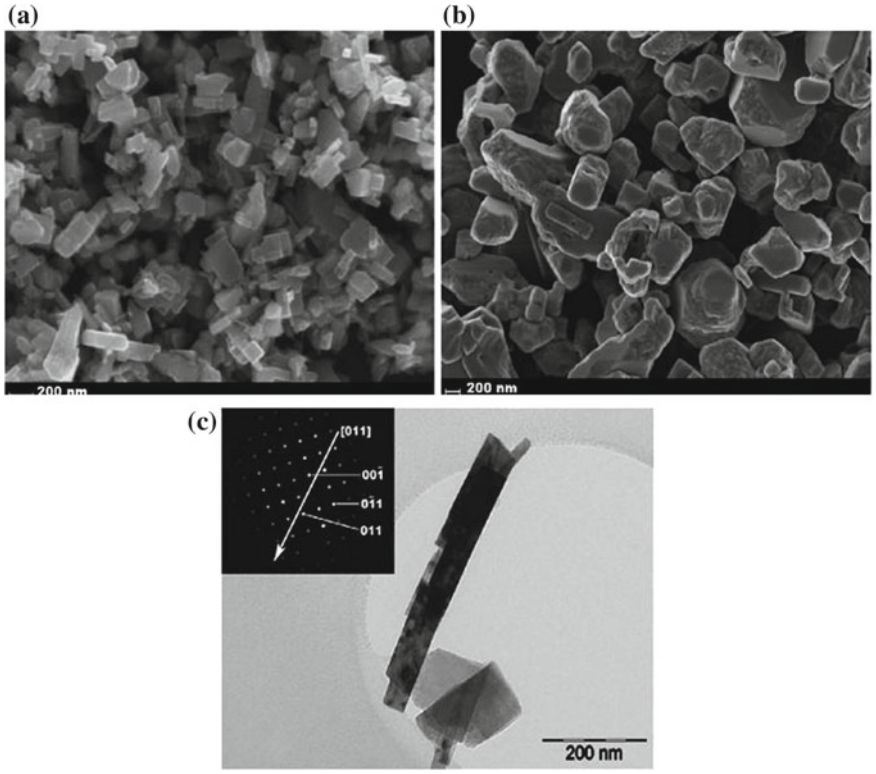

Fig. 5 Morphology of the powders obtained in different microwave-assisted hydrothermal synthesis times **a** 1 h (b) 12 h and the **c** TEM image of the $KNbO_3$ nanofingers after a 1 h reaction. Reprinted with permission from Paula et al. [9]

The combination of the microwave heating process with the modification of the synthesis parameters allows the preparation of different $KNbO_3$ morphologies for application in operations involving photodegradation [10].

2.3 Environmental Applications of Perovskites

The use of materials belonging to the family of perovskites has provided an improvement in processes involving photocatalysis since these materials present unique properties such as the generation of a photovoltage and photocurrent along the direction of spontaneous polarization [52] and the possibility of separation of the photoexcited charges [53]. As shown in Fig. 8, the ferroelectric polarization produces opposite charges on the surface of the c+ and c− domains. The depolarization fields that act to display the charge on the surface cause the photo-generated charge carriers to sep-

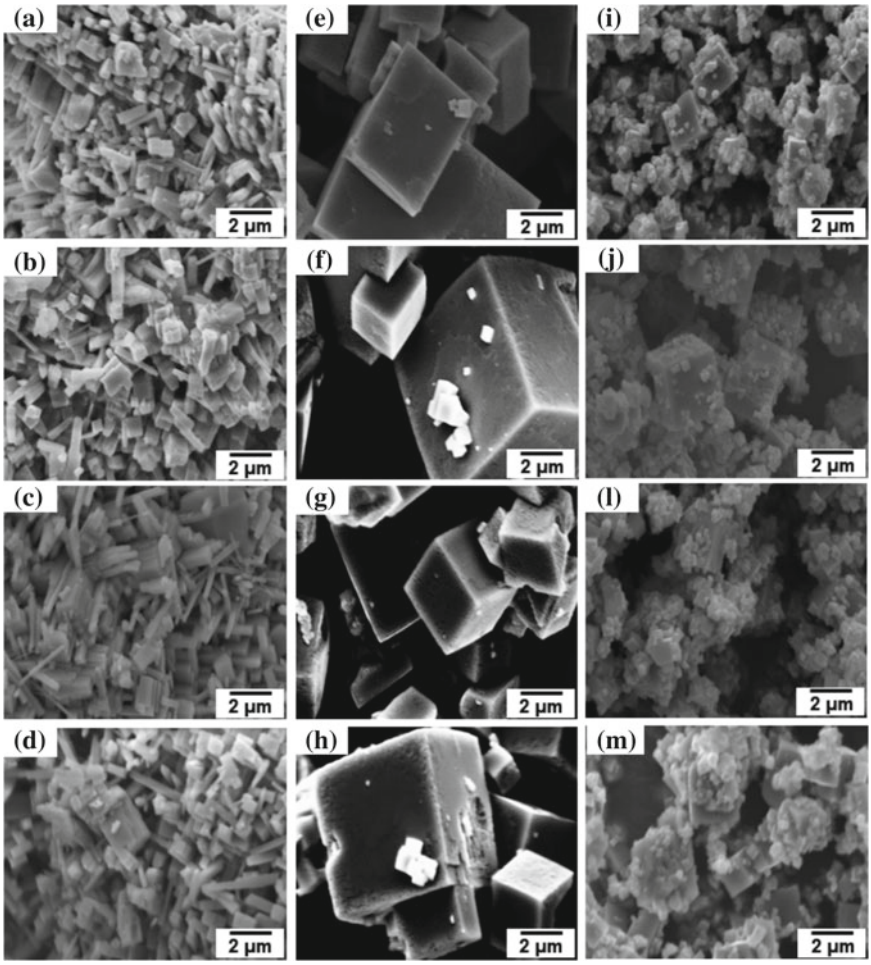

Fig. 6 SEM images of $KNbO_3$ powders synthesized by microwave hydrothermal-assisted synthesis at 200 °C, the function of both synthesis duration and KOH concentrations: [1:8] **a** 30 min, **b** 60 min, **c** 120 min, **d** 240 min; [1:12] **e** 30 min, **f** 60 min, **g** 120 min, **h** 240 min; [1:16], **i** 30 min, **j** 60 min, **l** 120 min and **m** 240 min. Reprinted with permission from [10]

arate and move in opposite directions. Electrons form a charge accumulation region in the c+ domain, and the gap transporters form a charge depletion region in the c− domains. In this way, the oxidation and photochemical reduction sites are spatially distinct.

Due to this peculiarity concerning the structural characteristics of the perovskite family, its use in environmental processes, mainly in photocatalysis, began to be investigated by different researchers. The Table 3 lists some of the works developed with different perovskite oxides with potential for application in processes involving photocatalysis.

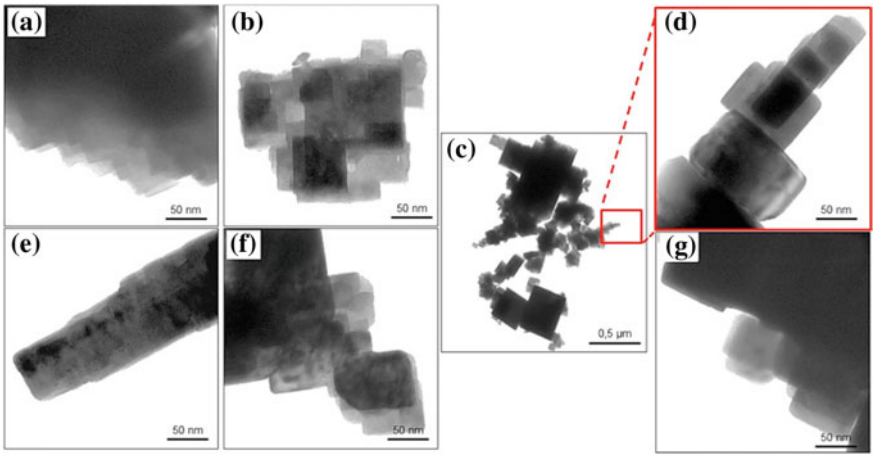

Fig. 7 TEM images of $KNbO_3$ powders synthesized by microwave hydrothermal-assisted synthesis at 200 °C, a function of both synthesis duration and KOH concentrations: [1:8] **a** 30 min **e** 240 min; [1:12] **b** 30 min **f** 240 min; [1:16] **c** and **d** 30 min **g** 240 min. Reprinted with permission from [10]

Table 2 Band-gap energies (Eg) of products from microwave hydrothermal-assisted synthesis at 200 °C as a function of both synthesis duration and molar ratios. Reprinted with permission from [10]

Synthesis duration (min)	Band-gap (eV)		
	[1:8]	[1:12]	[1:16]
30	3.14 ± 0.50	3.21 ± 1.03	3.37 ± 0.30
60	3.15 ± 0.26	3.20 ± 0.71	3.35 ± 0.25
120	3.16 ± 0.27	3.23 ± 0.84	3.38 ± 0.49
240	3.15 ± 0.01	3.20 ± 0.87	3.36 ± 0.29

The literature reports some studies involving the use of perovskites for the degradation of drugs. Among some perovskite type oxides is lanthanum ferrite ($LaFeO_3$), used for the removal of drugs contained in wastewater. Among the main features of this perovskite, a band-gap with narrow electronic bands stands out, making it a promising candidate for the applications involving photocatalysis [78, 79].

Hu et al. [80] synthesized $LaFeO_3$ and La_2FeTiO_6 by sol-gel methods and evaluated their potency as photocatalysts by assessing the degradation for p-chlorophenol under visible light. The sub-stoichiometric perovskite La_2FeTiO_6 showed degradation of 62.1% of p-chlorophenol with 56.6% of chemical oxygen demand (COD) after 5 h of visible light irradiation, while $LaFeO_3$ degraded 49.0% of p -chlorophenol with 45.1% removal of COD under the same conditions. The higher surface area and lower particle size contributed to the excellent photocatalytic activities of La_2FeTiO_6.

In order to evaluate the applicability of perovskites containing copper, Carrasco-Díaz et al. [81], synthesized $LaCu_{1-x}M_xO_3$ (with M = Mn, Ti at $0 \leq x \leq 0.8$) for paracetamol degradation. Manganese and titanium were chosen as metals in position B. From the analysis of the results of the present study, it was possible to observe

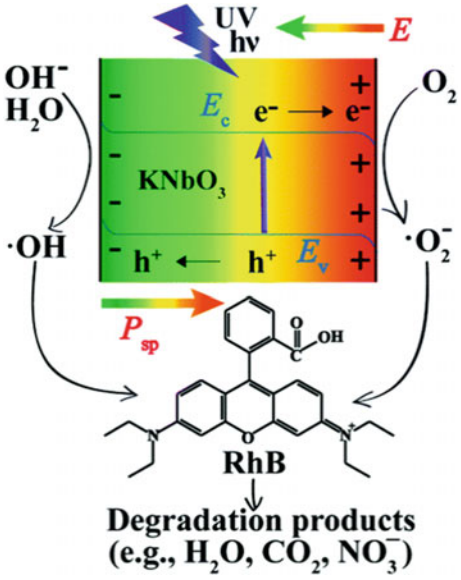

Fig. 8 Schematic representation of charge separation of $KNbO_3$ under the incidence of radiation (UV-Vis). Reprinted with permission from Zhang et al. [21]. Published by The Royal Society of Chemistry

that perovskite type $LaCu_{1-x}M_xO_3$ oxides (with M = Mn, Ti at $0 \leq x \leq 0.8$) pre-prepared by amorphous citrate decomposition exhibited high activity and stability for the degradation of paracetamol with H_2O_2 under mild pH conditions. A fraction of the organic pollutant was removed by adsorption; however, most of the clearance of paracetamol was produced by photo-Fenton reaction with H_2O_2. The decomposition of H_2O_2 decreased in the presence of paracetamol, which can be interpreted in terms of a competitive effect between the organic pollutant and the H_2O_2 by the active centers of the catalysts. From the XPS analysis, it was possible to verify that Cu^{2+}/Cu^{+} is the species with the highest catalytic activity. The high copper stability in the mixed oxide network and the negligible metal leaching in the solution, make these mixed oxides candidates to promote the catalysis of drugs in aqueous solutions [81].

3 Conclusion

In recent years, a significant number of works involving the synthesis, processing, characterization and properties of perovskites have been developed. This chapter deals with the different types of perovskites, properties, methods of synthesis and the main applications of these materials, especially in processes involving the photodegradation of organic pollutants. Among these materials, it is possible to highlight the studies focused on niobium perovskites ($ANbO_3$, A = Na, K, Ag, Cu), especially potassium niobate ($KNbO_3$). The properties presented in the course of this chapter demonstrate the potential use of these materials in the most varied fields.

Table 3 Perovskite oxides with potential application in photocatalysis. Reprinted with permission from Grabowska [4]

Perovskite—Oxide type ABO_3		Band-gap	Crystalline structure	References
BO_3	A			
(A)TiO_3	$SrTiO_3$	3.1–3.7	Cubic	[54]
	$BaTiO_3$	3.0–3.3	Cubic	[55]
	$CaTiO_3$	3.6	Cubic and orthromrobic	[56]
	$MaTiO_3$	3.1	Rhombohedral	[57]
	$CoTiO_3$	2.28	Rhombohedral	[58]
	$FeTiO_3$	2.8	Rhombohedral	[59]
	$PbTiO_3$	2.75	Tetragonal	[60]
(A)NbO_3	$KNbO_3$	3.14–3.24	Cubic, rhombohedral, orthromrobic and tetragonal	[3]
	$NaNbO_3$	3.0–3.5	Cubic, tetragonal and orthromrobic	[61]
	$AgNbO_3$	2.7	Orthromrobic	[11]
	$CuNbO_3$	2.0	Monoclinic	
	$LiNbO_3$	3.78	Rhombohedral	[62, 63]
	$SrNbO_3$	2.79	Cubic	[64, 64]
(A)VO_3	$PbVO_3$	2.93	Cubic	[65]
	$SrVO_3$	3.22	Cubic	
	$BaVO_3$	3.2	Cubic	
	$LaVO_3$	0.9–1.2	Orthromrobic	[66]
	YVO_3	1.6	Orthromrobic	[67]
(A)FeO_3	$LaFeO_3$	2.1	Cubic and orthromrobic	[68, 69]
	$BiFeO_3$	2.0–2.7	Rhombohedral	[70]
	$GaFeO_3$	2.7	Orthromrobic	[71]
	$YFeO_3$	2.43	Orthromrobic	[72]
(A)BiO_3	$LiBiO_3$	1.63	Orthromrobic	[73, 74]
	$KBiO_3$	2.04	Cubic	
(A)SnO_3	$SrSnO_3$	4.1	Orthromrobic	[75]
	$BaSnO_3$	3.0	Cubic	[76]
	$CaSnO_3$	3.8–4.96	Hexagonal, rhombohedral and orthromrobic	[77]

The ferroelectricity of this family of materials, allied to the band-gap situated in a very interesting region for environmental applications, make this material extremely interesting for future application as an eco-friendly photocatalyst.

References

1. Kanakaraju D, Glass BD, Oelgemöller M (2018) Advanced oxidation process-mediated removal of pharmaceuticals from water: a review. J Environ Manage 219:189–207. https://doi.org/10.1016/j.jenvman.2018.04.103
2. Dewil R, Mantzavinos D, Poulios I, Rodrigo MA (2017) New perspectives for advanced oxidation processes. J Environ Manage 195:93–99. https://doi.org/10.1016/j.jenvman.2017.04.010
3. Zhang T, Zhao K, Yu J, Jin J, Qi Y, Li H, Hou X, Liu G (2013) Photocatalytic water splitting for hydrogen generation on cubic, orthorhombic, and tetragonal $KNbO_3$ microcubes. Nanoscale 5:8375. https://doi.org/10.1039/c3nr02356g
4. Grabowska E (2016) Selected perovskite oxides: Characterization, preparation and photocatalytic properties—A review. Appl Catal B Environ 186:97–126. https://doi.org/10.1016/j.apcatb.2015.12.035
5. Chaiyo N, Ruangphanit A, Muanghlua R, Niemcharoen S, Boonchom B, Vittayakorn N (2011) Synthesis of potassium niobate ($KNbO_3$) nano-powder by a modified solid-state reaction. J Mater Sci 46:1585–1590. https://doi.org/10.1007/s10853-010-4967-5
6. Cao Y, Zhu K, Qiu J, Pang X, Ji H (2012) Sol-gel processing and characterization of potassium niobate nano-powders by an EDTA/citrate complexing method. Solid State Sci 14:655–660. https://doi.org/10.1016/j.solidstatesciences.2012.03.011
7. Simões AZ, Ries A, Riccardi CS, Gonzalez AH, Zaghete MA, Stojanovic BD, Cilense M, Varela JA (2004) Potassium niobate thin films prepared through polymeric precursor method. Mater Lett 58:2537–2540. https://doi.org/10.1016/j.matlet.2004.03.025
8. Shi G, Wang J, Wang H, Wu Z, Wu H (2017) Hydrothermal synthesis of morphology-controlled $KNbO_3$, $NaNbO_3$, and (K, Na) NbO_3 powders. Ceram Int 43:7222–7230. https://doi.org/10.1016/j.ceramint.2017.03.012
9. Paula AJ, Parra R, Zaghete MA, Varela JA (2008) Synthesis of $KNbO_3$ nanostructures by a microwave assisted hydrothermal method. Mater Lett 62:2581–2584. https://doi.org/10.1016/j.matlet.2007.12.059
10. Wermuth TB, Baibich MN, Ribeiro TMH, Bergmann CP (2018) The rapid synthesis of nanostructured orthorhombic $KNbO_3$ particles by a microwave-assisted hydrothermal method and their characterization. Ceram Int 44:4758–4765. https://doi.org/10.1016/j.ceramint.2017.12.060
11. Kanhere P, Chen Z (2014) A Review on visible light active perovskite-based photocatalysts. Molecules 19:19995–20022. https://doi.org/10.3390/molecules191219995
12. Zhao Z, Buscaglia V, Viviani M, Buscaglia MT, Mitoseriu L, Testino A, Nygren M, Johnsson M, Nanni P (2004) Grain-size effects on the ferroelectric behavior of dense nanocrystalline $BaTiO_3$ ceramics. Phys Rev B—Condens Matter Mater Phys 70. https://doi.org/10.1103/physrevb.70.024107
13. Cheng L-Q, Li J-F (2016) A review on one dimensional perovskite nanocrystals for piezoelectric applications. J Mater 2:25–36. https://doi.org/10.1016/j.jmat.2016.02.003
14. Lu W, Quilitz M, Schmidt H (2007) Nanoscaled $BaTiO_3$ powders with a large surface area synthesized by precipitation from aqueous solutions: preparation, characterization and sintering. J Eur Ceram Soc 27:3149–3159. https://doi.org/10.1016/j.jeurceramsoc.2007.01.002
15. George CN, Thomas JK, Kumar HP, Suresh MK, Kumar VR, Wariar PRS, Jose R, Koshy J (2009) Characterization, sintering and dielectric properties of nanocrystalline barium titanate

synthesized through a modified combustion process. Mater Charact 60:322–326. https://doi.org/10.1016/j.matchar.2008.09.012
16. Harizanov O, Harizanova A, Ivanova T (2004) Formation and characterization of sol-gel barium titanate. Mater Sci Eng B Solid-State Mater Adv Technol 106:191–195. https://doi.org/10.1016/j.mseb.2003.09.014
17. Du Y, Peng HY, Mao H, Jin KX, Wang H, Li F, Gao XY, Chen W, Wu T (2015) Evolution of the $SrTiO_3$–MoO_3 Interface Electronic Structure: An in Situ Photoelectron Spectroscopy Study. ACS Appl Mater Interfaces 7:11309–11314. https://doi.org/10.1021/acsami.5b01698
18. Yu T, Hu W, Jia L, Tan X, Huang J, Huang X (2015) Enhanced photoelectrochemical performance of coaxial-nanocoupled strontium-Rich SrTiO3/TiO2 001 nanotube arrays. Ind Eng Chem Res 54:8193–8200. https://doi.org/10.1021/acs.iecr.5b01903
19. Sharma P, Ryu S, Burton JD, Paudel TR, Bark CW, Huang Z, Tsymbal EY, Catalan G, Eom CB, Gruverman A (2015) Mechanical tuning of LaAlO3/SrTiO3 interface conductivity. Nano Lett 15:3547–3551. https://doi.org/10.1021/acs.nanolett.5b01021
20. Wang G, Selbach SM, Yu Y, Zhang X, Grande T, Einarsrud M-A (2009) Hydrothermal synthesis and characterization of $KNbO_3$ nanorods. CrystEngComm 11:1958. https://doi.org/10.1039/b907561p
21. Zhang T, Lei W, Liu P, Rodriguez JA, Yu J, Qi Y, Liu G, Liu M (2015) Insights into the structure–photoreactivity relationships in well-defined perovskite ferroelectric $KNbO_3$ nanowires. Chem Sci 6:4118–4123. https://doi.org/10.1039/C5SC00766F
22. Krad I, Bidault O, Said S, El Maaoui M (2015) Characterization of $KNbO_3$ nanoplates synthesized by a stirred hydrothermal process. Mater Lett 159:237–240. https://doi.org/10.1016/j.matlet.2015.06.121
23. Cruickshank FR (1992) Ferroelectric Materials and their Applications. J Mod Opt 39:1162–1163. https://doi.org/10.1080/09500349214551191
24. Maldonado-Orozco MC, Ochoa-Lara MT, Sosa-Márquez JE, Olive-Méndez SF, Pizá-Ruiz P, Quintanar-Sierra JJC, Espinosa-Magaña F (2017) Characterization of Mn-doped electrospun $LiNbO_3$ nanofibers by Raman spectroscopy. Mater Charact 127:209–213. https://doi.org/10.1016/j.matchar.2017.03.008
25. Nico C, Monteiro T, Graça MPF (2016) Niobium oxides and niobates physical properties: review and prospects. Prog Mater Sci 80:1–37. https://doi.org/10.1016/j.pmatsci.2016.02.001
26. Jiang L, Qiu Y, Yi Z (2013) Potassium niobate nanostructures: controllable morphology, growth mechanism, and photocatalytic activity. J Mater Chem A 1:2878. https://doi.org/10.1039/c2ta01056a
27. Ramos-Moore E, Baier-Saip JA, Cabrera AL (2006) Desorption of carbon dioxide from small potassium niobate particles induced by the particles' ferroelectric transition. Surf Sci 600:3472–3476. https://doi.org/10.1016/j.susc.2006.06.037
28. Hewat AW (1973) Cubic-tetragonal-orthorhombic-rhombohedral ferroelectric transitions in perovskite potassium niobate: Neutron powder profile refinement of the structures. J Phys C: Solid State Phys 6:2559–2572. https://doi.org/10.1088/0022-3719/6/16/010
29. Kinoshita T, Senna M, Doshida Y, Kishi H (2012) Synthesis of size controlled phase pure $KNbO_3$ fine particles via a solid-state route from a core-shell structured precursor. Ceram Int 38:1897–1904. https://doi.org/10.1016/j.ceramint.2011.10.018
30. Czechowska K, Psiuk B, Wrzalik R, Szade J, Burdyl M, Śliwa A, Stec K (2014) Preparation of $KNbO_3$ powders by sol-gel method using water-soluble potassium and niobium compounds as precursors. Glas Phys Chem 40. https://doi.org/10.1134/s1087659614010064
31. Amini MM, Mirzaee M (2009) Effect of solvent and temperature on the preparation of potassium niobate by hydrothermal-assisted sol-gel processing. Ceram Int 35:2367–2372. https://doi.org/10.1016/j.ceramint.2009.01.009
32. Wang R, Zhu Y, Qiu Y, Leung CF, He J, Liu G, Lau TC (2013) Synthesis of nitrogen-doped $KNbO_3$ nanocubes with high photocatalytic activity for water splitting and degradation of organic pollutants under visible light. Chem Eng J 226:123–130. https://doi.org/10.1016/j.cej.2013.04.049

33. Vayssieres L, Sathe C, Butorin SM, Shuh DK, Nordgren J, Guo J (2005) One-Dimensional quantum-confinement effect in α-Fe_2O_3 ultrafine nanorod arrays. Adv Mater 17:2320–2323. https://doi.org/10.1002/adma.200500992
34. Mohapatra SK, John SE, Banerjee S, Misra M (2009) Water photooxidation by smooth and ultrathin α-Fe_2O_3 nanotube arrays. Chem Mater 21:3048–3055. https://doi.org/10.1021/cm8030208
35. Liang L, Kang X, Sang Y, Liu H (2016) One-dimensional ferroelectric nanostructures: synthesis, properties, and applications. Adv Sci 3:1500358. https://doi.org/10.1002/advs.201500358
36. Moreno R (2012) Colloidal processing of ceramics and composites. Adv Appl Ceram 111:246–253. https://doi.org/10.1179/1743676111Y.0000000075
37. Wang Y, Xu G, Yang L, Ren Z, Wei X, Weng W, Du P, Shen G, Han G (2009) Preparation of single-crystal $PbTiO_3$ nanorods by phase transformation from $Pb_2Ti_2O_6$ nanorods. J Alloys Compd 481:27–30. https://doi.org/10.1016/j.jallcom.2009.03.073
38. Brinker CJ, Scherer GW (1990) Sol-gel science. Elsevier. https://doi.org/10.1016/c2009-0-22386-5
39. Paula AJ de [UNESP] (2008) Síntese de templates para aplicação em piezocerâmicas livre de chumbo. Universidade Estadual Paulista (UNESP)
40. Meng L-Y, Wang B, Ma M-G, Lin K-L (2016) The progress of microwave-assisted hydrothermal method in the synthesis of functional nanomaterials. Mater Today Chem 1–2:63–83. https://doi.org/10.1016/j.mtchem.2016.11.003
41. Byrappa K, Yoshimura M (2013) Handbook of hydrothermal technology. Elsevier. https://doi.org/10.1016/c2009-0-20354-0
42. López-Juárez R, Castañeda-Guzmán R, Villafuerte-Castrejón ME (2014) Fast synthesis of $NaNbO_3$ and $K_{0.5}Na_{0.5}NbO_3$ by microwave hydrothermal method. Ceram Int 40:14757–14764. https://doi.org/10.1016/j.ceramint.2014.06.065
43. Mazzo TM, Moreira ML, Pinatti IM, Picon FC, Leite ER, Rosa ILV, Varela JA, Perazolli LA, Longo E (2010) $CaTiO_3$:Eu^{3+} obtained by microwave assisted hydrothermal method: A photoluminescent approach. Opt Mater (Amst) 32:990–997. https://doi.org/10.1016/j.optmat.2010.01.039
44. Bilecka I, Niederberger M (2010) Microwave chemistry for inorganic nanomaterials synthesis. Nanoscale 2:1358. https://doi.org/10.1039/b9nr00377k
45. Patzke GR, Zhou Y, Kontic R, Conrad F (2011) Oxide nanomaterials: synthetic developments, mechanistic studies, and technological innovations. Angew. Chemie—Int. Ed. 50:826–859. https://doi.org/10.1002/anie.201000235
46. Bhattacharya M, Basak T (2016) A review on the susceptor assisted microwave processing of materials. Energy 97:306–338. https://doi.org/10.1016/j.energy.2015.11.034
47. Mirzaei A, Neri G (2016) Microwave-assisted synthesis of metal oxide nanostructures for gas sensing application: a review. Sens Actuators B Chem 237:749–775. https://doi.org/10.1016/j.snb.2016.06.114
48. Sousa Filho PC, de Serra OA (2015) liquid phase synthesis methodologies for the obtainment of rare earth-based inorganic nanomaterials. Quim Nova 38:679–696. https://doi.org/10.5935/0100-4042.20150049
49. Zhu XH, Hang QM (2013) Microscopical and physical characterization of microwave and microwave-hydrothermal synthesis products. Micron 44:21–44. https://doi.org/10.1016/j.micron.2012.06.005
50. Eliziário SA (2010) Síntese de perovskitas nanométricas com estrutura $Pb_{1-x}M_xTiO_3$ (M = Ba, Ca e Sr). Programa Pós-Graduação em Química
51. Yuan Y, Xiao Z, Yang B, Huang J (2014) Arising applications of ferroelectric materials in photovoltaic devices. J Mater Chem A 2:6027–6041. https://doi.org/10.1039/C3TA14188H
52. Khan MA, Nadeem MA, Idriss H (2016) Ferroelectric polarization effect on surface chemistry and photo-catalytic activity: A review. Surf Sci Rep 71:1–31. https://doi.org/10.1016/j.surfrep.2016.01.001
53. van Benthem K, Elsässer C, French RH (2001) Bulk electronic structure of $SrTiO_3$: Experiment and theory. J Appl Phys 90:6156. https://doi.org/10.1063/1.1415766

54. Maeda K (2014) Rhodium-doped barium titanate perovskite as a Stable p-type semiconductor photocatalyst for hydrogen evolution under visible light. ACS Appl Mater Interfaces 6:2167–2173. https://doi.org/10.1021/am405293e
55. Zhang H, Chen G, He X, Xu J (2012) Electronic structure and photocatalytic properties of Ag-La codoped $CaTiO_3$. J Alloys Compd 516:91–95. https://doi.org/10.1016/j.jallcom.2011.11.142
56. Dong W, Wang D, Jiang L, Zhu H, Huang H, Li J, Zhao H, Li C, Chen B, Deng G (2013) Synthesis of F doping $MnTiO_3$ nanodiscs and their photocatalytic property under visible light. Mater Lett 98:265–268. https://doi.org/10.1016/j.matlet.2013.02.056
57. Lu J, Jiang Y, Zhang Y, Huang J, Xu Z (2015) Preparation of gas sensing $CoTiO_3$ nanocrystallites using EDTA as the chelating agent in a sol–gel process. Ceram Int 41:3714–3721. https://doi.org/10.1016/j.ceramint.2014.11.044
58. Tang X, Hu K (2006) The formation of ilmenite $FeTiO_3$ powders by a novel liquid mix and H_2/H_2O reduction process. J Mater Sci 41:8025–8028. https://doi.org/10.1007/s10853-006-0908-8
59. Joseph J, Vimala TM, Sivasubramanian V, Murthy VRK (2000) Structural investigations on $Pb(Zr_xT_{1-x})O_3$ solid solutions using the X-ray Rietveld method. J Mater Sci 35:1571–1575. https://doi.org/10.1023/A:1004778223721
60. Wu SY, Liu XQ, Chen XM (2010) Hydrothermal synthesis of $NaNbO_3$ with low NaOH concentration. Ceram Int 36:871–877. https://doi.org/10.1016/j.ceramint.2009.11.006
61. Nath RK, Zain MFM, Kadhum AAH (2012) New material $LiNbO_3$ for photocatalytically improvement of indoor air—An overview. Adv Nat Appl Sci 6:1030–1035. ISSN: 19950772
62. Postnikov AV, Caciuc V, Borstel G (2000) Structure optimization and frozen phonons in $LiNbO_3$. J Phys Chem Solids 61:295–299. https://doi.org/10.1016/S0022-3697(99)00296-6
63. Shein IR, Kozhevnikov VL, Ivanovskii AL (2008) First-principles calculations of the elastic and electronic properties of the cubic perovskites $SrMO_3$ (M = Ti, V, Zr and Nb) in comparison with $SrSnO_3$. Solid State Sci 10:217–225. https://doi.org/10.1016/j.solidstatesciences.2007.09.013
64. Yan SY, Xie Y, Liu T, Yu HT (2010) Electronic structures and ferroelectric instabilities of cubic AVO_3(A = Sr, Ba, and Pb) perovskites by first-principles calculations. J Phys Condens Matter 22 https://doi.org/10.1088/0953-8984/22/12/125501
65. Lüders U, Li QR, Feyerherm R, Dudzik E (2014) The evolution of octahedral rotations of orthorhombic $LaVO_3$ in superlattices with cubic $SrVO_3$. J Phys Chem Solids 75:1354–1360. https://doi.org/10.1016/j.jpcs.2014.07.007
66. Tsvetkov AA, Mena FP, Van Loosdrecht PHM, Van Der Marel D, Ren Y, Nugroho AA, Menovsky AA, Elfimov IS, Sawatzky GA (2004) Structural, electronic, and magneto-optical properties of YVO_3. Phys Rev B—Condens Matter Mater Phys 69. https://doi.org/10.1103/physrevb.69.075110
67. Thirumalairajan S, Girija K, Hebalkar NY, Mangalaraj D, Viswanathan C, Ponpandian N (2013) Shape evolution of perovskite $LaFeO_3$ nanostructures: a systematic investigation of growth mechanism, properties and morphology dependent photocatalytic activities. RSC Adv 3:7549. https://doi.org/10.1039/c3ra00006k
68. Thirumalairajan S, Girija K, Ganesh I, Mangalaraj D, Viswanathan C, Balamurugan A, Ponpandian N (2012) Controlled synthesis of perovskite $LaFeO_3$ microsphere composed of nanoparticles via self-assembly process and their associated photocatalytic activity. Chem Eng J 209:420–428. https://doi.org/10.1016/j.cej.2012.08.012
69. Humayun M, Zada A, Li Z, Xie M, Zhang X, Qu Y, Raziq F, Jing L (2016) Enhanced visible-light activities of porous $BiFeO_3$ by coupling with nanocrystalline TiO_2 and mechanism. Appl Catal B Environ 180:219–226. https://doi.org/10.1016/j.apcatb.2015.06.035
70. Dhanasekaran P, Gupta NM (2012) Factors affecting the production of H_2 by water splitting over a novel visible-light-driven photocatalyst $GaFeO_3$. Int J Hydrogen Energy 37:4897–4907. https://doi.org/10.1016/j.ijhydene.2011.12.068
71. Tang P, Chen H, Cao F, Pan G (2011) Magnetically recoverable and visible-light-driven nanocrystalline $YFeO_3$ photocatalysts. Catal Sci Technol 1:1145. https://doi.org/10.1039/c1cy00199j

72. Takei T, Haramoto R, Dong Q, Kumada N, Yonesaki Y, Kinomura N, Mano T, Nishimoto S, Kameshima Y, Miyake M (2011) Photocatalytic activities of various pentavalent bismuthates under visible light irradiation. J Solid State Chem 184:2017–2022. https://doi.org/10.1016/j.jssc.2011.06.004
73. Ramachandran R, Sathiya M, Ramesha K, Prakash AS, Madras G, Shukla AK (2011) ChemInform abstract: photocatalytic properties of $KBiO_3$ and $LiBiO_3$ with tunnel structures. cheminform 42:no-no. https://doi.org/10.1002/chin.201142010
74. Chen D, Ye JH (2007) $SrSnO_3$ nanostructures: Synthesis, characterization, and photocatalytic properties. Chem Mater 19:4585–4591. https://doi.org/10.1021/Cm071321d
75. Singh DJ, Xu Q, Ong KP (2014) Strain effects on the band gap and optical properties of perovskite $SrSnO_3$ and $BaSnO_3$. Appl Phys Lett 104:1–5. https://doi.org/10.1063/1.4861838
76. Henriques JM, Caetano EWS, Freire VN, Costa JAPD, Albuquerque EL (2007) Structural, electronic, and optical absorption properties of orthorhombic $CaSnO_3$ through ab initio calculations. J Phys: Condens Matter 19:106214. https://doi.org/10.1088/0953-8984/19/10/106214
77. Yang J, Zhong H, Li M, Zhang L, Zhang Y (2009) Markedly enhancing the visible-light photocatalytic activity of $LaFeO_3$ by post-treatment in molten salt. React Kinet Catal Lett. https://doi.org/10.1007/s11144-009-0025-1
78. Tang P, Tong Y, Chen H, Cao F, Pan G (2013) Microwave-assisted synthesis of nanoparticulate perovskite $LaFeO_3$ as a high active visible-light photocatalyst. Curr Appl Phys. https://doi.org/10.1016/j.cap.2012.08.006
79. Dhinesh Kumar R, Jayavel R (2014) Facile hydrothermal synthesis and characterization of $LaFeO_3$ nanospheres for visible light photocatalytic applications. J Mater Sci: Mater Electron 25:3953–3961. https://doi.org/10.1007/s10854-014-2113-x
80. Hu R et al (2012) Photocatalytic activities of $LaFeO_3$ and La_2FeTiO_6 in p-chlorophenol degradation under visible light. Catal Commun 29:35–39
81. Carrasco-Díaz MR, Castillejos-López E, Cerpa-Naranjo A, Rojas-Cervantes ML (2016) Efficient removal of paracetamol using $LaCu_{1-x}M_xO_3$ (M = Mn, Ti) perovskites as heterogeneous Fenton-like catalysts. Chem Eng J 304:408–418. https://doi.org/10.1016/j.cej.2016.06.054

Nano Magnetite Based Magnetic Glass-Ceramic Obtained from Wastes

Tales Gonçalves Avancini and Sabrina Arcaro

Abstract Nano magnetic glass-ceramics can be a great alternative to the traditional use of nanoparticles in the various fields of engineering and biomedicine. The ability to generate nanoparticles in a glassy matrix, protected from oxidative processes, and choose the appropriate original glass, as well as the control of the crystallization process through thermal treatments and manufacturing processes, all these elements make the glass-ceramic extremely attractive for development of new strategies for science. In this chapter, was made an overview regarding the production of magnetic glass-ceramics from wastes, as well as the formation of nanocrystal phases in glass-ceramics and the importance of magnetite and alternative ferrites to enhance the magnetic proprieties. Several points were addressed to bring a general conception to the reader, and it dealt with possible future applications for these materials. In this way, magnetic glass-ceramics have great opportunities: magnetic devices, contrast agents for magnetic resonance imaging, magnetic hyperthermia, drug delivery, waste sorbents and microwave absorption devices.

Keywords Glass-ceramics · Magnetic · Wastes · Nanoparticles

Abbreviations

BISCOS	($Bi_2Sr_2CaCu_2O_8$)
HC	Coercive field
LAS	(Li_2O-Al_2O_3-SiO_2)
MAS	(MgO-Al_2O_3-SiO_2)
MMBG	Magnetic mesoporous bioactive glass
MNPs	Magnetic nanoparticles
MRI	Magnetic resonance imaging

T. G. Avancini (✉)
Universidade Federal do Rio Grande do Sul, Porto Alegre, Brazil
e-mail: talesavancini@gmail.com

S. Arcaro
Universidade do Extremo Sul Catarinense, Criciúma, Brazil

A. Kopp Alves (ed.), *Nanomaterials for Eco-friendly Applications*,
Engineering Materials, https://doi.org/10.1007/978-3-030-26810-7_11

MR	Remanent magnetization
MS	Saturation magnetization
PMAS	Polycrystalline (MgO-Al_2O_3-SiO_2)
SBF	Simulated body fluid
SW	Sintered waste
ZAS	(ZnO-Al_2O_3-SiO_2)

1 Introduction

Currently, the magnetic nanoparticles have attracted attention from the scientific community and the productive sector. This fact is due mainly to its excellent properties and possible applications in diverse areas such as biotechnology, biomedical sciences, ferrofluids devices, data storage, catalysis, image analysis by magnetic resonance imaging and [1. 2].

Magnetic nanoparticles show remarkable new phenomena such as superparamagnetism, high-field irreversibility, high saturation field, extraordinary anisotropy contributions, or shifted loops after field cooling. These phenomena arise from the finite size and surface effects that dominate the magnetic behavior of individual nanoparticles [3].

The major obstacles to the implantation of magnetic nanoparticles in the practical context are generally related to the surface/volume ratio of these systems. That is, the same characteristic that gives magnetic nanoparticles unique properties also generates stability problems over time. Magnetic nanoparticles tend to form agglomerates and, if not coated with a protective layer (core/shell systems), tend to oxidize [4, 5]. In this sense, the obtaining of nanoparticles by the synthesis of glass-ceramics can be a way to get stable magnetic nanoparticles. The amorphous matrix offers chemical as well as mechanical support and protection of the obtained crystals, thus preventing them from clustering or degradation during transportation, storage or operation of the devices in which they find the application.

Furthermore, synthesis of nanostructured materials via the glass-ceramic route has the advantage over the others as their preparation is easy and economical, and fine-grained microstructures could be achieved by controlling the crystal size by nucleation and growth processes [6]. Beyond a classical approach, with compositions constituted by virginal raw materials, many other opportunities had been studied to create reliable glass-ceramics from wastes [7–9]. The majority of those studies are focused on wastes neutralization (sludge and slag) through the glass phase and then try to find a suitable application. However, in case of glass-ceramic embedded with magnetic nanoparticles, a more sophisticated approach is necessary and targeting applications like the aerospace technology with development of new glass fibers, or biomedical application, such as nanostructures for drug delivery, or as markers in magnetic resonance imaging (MRI), for cancer treatment with hyperthermia [10].

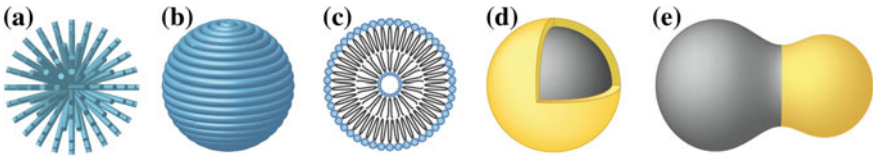

Fig. 1 MNP structures and coating schemes. **a** End-grafted polymer coated MNP. **b** MNP fully encapsulated in polymer coating. **c** Liposome encapsulated MNP. **d** Core–shell MNP. **e** Heterodimer MNP (Reprinted from [17])

2 Magnetic Nanoparticles

Magnetic nanoparticles (MNPs) are materials with particles size less than 100 nm and is possible to manipulate under the influence of an external magnetic field. MNPs generally can be ferrimagnetic or ferromagnetic. These particular types of particles have a magnetic behavior distinct from their bulk counterpart, and this feature makes them deeply attractive. MNPs have a lesser coercivity, which facilitates the manipulation of the magnetic moment and the results for the intended interactions. Furthermore, magnetic nanoparticles tend to have fewer magnetic domains and, if the particle is small enough (>20 nm), they may have only one domain, which means that they are in a superparamagnetic state, a single magnetic domains result in much higher magnetic susceptibilities than paramagnetic materials [11].

The study of these MNPs in recent decades has provided advances in the development of magnetic drug delivery to a specific site in the body (Fig. 1), or hyperthermia cancer treatment, or the development of sorbents, microwave dives technology, spintronics [12–14]. Moreover, MNPs are commonly composed of magnetic elements, such as iron, nickel, cobalt and their ferrites, like magnetite (Fe_3O_4), maghemite (Υ-Fe_2O_3), cobalt ferrite (Fe_2CoO_4) [15, 16]. These ferrites, soft magnets, are perfectly suitable to glass ceramics promoting a great synergy and can make a reliable alternative to working as a pure MNPs because the magnetic nanocrystals embedded in a glass matrix are already protected from any stabilization problems commonly occurred in some of those mentioned applications. In this way, magnetic nano glass-ceramic is ready for further research.

3 Magnetic Glass-Ceramics

Historically, glass-ceramics were discovered accidentally in 1953 by Stookey, one night he forgot to turn off the furnace and overheated their sample, activating the necessary temperature to promote the crystallization [18]. Since then, glass-ceramic have been worldwide researched and many patents and publications granted, like the well know glass ceramics system LAS (Li_2O–Al_2O_3–SiO_2) with her impressive negative thermal expansion coefficient (TEC), suitable for a thermal shock resistant, it was popularized in the domestic market used in the cooktops [19].

Glass-ceramics are inorganic, non-metallic materials, prepared by controlled crystallization of specific glass generally induced by nucleating additives. The glass-ceramics contain at least one type of functional crystalline phase and a glassy phase which may be only residual since the crystallized volume fraction can range from ppm to almost 100% [20]. Glass-ceramic materials are known for their unusual combination of properties, as a composite material, and with different products marketed to specific consumer markets. Its characteristics are correlated with the intrinsic properties of the crystals (morphology, quantity, size, and distribution) and the residual glassy phase, as well as the residual porosity of the sintered glass ceramics [21]. The type of crystalline phase and the properties of glass-ceramic materials can be controlled by the chemical composition of the parent glass, and the heat treatment applied [22].

Also, the heat treatment mechanism facilitates the success of the desired nucleation phenomenon, with the formation of sites, nuclei, for the growth of crystals in a controlled manner in the glass matrix. Depending on the characteristics of the constitution of the glass-ceramic material, the vitreous-crystalline system, the final properties determine and direct the materials to different applications such as optical (liquid crystal display), biological (restorative), electrical (insulators) and magnetic (hyperthermia) [6]. On the other hand, there is the rare phenomenon of spontaneous crystallization that does not require heat treatment to initiate the partial crystallization of the material, breaking with expectations of absolute control of the crystallization process with nucleation. There are records in the literature [23–26], of systems such as SiO_2-Fe_3O_4-B_2O_3 obtaining uncontrolled magnetite crystallization during the traditional air-cooling process, but usually a posteriori the thermal treatment to maximize the desired properties.

There is a wide variety of glass-ceramic systems; these are described and characterized through the main oxides of their composition that can provide a set of specific properties. The classification of glass-ceramics into groups according to the main crystalline phase present or chemical composition: alkali silicate and alkaline earth silicates; 16 aluminosilicates; fluorosilicates; silica-phosphate; iron silicate; phosphates; perovskites; ilmenite [6]. In addition to the traditional classifications of the groups, certain specific systems are gaining notoriety in the scientific field and carry the mark and focus of the study, such as LAS system (Li_2O-Al_2O_3-SiO_2) [27]. Numerous other systems have already been explored MgO-Al_2O_3-SiO_2 (MAS) and the polycrystalline variation (PMAS) for shielding and ballistic applications [28]; ZnO-Al_2O_3-SiO_2 (ZAS) optical properties [29]; Na–Ca-Si-PO, low density bioactive system [30]; CaO-SiO_2-Fe_2O_3-B_2O_3-P2O, bioactive, used in hyperthermia treatments [31]; superconducting fiberglass (BISCO, $Bi_2Sr_2CaCu_2O_8$) [32]. Therefore, the most diverse glass-ceramic systems can be found, due to the ease of designing the composition, with the appropriate thermal treatment, allowing the optimal control of the microstructure and a wide range of properties and functionalities can be explored.

Magnetic-property glass-ceramics can be classified into two main groups concerning their coercivity, such as soft or hard magnets. They can be made in the same way as other glass-ceramics, using glass base in traditional processes of melting, or, sintering, followed by further heat treatment with controlled crystallization [23].

The glass-ceramic hard magnets had their greatest relevance in the search for development of technologies for hard disk and magnetic tapes, using barium hexaferrite and strontium [33, 34]. However, the magnetic glass-ceramic from ferrites, soft magnets, stand out for remarkable applications. Applications in the body can be divided into therapies (hyperthermia for cancer treatment or drug delivery) and applications in imaging diagnostics (magnetic resonance imaging). Otherwise, in vitro applications are for laboratory diagnosis, cell separation, of tissues [35]. There are several investigations for applications for information storage, ferrofluid technology and refrigeration magneto caloric [36].

Ebisawa et al. [37] prepared ferrimagnetic glass-ceramic by treatment thermal analysis of vitreous systems (FeO, Fe_2O_3)-CaO-SiO_2 with the addition of nucleating agents while evaluating their bioactivity. It was verified that glass-ceramic with Na_2O or B_2O_3 in combination with P_2O_5 present bioactivity. The magnetite content nucleation of these systems increased with increasing heat treatment. Moreover, Sandu et al. [38] prepared and determined some structural properties of magnetic with nanometric magnetite obtained by the crystallization of borate glasses. Some glass compositions with different proportions of Fe_2O_3/SiO_2 were investigated, in which the nucleating, modifying and intermediaries were also systematically varied. Research shows ferromagnetic glass-ceramics containing nano-crystalline magnetite in the SiO_2-B_2O_3-Fe_2O_3-SrO system can be prepared using different manufacturing methods: for example, fiber drawing, melt tempering, natural cooling, and annealing. The best magnetic saturation result in this study reached 22 emu/g, and the coercivity depends more on the composition chemical and manufacturing method [39].

4 Magnetic Glass-Ceramics Applications

4.1 Biomedical Applications

The magnetic nanoparticles for biomedical applications are a useful technology that could work inside (in vivo) or outside (in vitro) the body. In vivo applications can be found in cancer treatment (hyperthermia), and drug delivery, and some diagnostic applications, as markers (magnetic resonance imaging, MRI). Otherwise, in vitro applications are mainly used in laboratory analysis for diagnostics, separation, selection, and magnetorelaxometry [5].

Ebisawa et al. discovered in 1997 that bioactive and ferromagnetic magnetite-based glass-ceramics could be useful as thermoseeds for hyperthermia treatment of cancer, especially in cases of deeply rooted cancers such as bone tumors [37]. Singh et al. tested the apatite-forming ability and magnetic properties of glass-ceramics containing zinc ferrite ($ZnFe_2O_4$). In 2015 researchers studied composite bone cement loaded with a bioactive and magnetite-based ferrimagnetic glass-ceramic, no release of iron was revealed in the physiological solution, and bioactivity tests show hydroxyapatite precipitates on the cement surface [40].

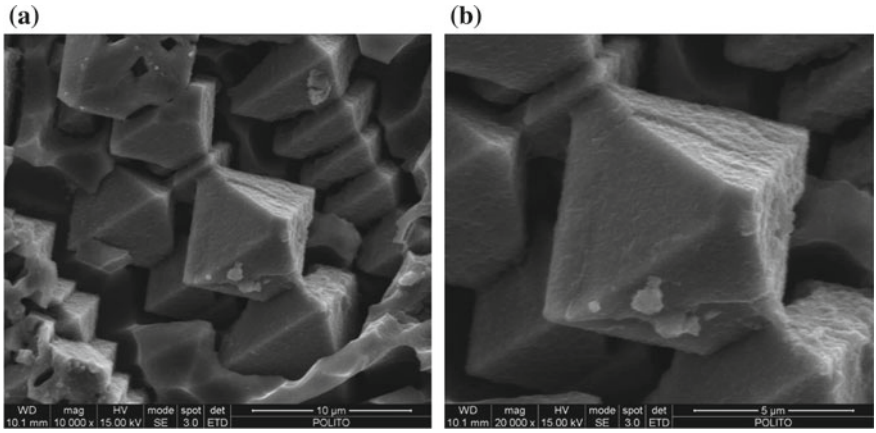

Fig. 2 SEM images of a SC45 bulk glass ceramic sample after chemical etching at different magnifications (Reprinted from [41])

Recently Bretcanu et al. studied a magnetic glass-ceramics containing magnetite crystals (Fig. 2); the work was focused on in vitro evaluation of the biocompatibility, before and after soaking in a simulated body fluid (SBF) with good results [41]. In the case of drug delivery, a multifunctional magnetic mesoporous bioactive glass (MMBG) with nano magnetite has been showing good results, improving drug sustained release property, but also possess bactericidal activity [42]. These results are a clear opening for new strategies with glass-ceramics.

4.2 Wastes to Produce Magnetic Glass-Ceramic

A large number of current studies in the literature addressing the magnetic glass-ceramics produced from waste. Rawlings et al. reviewed glass-ceramics and their production from wastes this at 2006 [43]. This works are similar in one way, in the crate the glass-ceramics from wastes targeting the neutralization, and make the characterization of the material. As an example, Francis et al. studied the feasibility of conversion of an intimate mixture of blast furnace slag and blast furnace flue dust into magnetic glass–ceramic product. The obtained glass-ceramic sample exhibited magnetic properties which were related to the presence of magnetite/maghemite phase besides the pyroxene Ca(Mg, Fe, Al)(Si, $Al)_2O_6$ crystalline phases. The activation energy of crystal growth for the first and second peaks was 355 and 329 kJ/mol respectively. The presence of sharp and broad crystallization peaks indicates that simultaneous surface and bulk nucleation mechanism may be operative. The results of various properties and acid resistance measurements suggest that the glass-ceramic samples are very promising applications in several engineering areas [8]. At 2018 researchers also used hazardous wastes, from ferronickel to create a magnetic glass

ceramic, leading to the formation of Fe-rich droplets with a size of 50–70 nm, subsequently, these droplets are transformed into nano magnetite crystals, and the growth of pyroxene, resulting in a complex structure and characterized [44]. These type of study using hazardous wastes like a slug, sludge, bast furnace are very relevant, but dependent on finding an application after to active her potential. This chapter is looking for this problem, without losing the effort into a more eco-friendly way, but focus on encouraging engineering to achieve goals with greater application potential.

Typically, magnetic glass-ceramics requires the magnetite phase or some ferrite variations, and the iron-rich residues may be an excellent source to the development of this material due to the low contamination of other metals. Indeed, this contaminations of other metals can be useful and act as nucleating agents. An enormous waste in this manner is the iron scale found in the metallurgical field, is the dust originated from the oxidation of steel.

Recently researchers discover more about magnetite-based nano glass-ceramics produced from wastes (borosilicate glass and iron scale) shown in Fig. 3. The author's authors produced glass-ceramics by increasing the amount of iron scrap in the composition. (20, 30, 45 wt%). The sample of 45 wt% was heat treated in three ways 700, 800, 900 °C/30 min, resulting in three new samples. The 900 °C/30 min heat treatment revealed to be detrimental for crystallinity of the magnetite. The 800 °C heat treatment was highly effective, their results revealed a magnetic nano glass-ceramics with high magnetic saturation (42 emus/g), and maintaining the lower coercivity (~200 Oe), with an average nanocrystal size of 50 nm. Those results are leveraging the application of the obtained magnetic nano glass-ceramics, and could be a substitute for the pure magnetite in applications such as hyperthermia, microwave absorption, or waste sorbent devices [45]. The research also proves that iron scale is highly underrated waste material, and can be an excellent supply for iron oxide (~95 wt% of Fe), and possibly will be considered a reliable co-product for the metallurgical steel plants shortly.

A ferrimagnetic glass-ceramic frit has been produced also by González-Triviño et al. using bauxite residue, coal fly ash, and glass cullet as raw materials. The glass-ceramic produced by them frit consists of small crystals (faceted and dendritic agglomerated particles) embedded in a glass matrix [46]. The size range was found between 10 and 30 nm for smaller faceted grains, the same order of magnitude as the estimated by the Scherrer equation, and between 100 and 400 nm for dendrites. The selected area electron diffraction patterns of the different particles analyzed exhibited a polycrystalline habit. The crystalline phases observed was magnetite and titanomagnetite, which provided a saturation magnetization (MS) of 6.3 emu/g, a remanent magnetization (MR) of 2.7 emu/g and a coercive field (HC) of 347 Oe. The synthesized material presents values of 5.55 ± 0.16 GPa for Vickers hardness and 1.64 ± 0.34 MPa ml/2 for fracture toughness. Those results grant more mechanical resistance for a frit and enables a magnetic approach [46].

Abdel-Hameed et al. [47], makes a smart work with recycling of iron from sintered wastes, converting into nanoparticles of barium hexaferrite and zinc-ferrite glass-

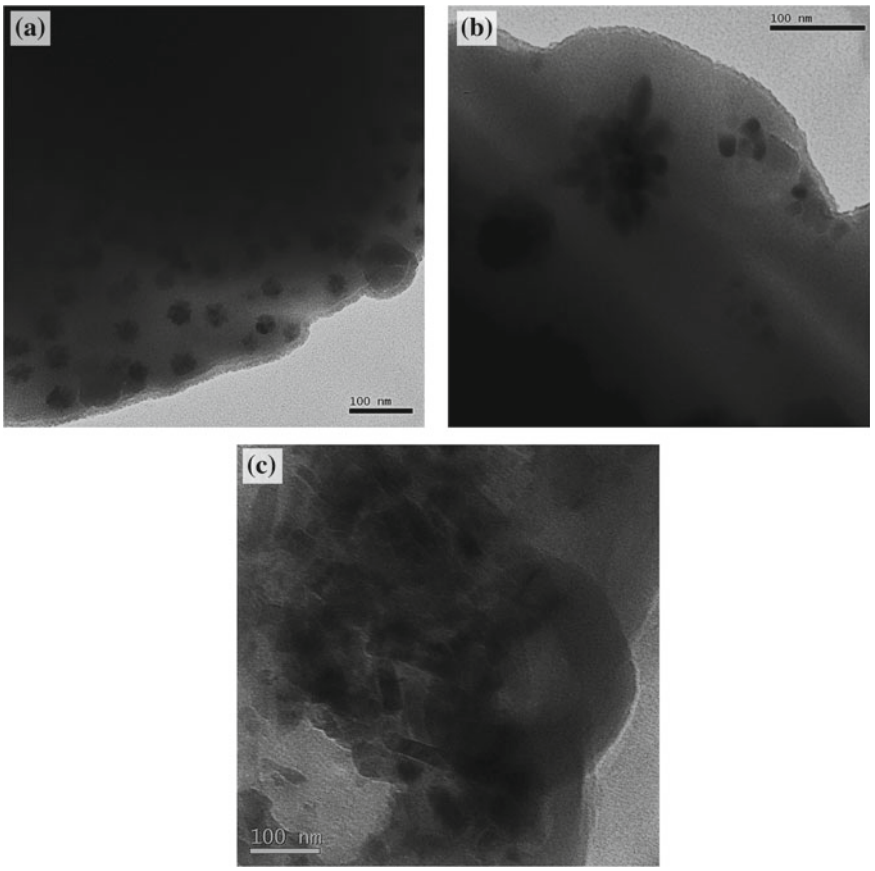

Fig. 3 TEM images from of the obtained magnetite nano glass-ceramics (**a**–**c**) respectively with 20, 30, 45 wt% of iron scale (Reprinted from [45])

ceramics. Because about 25% of iron oxides in the sintering process wastes. They sintered waste (SW) was used as a source of iron oxides to prepare both hard and soft magnetic glass-ceramics via a melting-quenching technique. About 71 wt% of sintered waste was used for making soft magnetic glass-ceramics, while 46% was used for making hard magnetic glass-ceramics. The characterization revealed a crystallization of both hematite and Zn-ferrite phases in sintered waste, while the glass-ceramic samples from sintered wastes showed Zn-ferrite or Ba-hexaferrite phases crystallized in soft magnetic and hard magnetic, respectively. Transmission electron microscopy determined the nano-particles size, about 20 and <15 nm for soft and hard magnetic glass-ceramics respectively. The results of magnetic proprieties for the hard magnetic glass-ceramics with the 900 °C/2 h heat treatment, shows the best result of 22.27 emu/g. However, without heat treatment, the soft magnetic glass ceramics revealed an unusual effect, a very high magnetic saturation of 44 emu/g.

After the heat treatment of 900 °C/2 h the magnetic saturation decreases, curiously the similar result revealed with the iron scale glass-ceramic research, with the loss of crystallinity [45].

5 Conclusions

The upset for the production of glass-ceramic from wastes is to apply the results obtained in the laboratory under practical conditions, and in case of biomedical applications, cytotoxicity tests are always required. Even if some novelty, like the magnetic magnetite-based nano glass-ceramic produced with iron scale, do not reach the requirements to be applied in hyperthermia cancer treatment, there is a lot of room to create nanostructured composites to break this barrier. After all, this kind of challenge in glass-ceramics must be the approach to more environmentally friendly engineering. In this way, magnetic glass-ceramics have great opportunities: magnetic devices [6], contrast agents for magnetic resonance imaging [48], magnetic hyperthermia [1], drug delivery [42], waste sorbents [49] and microwave absorption devices [50].

References

1. Ito A, Shinkai M, Honda H, Kobayashi T (2005) Medical application of functionalized magnetic nanoparticles. J Biosci Bioeng 100:1–11. https://doi.org/10.1263/JBB.100.1
2. Zahn M (2001) Magnetic fluid and nanoparticle applications to nanotechnology. J Nanoparticle Res 3:73–78. https://doi.org/10.1023/A:1011497813424
3. Batlle X, Labarta A (2002) Finite-size effects in fine particles: magnetic and transport properties. J Phys D Appl Phys 35:R15–R42. https://doi.org/10.1088/0022-3727/35/6/201
4. Lu A-H, Salabas EL, Schüth F (2007) Magnetic nanoparticles: synthesis, protection, functionalization, and application. Angew Chemie Int Ed 46:1222–1244. https://doi.org/10.1002/anie.200602866
5. Tartaj P, del Puerto Morales M, Veintemillas-Verdaguer S, González-Carreño T, Serna CJ (2003) The preparation of magnetic nanoparticles for applications in biomedicine. J Phys D Appl Phys 36:R182–R197. https://doi.org/10.1088/0022-3727/36/13/202
6. Höland W, Beall GH (2012) Glass-Ceramic technology. Wiley, Hoboken
7. Jordanova D, Jordanova N, Hoffmann V (2006) Magnetic mineralogy and grain-size dependence of hysteresis parameters of single spherules from industrial waste products. Phys Earth Planet Inter 154:255–265. https://doi.org/10.1016/J.PEPI.2005.06.015
8. Francis AA (2006) Crystallization kinetics of magnetic glass–ceramics prepared by the processing of waste materials. Mater Res Bull 41:1146–1154. https://doi.org/10.1016/J.MATERRESBULL.2005.11.002
9. Francis AA (2007) Magnetic characteristics of iron-containing glass originated from the mixture of various wastes. Ceram Int 33:163–168. https://doi.org/10.1016/J.CERAMINT.2005.09.005
10. Salunkhe AB, Khot VM, Pawar SH (2014) Magnetic hyperthermia with magnetic nanoparticles: a status review. Curr Top Med Chem 14:572–594. https://doi.org/10.2174/1568026614666140118203550

11. Blaney L (2007) Magnetite (Fe_3O_4): properties, synthesis, and applications. Lehigh Rev 15:33–81. https://doi.org/10.1016/j.ceramint.2011.11.027
12. Pardavi-Horvath M (2000) Microwave applications of soft ferrites. J Magn Magn Mater 215–216:171–183. https://doi.org/10.1016/S0304-8853(00)00106-2
13. Kotnala RK, Shah J (2015) Ferrite materials: nano to spintronics regime. Handb Magn Mater 23:291–379. https://doi.org/10.1016/B978-0-444-63528-0.00004-8
14. Indira T, Nanotechnol PL (2010) Magnetic nanoparticles–a review. Int J Pharm Sci Nanotechnol 3:1035–1042
15. Brabers VAM (1995) Chapter 3 Progress in spinel ferrite research. Handb Magn Mater 8:189–324. https://doi.org/10.1016/s1567-2719(05)80032-0
16. Broese van Groenou A, Bongers P, Stuyts A (1969) Magnetism, microstructure and crystal chemistry of spinel ferrites. Mater Sci Eng 3:317–392. https://doi.org/10.1016/0025-5416(69)90042-1
17. Sun C, Lee JSH, Zhang M (2008) Magnetic nanoparticles in MR imaging and drug delivery. Adv Drug Deliv Rev 60:1252–1265. https://doi.org/10.1016/J.ADDR.2008.03.018
18. Stookey SD (1959) Catalyzed crystallization of glass in theory and practice. Ind Eng Chem 51:805–808. https://doi.org/10.1021/ie50595a022
19. Guedes M, Ferro AC, Ferreira JMF (2001) Nucleation and crystal growth in commercial LAS compositions. J Eur Ceram Soc 21:1187–1194. https://doi.org/10.1016/S0955-2219(00)00333-2
20. Deubener J, Allix M, Davis MJ, Duran A, Höche T, Honma T, Komatsu T, Krüger S, Mitra I, Müller R, Nakane S, Pascual MJ, Schmelzer JWP, Zanotto ED, Zhou S (2018) Updated definition of glass-ceramics. J Non Cryst Solids 501:3–10. https://doi.org/10.1016/J.JNONCRYSOL.2018.01.033
21. Arcaro S (2013) Síntese e caracterização de compósitos de vitrocerâmica do sistema LZS/$A1_2O_{3-a}$ para aplicações na tecnologia LTCC. Universidade Federal de Santa Catarina
22. Doyle C (1989) Glass-ceramic materials, liquid phase separation, nucleation and crystallization in glasses. Elsevier Science Publishers, Amsterdam (Edited by Z. Strnad)
23. Marghussian V (2015) Nano-glass ceramics: processing, properties and applications, 1st edn. William Andrew, an imprint of Elsevier, Oxford
24. Liu J, Zhu C, Zhang M, Zhang Y, Yang X (2017) Ferromagnetic glass ceramics and glass fibers based on the composition of SiO_2-CaO-Al_2O_3-B_2O_3-Fe_2O_3 glass system. J Magn Magn Mater 426:375–379. https://doi.org/10.1016/J.JMMM.2016.11.055
25. Liu J, Zhang M, Zhu C, Liu S, Zhang Y (2017) Preparation and properties of ferromagnetic glass-ceramics and glass fibers in alkali-free and high-iron glass system. Ceram Int 43:4295–4301. https://doi.org/10.1016/J.CERAMINT.2016.12.072
26. Liu J, Zhu C, Zhang M, Zhang Y, Liu S, Yang X (2017) Preparation and properties of ferromagnetic glass ceramics and glass fibers based on the composition of SiO_2-B_2O_3-Fe_2O_3-SrO. J Eur Ceram Soc 37:4707–4714. https://doi.org/10.1016/J.JEURCERAMSOC.2017.05.041
27. Arnault L, Gerland M, Rivière A (2000) Microstructural study of two LAS-type glass-ceramics and their parent glass. J Mater Sci 35:2331–2345. https://doi.org/10.1023/A:1004716018522
28. Benitez T, Gómez SY, de Oliveira APN, Travitzky N, Hotza D (2017) Transparent ceramic and glass-ceramic materials for armor applications. Ceram Int 43:13031–13046. https://doi.org/10.1016/j.ceramint.2017.07.205
29. Suzuki T, Horibuchi K, Ohishi Y (2005) Structural and optical properties of ZnO–Al_2O_3–SiO_2 system glass–ceramics containing Ni^{2+}-doped nanocrystals. J Non Cryst Solids 351:2304–2309. https://doi.org/10.1016/j.jnoncrysol.2005.06.015
30. Mabrouk A, Bachar A, Atbir A, Follet C, Mercier C, Tricoteaux A, Leriche A, Hampshire S (2018) Mechanical properties, structure, bioactivity and cytotoxicity of bioactive Na-Ca-Si-P-O-(N) glasses. J Mech Behav Biomed Mater 86:284–293. https://doi.org/10.1016/J.JMBBM.2018.06.023
31. Ohura K, Ikenaga M, Nakamura T, Yamamuro T, Ebisawa Y, Kokubo T, Kotoura Y, Oka M (1991) A heat-generating bioactive glass-ceramic for hyperthermia. J Appl Biomater 2:153–159. https://doi.org/10.1002/jab.770020303

32. Zanotto E, Cronin J, Dutta B (1988) Melt processing of Bi-Ca-Sr-Cu-O superconductors. Ceram Supercond, II
33. Shirk BT, Buessem WR (1970) Magnetic properties of barium ferrite formed by crystallization of a glass. J Am Ceram Soc 53:192–196. https://doi.org/10.1111/j.1151-2916.1970.tb12069.x
34. Oda K, Yoshio T, Oka KO, Kanamaru F (1985) Morphology and magnetic properties of $BaFe_{12}O_{19}$ particles prepared by the glass-ceramic method. J Mater Sci Lett 4:876–879
35. Tartaj P, del Puerto Morales M, Veintemillas-Verdaguer S, González-Carreño T, Serna CJ (2003) The preparation of magnetic nanoparticles for applications in biomedicine. J Phys D Appl Phys 36:R182–R197. https://doi.org/10.1088/0022-3727/36/13/202
36. Abdel-Hameed SAM, Margha FH (2012) Preparation, crystallization behavior and magnetic properties of nanoparticles magnetic glass–ceramics in the systems Fe_2O_3 CoO MnO_2, Fe_2O_3 NiO MoO_3 and Fe_2O_3 CoO V_2O_5. J Non Cryst Solids 358:832–838. https://doi.org/10.1016/J.JNONCRYSOL.2011.12.073
37. Ebisawa Y, Miyaji F, Kokubo T, Ohura K, Nakamura T (1997) Bioactivity of ferrimagnetic glass-ceramics in the system FeO-Fe_2O_3-CaO-SiO_2. Biomaterials 18:1277–1284. https://doi.org/10.1016/S0142-9612(97)00067-7
38. Sandu V, Nicolescu MS, Kuncser V, Popa S, Pasuk I, Ghica C, Sandu E (2012) Structure and magnetic properties of nanosized magnetite obtained by glass recrystallization. J Nanosci Nanotechnol 12:5043–5050. https://doi.org/10.1166/jnn.2012.4943
39. Liu J, Zhu C, Zhang M, Zhang Y, Liu S, Yang X (2017) Preparation and properties of ferromagnetic glass ceramics and glass fibers based on the composition of SiO_2-B_2O_3-Fe_2O_3-SrO. J Eur Ceram Soc 37:4707–4714. https://doi.org/10.1016/J.JEURCERAMSOC.2017.05.041
40. Verné E, Bruno M, Miola M, Maina G, Bianco C, Cochis A, Rimondini L (2015) Composite bone cements loaded with a bioactive and ferrimagnetic glass-ceramic: leaching, bioactivity and cytocompatibility. Mater Sci Eng, C 53:95–103. https://doi.org/10.1016/J.MSEC.2015.03.039
41. Bretcanu O, Miola M, Bianchi CL, Marangi I, Carbone R, Corazzari I, Cannas M, Verné E (2017) In vitro biocompatibility of a ferrimagnetic glass-ceramic for hyperthermia application. Mater Sci Eng, C 73:778–787. https://doi.org/10.1016/J.MSEC.2016.12.105
42. Liu Y-Z et al (2014) Drug delivery property, bactericidal property and cytocompatibility of magnetic mesoporous bioactive glass. Mater Sci Eng, C 41:196–205. https://doi.org/10.1016/J.MSEC.2014.04.037
43. Rawlings RD et al (2006) Glass-ceramics: their production from wastes—a review. J Mater Sci 41:733–761. https://doi.org/10.1007/s10853-006-6554-3
44. Karamanov A et al (2018) Structure of glass-ceramic from Fe-Ni wastes. Mater Lett 223:86–89. https://doi.org/10.1016/J.MATLET.2018.04.036
45. Avancini TG et al (2019) Magnetic properties of magnetite-based nano-glass-ceramics obtained from a Fe-rich scale and borosilicate glass wastes. Ceram Int 45:4360–4367. https://doi.org/10.1016/J.CERAMINT.2018.11.111
46. González-Triviño I et al (2018) Synthesis and characterization of ferrimagnetic glass-ceramic frit from waste. Int J Appl Ceram Technol 15:775–782. https://doi.org/10.1111/ijac.12850
47. Abdel-Hameed SAM et al (2018) Recycling of iron sintered wastes into nanoparticles barium hexaferrite and zinc-ferrite glass-ceramics. Silicon 10:153–163. https://doi.org/10.1007/s12633-016-9410-3
48. Estelrich J et al (2015) Nanoparticles in magnetic resonance imaging: from simple to dual contrast agents. Int J Nanomedicine 10:1727–1741. https://doi.org/10.2147/IJN.S76501
49. Zhao X, Shi Y, Wang T, Cai Y, Jiang G (2008) Preparation of silica-magnetite nanoparticle mixed hemimicelle sorbents for extraction of several typical phenolic compounds from environmental water samples. J Chromatogr A 1188:140–147. https://doi.org/10.1016/J.CHROMA.2008.02.069
50. Salman SM, Salama SN, Abo-Mosallam HA (2016) Contribution of some divalent oxides replacing Li_2O to crystallization characteristics and properties of magnetic glass–ceramics based on Li_2O–Fe_2O_3–Al_2O_3–SiO_2. Ceram Int 42:8650–8656. https://doi.org/10.1016/J.CERAMINT.2016.02.097